Colección de Estudios de Física 95

Mechanisms for enhancing the optical transmission through a single subwavelength hole

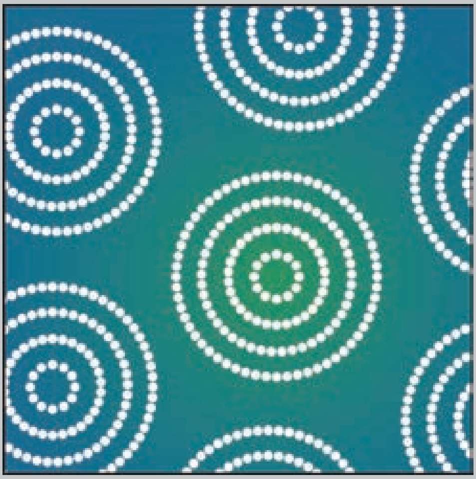

Sol Carretero Palacios

Mechanisms for enhancing the optical transmission through a single subwavelength hole

Colección de Estudios de Física
Vol. 95

Esta colección recoge las tesis presentadas en el Departamento de Física de la Materia Condensada de la Universidad de Zaragoza desde su constitución en 1987.

Colección de Estudios de Física Vol. 95

Mechanisms for enhancing the optical transmission through a single subwavelength hole

Sol Carretero Palacios

Prensas Universitarias
Universidad Zaragoza

CARRETERO PALACIOS, Sol
Mechanisms for enhancing the optical transmission through a single subwavelength hole / Sol Carretero Palacios. — Zaragoza : Prensas Universitarias de Zaragoza, 2011
XI, 220 p. ; 25 cm. — (Colección de estudios de física ; 95)
Bibliografía: p. 201-216. — ISBN 978-84-15274-57-5
1. Electromagnetismo–Tesis doctorales. 2. Nanoestructuras
537.8:539.24(043.2)

1.ª edición, 2011

Prensas Universitarias de Zaragoza. Edificio de Ciencias Geológicas, c/ Pedro Cerbuna, 12, 50009 Zaragoza, España. Tel.: 976 761 330. Fax: 976 761 063
puz@unizar.es http://puz.unizar.es

Impreso en España
Imprime: Servicio de Publicaciones. Universidad de Zaragoza
D.L.: Z-146-2012

A Lola y Lorenzo

Contents

Chapter 1

General Introduction

1.1 Optics in metal surfaces: Plasmonics

We should be more than grateful to optics scientists who, during the running wheel of history, enabled us to deeply understand optics, face and solve specific research tasks and design particular optical components and systems.

In antiquity, optics began when Egyptians and Mesopotamians developed the first lenses with impressive mechanisms based on reflection [1]. However, the word optics comes from the ancient Greek word Όπτική, which means "look" or "appearance". Also the ancient Romans and Greeks made lenses by filling glass spheres with water, and along with Indian philosophers, theories of light and vision led to the flowering of geometrical optics. Late after that, during the Middle Ages, optics was significantly reformed by writers in the Muslim world. Remarkably, in 984, the Persian mathematician Ibn Sahl described a law of refraction equivalent to Snell's law, in his treatise "On burning mirrors and lenses" [2].

However, as it happens many times in science, it was in the XVIIth century when the mathematical law of refraction, currently known as Snell's law, appeared. The principles of reflection and refraction were established at that time by Descartes, who assumed that light was emitted by objects which produce it [3]. He also stated that the speed of light was as high as the covered medium is dense. But Fermat's principle went further than that attributing indexes to the media [4]. This principle can be used to derive Snell's law of refraction and the law of reflection.

But this more modern progress still dealt only with geometrical optics and it was considered that light behavior with obstacles could be expressed just in terms of absorption, reflection and refraction. The effects of diffraction of light were first characterized and observed by Grimaldi, whose results regarding a corpuscular theory were published in 1665 [5]. Only 25 years after, Huygens proposed a wave theory for light, which a few years later, was displaced by Newton's corpuscular theory reported in his Opticks [6]. Probably due to Newton's fame, the nature of light was established and diffraction was understood as a result of a corpuscular theory.

Newtonian optics was generally accepted until the early XIX$^{\text{th}}$ century, when after some experiments on the colors of thin plates, Thomas Young observed a wonderful phenomenon which he called "interference" [7]. His observations in combination with Fresnel's studies enabled to develop the mathematics of how wave interference can account for diffraction, firmly establishing light's wave nature.

In the 1860s, wave optics and electromagnetic (EM) theory were successfully unified by Maxwell [8].

Also at the end of the XIX$^{\text{th}}$ century, Kirchhoff added a deeper mathematical basis to the novel diffraction theory established by Huygens and Fresnel, but a few years later, Sommerfeld and Lord Rayleigh considered Kirchhoff's formulation as a first approximation and they advanced what was later called the "Rayleigh-Sommerfeld diffraction theory". An additional phenomenon was added to those concerning the behavior of light in combination with obstacles: diffraction. Indeed, the definition given by Sommerfeld to diffraction was: "Diffraction is any deviation of light rays from the initial path which can be explained neither by reflection nor by refraction" [9].

All these amazing observations, experiments and theories contributed to the further development of optics in many different disciplines in physics, such as quantum optics or specialty areas of research which include the study of how light interacts with specific materials.

In particular, an exciting phenomenon arises when light interacts with metals. One interesting example relies on the "Lycurgus Cup". Probably without Romans' awareness, the recipe for this cup made of ruby glass contained a decisive ingredient which makes it particularly interesting [10]: nano-gold droplets. Due to these gold nanoparticles, the cup shines greenish in daylight, but it exhibits a ruby colour when it is illuminated from inside. This results from the interaction of visible light with the metallic particles of that size, where a surface plasmon resonance takes place.

Some of the scientific studies in which surface plasmons were first observed appeared at the beginning of the XX$^{\text{th}}$ century. Sommerfeld [11] and Zenneck [12] described mathematically the propagation of radio waves along conductors, and around that same time, Wood observed unexplained features in optical reflection measurements on metallic gratings [13]. From 1904 to 1908, Maxwell Garnett, Drude, Lord Rayleigh and Mie greatly developed further understanding of new phenomena in the form of surface plasmons by integrating optics with Maxwell's theories of electromagnetism.

Finally, in 1957, Rufus Ritchie discovered Surface Plasmon Polaritons (SPPs), EM waves trapped at metallic surfaces due to their interaction with the free electrons of the metal [14]. SPPs have often been regarded as unwanted by causing electronic damping effects and radiation losses (half of the energy they carry diffuses as heat after covering $\approx$ 0.1 mm). However recent research efforts in nanotechnology have shown that by understanding the physical sources for such losses and by clever engineering, plasmonic effects are potentially interesting to develop a wide range of plasmon-based optical elements and techniques including a variety of active switches, biosensors, lithography masks, and more. This growing development in science and technology of metal-based optics and nanophotonics is known as Plasmonics.

To understand more about these surface waves appearing at the surface of metallic films, let us start describing the optical properties of metals, which are largely determined by the behavior of free electrons. Drude Model [15] describes the dispersion of the dielectric constant of metals (ϵ_m) with frequency (ω) based on two parameters: first, the characteristic oscillation frequency of the free electrons, known as the plasma frequency (ω_p), and second, their damping time (γ), related to energy losses by heating (Joule's Effect)

$$\epsilon_m(\omega) = 1 - \frac{\omega_p^2}{\omega(\omega + i\gamma)} \tag{1.1}$$

For $\omega < \omega_p$, the dielectric constant is negative. Charges can oscillate in phase with light, and in the absence of damping, the metal would be perfectly reflecting. On the contrary, if $\omega > \omega_p$, the dielectric constant is positive, charges can no longer oscillate in phase with light and therefore, the material becomes transparent and behaves as a dielectric. All phenomena related to these charge oscillations are denominated as *plasmons.*

Surface plasmons occur at the interface between two materials, one with a negative dielectric constant (metals), and another with a positive one (dielectrics) due to the interaction between light and the free electrons of metallic surfaces. Their properties arise from their dispersion relation which shows that these metal-dielectric systems support *surface plasmon polaritons* (SPPs) at the optical regime. These modes are bound to the surface of the metal like modes of a waveguide and they are characterized by a surface wave vector (k_{spp}) that obeys the dispersion relation schematically presented in Fig.1.1.

As can be seen, the red and continuous line corresponding to k_{spp} is always

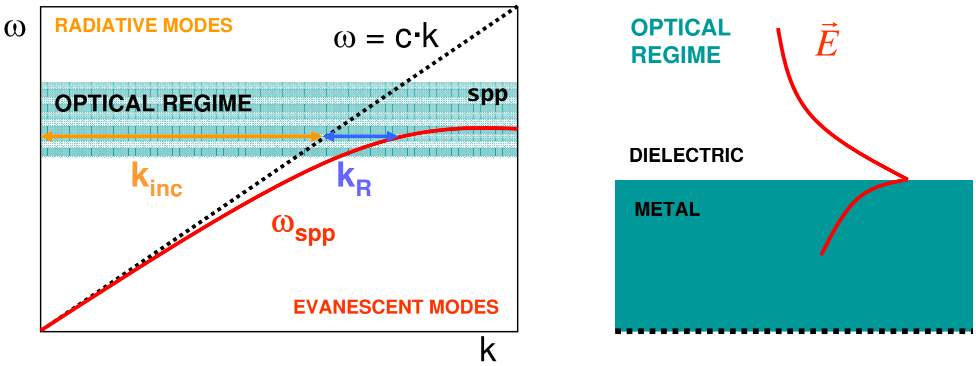

Figure 1.1: Right panel: Schematics of the electric field in a metal-dielectric interface in the optical regime. Left panel: SPP dispersion relation. The light line, in black, separates propagating modes from evanescent ones. k_{inc} corresponds to the transverse component of the incident wave, and k_R accounts for the momentum needed to couple to SPP.

beyond the light line (which separates free-space photons from evanescent ones) and only beyond certain energy values, the SPP dispersion relation is distinguished from the light line.

Also the decay in the z-component, and propagation lengths (in the plane) characterize these surface waves. The decay length is related to the penetration of the electric field into the metal, leading to confined EM fields; whereas the propagation length gives the distance that SPPs can travel before being attenuated by the electronic oscillations inside the metal. Since these two quantities are related one to each other, surface plasmons appear as propagative and confined EM waves.

At low frequencies, SPPs are hardly distinguished from the light line, they are weakly bound to the metal surface and this translates into both low energy losses inside the metal and large decay lengths. However, at high frequencies, SPPs dispersion relation separates from the light line, the absorption at the metal surface is boosted up, and therefore, both decay and propagation lengths decrease leading to confined surface waves.

An important consequence provided by the dispersion relation is that $\lambda_{spp} < \lambda_0$, with λ_0 the wavelength of free-space photons, and λ_{spp} the SPP wavelength. For a given wavelength, a photon in free space has a wavevector (or momentum) that is always smaller than the corresponding SPP one. This means that the momentum (and frequency) conservation required for their coupling cannot be fulfilled, i.e., the evanescent feature of SPPs implies that they cannot be excited directly by external light.

In Fig. 1.1 we can see that, to excite and couple external radiation to SPPs it is necessary an additional momentum k_R to go from the propagating sector (where external light falls) to the evanescent one (where SPPs "live"). These surface modes are often excited through prism [16, 17], grating coupling [18] and near-field coupling.

Other ways to excite SPPs arise when metals are structured at the nanoscale, giving rise to fascinating effects: on the one hand, periodic structuring of a metal surface results in the formation of SP Bloch modes which provide the extra momentum needed to couple the SPP to free space [19], therefore, *periodic structures* such as arrays of grooves or dimples, appear exceptionally attractive to excite surface plasmons. Also holes periodically arranged in a metal film can be used for coupling SPPs on the two sides of the metal film, leading to *enhanced transmission*. On the other hand, when a *single hole* is made in a metal film, localized Fabry-Perot (F-P) resonances take place [20] playing an important role when squeezing light efficiently through subwavelength apertures (apertures whose dimensions are much smaller than the incident wavelength). By combining the last effects, *beaming apertures* can be made where light not only passes through a subwavelength hole, but does not suffer from the usual diffraction afterwards.

1.1.1 Extraordinary Transmission, Light Harvesting and Field Enhancement

Transmission and field enhancement along with beaming phenomena have generated considerable interest not only because of the physics involved but also because of the potential technological applications. Their properties are indeed relevant in many areas of science and technology, ranging from pure optics to chemical sensing.

One of the most obvious applications resides in photonics, opening new possibilities to enhance emission and photodetection by controlling light at the subwavelength scale, and paving the way for a new generation of photonic components where high speed and small sizes are involved. Moreover, going a step further and exploiting nonlinear optical properties in such nanostructures would allow the control of light with light.

Next, we will present the concepts of: (a) Enhanced Transmission, (b) Light Harvesting and Beaming from subwavelength apertures, and (c) Field Enhancement.

(a) Enhanced Transmission.

One of the simplest optical devices we can imagine is a hole drilled in a metallic screen. Hans Bethe in 1944 described theoretically the diffraction of light at a fixed wavelength, λ, through a circular hole of radius $r << \lambda$ in an ideal situation where the screen was considered as a perfect electrical conductor (PEC) and the thickness was infinitely thin [21]. He found that transmission (T) of light at the other side of the metal screen follows $T \propto (r/\lambda)^4$. This means that if the hole radius is much smaller than the incident wavelength, transmission efficiency is extremely poor. Besides, while for large apertures light is transmitted in the same direction as the incident one, for subwavelength apertures the few transmitted light spreads isotropically (see schematic in Fig.1.2).

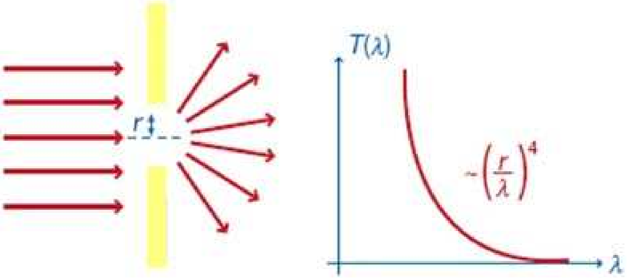

Figure 1.2: Diffraction and typical transmission spectrum of visible light through a subwavelength hole in an infinitely thin perfect metal film [22].

However, in 1998 Thomas Ebbesen and co-workers found experimentally a new and revolutionary phenomenon called Extraordinary Optical Transmission (EOT) [23], where transmission of light through an array of subwavelength apertures drilled in a metal film could exceed unity (when normalized to the area of the holes), i.e., it could be orders of magnitude greater than that predicted by standard aperture theory. This Extraordinary Transmission of EM radiation relies upon the interaction of light with a real-metal periodic structure of finite thickness with holes on it, resulting in the formation of SP modes at the metal surfaces. The grating serves to diffract and scatter the incident light providing the extra momentum needed so that the resulting diffraction orders of the incident light along the interface match the SP waves with the external light.

Afterwards, light “tunnels” through the apertures causing an energy transfer towards the exit surface of the film, where the SP modes are in turn excited and eventually decoupled into freely propagating light.

In this process, the excitation of SPPs enhances the EM field above the holes, increasing the probability of transmission via tunneling by orders of magnitude in such a way that the metal becomes “virtually invisible”: a large fraction of the light impinging directly on the metal surface is transmitted. Hence, the transmission spectra display peaks whenever a SP mode is excited.

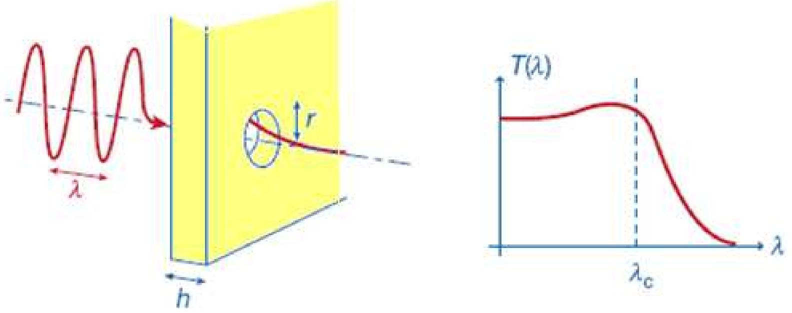

Figure 1.3: A cylindrical waveguide with radius r much smaller than the wavelength λ of the incident electromagnetic field milled in a metal film of thickness h [22].

To sum up, the enhanced transmission can essentially be understood as a three step process: **(i)** coupling of light to SPPs on the incident side, **(ii)** tunneling of light through the apertures, and **(iii)** decoupling of the surface plasmon to light on the exit side. The fact that the 3 steps can often be treated as independent phenomena opens the possibility of optimizing each of them to maximize the throughput for a given application.

(b) Light Harvesting and Beaming from a subwavelength aperture.

The enhanced transmission can be observed even for a single aperture when it is surrounded by a periodic corrugation. These systems are of great interest since the optical transmittance through them can be strongly boosted up with respect to that of an isolated aperture. In particular, Bull's Eye (BE) structures, consisting of a subwavelength aperture surrounded by annular grooves, and its one dimensional version (1D, a slit flanked by linear grooves), have stimulated many works to understand how these systems enhance and focus the transmitted light [24–36]. The principle of light harvesting is based on the effect of transmitting the same optical power density of an incoming light beam onto a smaller detection area. This may lead to interesting designs for photodetectors where SPPs propagating at the metal surface are efficiently coupled to a detection area that may be located even on the far of the metal structure (see Fig. 1.4).

In addition, such structures have revealed a new aspect of this phenomenon, namely, the modification of the intrinsic diffraction pattern of the subwavelength aperture. According to standard EM theories, like Bethe's one, a subwavelength hole diffracts light in all directions. In contrast, it is possible to concentrate the transmitted light into a narrow beam within an angular divergence of a few degrees, by surrounding the hole with an appropriate grating on the exit face of the metal film (Fig. 1.5). The origin of this directionality has

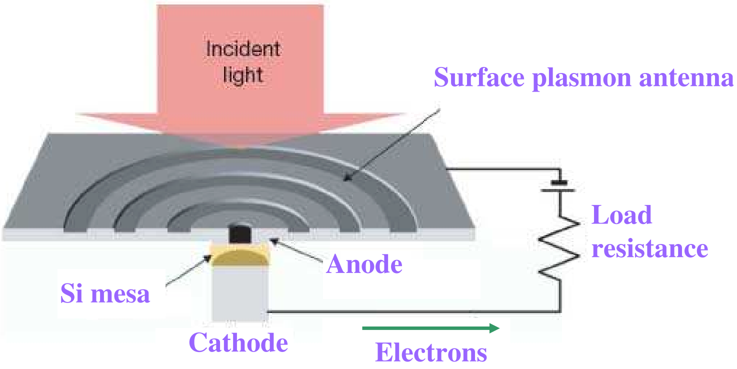

Figure 1.4: Ultrafast miniature photodetector. The device consists of a small Si photoelectric element and a bull's eye structure acting as an antenna where the incoming light is harvested and then transmitted through the central hole to the underlying photodetector [22].

been explained in 1D systems by the activation of SPPs on the exit grating illuminated by SPP surface waves [22, 25, 37].

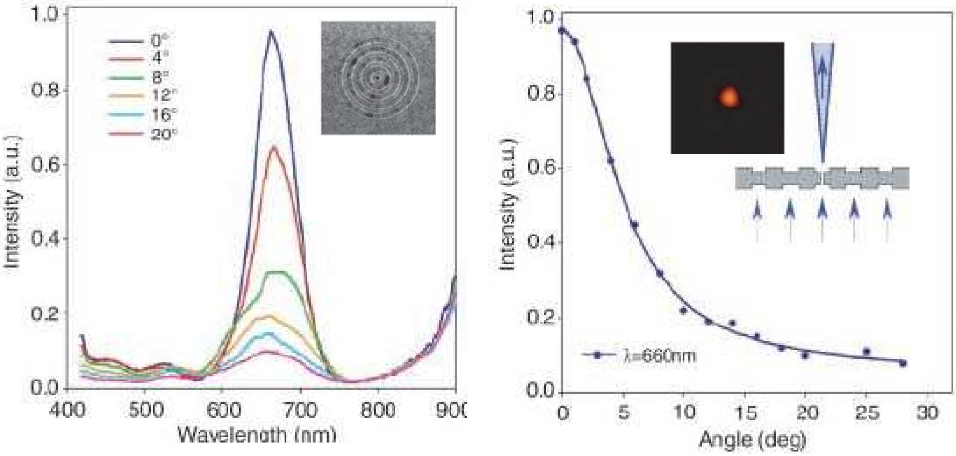

Figure 1.5: Experimental angular transmission-intensity distribution at resonance emerging from the bull's eye geometry [25].

(c) Field Enhancement.

Periodic structuring also provides additional local enhancement related to redistribution of SPP energy along the structured surface. This allows to achieve strong enhancement of the EM field in subwavelength size areas close to the structured surface. Both the resonant wavelength and the enhancement value are determined by the shape, size, dielectric constant and surroundings of the metallic systems. A thorough understanding of the mechanisms which produce large field enhancement at the surface, along with the interplay between plasmon modes on structured films, would lead to some benefits: the larger the field, the better the photo-detection sensitivity that can be achieved; and the stronger the confinement, the smaller the volume that can be used for photodetection. Small sizes translate into faster signal processing speeds, but also into a limitation in light harvesting, so optimization studies are also desired.

Field enhancement effects have been successfully used to enhance Raman scattering [38], second- and third-harmonic generation, Kerr non-linearity [39], chemical and biological sensing [40], security screening [41], communications [42], and other optical processes.

Another potential use of surface plasmons related to the phenomena previously described are the design of Light Emitting Diodes (LEDs). Basically, an LED is a semiconductor device which emits light when a PN union is directly polarized and an electric current flows along it. The idea consists of using periodic metallic hole arrays in contact with high index substrates (semiconductors) working as LEDs or transparent electrodes. The metallic part would provide the conductive function, while holes would both emit more light due to Extraordinary Transmission and improve the efficiency since the metallic film is carved with holes.

A fundamental aim is therefore to gain enough understanding of the individual steps of the enhanced transmission and field enhancement, as well as the collective process to maximize the efficiency when designing devices based on these phenomena. In fact, many topics have yet to be addressed such as the study of enhanced transmission structures with high index substrates, the coupling of guided modes through subwavelength apertures, the reduction of reflection losses in light harvesting structures, or the study of how light can be controlled with light, amongst others.

1.2 Annular Holes and Bull's Eye structures

A real aperture drilled in a screen of finite thickness is characterized by that thickness, and therefore, it possesses waveguide properties. Transmission of light through apertures depends on the hole shape. Boundary conditions at the waveguide edges determine the cutoff wavelength, λ_c (light does not propagate inside the waveguide at larger wavelengths than the cutoff), delimiting propagative modes from evanescent ones.

Some hole shapes present special characteristics making them suitable for different applications: the less decaying mode inside *slits* is a transverse electromagnetic (TEM) mode deprived of cutoff and their optical response is determined just by one parameter (their width), but also *rectangular* holes may have their cutoff at very large wavelengths. Both shapes at normal incidence depend on the polarization of the light. On the contrary, other simple shapes such as *circles* do not depend on the incident polarization, whereas *triangles* are independent on the angle of incidence for a large range of angles but are strongly dependent on the direction of the incident electric field [43]. Different studies showed that transmission through a rectangular hole presents strong polarization dependencies and higher transmittance than square or circular holes with the same area [44–47]. Moreover, other more sophisticated shapes such as *gammadion shapes*, allows that incident linearly polarized light becomes elliptically polarized upon interaction with them, with the same handedness as the gammadion itself (see Fig. 1.6).

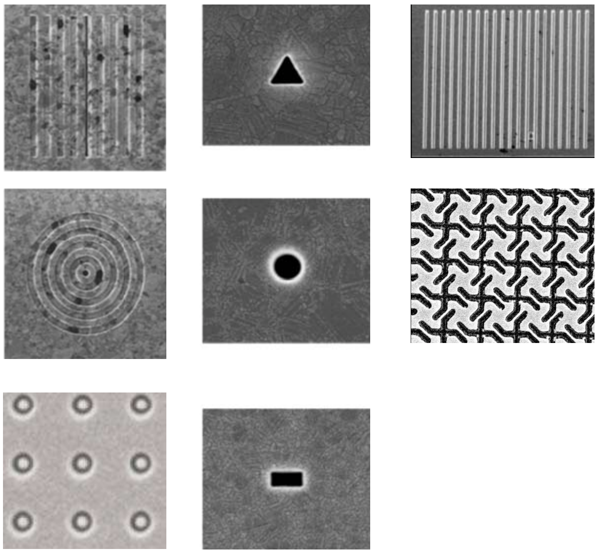

Figure 1.6: Several types of subwavelength apertures. From top to bottom and left to right: slit and linear grooves, single triangle, slit array, Bull's Eye Structure, single circular hole, gammadion array, annular hole array, and single rectangular hole.

Annular holes appear as an exceptionally potential shape. These coaxial apertures are interesting structures because they posses a TEM mode deprived of cutoff, as slits, and because the next fundamental mode, the TE_{11} mode, cutoffs at an unusually long wavelength, as rectangles.

The cutoff of the TE_{11} mode is given by:

$$\lambda_c = \frac{2\pi b}{\chi_{11}} \tag{1.2}$$

where b is the inner radius of the annular hole, and the quantity χ_{11} is the

1st non-vanishing root of the function

$$J_1'(x\,b)Y_1'(x\,a) - Y_1'(x\,a)J_1'(x\,b) = 0 \tag{1.3}$$

Here, a is the outer radius, and J_1' and Y_1' the derivatives of Bessel and Neumann functions of order 1.

Interestingly, for perfect electrical conductors (PECs), it can be approximated as [48]:

$$\lambda_c \approx \pi(a+b) \tag{1.4}$$

In Fig. 1.7 we show both the cutoff wavelength (computed exactly and with the approximation) of a TE_{11} mode of coaxial waveguides drilled in PEC with a fixed outer radius $a = 0.45$ and a variable inner one, r, along with the cutoff wavelength of a TE_{11} mode of a circular aperture where the radius is also labeled as r (in arbitrary units). For annular holes, increasing r entails "narrowing" the openings, whereas for circular holes, increasing r means "widening" the apertures. From this figure we observe that coaxial waveguides can support a propagating mode at much longer wavelengths than circular waveguides of the same outer radius, and that the "narrower" the ring, the longer the cutoff wavelength.

Remarkably, as we will show throughout this thesis, in annular holes:

- a more confined field (smaller hole), a larger λ_c
- a smaller hole presents larger transmission

A schematics of the electric field of the two fundamental modes of annular holes, the TEM and TE_{11}, can be seen in Fig 1.8. Note that **(i)** the electric field of the TEM mode is radially polarized and it cannot be accessed by linearly polarized light impinging at normal incidence, and that **(ii)** the TE_{11} mode could be represented with the electric field pointing "vertically" (the equivalent horizontal mode), making annular holes insensitive to polarization.

Moreover, from the theoretical point of view this shape is interesting because the exact solution of the modes of an infinite annular hole shaped waveguide are analytically known. Explicit expressions can be found in Appendix A.

Finally, and more obvious, this shape is also the basis for studying bull's eye (BE) structures, where a circular aperture is surrounded by concentric annular grooves (see schematics in Fig. 1.9).

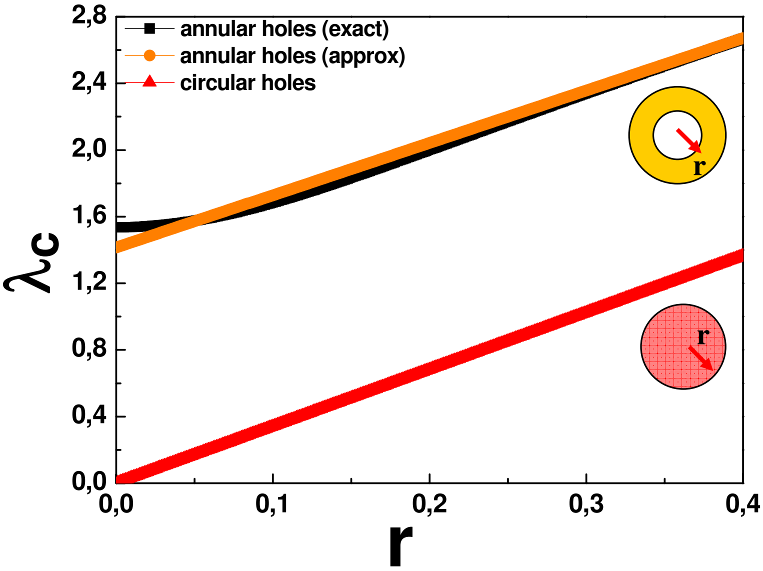

Figure 1.7: Cutoff wavelength for TE_{11} modes of an annular hole, computed exactly (black curve) and approximately (orange curve), and a circular hole (red curve) as a function of r. For the annular hole, the outer radius is fixed to $a = 0.45$ and r accounts for the inner one. For the circular hole, r accounts for the radius.

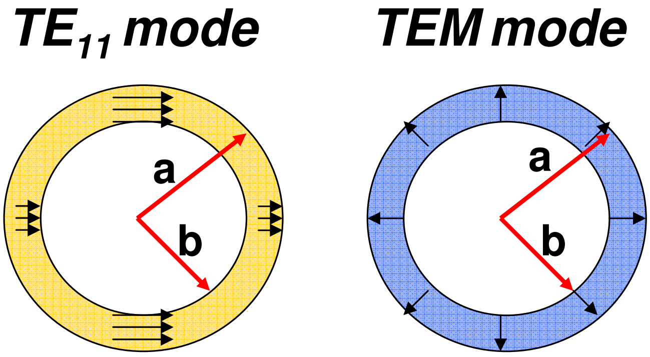

Figure 1.8: Schematics of the electric field of the TE_{11} and TEM modes inside annular apertures of inner radius b and outer one, a.

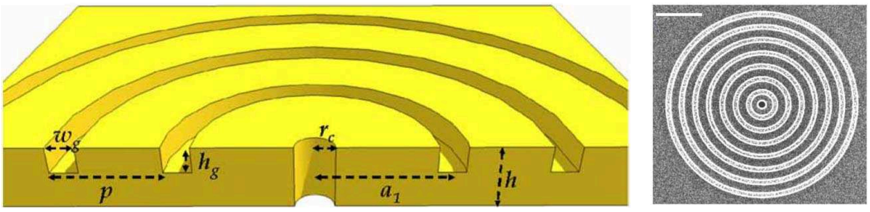

Figure 1.9: Schematics of a Bull's Eye structure and a SEM image of an experimental one.

BE structures are very interesting systems for their potential technological applications as we showed in the previous summary. However, their study appears especially difficult. First of all, while in the 1D version all linear grooves have the same electromagnetic (EM) response, in BE structures the optical response of each annular groove depends on its radius, and therefore, it is different from that of other grooves. Hence, we must deal with resonances related to isolated grooves which will also depend upon the groove depth, but also with collective resonances which result from the interplay between the finite set of concentric grooves.

If each annular groove is allowed to vary its width and depth, but also its position regarding the center of the structure, then the number of parameters entering the optimization process is too large to handle. As a result, we must play several tricks to differentiate amongst the diverse mechanisms controlling the overall optical response in BE structures.

1.3 Thesis Structure

The first part of this thesis is devoted to the theoretical study of optical properties assisted by surface EM waves in metal films periodically pierced with annular holes or dimples, together with the EM phenomena arisen in finite systems where both isolated (circular and annular) holes and BE structures are considered. In the last part of the thesis we will go a step forward, moving from linear to nonlinear physics and we will study transmission properties in nanostructured metal films drilled with slits and combined with nonlinear Kerr-type dielectrics. In more detail:

In Chapter 2 the theoretical formalisms used along this thesis are described. First, we present fundamentals of our modal expansion formalism (the Coupled Mode Method, CMM.). We demonstrate the suitability of this approach for analyzing the scattering properties of perforated metallic films. We show how both infinitely periodic and finite systems can be treated within this framework. In the last section, the Finite-Difference Time-Domain (FDTD) method is briefly described. In this chapter we summarize the most relevant aspects of these two techniques, emphasizing the personal contribution developed in the course of this thesis and which, to our knowledge, cannot be found in literature.

In Chapter 3 we study the optical properties of infinite periodic systems. In particular, we study the EM modes sustained in the Terahertz (THz) regime by metallic structures pierced with annular dimples that give rise to high field enhancement and that allows the system to work as a dual band waveguide.

Additionally, in this chapter we consider a complex system composed by an array of annular holes drilled in a metal film and combined with high index dielectrics (semiconductors). To reach this degree of elaboration, first we study extraordinary transmission of EM radiation through annular hole arrays where the metal is taken as a perfect electrical conductor (PEC) in free standing systems. After that, we consider the metal as a real metal (with finite dielectric constant), and finally, high index substrates are taken into account.

In Chapter 4 transmission of light through isolated annular holes and BE structures is described. Due to the complexity of BE systems, several approaches in the optimization of enhanced transmission are considered. We start from a simplified optimization procedure guided by physical intuition, then move to Conjugate Gradient Methods, and finish with a microscopic study where phenomena controlling transmission of light through these systems are described. Finally, also the spatial distribution of fields radiated by isolated annular holes and BE structures is presented.

In Chapter 5 we analyze resonances appearing at unusual wavelengths beyond the cutoff of the holes. We name this phenomenon Localized Extraordinary Optical Transmission (LEOT). Interestingly, no surface modes are involved; therefore, the physical mechanism is valid for both single holes, and hole arrays. We give analytical expressions for the LEOT peak position as a function of film thickness, and all dielectric constants of the environment (cover, substrate, and inside the holes), for any hole shape, provided they support large cutoff wavelengths.

In Chapter 6 we go a step forward and move to nonlinear problems. We study the nonlinear optical response in arrays of subwavelength slits in combination with nonlinear Kerr-type dielectrics. We propose a scheme for both an optical limiter and a switch of the transmitted light intensity, for operation at telecom wavelengths. We also investigate the Optical Kerr Effect and the Third Harmonic Generation undergone by these kind of structures.

Chapter 2

Theoretical Formalism

2.1 Introduction

In this chapter we present the theoretical methods used along this thesis to describe the optical properties of subwavelength apertures perforated in metallic films: the Coupled Mode Method (CMM) and the Finite-Difference Time-Domain (FDTD) Method.

Electromagnetic (EM) phenomena in metallo-dielectric structures are defined by the well established macroscopic Maxwell equations. However, due to the wide range of length scales appearing in these combined systems, it is difficult to solve them. For instance, the wavelength of light propagating in vacuum in the optical regime varies from 400 to 800 nm; typically, the penetration of the EM field in metals is of the order of 30 nm; and the length scale associated with the periodicity in arrays of dimples and holes in metallic surfaces generally varies from hundreds of nanometers to a couple of microns.

Therefore, in order to compute the optical properties of the metallo-dielectric systems here studied, two different methods have been employed. These techniques display special advantages that make them more suitable for solving certain kind of problems and overcoming different drawbacks.

2.2 Coupled Mode Method

The Coupled Mode Method (CMM) is a general method for solving linear differential equations based on the modal expansion of the fields: the EM fields inside the apertures are expanded into waveguide modes and the EM fields in free space are expanded into an infinite set of plane waves. By imposing the appropriate matching conditions at the metal/dielectric interfaces, Maxwell equations can be solved in all the space. A full description of this method can be found in Ref. [49] and references therein.

One of the most important advantages of this method is that the same equations can deal with the physics of very different structures and it is not restricted by the size of the system under study. Hence, the same equations are applicable to the analysis of large schemes with either infinite periodic arrays or finite systems.

Transmission of light through slit arrays [50–52], hole arrays [49, 53–56], as well as through quasi-periodic hole arrays [57, 58] have been widely investigated. Also finite systems made up of isolated holes [59–61], finite chains of subwavelength apertures [62] or Bull's Eye (BE) structures [63] together with its 1D version with slit and linear grooves [64] have been studied as well. Band structures [65], scattering of surface plasmon polaritons (SPPs) by one-dimensional periodic nano-structured surfaces [66] and by array of holes [67] are also attainable with the CMM. Even approximate nonlinear properties can be treated within this approach [68]. And finally, the CMM has been also applied to other undulatory entities such as cold atoms (matter waves) [69] or sound (acoustic waves) [70].

This method is fast and does not consume exaggerated computer resources compared to other numerical methods, and we can easily accommodate for arbitrary illumination plane waves at non-normal incidence or focused beams.

Another main advantage of this modal expansion arises when we first approximate the metal as a perfect electrical conductor (PEC), i.e., $\varepsilon_m = -\infty$ which allows, for some geometries, to express analytically the waveguide modes inside the apertures. The PEC approximation neglects the penetration of the fields inside the metal, providing a quasiexact model in the terahertz (THz) or microwave regime where also surface waves (Spoof Plasmons) may appear when holes are periodically arranged [71]. The finite dielectric constant of metals at optical frequencies can be incorporated into the formalism using the Surface Impedance Boundary Conditions (SIBCs) [72], giving semiquantitative value in the optical regime and providing proper SPPs to the method.

2.2.1 Periodic Systems

2.2.1.1 Perfect Electrical Conductor, PEC

Despite we introduced in Chapter 1 the Extraordinary Optical Transmission by saying "One of the simplest optical devices we can imagine is a hole drilled in a metallic screen", concerning computation it is much simpler to calculate the optical properties of an infinite periodic array perforated with holes than those of an isolated aperture. The theoretical analysis of infinite periodic arrays is greatly simplified because, with the help of Bloch's theorem, only EM fields within one unit cell need to be computed, and a discrete set of diffracted wavevectors enters into the calculation.

Let us first consider the PEC approximation in a periodic system. In Fig. 2.1 it is shown schematically a general structure with holes drilled in a metallic film and periodically arranged in a rectangular lattice. The geometrical parameters defining the metallic system are the film thickness, h (located at $z = 0$ and $z = h$) and the array periods, L_x and L_y along the x and y axes, respectively. The whole space is divided into three regions: we will refer to regions I ($z < 0$) and III ($z > h$) as the illumination and transmission regions, respectively, and region II as the holey-metal one. Finally, ϵ_1, ϵ_2, and ϵ_3 account for the dielectric constants of regions I, II and III, respectively. Unless otherwise stated, we assume that the structure is illuminated by a normal-incident linearly polarized plane wave coming from region I.

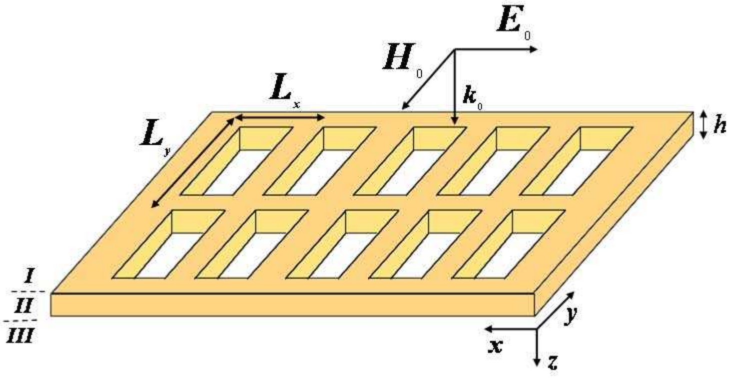

Figure 2.1: Schematic picture of a square array of rectangular holes perforated on a free-standing metallic film of thickness h. Parameters L_x and L_y define the period of the array. The system is illuminated by a linearly polarized plane wave at normal incidence.

Within the CMM we can write the EM fields in a compact format using Dirac's notation in terms of the transverse components (parallel to the xy plane) of the electric and magnetic fields, $\langle \mathbf{r}_{||}|\mathbf{E}\rangle = \mathbf{E}(\mathbf{r}_{||}) = (E_x(\mathbf{r}_{||}), E_y(\mathbf{r}_{||}))^t$ and $\langle \mathbf{r}_{||}|\mathbf{H}\rangle = \mathbf{H}(\mathbf{r}_{||}) = (H_x(\mathbf{r}_{||}), H_y(\mathbf{r}_{||}))^t$, where $\mathbf{r}_{||} = (x, y)$ and the superscript t stands for transposition. The longitudinal components, E_z and H_z are obtained straightforward from the transverse ones through the divergence of the EM fields: $\nabla \cdot \mathbf{E} = 0$ and $\nabla \cdot \mathbf{H} = 0$. We consider Maxwell equations in the CGS system of units, $\mathbf{H} = \frac{-i}{g}\nabla \times \mathbf{E}$ and $\mathbf{E} = \frac{i}{g\epsilon}\nabla \times \mathbf{H}$, with $g = 2\pi/\lambda$ and λ the wavelength of the EM incident radiation.

The EM fields in regions I and III are expressed as plane waves eigenmodes $|\mathbf{k}_{||}\sigma\rangle$, characterized by the in-plane component of the wavevector $\mathbf{k}_{||} = (k_x, k_y)$ and the polarization $\sigma = p$ (transverse-magnetic, TM) or $\sigma = s$ (transverse-electric, TE). The temporal dependance is assumed to follow $e^{-i\omega t}$.

The representation of the modes in the illumination (I) and transmission (III) regions reads,

$$\begin{aligned} \langle \mathbf{r}_{||}\ \mathbf{k}_{||}|\ p\rangle &= \frac{e^{i\mathbf{k}_{||}\mathbf{r}_{||}}}{\sqrt{L_x L_y}} \frac{1}{k_{||}} (k_x, k_y)^t \\ \langle \mathbf{r}_{||}\ \mathbf{k}_{||}|\ s\rangle &= \frac{e^{i\mathbf{k}_{||}\mathbf{r}_{||}}}{\sqrt{L_x L_y}} \frac{1}{k_{||}} (-k_y, k_x)^t \end{aligned} \tag{2.1}$$

where $k_z = \sqrt{g^2\,\epsilon_1 - \mathbf{k}_{||}^2}$ in region I (or $k_z = \sqrt{g^2\,\epsilon_3 - \mathbf{k}_{||}^2}$ in region III). According to Bloch's Theorem, $\mathbf{k}_{||} = \mathbf{k}_{||}^0 + \mathbf{k}_R$, being $\mathbf{k}_R$ a reciprocal lattice vector and $\mathbf{k}_{||}^0$ the incident wave-vector.

In particular, in region I the EM fields can be expressed as an incident plane wave $|\mathbf{k}_{||}^0\ \sigma_0\rangle$, plus a sum of the reflected Bloch waves $|\mathbf{k}_{||}\ \sigma\rangle$ weighed with their corresponding reflection coefficients, $\rho_{\mathbf{k}_{||}\sigma}$,

$$\begin{aligned} |\mathbf{E}\rangle &= |\mathbf{k}_{||}^0\ \sigma^0\rangle e^{ik_z^0 z} + \sum_{\mathbf{k}_{||}\sigma} \rho_{\mathbf{k}_{||}\sigma} |\mathbf{k}_{||}\ \sigma\rangle e^{-ik_z z} \\ |-\mathbf{u}_z \times \mathbf{H}\rangle &= Y_{\mathbf{k}_{||}^0\sigma^0} |\mathbf{k}_{||}^0\ \sigma^0\rangle e^{ik_z^0 z} - \sum_{\mathbf{k}_{||}\sigma} Y_{\mathbf{k}_{||}\sigma} \rho_{\mathbf{k}_{||}\sigma} |\mathbf{k}\ \sigma\rangle e^{-ik_z z} \end{aligned} \tag{2.2}$$

Here the electric and magnetic fields are related one to each other by means of the admittances $Y_{\mathbf{k}_{||}s} = k_z/g$ and $Y_{\mathbf{k}_{||}p} = \epsilon_1 g/k_z$ for TE and TM modes, respectively. $\mathbf{u}_z$ is the unitary vector along the z-direction and we have assumed the normalization $\langle \mathbf{k}_{||}\sigma|\mathbf{k}_{||}\sigma\rangle = 1$.

In the same way, the EM fields in region III are expanded into plane waves and weighed with their corresponding transmission coefficients, $t_{\mathbf{k}_{||}\sigma}$:

$$\begin{aligned} |\mathbf{E}'\rangle &= \sum_{\mathbf{k}\sigma} t_{\mathbf{k}_{||}\sigma} |\mathbf{k}_{||}\ \sigma\rangle e^{ik_z'(z-h)} \\ |-\mathbf{u}_\mathbf{z} \times \mathbf{H}'\rangle &= \sum_{\mathbf{k}_{||}\sigma} Y'_{\mathbf{k}_{||}\sigma} t_{\mathbf{k}_{||}\sigma} |\mathbf{k}_{||}\ \sigma\rangle e^{ik_z'(z-h)} \end{aligned} \tag{2.3}$$

Admittances in region III are primed in order to distinguish them from those in region I (ϵ_1 in region I becomes ϵ_3 in region III). Additionally, $\mathbf{k}_{||}^2 =$

$\left(\frac{2\pi n_x}{L_x}\right)^2 + \left(\frac{2\pi n_y}{L_y}\right)^2$, with discrete diffraction orders n_x and n_y ($n_x, n_y = -\infty, ..0.., \infty$). Usually, considering just a few of them in the calculations already provides converged results.

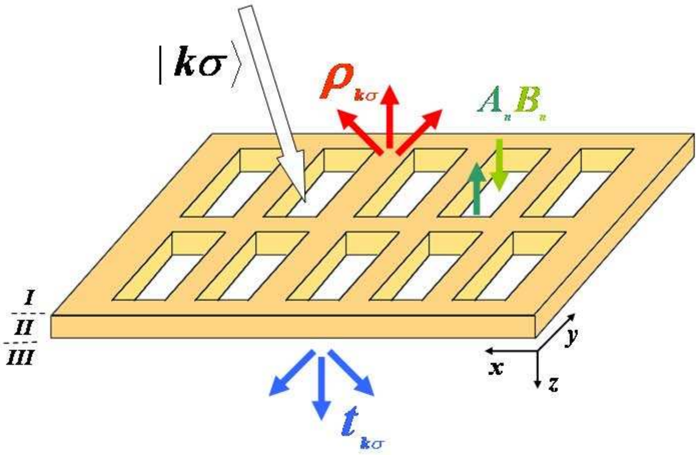

Figure 2.2: Schematics of the coupled mode procedure for the case of hole arrays. The space is divided into three regions. In region I, EM fields are expressed as a sum of the impinging plane wave (white arrow) plus reflected waves (red arrows). In region II, the basis is comprised by waveguide modes propagating back and forth (green arrows) along z-direction. Finally, EM fields in region III are expanded as a sum of diffracted waves (blue arrows).

Region II ($0 \leq z \leq h$) comprises the holey-metal region. Despite we are considering infinite periodic arrays, this formalism is also valid for finite systems as we will see next in Section 2.2.3. We said before that in infinite arrays we compute the EM fields within one unit cell, which may contain one or more cavities. We use a compact notation, denoting as "object" n any *waveguide EM mode* in any aperture considered in the expansion (any *hole* within one unit cell in the case of infinite arrays). The infinite periodic arrays considered in this thesis contain just one aperture per unit cell. Therefore, **in arrays**, an object is defined by **i)** the waveguide EM mode, **ii)** its polarization (TM or TE modes), and **iii)** the indices characterizing the waveguide mode and its position, whereas in **finite systems**, **iv)** it will be also characterized by the indentation it belongs to.

Under PEC approximation, EM fields vanish within the metal except inside the apertures, where they can be expressed in terms of the waveguide eigenmodes $|n\rangle$ (that can be written analytically for some geometries) propagating back and forth along the z-direction with a propagation constant k_{nz}:

$$\begin{aligned}|\mathbf{E}^{II}\rangle &= \sum_n (A_n e^{ik_{nz}z} + B_n e^{-ik_{nz}z})|n\rangle \\ |-\mathbf{u_z}\times\mathbf{H}^{II}\rangle &= \sum_n Y_n (A_n e^{ik_{nz}z} - B_n e^{-ik_{nz}z})|n\rangle \end{aligned} \tag{2.4}$$

A_n and B_n are unknown expansion coefficients that can be calculated imposing appropriate continuity conditions to the EM fields at the interfaces of the system ($z = 0$ and $z = h$). Besides, $Y_n^s = k_{nz}/g$ and $Y_n^p = \epsilon_2\, g/k_{nz}$ are the admittances for TE and TM modes, respectively.

Additionally, the function $|n\rangle$ defining the eigenmode within an indentation at a given position $r_n = (x_n, y_n)$ can be written as:

$$\langle r_n, z|n\rangle = e^{ik_{nz}z}\Psi_n(x - x_n, y - y_n) \tag{2.5}$$

In Appendix A we provide analytical expressions for the waveguide modes sustained by annular holes under PEC approximation.

As we showed in Chapter 1, the two fundamental modes in annular holes are the TEM and the TE_{11} modes. The propagation constants k_{nz} along the z-direction in PEC can be written as:

$$k_{nz}^{TE} = \sqrt{g^2 - \left(\frac{\chi_{11}}{b}\right)^2} \tag{2.6}$$

$$k_{nz}^{TEM} = g \tag{2.7}$$

where the quantity χ_{11} is the 1st non-vanishing root of the function

$$J_1'(x\,b)Y_1'(x\,a) - Y_1'(x\,a)J_1'(x\,b) = 0 \tag{2.8}$$

with a and b the outer and inner radius of the annular hole, respectively, and J_1' and Y_1' the derivatives of Bessel and Neumann functions of order 1.

Once we expand the EM fields into proper eigenmodes in each region, we must impose matching conditions at both the interfaces $z = 0$ and $z = h$. The transverse resolute of the electric field must be continuous along the surface, while the transverse component of the magnetic field is required to be continuous only across the apertures. The use of PEC boundary conditions in our model leads to the appearance of discontinuities in the parallel components of the magnetic field at the structure interfaces. Their origin resides in the formation of induced surface charge densities and currents at the film sides.

Therefore, for fundamental and technical reasons, EM fields are projected over different eigenmodes: plane waves $\{|\mathbf{k}_{||}\sigma\rangle\}$ for electric fields, and waveguide modes $\{|n\rangle\}$ for magnetic ones.

From the continuity of the parallel component of the electric field, we obtain:

$$\begin{aligned}
\delta_{\mathbf{k}_{||},\mathbf{k}^0_{||}}\delta_{\sigma,\sigma^0} + \rho_{\mathbf{k}_{||}\sigma} &= \sum_n (A_n + B_n)\,\langle \mathbf{k}_{||}\sigma|n\rangle \\
t_{\mathbf{k}_{||}\sigma} &= -\sum_n (A_n e^{ik_{nz}z} + B_n e^{-ik_{nz}z})\,\langle \mathbf{k}_{||}\sigma|n\rangle \qquad (2.9)
\end{aligned}$$

Whereas from the continuity of the tangential component of the magnetic field, we get:

$$\begin{aligned}
\langle n|\mathbf{k}^0_{||}\sigma^0\rangle Y_{k^0_{||}\sigma^0} - \sum_k Y_{k_{||}\sigma}\,\rho_{\mathbf{k}_{||}\sigma}\,\langle n|\mathbf{k}_{||}\sigma\rangle &= (A_n - B_n)Y_n \\
\sum_k t_{\mathbf{k}_{||}\sigma} Y'_{k_{||}\sigma}\,\langle n|\mathbf{k}_{||}\sigma\rangle &= (A_n e^{ik_{nz}z} - B_n e^{-ik_{nz}z})Y_n \; (2.10)
\end{aligned}$$

We have defined overlapping integrals of plane waves $|\mathbf{k}_{||}\sigma\rangle$ and waveguide modes $|n\rangle$ as

$$\langle \mathbf{k}_{||}\sigma|n\rangle = \int d\mathbf{r}_{||}\langle \mathbf{k}_{||}\sigma|\mathbf{r}_{||}\rangle\langle \mathbf{r}_{||}|n\rangle \qquad (2.11)$$

If waveguide modes are known analytically, these integrals may also be known analytically. In Appendix B, expressions for these overlaps are given for the particular case of annular holes.

It is convenient to define the following quantities:

$$\begin{aligned}
E_n &= A_n + B_n \\
E'_n &= -(A_n e^{ik_{nz}z} + B_n e^{-ik_{nz}z}) \qquad (2.12)
\end{aligned}$$

which are the modal amplitudes of the transverse electric field at the entrance (E_n) and the exit (E'_n) of the apertures.

Therefore, we can explicitly write reflection and transmission coefficients as:

$$\begin{aligned}
\rho_{\mathbf{k}_{||}\sigma} &= -\delta_{\mathbf{k}_{||},\mathbf{k}^0_{||}}\delta_{\sigma,\sigma^0} + \sum_n \langle \mathbf{k}_{||}\sigma|n\rangle E_n \\
t_{\mathbf{k}_{||}\sigma} &= -\sum_n \langle \mathbf{k}_{||}\sigma|n\rangle E'_n
\end{aligned} \tag{2.13}$$

Interestingly, in periodic systems, divergencies in $\rho_{\mathbf{k}_{||}\sigma}$ provide the eigenmodes of the system (finite fields at infinitesimal excitation). This property will be used in Chapter 3, when studying an array of annular dimples in a metal film.

Finally, we can also rewrite Eqs. 2.9 and 2.10 as a set of linear equations for E_n and E'_n which describes the behavior of the EM fields at the illumination and transmission regions:

$$\begin{aligned}
(G_{nn} - \Sigma_n)E_n + \sum_{n\neq m} G_{nm}E_n - G^{\nu}_n E'_n &= I_n \\
(G'_{nn} - \Sigma_n)E'_n + \sum_{n\neq m} G'_{nm}E'_n - G^{\nu}_n E_n &= 0
\end{aligned} \tag{2.14}$$

where, for holes

$$\begin{aligned}
I_n &= 2Y_{\mathbf{k}^0_{||}\sigma^0}\langle n|\mathbf{k}^0_{||}\sigma\rangle \\
\Sigma_n &= Y_n \frac{e^{ik_{nz}h} + e^{-ik_{nz}h}}{e^{ik_{nz}h} - e^{-ik_{nz}h}} \\
G^{\nu}_n &= \frac{2Y_n}{e^{ik_{nz}h} - e^{-ik_{nz}h}} \\
G_{nm} &= \sum_{\mathbf{k}_{||}\sigma} Y_{\mathbf{k}_{||}\sigma}\langle n|\mathbf{k}_{||}\sigma\rangle\langle \mathbf{k}_{||}\sigma|m\rangle
\end{aligned} \tag{2.15}$$

In the case of dimples or grooves, h must be substituted by the indentation depth (h_g) in the expression given for Σ_n. Besides, the continuity of the parallel component of the electric field imposes $E'_n = 0$, which leads to $G^{\nu}_n = 0$.

The different terms above can be interpreted as follows (see schematics in Fig. 2.3): I_n is the direct illumination impinging over aperture n; Σ_n is related to the bouncing back and forth of the EM fields inside object n, and the coupling between the two sides of the aperture is accounted for G^{ν}_n.

Finally, the "propagator" or "effective admittance" G_{nm} unveils how apertures are coupled through the EM field. This propagator takes into account

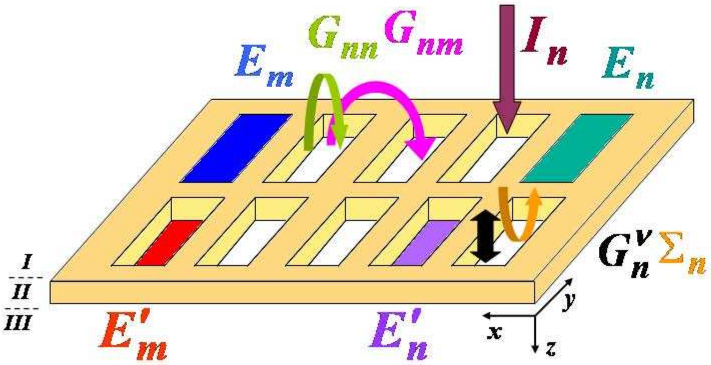

Figure 2.3: Schematics of the physical interpretation of the terms appearing in Eq.2.14.

that the EM field emitted by each point within object m can be collected by object n. Once again, G_{nm} and G'_{nm} differs one from each other through the dielectric constant of each media, since G_{nm} belongs to region I and G'_{nm} to region III (ϵ_1 and ϵ_3, respectively). As we will see next in Section 2.2.3 where finite systems are considered, L_x and L_y will define an artificial supercell with periodicity L_x,$L_y \rightarrow \infty$ which allows to replace the previous sums over Bragg diffraction modes by integrals in $\mathbf{k}_{||}$, i.e., $\sum\limits_{\mathbf{k}_{||}\sigma} \rightarrow \sum\limits_{\sigma} \int d^2\mathbf{k}_{||}$, and can be computed semi-analytically.

Note that for p-polarized modes and for any n_x and n_y, when $k_{nz} = 0$, a singularity in $Y_{\mathbf{k}_{||}p}$ takes place, which translates into $G_{nm}^{\sigma=p} = \infty$. The last has been reported [71] to be the origin of the existence of geometrical induced EM waves bounded at both sides to the PEC metal surfaces (Spoof Plasmons). In Chapter 3 we will extend our work to the study of these Spoof Plasmons in arrays of annular dimples in the THz regime.

The EM field everywhere in space can be obtained from the set of modal amplitudes $\{E_n, E'_n\}$. Therefore, the CMM reduces the computation of any EM property to determination of the EM field distribution just at the aperture openings. This is extremely efficient, especially for subwavelength apertures, where convergence is quickly reached with the number of waveguide modes considered. In fact, in this regime, accurate results for transmittance can be achieved by considering only the fundamental waveguide mode inside each aperture [56].

For the cases of either a single aperture or an infinitely periodic array, the single-mode approximation allows a quasianalytical treatment of the set of equations given by Eq. 2.14, that then transforms into a set of just two linear equations. Actually, along this thesis we will fit to this minimal model and, despite annular holes posses two fundamental modes, all calculations will be done considering just the TE_{11} mode (see Appendix A for further details). The reason is that, as we said in Chapter 1, the electric field of the TEM mode is radially polarized so it cannot be accessed by linearly polarized light impinging at normal incidence, which is the illumination source we will use in this thesis. However, in Chapter 3 we will study the dispersion curves of annular dimples and the TEM mode will be also considered.

In order to know the transmittance of light at the other side of the metal film we must calculate the ratio between the transmitted EM power and the incident one, $T' = P_t/P_i$, by integrating the time-averaged z-component of the Poynting vector in each region within one unit cell. The EM energy carried by an the incident plane wave is

$$\begin{aligned} P_i &= \frac{1}{2}\int d\mathbf{r}_{||} Re(\mathbf{E}\times\mathbf{H}^*) \\ &= \frac{1}{2} Re \int d\mathbf{r}_{||}(E_x H_y^* - E_y H_x^*) = \frac{1}{2} Re(\langle -\mathbf{u}_z \times \mathbf{H}|\mathbf{E}\rangle) \\ &= \frac{1}{2} Re(\langle \mathbf{E}| - \mathbf{u}_z \times \mathbf{H}\rangle) = \frac{1}{2} Y_{\mathbf{k}_{||}^0\sigma^0} \end{aligned} \tag{2.16}$$

In the same way, the corresponding EM power transmitted through the structure in the far field in **region III**, can be written as

$$P_t = \frac{1}{2} Re\left(\sum_{\mathbf{k}_{||}\sigma} Y_{\mathbf{k}_{||}\sigma}\left|t_{\mathbf{k}_{||}\sigma}\right|^2\right) = \frac{1}{2} Im\left(\sum_{nm} E_m'^* E_n' G_{nm}'\right) \tag{2.17}$$

therefore,

$$T' = \frac{P_t}{P_i} = \frac{1}{Y_{\mathbf{k}_{||}^0\sigma^0}} \sum_{k}^{p} Y_{\mathbf{k}_{||}\sigma}|t_{\mathbf{k}_{||}\sigma}|^2 = \frac{1}{Y_{\mathbf{k}_{||}^0\sigma^0}} Im\left(\sum_{nm} E_m'^* E_n' G_{nm}'\right) \tag{2.18}$$

where the sum is done over propagative modes and we have used Eq. 2.13.

Additionally, we can compute the EM power transmitted through the structure by integrating the z-component of the Poynting vector associated to EM fields through the holes, in **region II**:

$$\begin{aligned} T_{II} &= \frac{1}{Y_{\mathbf{k}_{||}^0\sigma^0}} Re \sum_{nm} Y_n^* \left[A_n^* e^{-ik_{nz}^*} - B_n^* e^{ik_{nz}^*}\right] \left[A_n e^{-ik_{nz}} - B_n e^{ik_{nz}}\right] \\ &= \frac{1}{Y_{\mathbf{k}_{||}^0\sigma^0}} Im \left(\sum_{nm} E_m'^* E_n G_n^\nu \right) \end{aligned} \tag{2.19}$$

where we have used Eq. 2.12.

And finally, we can do the same in **region I**, getting:

$$T = 2Re \sum_n E_n \langle \mathbf{k}_{||}^0 \sigma | n \rangle - \frac{1}{Y_{\mathbf{k}_{||}^0\sigma^0}} \sum_{nm} E_m^* E_n G_{nm}^p \tag{2.20}$$

These three expressions are especially useful to check our results since in the PEC approach there are no absorption losses and therefore, the law of conservation of energy entails $T' = T_{II} = T$. Additionally, all geometrical parameters and wavelengths can be scaled because none of these expressions depend on them.

2.2.2 Surface Impedance Boundary Conditions and wavevector of a real metal waveguide

2.2.2.1 Surface Impedance Boundary Conditions, SIBCs

Proper surface plasmon polaritons (SPPs) appear as a new ingredient in our formalism by incorporating Surface Impedance Boundary Conditions (SIBCs), where the finite dielectric constant of metals is considered.

In our implementation, electromagnetic fields vanish inside PECs, whereas in the surface impedance approach the effect of the penetration of the fields is taken into account just at the horizontal metallic surface, i.e., vertical walls where apertures are opened are still considered PECs, and therefore, analytical expressions for waveguide modes still hold. As we will see next, this approach is valid whenever the skin depth is less than any other lengthscale entering the problem.

Within SIBCs, the conditions on continuity of EM fields are different, establishing for the tangential components (at the horizontal surfaces) that:

$$\mathbf{E} = +Z_s \mathbf{H} \times \mathbf{u}_n \tag{2.21}$$

where $\mathbf{u}_n$ is a unitary vector normal to the surface and points to the interior of the metal, and

$$Z_s = 1/\sqrt{\varepsilon_m(\omega)} \tag{2.22}$$

is the surface impedance [67, 72]. This surface impedance approach is an excellent approximation in the THz and microwave regime, but it also serves reasonable results in the telecom and optical regime. The approach may be understood as if we used a finite number of terms (first order truncation) of the series to approximate the function $\varepsilon_m^{-1/2}$.

Importantly, the system of linear equations given by Eqs. (2.14) is still valid, but with some minor modifications in the constitutive elements which now depend on the surface impedance Z_s [73, 74].

For holes, we now get:

$$\begin{aligned}
I_n &= \frac{2Y_{\mathbf{k}_{||}^0\sigma^0}}{f^+_{\mathbf{k}_{||}^0\sigma^0}}\langle n|\mathbf{k}_{||}^0\sigma^0\rangle \\
\Sigma_n &= Y_n\frac{f_n^+e^{ik_{nz}h}+f_n^-e^{-ik_{nz}h}}{f_n^{+^2}e^{ik_{nz}h}-f_n^{-^2}e^{-ik_{nz}h}} \\
G_n^\nu &= \frac{2Y_n}{f_n^{+^2}e^{ik_{nz}h}-f_n^{-^2}e^{-ik_{nz}h}} \\
G_{nm} &= \sum_{\mathbf{k}_{||}\sigma}\frac{Y_{\mathbf{k}_{||}\sigma}}{f^+_{\mathbf{k}_{||}\sigma}}\langle n|\mathbf{k}_{||}\sigma\rangle\langle\mathbf{k}_{||}\sigma|m\rangle
\end{aligned} \tag{2.23}$$

being $f^\pm = 1 \pm Z_sY$.

Once again, for the case of dimples or grooves of finite depth (h_g) we set $G_n^\nu = 0$, and Σ_n reads:

$$\Sigma_n = Y_n\frac{f_n^-e^{ik_{nz}h_g}+f_n^+e^{-ik_{nz}h_g}}{f_n^+f_n^-\left(e^{ik_{nz}h_g}-e^{-ik_{nz}h_g}\right)} \tag{2.24}$$

Transmission formulae appearing in Eq. 2.18, 2.19, and 2.20 are not modified, however, the expression of G_{nm} in those equations becomes:

$$G_{nm}^T = \sum_{\mathbf{k}_{||}\sigma}\frac{Y_{\mathbf{k}_{||}\sigma}}{\left|f^+_{\mathbf{k}_{||}\sigma}\right|^2}\langle n|\mathbf{k}_{||}\sigma\rangle\langle\mathbf{k}_{||}\sigma|m\rangle \tag{2.25}$$

As for PECs, within SICBs also surface EM waves appear whenever $G_{nm}^{\sigma=p}$ diverges, but now the new resonant condition turns into $1 + Z_sY_{\mathbf{k}_{||}\sigma} = 0$. This condition describes the appearance of proper SPPs through SIBC approximation.

To further improve our theoretical approach where vertical walls inside holes are still taken as perfect conductors, we can:

- Compute exactly the propagation constant inside the waveguide, k_{nz}.

  Considering the propagating constant along the z-direction inside an infinite annular hole made of real metal, k_{nz}, provides an exceptional improvement for both resonant positions and intensity in transmission spectra. In Appendix C we present all details concerning the computation of k_{nz} of a coaxial waveguide made of real metal.

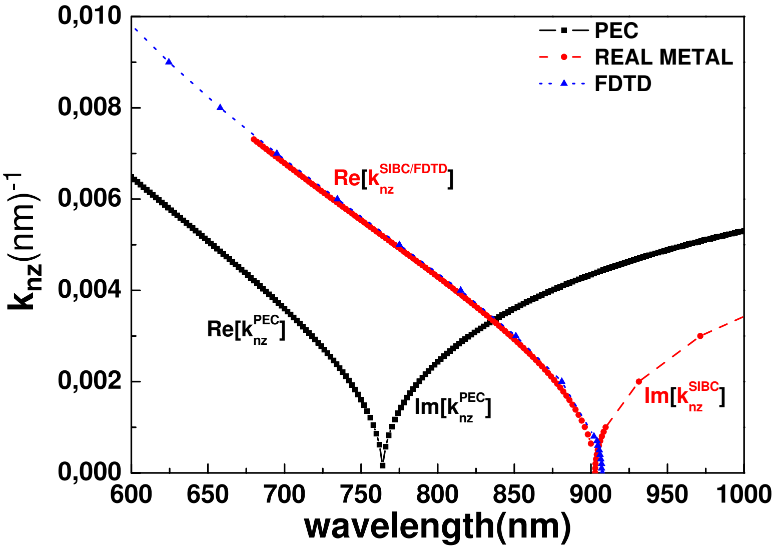

Figure 2.4: Calculation of k_{nz} as a function of the wavelength for an infinite coaxial waveguide with inner radius $a = 200$nm and inner radius $b = 50$nm in gold. Squares depict calculation for a PEC, circles for a real metal, and triangles correspond to the exact calculation done with the FDTD method (performed by Sergio G. Rodrigo).

Figure 2.4 shows k_{nz} versus the wavelength of an infinite coaxial waveguide with outer radius $a = 200$nm and inner radius $b = 50$nm in gold. To further corroborate this calculations, FDTD numerical simulations were conducted. The gold dielectric constant is taken from the experimental data appearing in Ref. [75]. In the figure, squares depict calculations for a PEC (following the expression given by Eq. 2.6); circles correspond to the modified propagation constant of a gold waveguide, and triangles correspond to the exact calculation done for the real part of k_{nz} with the FDTD method. This FDTD calculation was performed by Dr. Sergio. G. Rodrigo. It can be demonstrated that within this non-absorbing approximation, k_{nz} is pure real when $\lambda < \lambda_c$ (where λ_c is defined as the wavelength at which $k_{nz} = 0$), and pure imaginary when $\lambda > \lambda_c$ [76]. Remarkably, in the optical regime the cutoff wavelength of a waveguide made of real metal is much longer than that of a perfect electrical conductor.

- Effectively enlarge the dimensions of the apertures.

  This would take into account the effect of the penetration of the fields within the apertures by increasing the nominal parameters ~ 2 skin depths. In the case of annular holes, we would enlarge the outer radius ~ 1 skin depth, and reduce the inner one also ~ 1 skin depth. However, we did not find any systematic improvement in intensity and spectral location of transmission features when CMM and FDTD calculations were compared. Therefore, calculations along this thesis will always consider the nominal values of the inner and outer radius.

- Define the surface impedance as $\widetilde{Z_s} = 1/\sqrt{\varepsilon_m + \varepsilon}$.

  For a flat metal-dielectric surface without holes, where the metal is characterized by a dielectric constant ε_m, and the dielectric by ε, SIBC approximation is valid whenever $q_{zm} >> q_z, q_{||}$, being $q_{zm} = \sqrt{\varepsilon_m - q_{||}^2}$ and $q_z = \sqrt{\varepsilon - q_{||}^2}$ (with $q = k/g$). This enables to neglect the parallel components of the derivatives in the EM fields, being faster the variations along the component normal to the surface. Consequently, SIBC approach is a good approximation when $\varepsilon_m >> \varepsilon$.

  Additionally, for a vacuum-metal flat surface, the appearance of surface plasmons within SIBC is associated to divergencies in the impedance $Z_s = 1/\sqrt{\varepsilon_m}$, that is, $\varepsilon_m = 0$. However, the dispersion relation of SPPs can be exactly taken into account if we define the surface impedance as $\widetilde{Z_s} = 1/\sqrt{\varepsilon_m + 1}$, that is $\varepsilon_m = -1$, where 1 accounts for the dielectric constant of vacuum.

  As it is schematically shown in Fig. 2.5, this approximation where SPPs are described by either $\varepsilon_m = 0$ or $\varepsilon_m = -1$ is pretty much the same (red and green curves). However, for any dielectric-metal flat surface, the previous condition becomes $\varepsilon_m = -\varepsilon$. Therefore, the larger the value of ε, the worse the impedance approximation, as it is also shown schematically with the blue curve in the same figure.

  Regarding the PEC approximation inside the apertures, we must also bear in mind that the spatial profile of the fundamental mode is obtained

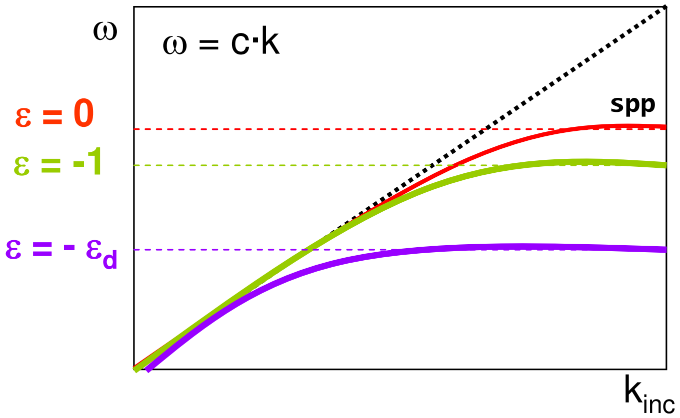

Figure 2.5: Schematics of the dispersion relation of a dielectric-metal flat surface, when the dielectric is taken as vacuum ($\varepsilon = 1$) or as any other material with $\varepsilon > 1$.

> through this approximation. The penetration of the field as a decaying exponential is taken as zero, or equivalently, the skin depth is $\delta = 0$. In this situation if FDTD and CMM calculations are compared, the results are exactly the same.
>
> Also if the skin depth is $\delta > 0$, but small enough compared to the dimensions of the aperture, the approach of the fundamental mode and its coupling with external radiation still holds, and FDTD and CMM results look very similar. This result where the PEC approach is still valid, that is, for δ small enough, is precisely the limit where SIBC approach does not fail.
>
> However, if the skin depth cannot be neglected compared to the dimensions of the apertures, then, the approximation we are doing for the fundamental mode of a waveguide made of PEC is not valid anymore, and CMM results fail.
>
> As a result, when considering real metals in combination with high refractive index dielectrics ($\varepsilon >> 1$) in the optical regime and small apertures, we will use the exact FDTD method.

In Fig. 2.6 it is shown the transmittance of light as a function of the wavelength in a silver array with annular holes deposited on a glass substrate ($\varepsilon_3 = 2.25$). The periodicity is taken $L_x = L_y = 900$nm, film thickness $h = 140$nm, outer radius $a = 290$nm and inner one $b = 230$nm. Comparing CMM and FDTD simulations, we observe that exceptional improvements for both transmittance intensity and peak position are found when both SIBCs and k_{nz} of a real metal are taken within the CMM. If absorption was considered in the computation of k_{nz}, the spectral band-width of transmission resonances would be wider and the intensity would further decrease.

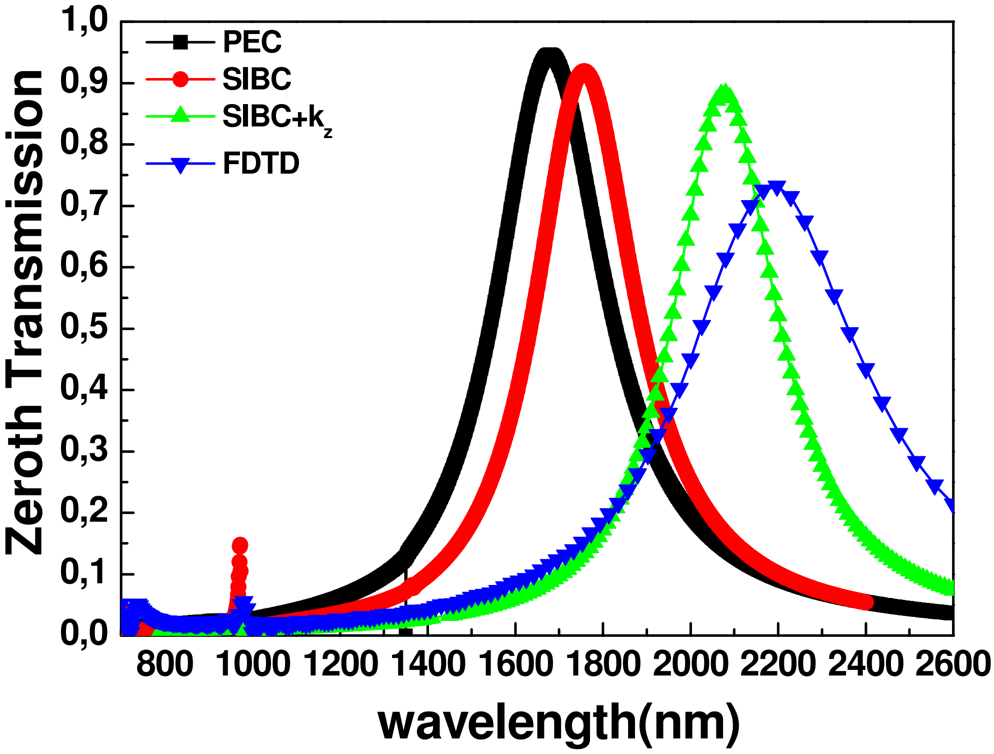

Figure 2.6: Zeroth order transmission as a function of the wavelength of a silver array with annular holes drilled in it, on a glass substrate. The periodicity is $L_x = L_y =$ 900nm, film thickness $h = 140$nm, inner radius $a = 290$nm and inner one $b = 230$nm.

2.2.3 Finite Systems

As we previously said, finite systems can also be investigated within the CMM. The only difference with infinite systems relies on the computation of the propagator G_{nm}, while the rest of magnitudes and expressions remain invariable. When dealing with a finite set of cavities, the limit $L_x, L_y \to \infty$ must be taken. Within SIBC, the latter leads to an integral over diffraction modes:

$$G_{nm} = \lim_{L_x L_y \to \infty} \frac{L_x L_y}{2\pi} \sum_{\sigma} \int d^2 k_{||} \frac{Y_k}{f_k^+} \langle n|k\rangle \langle k|m\rangle \tag{2.26}$$

Note that the product $L_x L_y$ exactly cancels the normalization factor of plane waves. To retrieve the expressions for PECs we must just take $Z_s = 0$ in the corresponding quantities. It is important to remark that, for finite systems, subscripts n and m may label either the object (aperture) or the mode we are considering inside the cavity. However, as we said before, throughout this thesis we will apply the minimal model for subwavelength apertures and we will just consider the TE_{11} mode (except in Chapter 3 where a TEM mode is also taken). Therefore, except otherwise stated, in finite systems n and m will always refer to an aperture, not a mode.

As for infinite systems within SIBC, $G_{nm}^{\sigma=p}$ diverges whenever $1+Z_s Y_{\mathbf{k}_{||}\sigma}=0$. If we rewrite this object in terms of the normalized wavevector $\mathbf{q}$, where $\mathbf{k}=\sqrt{\varepsilon}\, g\, \mathbf{q}$, it is easy to find out that $G_{nm}^{\sigma=p}$ presents a branch point at $q=1$, and a pole at $q_p=\sqrt{1-Z_s^2}$ very close to the real axes which contains the contribution of the surface plasmon. These two singularities must be treated specially when computing $G_{nm}^{\sigma=p}$. Full details for the computation of these integrals can be found in Appendix B.

2.3 Finite-Difference Time-Domain Method

The Finite-Difference Time-Domain (FDTD) method and related space-grid time-domain techniques are direct solution methods for Maxwell's equations. Both the basic FDTD space grid and time-stepping algorithm trace back to a seminal 1966 paper by Kane Yee [77]. The time-dependant Maxwell's equations (in partial differential form) are discretized using central-difference approximations to the space and time partial derivatives.

As Allen Taflove [78] foresaw in 1975, the electromagnetics community seized upon the marvelous Yee algorithm and applied it to just *everything*. As a result, the FDTD technique turns out to be one of the most extensively developed and used method in computational electromagnetism [79].

In this thesis we will use the FDTD method to solve very specific problems not attainable with the CMM, and also as a tool to check the range of validity of the results obtained with the last CMM approach. In particular, the FDTD method will be used in Chapter 3 to investigate the Extraordinary Optical Transmission phenomenon through arrays of annular holes in combination with high index dielectrics, and also to study the Dispersion Relation in the THz regime of a system with annular dimples periodically arranged; in Chapter 4 we will employ FDTD calculations to validate the results obtained within the modal approximation when studying EOT through Bull's Eye Structures. And finally, this method will be the fundamental tool for studying exactly optical properties in nonlinear systems, in Chapter 6.

We do not aim here to fully explaining this technique since it is impossible to cover all aspects of the FDTD method in an introductory section, but instead, we limit to briefly present the general ideas behind this method as well as some of its advantages compared to the CMM. Nevertheless, a full description of this algorithm can be found in Ref. [80], and more importantly, the details of the proper “homemade” FDTD here used can be found in Dr. Sergio G. Rodrigo’s thesis [81], who developed the code.

Let us start by mentioning some of the advantages and available options of the use of FDTD method: first, different material properties can be conducted with the FDTD method, so dielectrics, metals and nonlinear materials can be considered. Additionally, several illumination sources such as plane waves, dipole sources or gaussian beams can be employed. Finally, optical properties can be easily described by means of transmission and reflection coefficients, dispersion relation curves, field maps in frequency domain and, actually, any other quantity which depends on the EM fields.

Next, we will give some tips on the FDTD algorithm itself.

Maxwell’s equations must be brought from the “continuous” space to the “discret”’ space, and although it can be handled in different ways, it must be properly carried out so that the results provided are accurate, free of divergencies and also free of numerical instabilities. In the MKS system of units, the curl Maxwell’s differential equations for isotropic, homogeneous and lineal media read:

$$\begin{aligned}\frac{\partial \vec{H}(\vec{r},t)}{\partial t} &= -\frac{1}{\mu_0\mu}\nabla\times\vec{E}(\vec{r},t)\\ \frac{\partial \vec{E}(\vec{r},t)}{\partial t} &= \frac{1}{\varepsilon_0\varepsilon}\nabla\times\vec{H}(\vec{r},t)\end{aligned} \tag{2.27}$$

It can be seen that the change in time of the E-field (the time derivative) depends on the change across space of the H-field (the curl) and viceversa. The base of the FDTD algorithm consists of 6 independent equations obtained by replacing the curl of both the E-field and H-field with their corresponding derivatives, that is,

$$\begin{aligned}\nabla\times\vec{F} &= \begin{vmatrix}\vec{i} & \vec{j} & \vec{k}\\ \frac{\partial}{\partial x} & \frac{\partial}{\partial y} & \frac{\partial}{\partial z}\\ F_x & F_y & F_z\end{vmatrix} =\\ &= \left(\frac{\partial F_z}{\partial y}-\frac{\partial F_y}{\partial z}\right)\vec{i}+\left(\frac{\partial F_x}{\partial z}-\frac{\partial F_z}{\partial x}\right)\vec{j}+\left(\frac{\partial F_y}{\partial x}-\frac{\partial F_x}{\partial y}\right)\vec{k}\end{aligned} \tag{2.28}$$

being $\vec{F}(\vec{r},t)=\vec{E}(\vec{r},t)$ or $\vec{F}(\vec{r},t)=\vec{H}(\vec{r},t)$.

In 1966, Kane Yee propounded a distribution in space for the EM field components. Figure 2.7 shows an illustration of a standard Cartesian Yee's cell used for FDTD, and how electric and magnetic field vector components are distributed [77]. Visualized as a cubic box, the E-field components form the edges of the cube, and the H-field components form the normals to the faces of the cube.

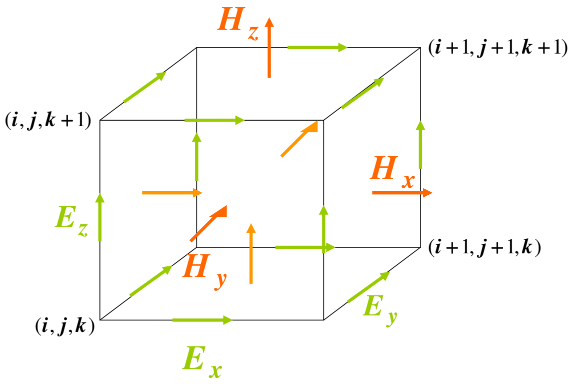

Figure 2.7: Illustration of a standard Cartesian Yee cell used for FDTD.

A three-dimensional space lattice is comprised of a multiplicity of such Yee cells. A given structure is mapped into the space lattice as it is schematically shown in Fig. 2.8, by assigning appropriate values of permittivity to each electric field component, and permeability to each magnetic field component. As a result, this method is based upon volumetric sampling of the unknown electric field and magnetic field within and surrounding the structure of interest (and over the period of time), whose coordinates can be written as:

$$(i, j, k) = (i\Delta x, j\Delta y, k\Delta z) \tag{2.29}$$

with Δx, Δy, and Δz the spatial increment or mesh size. Additionally, each function in space and time can be written as

$$F(i\Delta x, j\Delta y, k\Delta z, n\Delta t) = F^n(i, j, k) \tag{2.30}$$

being Δt the time step.

The spatial and temporal derivatives will be implemented in terms of an approximation in finite difference both centered and evaluated in consecutive/overlapping cells:

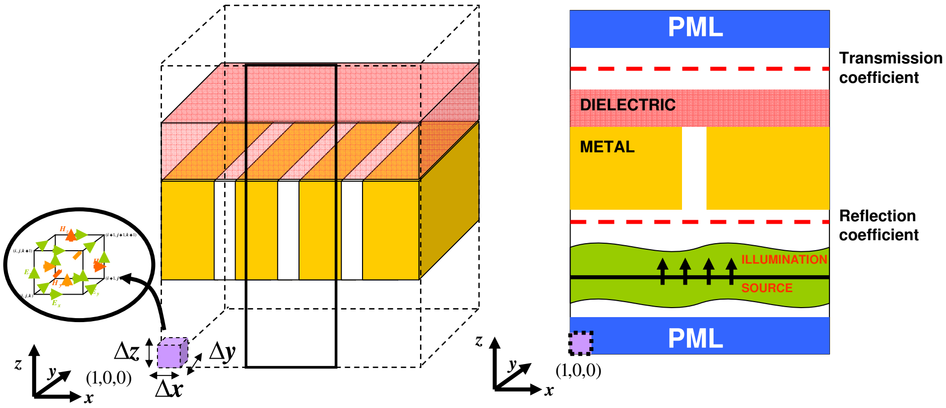

Figure 2.8: Schematics of a metal-dielectric structure studied within the FDTD method, in 3D (left hand side) and a cross section of it (right hand side).

$$\begin{aligned} \frac{\partial F^n(i,j,k)}{\partial x} &= \frac{F^n(i+1/2,j,k) - F^n(i-1/2,j,k)}{\Delta x} \\ \frac{\partial F^n(i,j,k)}{\partial t} &= \frac{F^{n+1/2}(i,j,k) - F^{n-1/2}(i,j,k)}{\Delta t} \end{aligned} \tag{2.31}$$

Overall, FDTD technique is a marching-in-time procedure which allows that the resulting finite-difference equations are solved in a leapfrog manner: the electric field vector components in a volume of space are solved at a given instant in time; then the magnetic field vector components in the same spatial volume are solved at the next instant in time; and the process is repeated time and time again until the desired transient or steady-state electromagnetic field behavior is fully evolved. Once all the components are calculated, this algorithm allows us to simulate propagation of EM waves through isotropic, homogeneous and lineal media, defined by the dielectric constant ε, and the magnetic permeability μ.

But our algorithm must also satisfy some criteria in order to be numerically stable. The FDTD method has been proven to be very memory and CPU-time intensive and consequently it is not suitable for large-scale problems. Such intensive memory and CPU time requirements come from two reasons: **i)** the spatial increment steps must be small enough in comparison with the wavelength in order to make the numerical dispersion error negligible, and **ii)** the time step must be small enough to satisfy the following stability condition (Courant condition):

$$c\,\Delta t/L \geq 1 \tag{2.32}$$

Here c is the maximum wave phase velocity within the model, L is a lineal quantity such as the grid width or length, and Δt the time step. For 3 dimensions, Courant criterium can be generalized as

$$\Delta t \leq \frac{1}{c\sqrt{\frac{1}{(\Delta x)^2}+\frac{1}{(\Delta y)^2}+\frac{1}{(\Delta z)^2}}} \tag{2.33}$$

Therefore, the mesh size and the time step are related one to each other by means of the above equation. Moreover, for a given structure, the mesh size is also subject to two more constraints: **i)** when the structure of interest does not fit properly in cartesian coordinates, then the mesh size should be fine enough to ensure that the discrete structure represents the actual one, and **ii)** since the EM field decays in length scales of the order of 25nm within metals, the faithful representation of such fast variations is a great challenge forcing the mesh size to be usually of the order of 5nm.

Next, concerning **implementation**, here I present my personal contribution done to this "homemade" FDTD algorithm, previously developed by Dr. Sergio G. Rodrigo.

The FDTD method appears as an exceptional tool for studying optical properties in nonlinear materials. In Chapter 6 we study the nonlinear optical response in arrays of subwavelength slits in combination with nonlinear Kerr-type dielectrics. In particular, we investigate the Third Harmonic (TH) Generation and the Optical Kerr Effect (OKE) undergone by these kind of structures. The former describes processes in which light at frequency 3ω is generated from an applied field at frequency ω, whereas OKE processes produce a variation of the local dielectric constant which has an effect at the incident frequency ω, through a variation of the local dielectric constant. The last effect appears exceptionally attractive so as to design optical limiters and switchings.

One of the key numerical issues concerns the updating of EM fields within the leapfrog FDTD algorithm.

We use the FDTD method to treat both the linear optical properties of metals and the nonlinear third order response of dielectrics [80]. The third order nonlinear dielectric is considered isotropic, homogeneous and dispersionless in frequency, so the relationship between the displacement ($\vec{D}$) and the electric field ($\vec{E}$) is

$$\begin{aligned} \vec{D} &= \varepsilon_o \vec{E} + \vec{P} \\ \vec{P} &\backsimeq \varepsilon_o \chi^{(1)} \vec{E} + \varepsilon_o \chi^{(3)} (\vec{E}.\vec{E})\vec{E} \end{aligned} \tag{2.34}$$

in the MKS system of units, where "." denotes the scalar product, ε_o is the dielectric constant of vacuum, $\chi^{(1)}$ the linear susceptibility and $\chi^{(3)}$ the third order one.

In the particular case of harmonic fields, that is, $\vec{E} = \vec{E}_o(\vec{r})e^{-i\omega t}$, and taking into account that EM fields must be defined as real numbers, it can be easily found that [39]

$$\begin{aligned} \vec{P}_R &= \varepsilon_o\{\chi^{(1)}\vec{E}_R + \frac{3\chi^{(3)}}{4}|E|^2\vec{E}_R + \frac{\chi^{(3)}}{8}[\vec{E}^3 + (\vec{E}^*)^3]\} \\ \vec{D}_R &= \varepsilon_o\left[\varepsilon + \frac{3\chi^{(3)}}{4}|E|^2\right]\vec{E}_R + \frac{\varepsilon_o\chi^{(3)}}{8}[\vec{E}^3 + (\vec{E}^*)^3] \end{aligned} \tag{2.35}$$

being $\vec{E}_R = \left(\frac{\vec{E}+c.c}{2}\right)$, $\varepsilon = 1 + \chi^{(1)}$, and where *c.c.* stands for "complex conjugate". Note that the local change of the dielectric constant associated to OKE is given by the term $\Delta\varepsilon = \frac{3\chi^{(3)}}{4}|E|^2$, whereas $\frac{\varepsilon_o\chi^{(3)}}{8}\left[\vec{E}^3 + (\vec{E}^*)^3\right]$ describes TH Generation processes.

In what follows we sketch how these expressions are implemented within a FDTD nonlinear algorithm. A full description of this algorithm can be found in Ref. [80].

Let us start from the relation given by Eq. 2.34. Within the FDTD method, at each position inside the nonlinear medium, the displacement vector at instant $n+1$, $\vec{D}^{n+1}$, is obtained from its value at the previous instant n, and from the curl of the magnetic field at $n - 1/2$. From Eq. 2.34, once $\vec{D}^{n+1}$ is known, the electric field at $n+1$ must satisfy:

$$\vec{E}^{n+1} = \frac{\vec{D}^{n+1}}{\varepsilon_o(\varepsilon + \chi^{(3)}|\vec{E}^{n+1}|^2)} \tag{2.36}$$

Taking the modulus of this expression, a cubic polynomial in $|\vec{E}^{n+1}|^2$ must be solved at each FDTD iteration. Because both ε and $\chi^{(3)}$ are taken positive, there is only one real and positive root which must be chosen to ensure that $|\vec{E}^{n+1}|^2$ is real and positive.

In the FDTD method, illumination and data processing for retrieving the optical properties are key issues. We use *p*-polarized light sources at normal incidence (wavevector along the *z*-direction). Let us consider a gaussian wave packet (GW), centered at a carrier frequency ω_o. We are interested in nonlinear optical responses at a fixed wavelength, hence long standing pulses (narrow in frequency) must be launched. Such pulses have a wide spread in space at $t = 0$, requiring a very large and inefficient computational box.

To avoid this constraint we implemented the Total Field Scattered Field (TFSF) [78] technique, which allows the incorporation of almost monochromatic sources. The system is divided into two regions: one is the Total Field

(TF) region (where the EM field is the sum of the scattered and the incident field), and the Scattered Field (SF) region (where only the scattered field is computed). The incident EM wave is launched into the system precisely at the boundaries defined by the TF/SF regions.

The GW is defined as:

$$E_x(z,t) = \frac{1}{2}\left(E_x^o e^{\imath \frac{\omega_o}{c} s} e^{-\left(\frac{s}{\sigma}\right)^2} + c.c.\right) \tag{2.37}$$

where $s = z - z_o - ct/n_1$, being z_o the position where the gaussian field reaches its maximum at $t = 0$, and $n_1 = \sqrt{\varepsilon}_1$ corresponds to the refractive index of the illumination region. The parameter σ controls both the spectral width and the pulse duration. Without lack of generality E_x^o is chosen to be a real number. This wave-packet carries an instantaneous intensity:

$$I(z,t) = n_1 \epsilon_o c\, |E_x^o|^2 \cos\left(\frac{\omega_o}{c} s\right)^2 e^{-2\left(\frac{s}{\sigma}\right)^2} \tag{2.38}$$

In the case of linear calculations ($\chi^{(3)} = 0$), σ is chosen so that the wave-packet contains all the frequencies of interest. To calculate transmission (T_L) and reflection (R_L) as a function of the wavelength of the incoming light, we project onto diffracted modes in each dielectric half-space, so we can distinguish among the different diffracted orders (see Ref. [82] for further details).

Additionally, the TFSF method enables the calculation of transmitted and reflected currents within a single simulation: the reflection region is chosen to be the SF region; and the structure along with the transmission half-space cover the TF one. These quantities are calculated integrating the Poynting vector flux through a unit cell, in the frequency domain.

In the nonlinear case, transmittance and reflectance, for both the Fundamental Harmonic (FH) and the Third Harmonic (TH), are easily obtained by integrating the transmitted and reflected power in a frequency range around the different harmonics, and normalizing to the power of the incident field. The width of the frequency window used in the integration is not important, provided that it is both much smaller than the fundamental frequency and larger than the spectral width of the incident wavepacket.

Further details of the specific calculations and system studied will be given in Chapter 6.

Chapter 3

Infinite Periodic Systems

3.1 Introduction

The interaction of light with a metal surface is dominated by the free electrons that behave like a plasma with a dielectric function $\varepsilon_m = 1 - \omega_p^2/\omega^2$, which is negative below the plasma frequency, ω_p. As a consequence, metals support surface plasmons (SPs) [14], responsible for a host phenomena unique to metals [49] (and references therein), as we introduced in Chapter 1. For instance, an interesting effect of light interacting with structured metals in the optical regime is that the transmission of light through subwavelength hole arrays made in a metal film can be orders of magnitude larger [23] than expected from standard aperture theory [21]. This is the so called Extraordinary Optical Transmission (EOT), that we also explained in the introductory chapter.

There has been also recent interest in surface electromagnetic (EM) modes for possible applications in guiding and sensing at terahertz (THz) frequencies. Pendry et al. [71] outlined how the dispersion of surface EM modes can be engineered even in perfectly conducting surfaces by texturing the surface. They showed that these surface modes resembling surface plasmons (thus their name *Spoof Surface Plasmons*), have an effective plasma frequency completely determined by the geometry of the structure. Periodic structuring also provides additional local field enhancement related to redistribution of SPP (or spoof) energy along the structured surface. This induces strong field enhancement in subwavelength size areas close to the surface.

Surface structuring thus facilitates an extension of visible plasmonic concepts for subwavelength localization of EM energy to frequencies significantly lower than the intrinsic plasma frequency of the conductor. In the technologically emergent THz regime, this creates opportunities for planar waveguides with high out-of-plane confinement and added functionality such as focusing, guiding and sensing. Therefore if large field enhancement is obtained, then the sensitivity of our systems acting as photodetectors will be much better, and if strong confinement is also attainable, the volume of the sample needed to be analyzed or detected will be significantly reduced.

Clearly, fascinating possibilities are offered by metallic surfaces corrugated with periodic apertures. However, every hole shape provides singular and special properties not attainable with others, so...which shape should we choose and why? Well, as we said in Chapter 1, coaxial circular apertures were proposed as an extension of circular apertures in plasmonic films [83,84]. Initially, these coaxial structures were deemed interesting due to the TEM mode without cutoff [85] that they support. This property was expected to provide greater transmission intensity than the observed through hole arrays. Additionally, as we also showed in Chapter 1, they also posses a TE_{11} mode that cutoffs at an unusually long wavelength [85]. This allows the design of structures able to guide in 2 independently variable and relatively low loss frequency bands [86], useful in biochemical sensing, for instance.

The optical properties of annular hole arrays have been studied theoretically and experimentally in depth using perfect conductors and real metals [26, 48, 83, 87–90]. It was shown that the cavity resonances formed by (plasmonic or photonic) waveguided modes in a finite thickness metal film are the reason of strongly enhanced transmission. In the first experiments, the enhanced transmission was demonstrated in the visible spectral range up to around 17% for annular apertures periodically arranged in a gold film [90]. After that, it was demonstrated experimentally that these systems may present transmission around 90% when they are arranged in Ag films in the optical regime [91].

Also near-infrared properties have been studied for coaxial apertures and strongly localized fields in the apertures were found both experimentally and numerically [92].

Coupled to SP modes on metal film interfaces, the modes of annular apertures provide the possibility to achieve high transmission, field enhancement as well as high extraction efficiency of light trapped in the substrate. The latter is especially important for high-refractive index substrates with small angles of total internal reflection. Such nanostructures are thus promising candidates in a wide range of applications for light extraction such as LEDs, organic LEDs or vertical-cavity surfaceemitting lasers (VCSELs) [93–95], despite the fact that studies of the enhanced optical transmission through the plasmonic structures on high-refractive index substrates are virtually absent [96, 97] in the literature.

Along this chapter we will summarize the results obtained during the course of this thesis when studying the optical properties of periodic arrays with annular dimples and holes drilled in a metal surface [86, 96]. In particular,

- in Section 3.2, we describe experiments and numerical simulations to study dual band THz spoof plasmon propagating on a copper surface textured with an array of blind annular holes. The 2 fundamental modes in annular structures (the TEM and TE_{11} modes) will provide 2 different bands that we can control at will just by varying the geometrical parameters. The experiments were performed at the University of Bath (United Kingdom) within the group headed by Prof. S.R. Andrews, and at the Imperial College of London (United Kingdom) by Prof. S.A. Maier. For the theoretical simulations we used both the Finite-Difference Time-Domain (FDTD) method and the Coupled Mode Method (CMM) (see Chapter 2 for further details).

- in the following sections, we will study the optical properties of a hole array acting as a transparent electrode or LED. The system consists of a periodic array of annular holes drilled in a metal film and in combination with semiconductors. We will follow the next steps to achieve this degree of complexity: **(i)** first, we study transmission properties of free standing systems ($\varepsilon_1 = \varepsilon_3 = 1.0$) of arrays of annular holes where the metal is taken as a perfect electrical conductor (PEC); **(ii)** next, we add dielectric covers and substrates of either low- or high-refractive index; **(iii)** and finally, Surface Impedance Boundary Conditions (SIBCs) are incorporated into the model, where the finite dielectric constant of metals is considered and proper SPs appear as an ingredient in our studies. The limitations of the CMM, when SIBC and high refractive index dielectrics are combined, will be analyzed.

  In particular, in Section 3.5 we will present systematic studies of the enhanced transmission in hole arrays on high refractive index substrates, and the dependance of the geometrical parameters. Also the role played by the central nanopillar in annular holes [96] periodically arranged will be studied. This work was done in collaboration with the experimental group headed by Prof. A. V. Zayats at the Queen's University of Belfast(QUB) (United Kingdom). To study theoretically the optical response of those annular hole arrays we used the FDTD method.

3.2 Dual band terahertz waveguiding on a planar metal surface patterned with annular holes

The THz regime is conventionally taken to be between about $0.1 - 10$ THz ($\lambda = 3 - 0.03$mm) and lies between the domains of microwave electronics and mid infrared optics.

Developments in the THz band are strongly motivated by applications in fundamental science and the quest for higher bandwidth signal processing and new imaging and sensing modalities [98]. Examples of current or emerging applications include the dielectric characterization of materials [99], medical imaging [100], pharmaceutical quality control [101], communications [42], security screening [41], and chemical and biochemical sensing [40].

Potential sensing applications, for example in label free genetic testing, often involve small volumes of material. In this case it is desirable to enhance the sensitivity by confining the probing radiation in the region of the sample on a wavelength scale or better in at least one dimension.

Other important considerations are whether guiding can be achieved over a frequency range sufficient for spectroscopic discrimination and whether there is easy access to the guided mode. Various approaches to sensing have been suggested, including the use of stripline resonators [102], parallel plate waveguides [103], attenuated total internal reflection [104], and plasmonic metamaterials [105].

It is well known that every molecule has a set of own frequencies, and that for molecules of the same family, some of these own frequencies are repeated among them, that is, they resonate at the same frequency. Every set of these own frequencies is a kind of “fingerprint” for each one. Figure 3.1 shows the absorbance spectra of two different saccharides [106], Myo-inositol and D-ribose. Both molecules resonate at 1.58 THz. The aim of our work is the design of a detector able to differentiate 2 different frequencies at the same time in the THz regime.

Next we will show how annular dimples of finite depth may provide two different planar bands that can be tuned in order to make them coincide with the own frequencies of the molecule to be detected. This tunability is made just by choosing the suitable groove depth, and outer and inner radius of the rings.

The study of the dispersion relation of a system with two semi-infinite media, a dielectric and a metal, reveals that this system supports surface modes in the optical regime (SPPs). This is because at those frequencies, the electric field may penetrate into the metal, leading to confined EM fields.

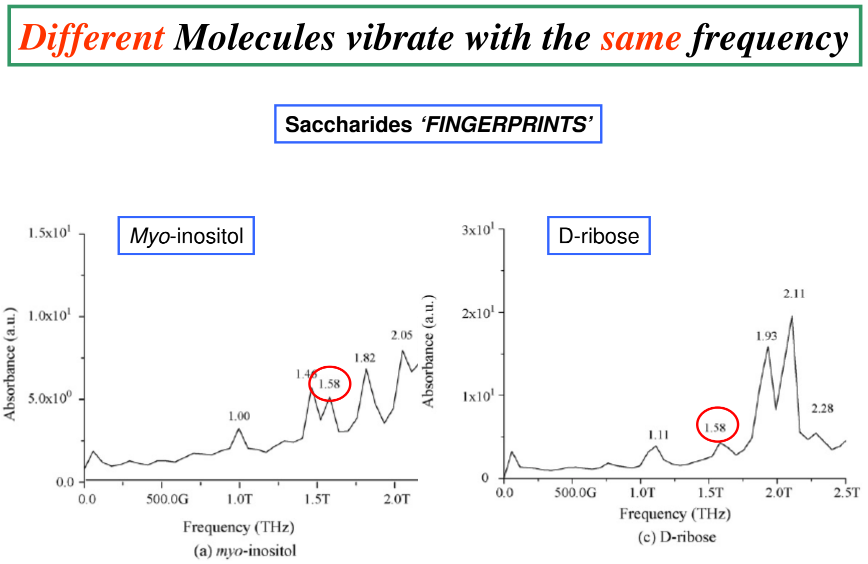

Figure 3.1: Absorbance spectra for two different saccharides, Myo-inositol and D-ribose [106].

However, in the THz regime, where metals behave as PECs, the electric field does not penetrate into them, and no tight surface modes are allowed.

Nevertheless, as we already shown, the periodic corrugation of an infinite metallic media with an array of holes allows the penetration of the electric field "through" the holes, by means of the least decaying eigenmode inside the apertures. This fact enables the appearance of tight surface modes in the THz regime, the Spoof Surface Plasmons, with similar characteristics to the canonical SPPs.

In particular, in 2004 it was demonstrated that an array of square holes in PEC under the approximation of a single mode inside the apertures, provided that the wavelength is much larger than the period of the array and the side of the squares, $\lambda > p > a$, could be understood as an effective media [71] with an effective dielectric constant and a magnetic permeability given by a Drude Model:

$$\begin{aligned} \varepsilon_{eff}(\omega) &\propto \left(1-\frac{\omega_p^2}{\omega^2}\right) \\ \mu_{eff} &= cte \end{aligned} \tag{3.1}$$

The plasma frequency of this effective system is given by the cutoff of the apertures, i.e., $\omega_p = \omega_c$, meaning that the geometry of the system controls the properties of the induced surface modes.

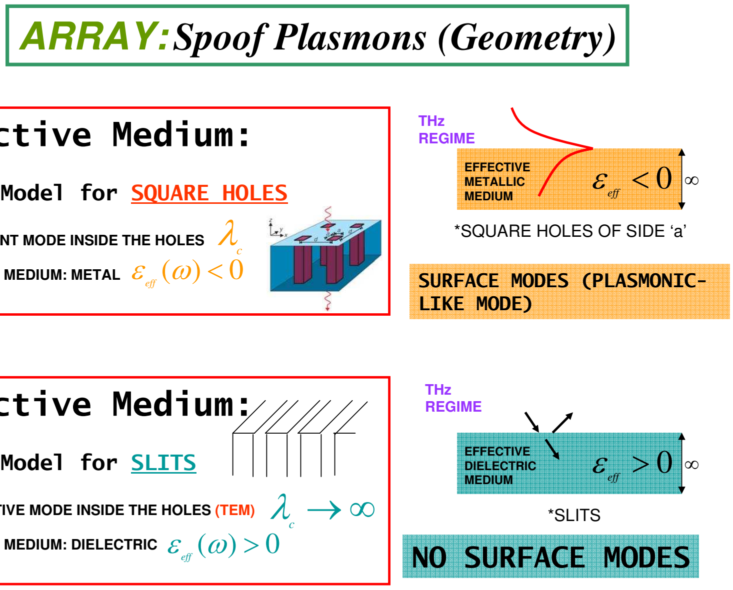

Figure 3.2: (Top) Schematics of the effective media related to an array with square holes drilled in a metal film. (Bottom) Schematics of the effective media related to an array with slits drilled in a metal film

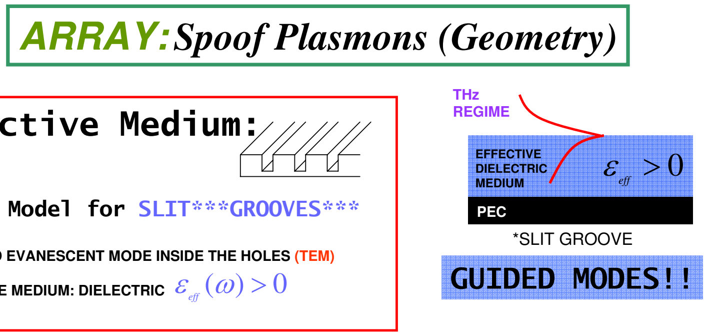

Figure 3.3: Schematics of the effective media related to an array with slit-grooves of finite depth drilled in a metal film.

Concerning the dispersion relation of these systems (with rectangular holes) when $\omega < \omega_c$, then $\varepsilon_{eff} < 0$, so the media "effectively" behaves as a metal, and surface modes can exist (see upper panel in the schematics in Fig. 3.2).

In contrast, other geometries such as slit arrays, present different effective behaviors. The fundamental mode inside slits is a propagative TEM mode (with no cutoff). In this case, $\varepsilon_{eff} > 0$, so the media behaves as a dielectric, and therefore, a slit array does not support surface modes (see lower panel in the schematics in Fig. 3.2).

However, slit grooves of *finite depth* can be considered effectively as a dielectric layer over a PEC where guided modes can exist [54]. Interestingly, TEM modes differentiate between waveguides of finite or infinite depth, while evanescent modes do not (see schematics in Fig. 3.3).

Based on these results, it is clear then, that using coaxial apertures of finite depth that support both TE_{11} and TEM modes will provide two bands that we can control geometrically.

To reach our goal, we consider a PEC drilled with annular dimples of finite depth, h_g, with outer radius a and inner radius b, periodically arranged with periodicity p. The PEC approximation considers $\varepsilon_m = -\infty$, and it is an excellent approximation in the THz regime. It allows to express analytically the waveguide modes inside the apertures. Within the CMM, considering just the fundamental TE_{11} and TEM modes provides accurate results [56]. Details of the expressions for these modes can be found in Appendix A.

As we said in Chapter 1, the cutoff of the TE_{11} mode can be approximated in the PEC approach as $\lambda_c^{TE} \approx \pi(a+b)$. Though propagative TEM modes do not have a cutoff wavelength, these annular grooves of finite depth support Fabry-Perot resonances at $\lambda^{TEM} = 2h_g/n$, with $n = 1, 2, 3..$ [37]. In terms of frequencies, we can write these resonant wavelengths as $f_c^{TE} = c/\pi(a+b)$ and $f^{TEM} = c/(4h_g)$, with c the speed of light.

As an example, we will design our system in order to have planar bands at two frequencies that coincide with two of the own frequencies of the tartaric acid, $f = 1.06$ THz and $f = 1.8$ THz. This molecule is a natural preservative (E-334) used to improve and correct wine acidity, also as a flavouring, and at industrial scale to prepare soft drinks as well. It can be applied in photography and as a varnish, and even as a fertilizer in some laboratories.

The set of parameters providing planar bands at 1.06 and 1.8 THz are the following: the period is taken $p = 80\mu$m, and the hole depth is approximately $h_g = 60\mu$m. For the annular dimples, the inner and outer radius are $b = 10\mu$m and $a = 30\mu$m, respectively. This system supports spoof plasmons with local field patterns similar to those of the TEM and TE_{11} modes of the infinite guides. The dispersion curves of these TEM-like and TE_{11}-like spoof plasmon modes were calculated in the PEC approximation using both FDTD simulations and, with very similar results, with the CMM (see Fig. 3.4). In particular, for the set of geometrical parameters considered, TM and higher order TE modes have frequencies above 7 THz and can be neglected. The TEM-like spoof plasma frequency is determined by the hole depth and lies at $f^{TEM} = 1.06$ THz. However, the TE_{11} waveguide cutoff lies near 5 THz and is above the free space frequency at the zone boundary so that the effective TE_{11}-like cut off is instead determined by the period of the structure. A Gap is opened due to diffraction and the planar band then appears at $f_c^{TE*} = 1.8$ THz.

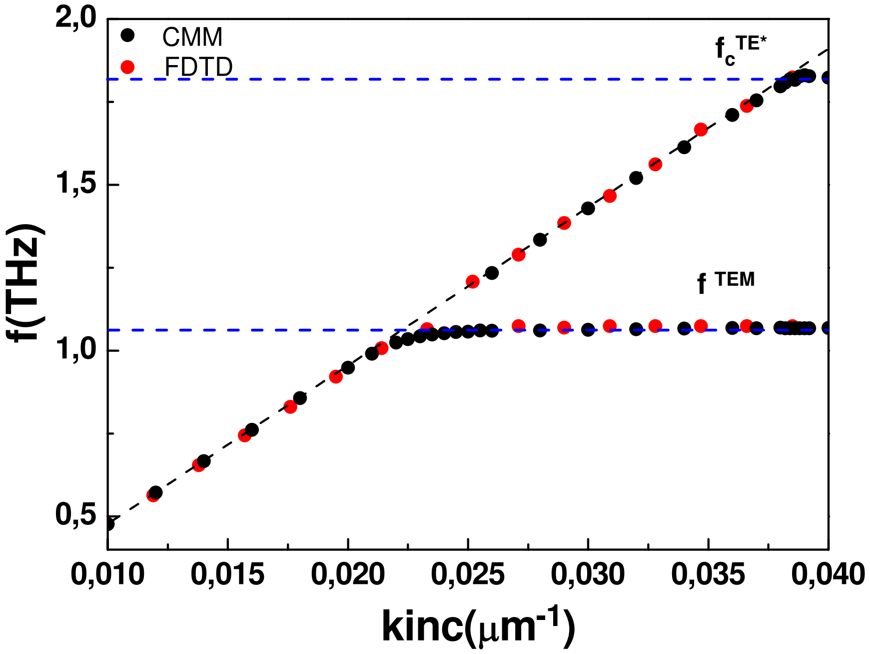

Figure 3.4: Metamaterial dispersion curves calculated using both CMM simulations (black dots) and FDTD calculations (red dots). k_{inc} is the wavevector parallel to the surface in the direction of propagation. With dashed lines it is depicted the spoof plasma frequencies $f^{TEM} = 1.06$ THz and $f_c^{TE*} = 1.8$ THz. The geometrical parameters of the dimple array with annular apertures are: $b = 10\mu$m, $a = 30\mu$m, $h_g = 60\mu$m and $p = 140\mu$m.

Interestingly, the TEM-like spoof plasma frequency could be tuned between roughly 1.7 and 0.3 THz by varying h_g, as it can be seen in Fig. 3.5, where theoretical results using the CMM are shown. In that figure, $p = 140\mu$m, $a = 60\mu$m and $b = 50\mu$m.

The theoretical design of the system was also investigated experimentally at the University of Bath. The structure was made using photolithography, and an electron micrograph of the top surface and cross section of it can be seen in Fig. 3.6.

Figure 3.7 shows the measured difference between k_x and g, Δk_x (with $g = 2\pi/\lambda$), together with that calculated using the CMM. This calculation provides information about the confinement of the TEM and TE$_{11}$ modes. The agreement between calculations and experiments for the TE$_{11}$ mode is excellent, and the noticeably worse agreement for the TEM mode is probably due to the variation in h_g across the sample.

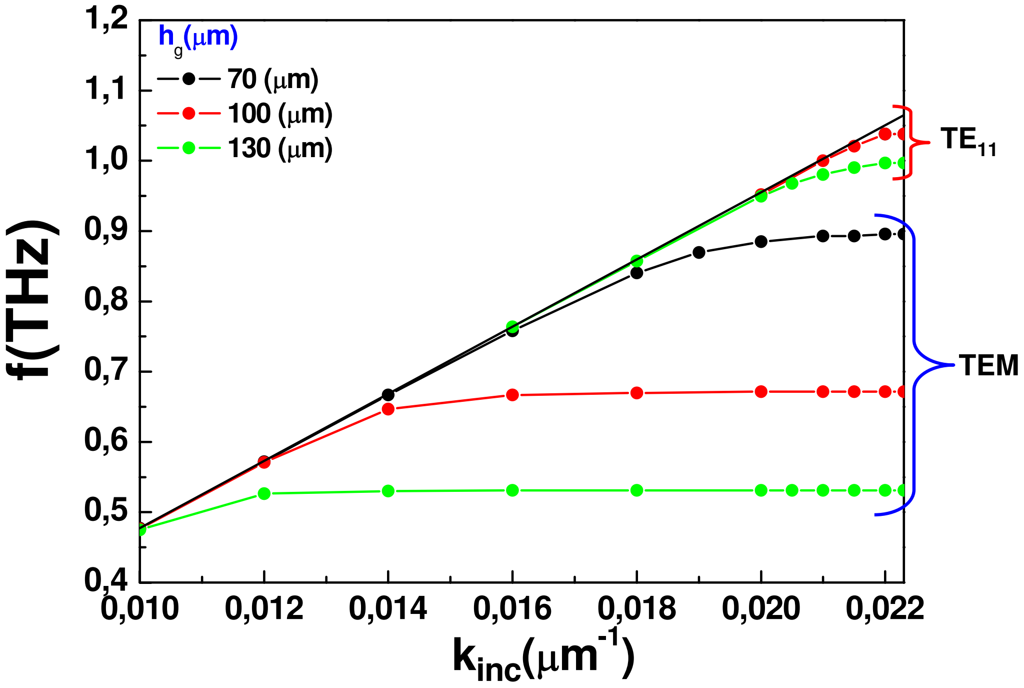

Figure 3.5: Metamaterial dispersion curves calculated using CMM simulations. k_{inc} is the wavevector parallel to the surface in the direction of propagation. The geometrical parameters of the dimple array with annular apertures are: inner radius $b = 50\mu$m, $a = 60\mu$m and $p = 140\mu$m, and we let vary h_g.

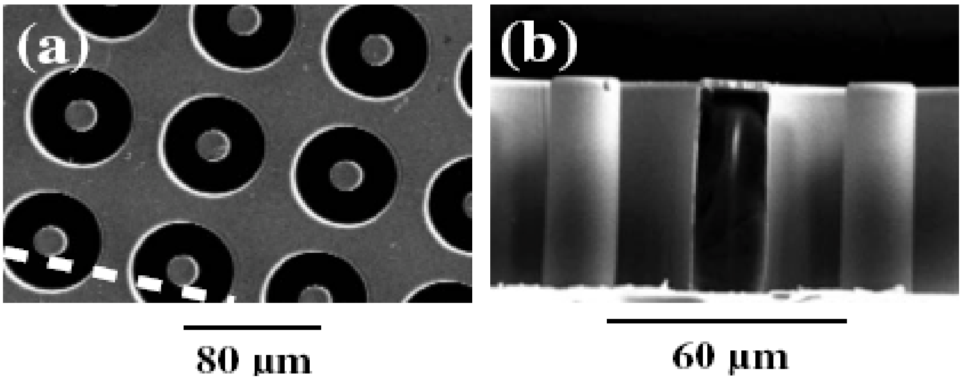

Figure 3.6: (a) Electron micrograph of the metamaterial top surface. (b) Cross section along the dotted line in (a). The white area at the bottom of (b) is the pyrex substrate.

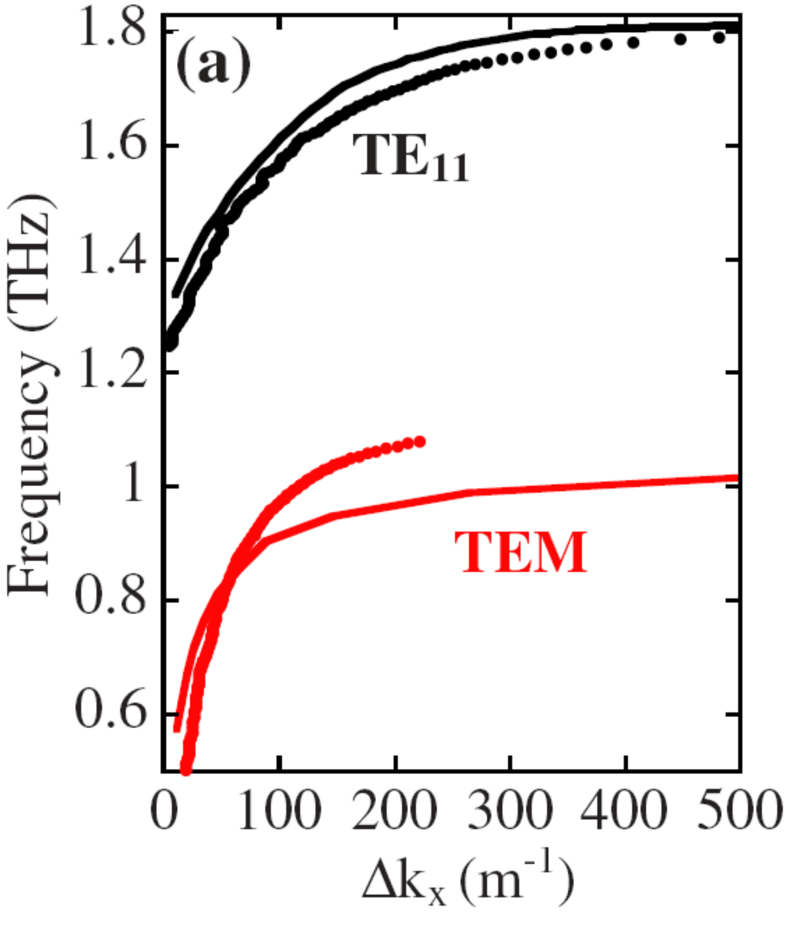

Figure 3.7: Deviation of spoof plasmon dispersion curves from the light line. Red and black points are from experiment, continuous curves are calculated using the CMM.

As a technical note, it is worth remarking that we can only analyze theoretically this region so close to the light cone with the CMM approach, but not with the FDTD method. The reason is that due to the strong out-of-plane confinement of the fields, the system to be implemented within the FDTD method in order to analyze the optical properties, was too large. However, in order to further check the experimental and CMM results, we did calculations for asymptotic values for the TEM mode (far from the light cone) with the FDTD method, finding the same tendency as the CMM results.

The dispersion results shown in Fig. 3.7 allow us to estimate the out of plane extent of the guided waves. In the experiments, the amplitude of the signal is maximum at 0.90 THz for the TEM mode [86]. We estimate the exponential field decay length, $L_z = 1/\sqrt{k_x^2 - g^2}$, to be $620 \pm 40\mu$m ($\sim 2\lambda$). For the TE$_{11}$ mode at 1.50 THz we obtain $L_z = 500 \pm 50\mu$m ($\sim 2.5\lambda$). These values are a hundred times smaller than expected for a fully evolved SPP on a flat copper surface, known as a Zenneck wave [107]. The narrow frequency window where the group velocity of the TEM mode is very small and over which L_z theoretically approaches $\lambda/8$ at the band edge, was not accessible in the measurements. This is because of poor field overlap with the THz beam, higher attenuation, and the broadband nature of time domain spectroscopy.

Notably, since the bands are so planar, there is a strong confinement of the EM fields ($k >> g \rightarrow |k_z| >> g$). This fact along with the large density of states, lead to a strong absorption of the reflected beam. Therefore, in order to detect the presence of tartaric acid in a sample, a small volume of it would be needed. We expect that, despite the measurements were performed without the sample itself, the small volume of the sample to be analyzed would not affect the optical properties of the whole system.

3.3 Free-standing Periodic Arrays with Annular Holes

Let us now explore the properties of hole arrays as transparent contacts in LEDs. The structure consists of periodic annular hole arrays in combination with high refractive index dielectrics.

First, we consider a PEC pierced by periodic arrays of subwavelength annular holes. Unless otherwise stated, we illuminate the system with a normal-incident plane wave with the electric field pointing along one of the axes of the array. We consider a minimal model where just the fundamental TE$_{11}$ mode inside the apertures is taken into account, because the coupling with the TEM mode at normal incidence is zero (see Appendix A for further details).

For PECs, all geometrical lengths can be scaled since the expressions for transmission appearing in Chapter 2 (Eqs. 2.18, 2.19, and 2.20) do not depend on them.

Let us first consider the *theoretical* situation in which the dielectric constant of the cover and the substrate are the same and equal to unity, $\varepsilon_1 = \varepsilon_3 = 1$.

Figure 3.8 shows the transmission spectrum in an array (lattice parameter $p = 1\mu\text{m}$) of annular holes with outer radius $a/p = 0.45$ and inner radius $b/p = 0.40$ in a metal film of thickness $h/p = 0.40$. Typically, for these calculations the number of diffraction orders considered are $n_x = (-10, 10)$ and $n_y = (-10, 10)$, for both TE and TM modes, what provides converged results. Transmission is normalized to the intensity that impinges in a unit cell, so in the absence of losses, $T = 1$ entails that all the incident light is transmitted.

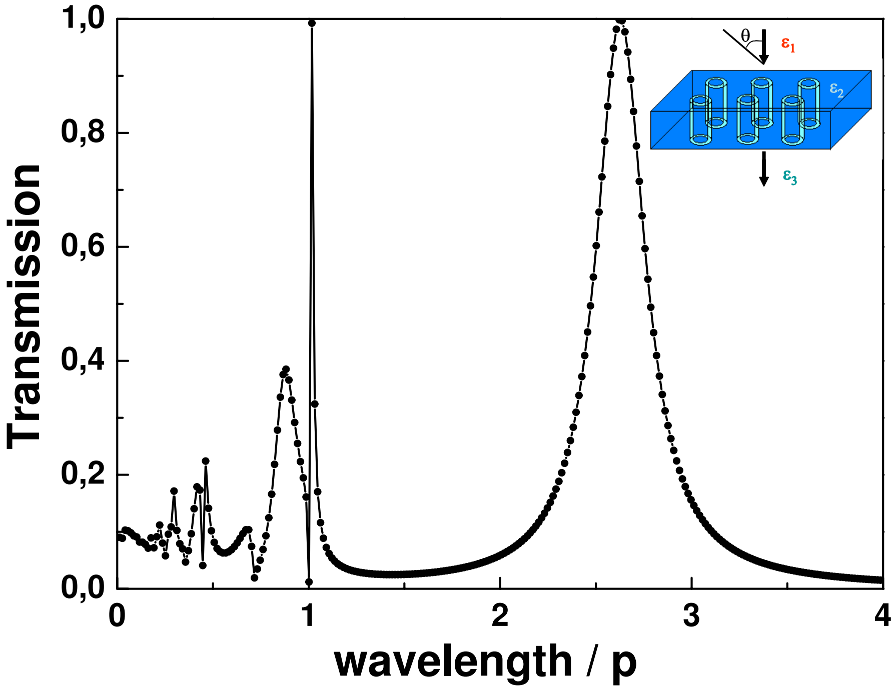

Figure 3.8: Transmission spectrum for a perfect electrical conductor pierced by an annular hole array (with periodicity $p = 1\mu\text{m}$), with outer radius $a/p = 0.45$, inner radius $b/p = 0.40$ and film thickness $h/p = 0.40$).

In Fig. 3.8 we observe a sharp drop in transmission with $T = 0$ exactly when the wavelength approaches the period, $\lambda/p = 1$. This is known as the Rayleigh condition wavelength, $\lambda_R = \sqrt{\varepsilon}p$, when the $(n_x, n_y) = (1, 0)$ diffraction order changes its character from evanescent to radiative. In general, there will appear minima in transmission whenever $k_{||}$ for any of the diffraction orders satisfies: $k_{||}^2 = (g\sqrt{\varepsilon})^2$, that is, $\left(\frac{2\pi n_x}{p}\right)^2 + \left(\frac{2\pi n_y}{p}\right)^2 = \left(\frac{2\pi\sqrt{\varepsilon}}{\lambda}\right)^2$.

These minima are accompanied by a strong peak arising slightly redshifted compared to λ_R, which is connected to the excitation of surface modes. More precisely, this peak is related to the spectral location of the surface plasmon polaritons (SPPs) of the corrugated structure [108–110]. Note however that PECs do not support SPPs, but surface modes geometrically induced (spoof plasmons) hold when the metal surface is structured [71, 111]. Therefore, transmission peaks appearing in PECs close to $\lambda_R = \sqrt{\varepsilon}p$ will characterize the equivalent Extraordinary Optical Transmission (EOT) in real metals.

Additionally, Fig. 3.8 presents another resonance at $\lambda/p = 2.67$. Several works have shown that the shape of the subwavelength apertures is of great importance since they influence both the resonant wavelength and the polarization in the transmission spectra [44–46, 112, 113]. Essentially, these are Fabry-Perot (F-P) resonances. In fact, it has been experimentally and theoretically demonstrated that for a symmetric and uniform dielectric environment (the dielectric constant is the same in all non-metallic regions), the spectral location of this resonance occurs at approximately the cutoff wavelength of the apertures, λ_c [44–47, 59, 76, 112–115].

Their appearance is related to the vanishing of the group velocity inside the hole. Therefore, photons spend a long time in the system, and transmission resonances could eventually take place. We will denote these cutoff resonances as **Zero-order Fabry-Perot** in order to distinguish them from higher order F-P resonances. The equation defining a F-P is given by [20]

$$2\,k_{nz}\,z + 2\,\phi_R = 2\,m\,\pi \tag{3.2}$$

being ϕ_R the scattering phase at the interface, which can be neglected for resonances appearing close to λ_c. Since at cutoff, $k_{nz} = 0$, in order to fulfil the above expression m must be zero. That is why we will denote resonances appearing at $\sim \lambda_c$ as Zero-order F-P.

To demonstrate that the resonances appearing close to $\lambda_R/p = 1$ and $\lambda_c/p = 2.67$ correspond to the excitation of SPPs and Zero-order F-P modes inside the aperture, respectively, we can (for instance) vary the periodicity of the array and modify the inner radius of the annular holes and observe how these resonances behave.

Figure 3.9 (a) depicts transmission of light for the same system as before, with $p = 1\mu$m and $p = 0.75\mu$m. We observe that minima in transmission occur at both $\lambda_R = 1\mu$m and $\lambda_R = 0.75\mu$m in each case, and that these zeroes in transmission are followed by sharp maxima. These are typical EOT resonances

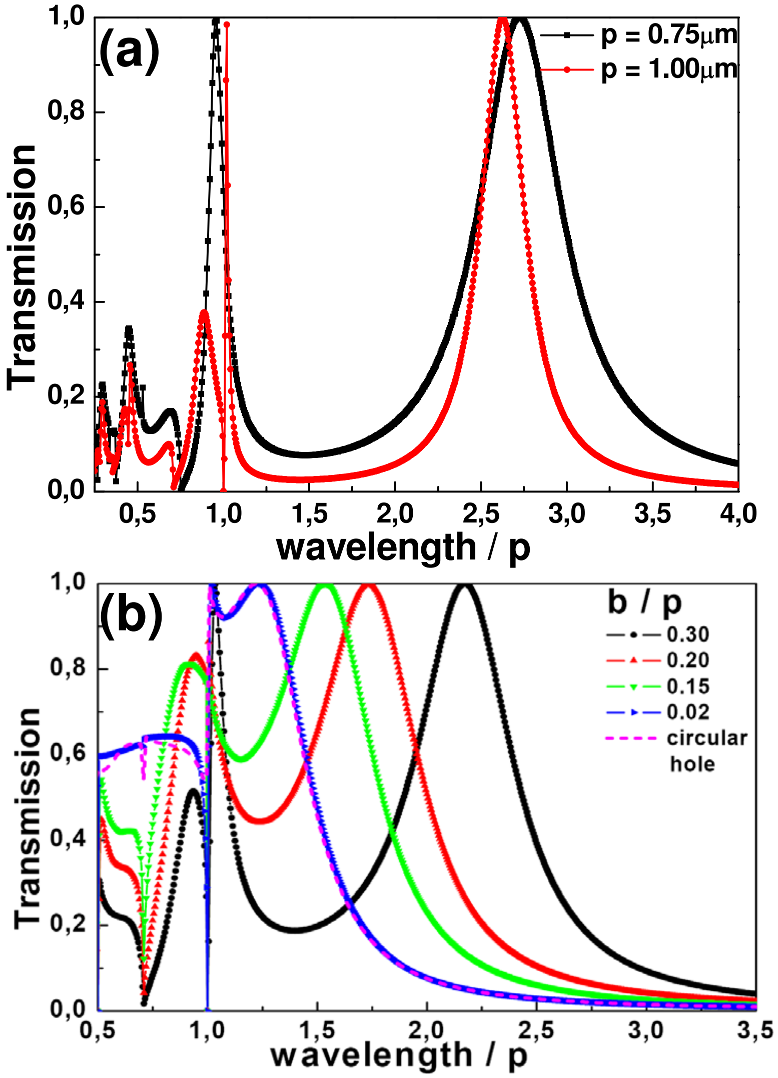

Figure 3.9: (a) Transmission spectra for the same parameters as those in Fig. 3.8 with $p = 1\mu\text{m}$ and $p = 0.75\mu\text{m}$. (b) Transmission spectra for the same system as in Fig. 3.8 for several inner radius $b/p = 0.30, 0.20, 0.15$ and 0.02. Dashed magenta curve accounts for the transmittance of an equivalent grid of circular holes.

appearing when surface modes are excited.

Panel (b) shows transmission spectra for the same geometrical parameters as in Fig. 3.8 for several b/p values, which cover the circular hole case and annular holes of high aspect ratio ($b \to a$). Whereas the resonance emerging at $\lambda_R/p = 1$ remains invariable, when we vary b, the localized resonance follows $\lambda/p \approx \lambda_c/p$, making evident that these are localized resonances associated to the λ_c of the TE$_{11}$ mode. Since $\lambda_c \approx \pi(a+b)$, the more redshifted resonances correspond to those annular holes of higher aspect ratio. The magenta curve in this figure accounts for the transmission of light through a grid of circular holes with radius $r_c/p = 0.45$, equivalent to that with annular holes when $b/p = 0.02$.

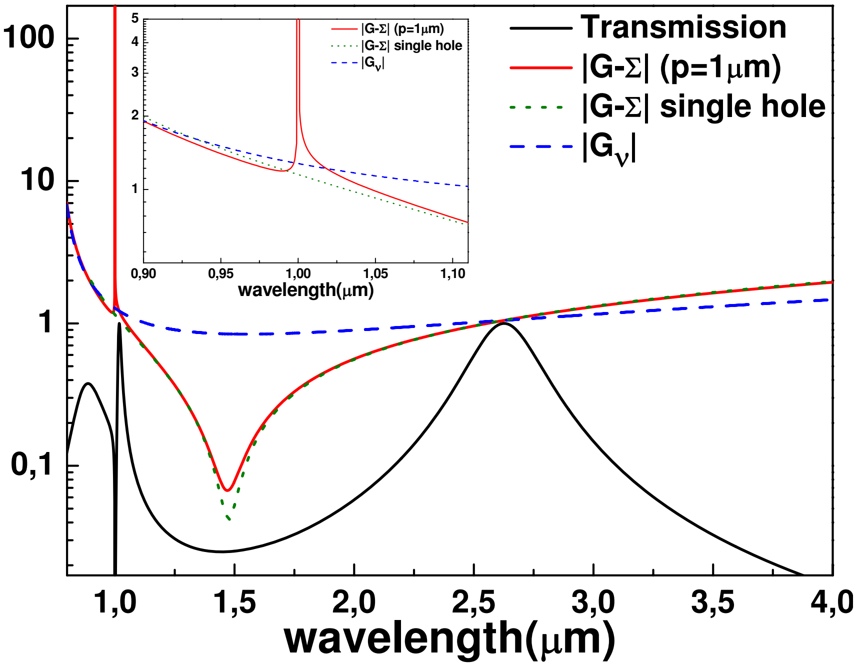

Figure 3.10: Transmission of light, absolute values of $|G-\Sigma|$ and $|G_\nu|$ (in logarithmic scale) for a hole array (with $p = 1\mu$m) and a single annular hole.

From Eq. 2.18 given in Chapter 2, it can be demonstrated [59] that maxima and minima in transmission occur when $|G-\Sigma| = |G_\nu|$, for both single holes and hole arrays (for $\lambda > \sqrt{\varepsilon}p$). In Fig. 3.10 we show, for the same geometrical parameters as those in Fig. 3.8, transmission of light through a hole array ($p = 1\mu$m), the term $|G-\Sigma|$ for the same hole array, but also for a single hole, together with $|G_\nu|$. Remember that for single holes, the sum over diffraction orders in G must be substituted by an integral (see Appendix B). Inset in that figure is a zoom in wavelengths to highlight what happens around the periodicity. On the one hand, the condition $|G-\Sigma| = |G_\nu|$ with hole arrays is fulfilled in two cases, that coincide with resonances in transmission maxima related to the excitation of surface plasmons at λ_R and Zero-order F-P modes at λ_c. On the other hand, $|G-\Sigma| = |G_\nu|$ is only fulfilled at λ_c for single holes, throwing further evidence in the fact that transmission features around the periodicity of the array are connected to the excitation of surface waves, and that the other resonances already occurs in isolated apertures.

3.4 Dielectric covers and substrates in periodic arrays with Annular Holes

Actually, any real grid containing annular holes must be supported by a substrate (or cover, indicating in that case that the dielectric is placed at the illumination region), because otherwise, the central metallic part would fall.

Since the final goal in this chapter is the study of the optical properties of hole arrays acting as transparent electrodes, we must consider high refractive index dielectrics that will account for semiconductors ($\varepsilon \sim 10$) in our system.

Going on with the PEC approximation, we differentiate between symmetric configurations, where the cover and the substrate have the same dielectric constant ($\varepsilon_1 = \varepsilon_3$), and asymmetric ones ($\varepsilon_1 \neq \varepsilon_3$). In particular, we are interested on the effect of a dielectric environment in peak intensities and peak positions.

Figure 3.11 shows transmission spectra for the same geometrical parameters as those considered in Fig. 3.8, but adding different dielectrics in both symmetric (left panel) and asymmetric configurations (right panel). For the sake of clarity, first we consider low refractive index dielectrics with $\varepsilon = 1, 2, 4$ and 6.

In **asymmetric systems** where the dielectric is placed as a substrate, the most obvious qualitative effects when ε increases, are:

- the $(1,0)$ Wood anomaly related to the metal-dielectric at $\lambda_R = \sqrt{\varepsilon}p$ redshifts, whereas the metal-air anomaly ($\lambda_R = p$) remains the same.
- the Zero-order Fabry-Perot transmission peak red shifts.
- this peak broadens.
- the intensity of this peak decreases.

For **symmetric configurations**, the above effects also happen, but

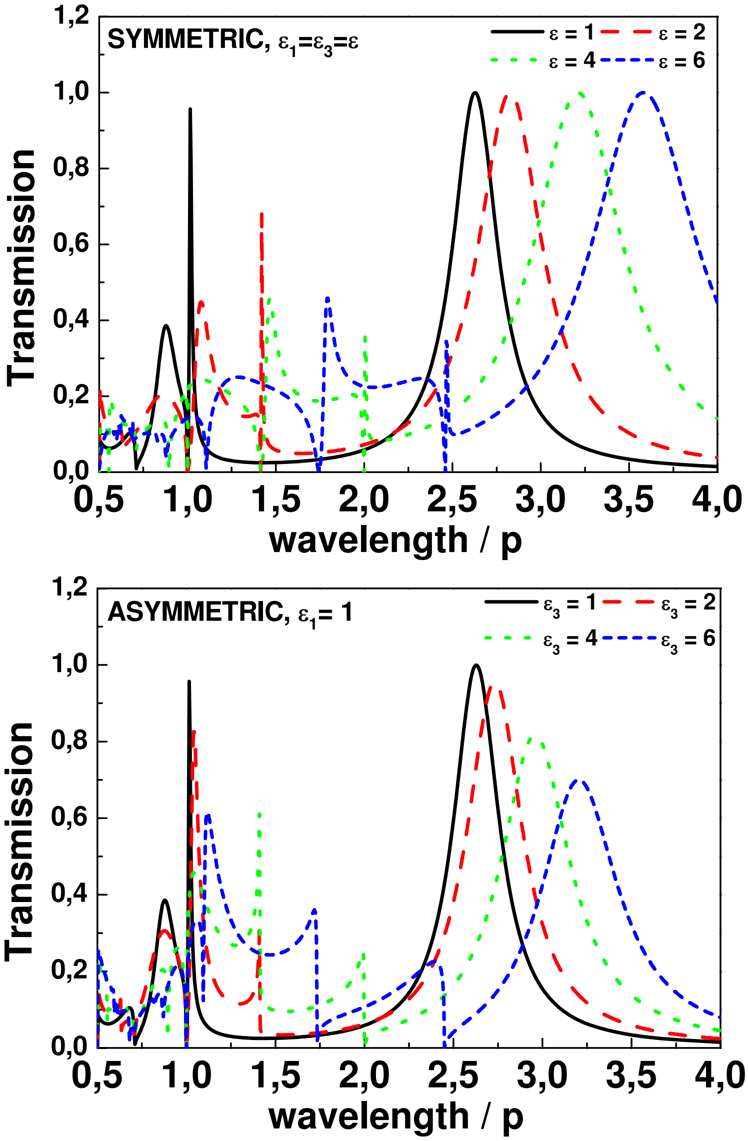

Figure 3.11: Transmission of light for the same system as in Fig. 3.8 for symmetric systems (top panel) where the cover and the substrate have the same dielectric constant, and for asymmetric systems (bottom panel), where they are different.

- there is no transmission decrease in the Zero-order Fabry-Perot resonance, since the amount of diffraction orders to couple with in the illuminated and transmission regions are exactly the same.

A further study of these results found for F-P resonances in combination with dielectric environments and thin films will be discussed in detail in Chapter 5.

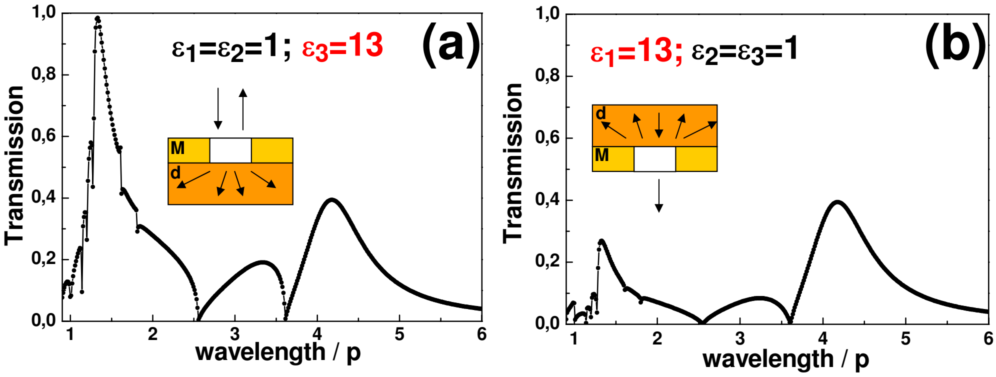

Figure 3.12: Transmission of light for the same system as in Fig. 3.11 for asymmetric systems where the dielectric is placed either as a substrate (panel (a)), $\varepsilon_3 = 13$, or as a cover (panel (b)), $\varepsilon_1 = 13$.

Additionally, we study these annular hole arrays in combination with high refractive index dielectrics in asymmetric systems where the dielectric is placed either as a substrate (ε_3) (panel (a) in Fig. 3.12), or as a cover (ε_1) (panel (b) in Fig. 3.12). We choose $\varepsilon = 13$, a typical value for semiconductors.

First, we observe that in both cases, transmission spectra show several minima that correspond to different diffraction orders satisfying $\left(\frac{2\pi n_x}{p}\right)^2 + \left(\frac{2\pi n_y}{p}\right)^2 = \left(\frac{2\pi\sqrt{\varepsilon}}{\lambda}\right)^2$.

Besides, we observe that at $\lambda/p > \sqrt{\varepsilon} = 3.60$, transmission spectra are identical since there is only one diffraction order to couple with. However, at $\lambda/p < 3.60$, intensity in transmission features when the dielectric is placed as a substrate (panel (a)) is larger than in the case when the dielectric is places as a cover (panel (b)).

The main difference between these two panels is associated to the transmission intensity at $\lambda/p \approx 1$. When the dielectric is placed as a substrate, $T \approx 1$, whereas if the dielectric is placed as a cover, then $T << 1$.

This is related to the different amount of available diffraction orders to couple with in the illuminated and transmission regions, as it is schematically shown in the inset of the figure. When the dielectric is placed as a substrate, transmission coefficients take priority to the detriment of reflection ones, and the other way around occurs when the dielectric is placed as a cover.

These results suggest that, in order to obtain maximum transmission taking advantage of the localized resonance, symmetric configurations are desired, where wide resonances and $T = 1$ are obtained; whereas, if EOT resonances are our target, then, asymmetric systems with $\varepsilon_3 > \varepsilon_1$ seem to be the best configurations.

Let us now consider real metals by including Surface Impedance Boundary Conditions (SIBCs) in the horizontal surfaces. We also calculate the propagation constant of an infinite coaxial waveguide made of real metal, k_{nz}, as it is explained in Chapter 2 and Appendix C. As we showed in Chapter 2, the combination of SIBC and high refractive index dielectrics within the CMM may reduce the range of validity of this CMM approach.

In Fig. 3.13 we show the comparison between CMM (SIBC+k_{nz}) and FDTD calculations of the transmittance of light as a function of the wavelength in periodic arrays with annular holes drilled in a gold film of $h = 100$nm thickness on a glass substrate ($\varepsilon_3 = 2.25$). The gold dielectric constant is taken from the experimental data appearing in Ref. [75]. The periodicity is $p = 600$nm, and for annular holes the outer radius is fixed to $a = 175$nm. We consider several inner ones (see inset in the figure). Both peak position and intensity in transmission spectra agree very well when the two methods are compared. Nevertheless, since the spatial profile of the fundamental mode is obtained considering the PEC approach in the waveguide (what provides analytical expressions for the overlap with plane waves), and based on the experience of our group, we expect that the use of the PEC approximation provides slightly larger intensity values, and blue-shifts in transmission spectra of ≈ 50nm compared to the results obtained with the FDTD mehod.

However, Fig. 3.14 shows CMM and FDTD calculations of the transmission of light through a similar array to that in Fig. 3.13, but with smaller annular holes of outer radius $a = 100$nm, and a semiconductor placed as a substrate $\varepsilon_3 = 13$. This time, although the results obtained with the two methods agrees very well for transmission features emerging at long wavelengths (in both intensity and peak position), this is not the case for the general appearance of transmission spectra at shorter wavelengths, $\lambda < 1000$nm. This has to do with the fact that SIBC approach is only valid when the dielectric constant of the metal surface is much larger than the dielectric constant of the environment, $\varepsilon_m >> \varepsilon$, and when the skin depth is $\delta > 0$ but small enough compared to the dimensions of the apertures. This was thoroughly explained in Chapter 2.

Additionally, in order to gain physical insight, we analyze near field maps

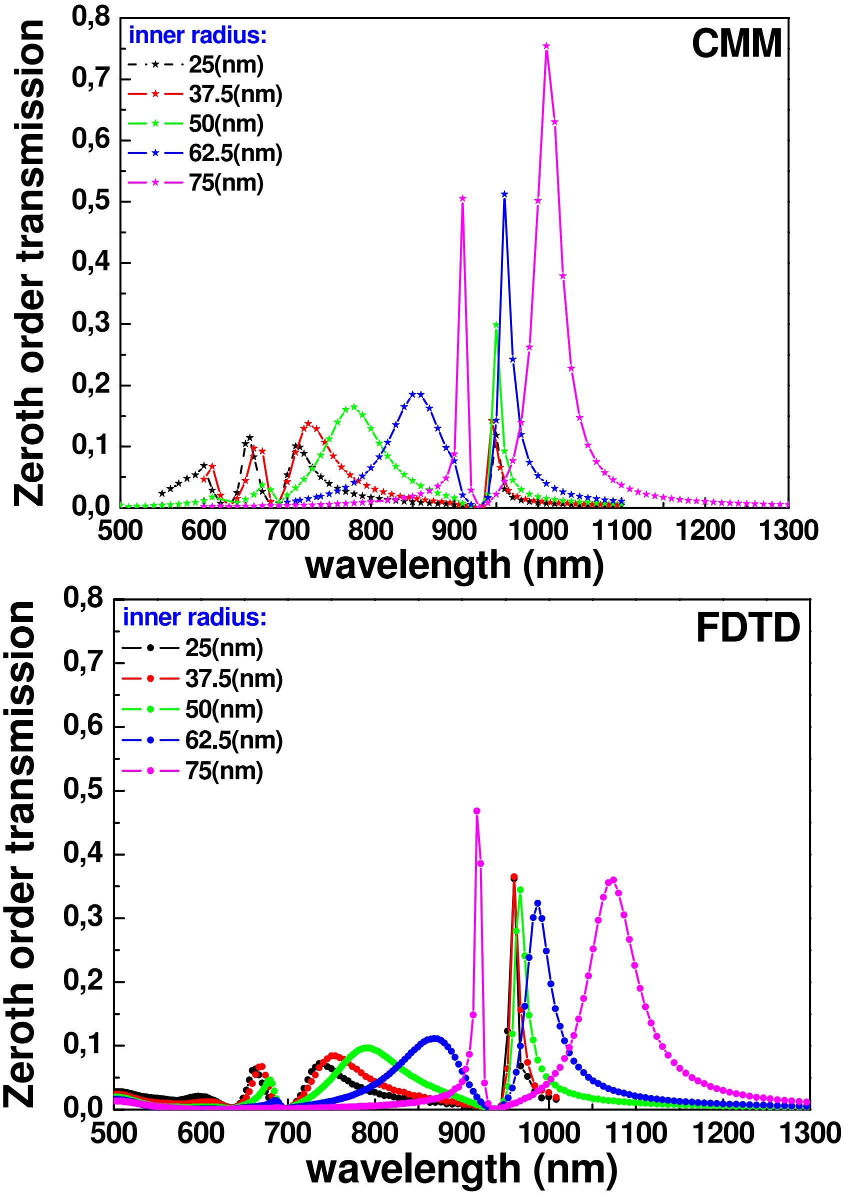

Figure 3.13: CMM and FDTD calculations of the transmission of light as a function of the wavelength in square arrays with annular holes drilled in a gold film of $h =$ 100nm thickness on a glass substrate ($\varepsilon_3 = 2.25$). The periodicity is $p = 600$nm, and annular holes with different inner radios are considered (with outer radius fixed to $a = 125$nm. (a) CMM calculations within SIBC and the modified wavevector. (b) FDTD calculations (performed by Dr. Sergio G. Rodrigo).

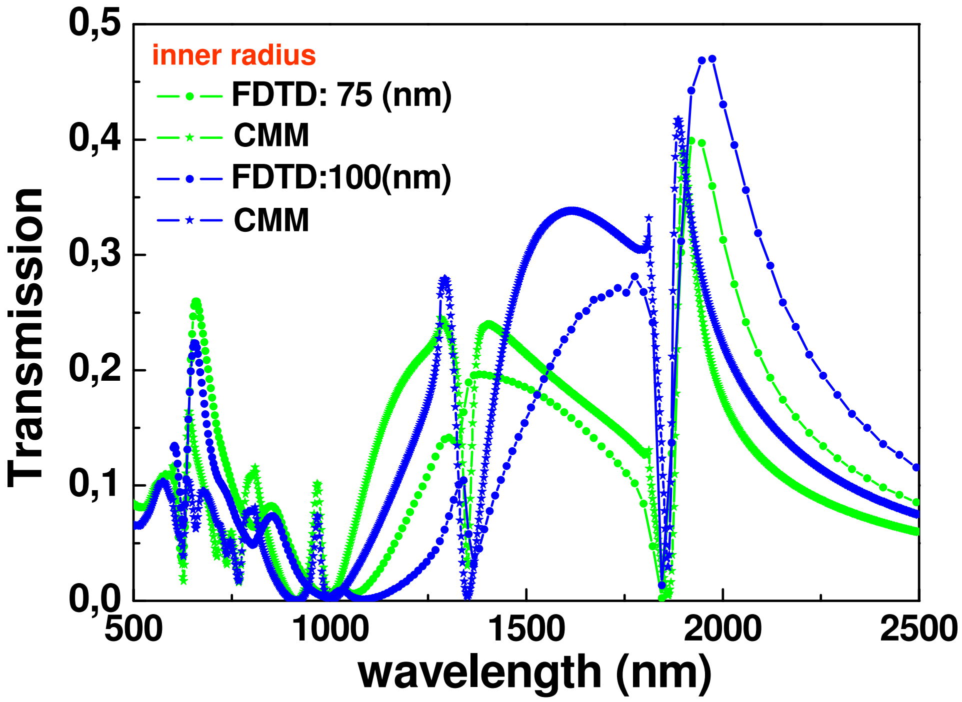

Figure 3.14: CMM and FDTD calculations of the transmission of light as a function of the wavelength in square arrays with annular holes drilled in a gold film of $h =$ 100nm thickness on a substrate with $\varepsilon_3 = 13$. The periodicity is $p = 600$nm, and annular holes with different inner radios are considered (with outer diameter fixed to $r_{out} = 100$nm. (a) CMM calculations within SIBC and the modified wavevector. (b) FDTD calculations.

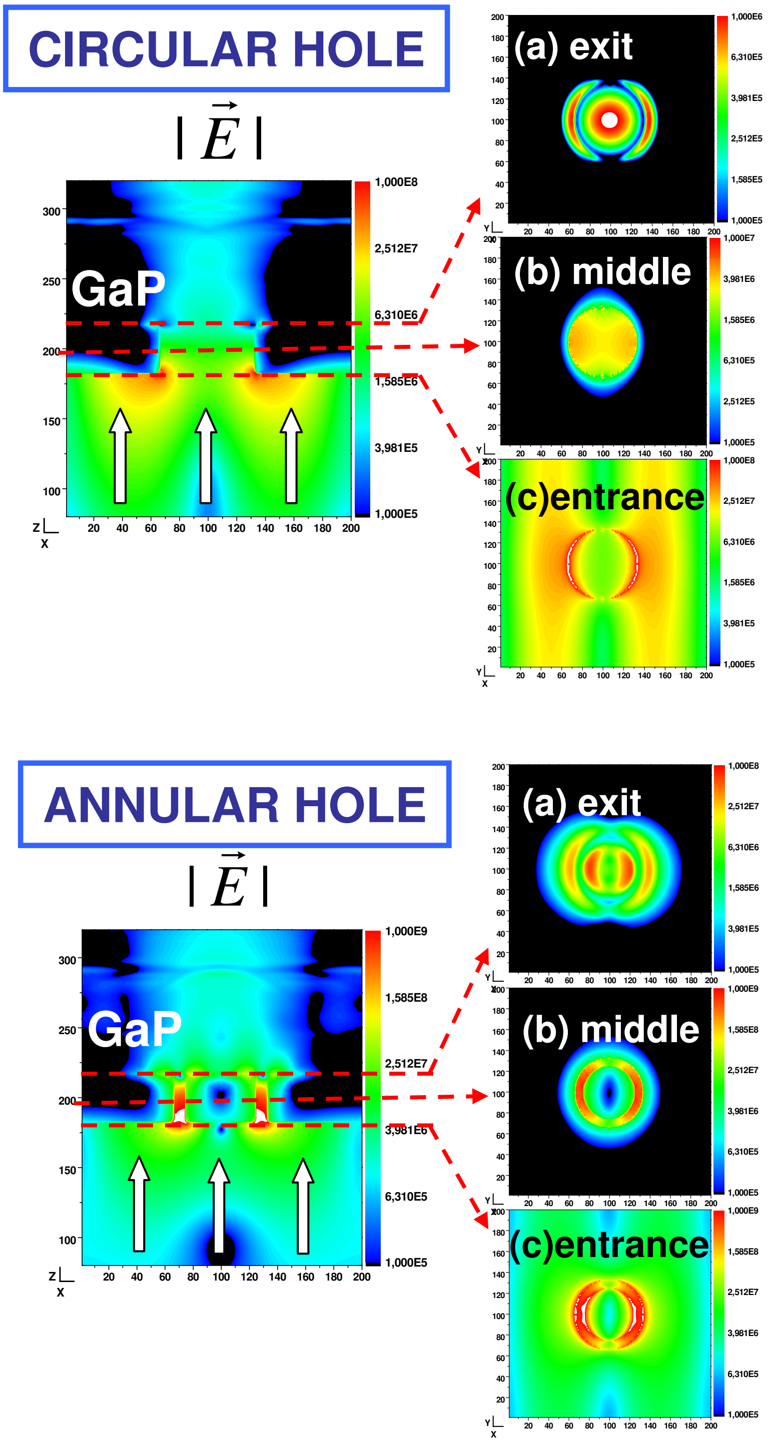

Figure 3.15: Modulus of the electric field in the zx plane for circular and annular holes, together with calculations in the xy plane at the entrance (c), in the middle (b) and at the exit (a) of the apertures. The geometrical parameters are: gold arrays with p = 600nm and film thickness h = 100nm, on a GaP substrate (ε_3 = 12.88). Left panels correspond to circular holes with outer radius r_{out} = 100nm, and right panels to annular holes with outer radius a = 100nm and inner one b = 75nm.

with the FDTD method for these systems with annular holes. Figure 3.15 shows contour plots of the modulus of the electric field $\left|\vec{E}\right|$ in the zx plane for circular and annular holes for a unit cell, together with calculations in the xy plane at the entrance (c), in the middle (b) and at the exit (a) of the apertures. The geometrical parameters are: arrays in gold with $p = 600$nm, film thickness $h = 100$nm, on a Gallium Phosphide (GaP) substrate ($\varepsilon_3 = 12.88$). Upper panels correspond to circular holes with radius $r_c = 100$nm, and lower ones to annular holes with outer radius $a = 100$nm and inner one $b = 75$nm. As expected, for circular holes perforated in a metal film, the E-field is highly concentrated near the edges of the hole, whereas for annular holes, high field enhancement is found inside the apertures. Since the field is also more intense and spreads at the exit of annular holes, it also spreads more in the transmission region where the GaP substrate is placed.

3.5 Optical transmission of periodic annular apertures in a metal film on high-refractive index substrate: The role of the nanopillar shape

Next, we present systematic studies of the enhanced transmission through periodic arrays drilled with annular holes and the dependence on the size, shape, and period on high refractive index substrates emulating plasmonic structures on LED chips. Also experimental measurements carried out at QUB are presented. The influence of nanofabrication tolerances on the optical properties of these plasmonic annular aperture arrays on high-index substrates is also investigated.

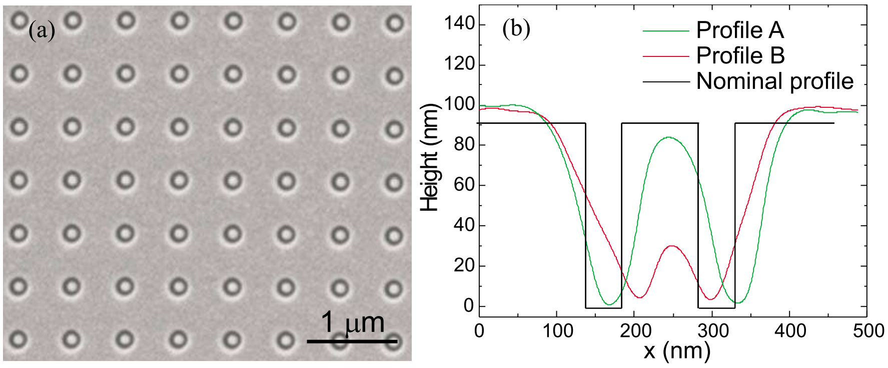

Figure 3.16: (a) SEM image of a typical array of the FIB-milled annular apertures. (b) The cross-sections of AFM images showing the annular apertures profile for 100 nm inner diameter and 200 nm outer diameter apertures in the 600 nm period array milled with different FIB parameters.

The experimental samples consist of a 100nm thick gold film on a GaP substrate ($n = 3.14, 3.59$ in the visible spectral range). Four different types of arrays of annular holes with a constant outer diameter of 200nm and four different inner diameters: 0 (circular holes), 50, 75, and 100nm are considered. Also three different lattice periods are investigated 600, 650, and 700nm. The structures were fabricated using a focused ion beam (FIB) milling on magnetron sputtered Au films. The measurements confirmed good correspondence between the designed and actual parameters of the structures in terms of lateral sizes (Fig. 3.16 (a)). The profiles of the central pillar were, however, strongly dependent on the FIB milling parameters, so ideal annular apertures were difficult to obtain on the required length scales (Fig. 3.16 (b)).

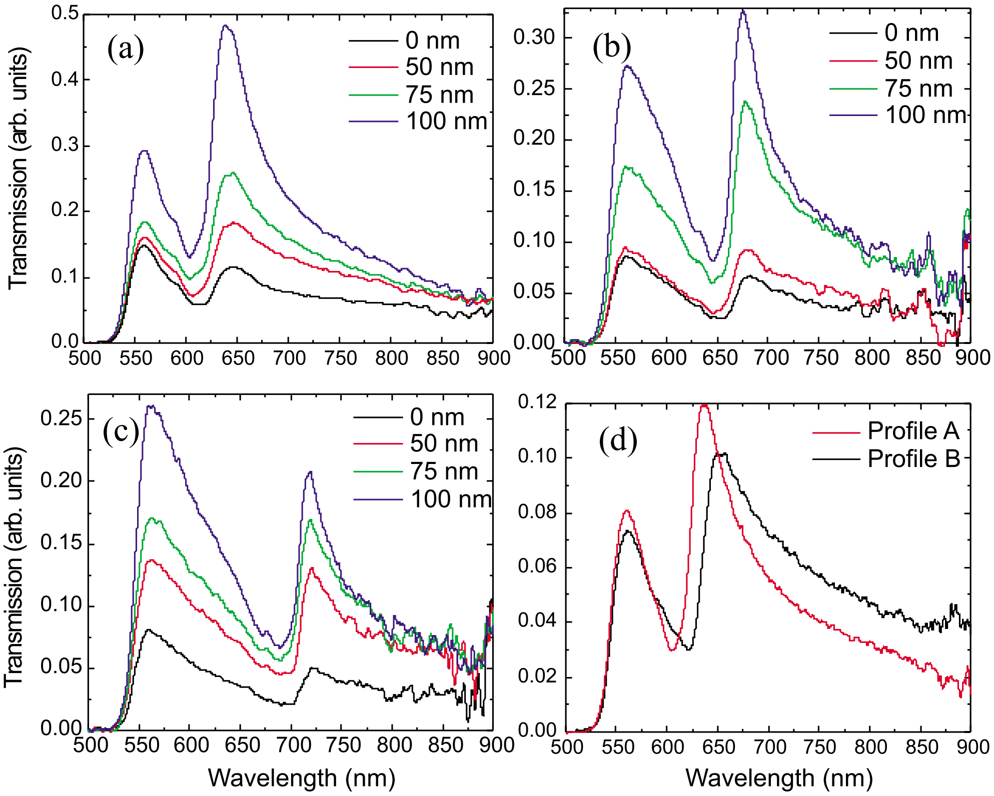

Figure 3.17: Experimental transmission spectra of the aperture arrays fabricated in the 100 nm thick Au films on the GaP substrate for different periods of the array: (a) 600, (b) 650, and (c) 700nm. The outer diameter of the apertures is 200nm, the inner diameters are indicated in the legends. (d) Experimental transmission spectra of the annular hole array with different profiles of the central nanopillar, corresponding to the AFM images of Fig.3.16 (b).

In order to compare with experiments, the zeroth order transmission is computed. The calculations were made taking into account a substrate with

$n = 3.59$ coated with 100nm of Au. The Au dielectric constant is taken from the experimental data appearing in Ref. [75]. The dispersion of the refractive index and absorption of GaP substrates were neglected for technical reasons, but the comparison with experiments shows that this is not an important effect for wavelengths longer than 550nm. Due to the spectral range and high refractive index dielectric here considered, all calculations are performed with the FDTD method, not attainable with the CMM and SIBCs approximations, as we previously showed. Additionally, since characterizing the experimental samples led to some problems and most of these samples had annular holes of extremely high aspect ratio but with a central cylindrical pillar far from being cylindrical (as it can be seen in Fig. 3.16), the actual experimental profiles of the annular holes were implemented also within the FDTD method.

The experimental transmission spectra of the systems described above are presented in Fig. 3.17 for different annular apertures and lattice periods. Note that the strong extinction for wavelengths shorter than 550nm is due to the strong absorption of GaP substrate in this spectral range [116]. In general, the transmission spectra exhibit one dominating resonance with a period-dependent spectral position. Increasing the diameter of the inner pillar leads to a significant increase in transmission despite the reduction in the total area of the openings. This is accompanied by a small redshift of the transmission peak position. The maximum transmission was experimentally observed for annular holes with inner diameters of approximately 100nm.

The spectra of the annular holes milled with different parameters and therefore featuring differently shaped central nanopillars (Fig. 3.16 (b)) are shown in Fig. 3.17 (d). The two nanopillar types are designated “A” (tall) and “B” (short); they have different heights and while the aperture outer diameter is approximately the same, the effective diameter is different for each nanopillar. While exhibiting a similar spectrum defined by the SPP Bloch mode of the crystal, the resonant transmission of sample B is redshifted and slightly smaller than for the array with taller nanopillars.

Simple analysis of plasmonic modes supported by the nanostructures under consideration shows that SPPs are not supported on the GaP/Au interface in the visible spectral range, since $\varepsilon_{Au} + \varepsilon_{GaP} > 0$ for $\lambda < 620$nm. Although SPPs exist at lower frequencies, their wavelength is much shorter than that at the Au/air interface and the propagation length is small in the visible spectral range due to the high-refractive index of the GaP. This considerably simplifies the discussion of the transmission mechanisms that, therefore, mainly involve waveguided modes in annular apertures and SPP Bloch modes on the air/Au interface of the plasmonic crystal [110, 117].

The efficiency with which the waveguided modes transmit energy depends on the thickness of the film as well as the inner and outer diameters of the annular apertures as the propagation constant of the mode depends on these parameters. These waveguided modes are then hybridized with SPP Bloch modes of the crystal lattice which are then coupled to photons. Therefore, the modification of the lattice period leads to the modification of the spectral position of the available SPP Bloch states and their overlap with the waveguided modes. This translates into both a redshift of the transmission peaks and the reduction in the absolute transmittance as the period increases. Numerical modeling reproduces not only the experimental transmission spectra with good agreement but also the trends observed when the inner diameter and the pillar heights are varied (Fig. 3.18 and Fig. 3.19). The spectra obtained with the ideal apertures show that transmission increases in the dominating resonance with an increase in the nanopillar diameter. The position of the peak is strongly sensitive to nanopillar diameter and exhibits a strong redshift when the nanopillar diameter becomes close to the aperture diameter. Since the absorption in the substrate is neglected, the second resonance is observed on the short-wavelength side of the SPP band gap. A good agreement between theory and experiment is observed for the position of each transmission peak as well as the relative transmitted intensity for each structure. Note also that the experiment and modeling are compared for zeroth-order transmission; the calculated total transmission can be up to 20%.

The transmission spectra modeled for different heights of the central pillar are shown in Fig. 3.19. Again, increasing the nanopillar height leads to an increase in the transmission of the annular hole array. Initially, the resonance redshifts in comparison to the simple hole resonance until the nanopillar height is half of the film thickness; for taller nanopillars the opposite trend, a blueshift of the resonance, is observed. However, the resonance on the short-wavelength side of the band gap behaves monotonically.

Finally, modeling the transmission spectra using the experimentally acquired profiles almost perfectly recovers the observed experimental spectra (Fig. 3.19). In these spectra, the short wavelength peak near the absorption edge of the GaP is not resolved, clearly as a result of the nanopillar profile and not the dispersion of the optical properties of the substrate is the reason. In both the experiment and model, it is also clear that this peak is present as a broad shoulder. The interplay between variations in both the effective diameter and pillar height, having opposite trends, minimizes the shift of the resonant wavelength but has an impact on the absolute transmission.

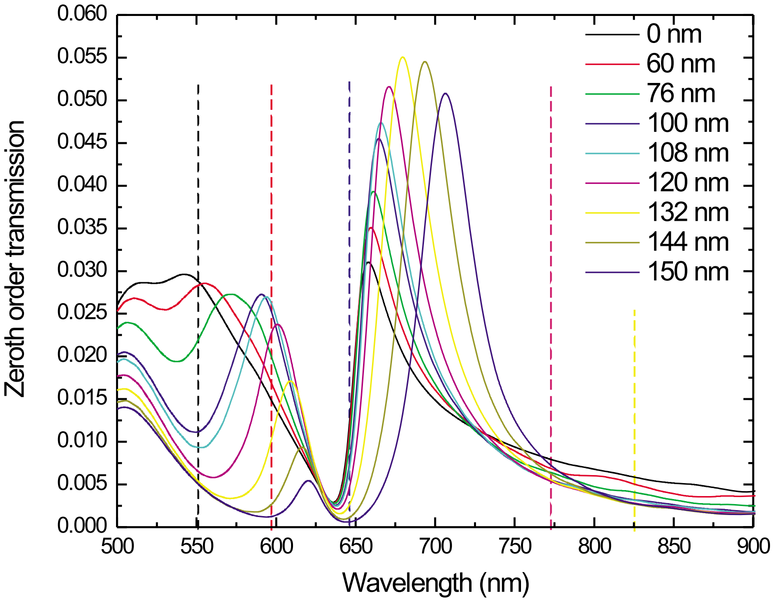

Figure 3.18: Calculated transmission spectra of the annular hole array in Au film for different diameters of the inner nanopillar. GaP substrate is considered dispersionless and lossless in the calculations. The film thickness is 100nm, the period is 650nm, and the outer diameter of the apertures is 200nm. The inner diameters are indicated in the legends. The dashed vertical lines indicate the cutoff wavelengths for holes and annular apertures of several inner diameters.

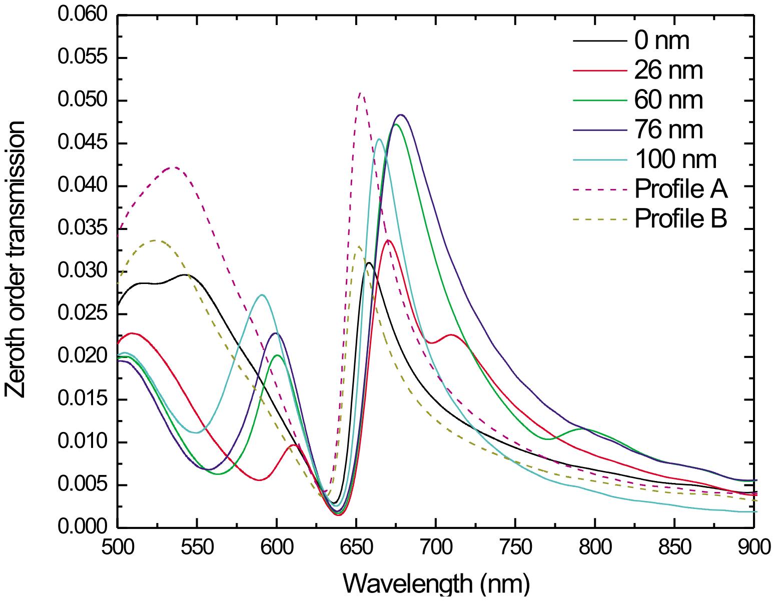

Figure 3.19: Calculated transmission spectra for the same system as in Fig. 3.18 with the inner diameter 100nm. The transmission spectra calculated for real nanopillar shapes, as in Fig. 3.16 (b) are also presented.

3.6 Conclusions

In conclusion we have shown that periodic arrays with annular holes or dimples present special features that enables the design of potential sensing detectors and transparent electrodes.

In particular, we have demonstrated that the use of coaxial apertures of finite depth that support both TE_{11} and TEM modes, provide two planar bands that can be controlled geometrically. This enables the experimental and theoretical design of detectors able to differentiate 2 frequencies at the same time in the THz regime. We have presented experimental results and numerical simulations showing propagation of tightly bound and relatively low loss spoof plasmon-THz waves on a metamaterial surface containing annular cavities. Guiding in two independently variable frequency bands can be supported and geometrically controlled. Together with efficient end-fire coupling, this could be useful in waveguide-based chemical or biochemical sensing where the ability to ratio responses in at least two distinct frequency bands with high dynamic range is desirable for quantitative analysis. In this particular case, the array was design so that it could distinguish 2 frequencies of the tartaric acid.

Finally, we have considered high refractive index dielectrics to explore the properties of holes arrays as transparent contacts in LEDs. We have studied the influence of the nanopillar shape on the resonant transmission through annular holes in Au film on a high-refractive index substrate. High-refractive index substrates prevent the efficient use of the SPP modes on Au/substrate interface for tailoring the transmission properties. However by varying the nanostructure parameters, some degree of tunability may be achieved. At the same time, simplification of the available SPP Bloch mode spectrum leads to the observed spectral response which is robust over a range of fabrication tolerances, although the absolute transmission is significantly influenced.

Chapter 4

Finite Systems

4.1 Introduction

A subwavelength aperture is a key element in near-field optical devices and many recent photonic structures. When the lateral dimensions of such aperture is smaller than half the wavelength, light cannot propagate through the hole and the transmission is typically very weak. Hans Bethe in 1944 stated that transmission scaled as the fourth power of the aperture diameter [21], when he analyzed the transmission through a small hole in an infinitely thin perfectly metal screen. However, a real subwavelength aperture is very different because the thickness and the finite conductivity of the metal has significant consequences in transmission.

The invention of the scanning near-field optical microscope (SNOM) in the 1980s [118, 119], and the discovery of the Extraordinary Optical Transmission (EOT) phenomenon [23] stimulated new experimental and theoretical studies on both the total intensity and the spatial distribution of the light transmitted through a small hole [27, 56, 120–124].

These works mostly indicated that there is a resonance that stems from the excitation of a localized surface plasmon at the edges of the hole. Additionally, FDTD calculations revealed that the spectral position of the transmission maximum through a circular hole, redshifts with increasing hole diameter, and blueshifts with increasing film thickness. Interestingly, it was also reported that this resonance in a free standing system is spectrally located "close" to the cutoff wavelength, λ_c, of the lowest-order mode [59]. It has been attributed to the tunneling of light through the fundamental waveguide mode inside the holes and its appearance could be expected since the modulus of the propagating constant of such mode is almost negligible close to λ_c. Therefore, the field inside the holes does not experience a strong decay, photons spend a long time in the system, and transmission resonances can eventually take place.

However, further theoretical investigations are still needed in order to reveal the physics behind this resonance appearing for isolated holes and its relation to the cutoff of the apertures.

As it was previously discussed, the main ingredient for the appearance of EOT resonances in periodic arrays of subwavelength holes is the presence of surface electromagnetic (EM) modes that couple to the incident light. This idea suggested that the EOT phenomenon should also occur in single apertures if they were surrounded by a finite periodic array of indentations. This hypothesis was experimentally verified [24,25] in both a 1D slit flanked by a finite array of linear grooves, and in Bull's Eye (BE) structures, a 2D cylindrical hole surrounded by concentric annular trenches.

Despite in the 1D version the dependence of the optical transmission with the geometrical parameters such as the period of the array or the depth of the grooves, has been extensively analyzed experimentally and theoretically, in the case of BEs, this dependance is not that clear [30, 32–37, 125]. The reason is that, in contrast to the 1D version, the optical response of each annular groove depends on its radius, and therefore, it is different one from each other [24–29, 63, 126–128]. Experiments have also revealed that the total transmission through a BE structure can be understood as the product of three distinct contributions: the coupling efficiency on the input surface, the transmission or cutoff function of the aperture, and the decoupling efficiency of the output surface [27].

Unexpectedly, when the periodic corrugation is placed at the output surface of the aperture, the angular distribution of the transmitted radiation may be strongly modified [25], and at some resonant wavelengths light emerges from the structure as a strongly collimated beam controlled by the corrugations of the output surface. These results were observed in both BE structures and its 1D version.

Nevertheless, there are also questions that remain, notably about how to optimize these BE structures for different optical functionalities, which need to be elucidated.

In the following sections, we will characterize and optimize transmission of light through,

- A single (circular and annular) hole

- Bull's Eye Structures

4.2 Extraordinary Optical Transmission

4.2.1 Single Holes

In order to investigate the optical properties of BE structures, we first characterize the resonance of an isolated circular and annular hole, since these will be the kind of apertures that will be placed at the centre of the structures.

Circular Holes

To gain physical insight in how transmission through isolated apertures can be optimized at a fixed wavelength (λ_R), let us first consider a **single circular hole**, whose dimensions depend on just one parameter (its radius), in a free standing system, with $\varepsilon_2 = 1$.

Subwavelength apertures may behave as *effective* apertures whose optical cross section, $r_R(\varepsilon_2 = 1)$, is represented by a radius which can be different from the nominal parameters, $r(\varepsilon_2 = 1)$ (see Fig. 4.1).

A single hole is at resonance when it is at cutoff, i.e., when $\lambda_c = \lambda_R$. In the case of circular apertures: $\lambda_c = \frac{2\pi r}{1.84} \approx 3.5r$. As a result, the effective dimension will be determined by the cutoff wavelength.

Let us then characterize an empty circle by its:

- cutoff wavelength $\lambda_c(1)$
- nominal radius $r(1)$
- effective radius $r_R(1) = (1/3.5)\lambda_c(1) \approx 0.3\lambda_c(1)$
- $Area(1) = \pi r(1)^2$

Interestingly, we have found that an empty circle ($\varepsilon_2 = 1$) presents $T_R(\varepsilon_2 = 1) \approx 1$ at $\lambda_R = \lambda_c$ (as it can be see in Fig. 4.4, for instance). This important result entails that for circular holes, the nominal and effective parameters are the same:

$$r_R(1) \approx r(1) \tag{4.1}$$

However, when the single hole is filled with $\varepsilon_2 > 1$, then, the above parameters become [59, 129] (see Fig.4.1):

- $\lambda_c(\varepsilon_2) = \lambda_c(1) \cdot \sqrt{\varepsilon_2}$

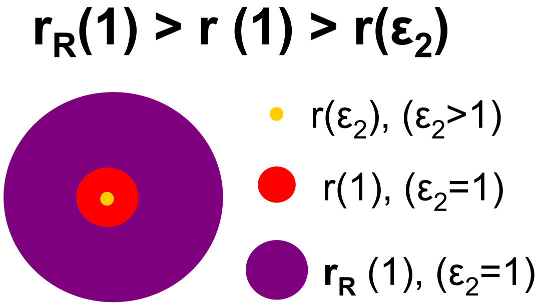

Figure 4.1: Schematics of the different areas involved described in the text.

- $r(\varepsilon_2) = \frac{r(1)}{\sqrt{\varepsilon_2}}$
- $r_R(\varepsilon_2) = \frac{r_R(1)}{\sqrt{\varepsilon_2}} = \frac{1}{\sqrt{\varepsilon_2}}\, 0.3\, \lambda_c(1)$
- $Area(\varepsilon_2) = \frac{1}{\varepsilon_2}\, Area(1)$

That is, if a circular hole is filled with ε_2, the radius of an empty circle must be reduced a factor $\sqrt{\varepsilon_2}$ to still operate at $\lambda_R = \lambda_c$. Therefore, transmission normalized to the area of the new smaller and filled hole, becomes:

$$T_R(\varepsilon_2) = \varepsilon_2 \cdot T_R(1) \tag{4.2}$$

The last expression indicates that if we fill up the circle with, for instance, a dielectric constant $\varepsilon_2 = 25$, then, $T_R(25) = 25$ (since $T_R(1) \approx 1$). We have found that Eq. 4.2 also holds for annular holes.

We can further corroborate these findings using the general analytical expression given in Ref. [59] for transmission at resonance:

$$T_R \approx \frac{|I_0|^2}{4Im(G)} \tag{4.3}$$

where I_0 accounts for the direct illumination impinging on the system, and $Im(G)$ is the imaginary part of the effective admittance (or Green function), G (see Chapter 2 for further details). This expression only holds for resonant systems like rectangles, annular holes or circular holes filled with $\varepsilon_2 >> \varepsilon_1$, ε_3.

Results for Eq. 4.2 and 4.3 are shown with an illustrative example in Fig. 4.2. There, transmission of light (normalized to the area of the radius, $A = \pi r^2(\varepsilon_2)$) as a function of the radius is calculated with the Coupled Mode Method (CMM) (extensively explained in Chapter 2). The system is illuminated by a normal-incident linearly polarized plane wave, and we consider a

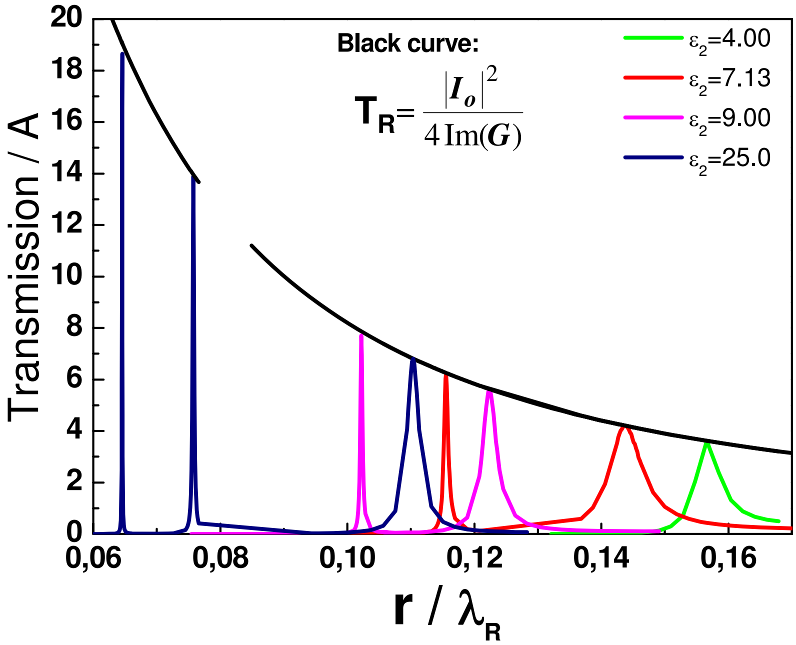

Figure 4.2: Transmission of light at a fixed wavelength, λ, for a single circular hole, as a function of its radius, r/λ. The film thickness is $h/\lambda = 0.4$. The hole is filled with a dielectric constant $\varepsilon_2 = 4, 7.13, 9$ and 25, corresponding to green, red, pink and blue curves. The black curve represents the condition $T_R \approx \frac{|I_0|^2}{4ImG}$.

minimal model where just the fundamental TE_{11} mode inside the apertures is taken into account.

The metal is considered as a perfect electrical conductor (PEC), and all geometrical parameters are normalized to the resonant wavelength, λ_R: the film thickness is $h/\lambda_R = 0.4$, and the hole is filled with several dielectric constants: $\varepsilon_2 = 4$, 7.13, 9 and 25. The black curve represents the condition given by Eq. 4.3.

We observe several Fabry-Perot resonances emerging at different r/λ_R values. The narrowest ones are Zero-order Fabry-Perot resonances related to λ_c, and they fulfil both Eq. 4.2 and 4.3. Wider peaks correspond to other higher order F-P modes. Note that, the larger the value of ε_2, the higher the value of T_R, and the narrower the resonances become.

Annular Holes

Let us now move to annular holes, whose optimization at a fixed wavelength will be more complex since their dimensions depend on two parameters, the inner (b) and the outer (a) radios.

In this case, within the minimal model, we just consider the fundamental TE_{11} mode inside the apertures, because as said before, the coupling with the other fundamental mode, the TEM mode, carries no energy at normal incidence.

We take the metal as a PEC, so all lengths (geometrical parameters and wavelengths) can be given in arbitrary units, or normalized. As we showed in Chapter 3, transmission spectra in annular hole arrays present Zero-order F-P resonances appearing at wavelengths close to the cutoff of the lowest-order mode (the TE_{11} mode), which under PEC approach can be approximated as $\lambda_c \approx \pi(a+b)$.

In order to compare with the studies developed in Chapter 3 about how the dielectric environment affects transmission spectra in hole arrays, in Fig. 4.3 we show the transmission of light calculated with the CMM, through both hole arrays and single holes in asymmetric systems where $\varepsilon_1 = \varepsilon_2 = 1.0$, and ε_3 varies from 1 to 9. The metal film thickness is taken $h = 100$, and it is drilled with annular holes with $a = 125$ and $b = 100$ (in arbitrary units).

Transmission is normalized to the area of the equivalent circular hole of radius a, $A = \pi a^2$, and it appears in logarithmic scale to highlight the features.

In the figure it is observed a resonance at $\lambda \approx \lambda_c = 705$ emerging in both hole arrays and single holes when $\varepsilon_3 = 1$. This is the Zero-order F-P resonance associated to the cutoff of the holes. When the dielectric constant of the substrate is increased, this resonance redshifts and decrease in intensity as it is also observed in hole arrays. Due to the localized nature of this resonance, it appears in both single holes and hole arrays at the same spectral position. However, only in arrays, transmission spectra are affected by the Rayleigh condition which provokes sharp deeps in transmission spectra of zero transmission whenever $k_{||}^2 = (g\sqrt{\varepsilon})^2$.

A detailed study of these results found for Zero-order F-P resonances in combination with dielectric environments and thin films will be discussed in detail in Chapter 5.

We can also study how this resonance related to the cutoff of the less decaying TE_{11} mode varies in intensity and position with the inner radius of the annular hole. In Fig. 4.4, transmission spectra are shown for isolated annular holes drilled in a PEC of 100 thickness, with a fixed outer radius $a = 200$ and several inner one $b = 1, 50, 100$ and 150 (in arbitrary units), in a free standing system ($\varepsilon_1 = \varepsilon_3 = 1$).

In this figure we observe those remarkable properties of annular holes indicated in the introductory chapter:

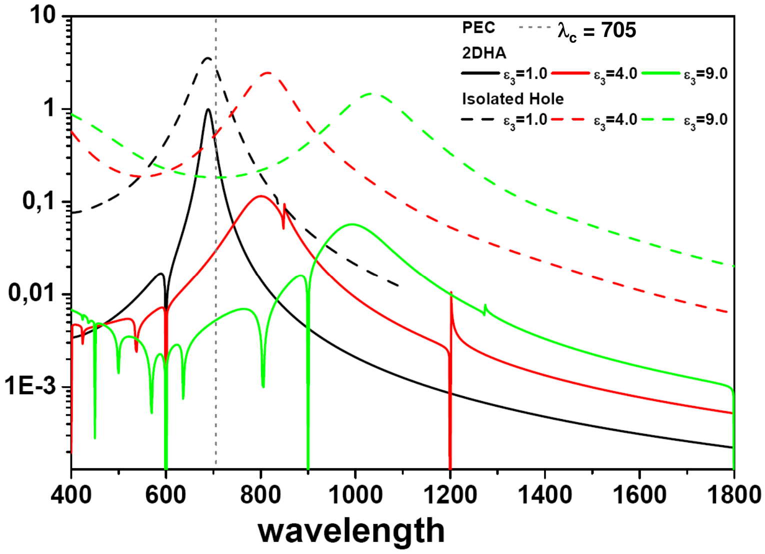

Figure 4.3: Transmission spectra in logarithmic scale for arrays (with periodicity $p = 600$) and single holes pierced in a PEC with annular holes with outer radius $a = 125$, inner radius $b = 100$, and film thickness $h = 100$ (in arbitrary units). The dielectric constants are $\varepsilon_1 = \varepsilon_2 = 1.0$, and ε_3 varies from 1 to 9. For isolated holes, the transmission is normalized to πa^2.

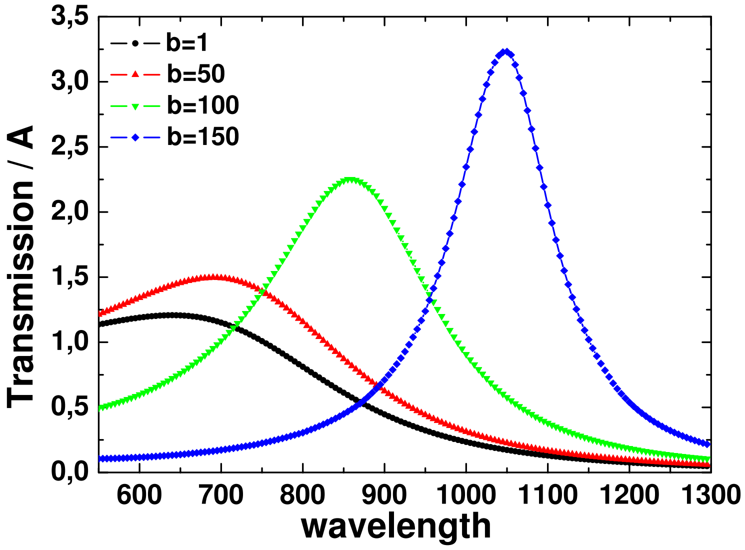

Figure 4.4: Transmission spectra as a function of the wavelength of isolated annular holes pierced in a $h = 100$ PEC film thickness with outer radius $a = 200$, and different inner radius b, in a free standing system. All lengths are in arbitrary units and transmission is normalized to $A = \pi a^2$

- a more confined field (smaller hole), a larger λ_c
- a smaller hole presents larger transmission

Since $\lambda_c \approx \pi(a+b)$ in PEC, when the inner radius increases, so does the resonant wavelength. Usually, obtaining more transmission translates into narrower resonances. Notably, compared to circular apertures, transmission of light (normalized to the area of the external circle) in annular holes can be enhanced by a factor ~ 3. If transmission is normalized to the area of the annular hole, $A = \pi(a^2 - b^2)$, it can be booted up a factor 6.

With this framework, one can ask her/himself, for instance, which is the optimum annular hole with highest transmission at a fixed wavelength, since several pairs $\{a, b\}$ provide a resonance at the desired wavelength.

Let us consider a single annular hole drilled in a PEC of $h/\lambda = 0.35$ thickness in a free standing system. In the contour plot appearing in Fig. 4.5 we look for the optimum annular hole with highest enhanced transmission at a fixed wavelength, λ, by varying both the inner (b/λ) and outer radius (a/λ) at the same time. In this case we obtain maximum transmission normalized to $A = \pi a^2$ for the pair $a/\lambda = 0.20$ and $b/\lambda = 0.13$.

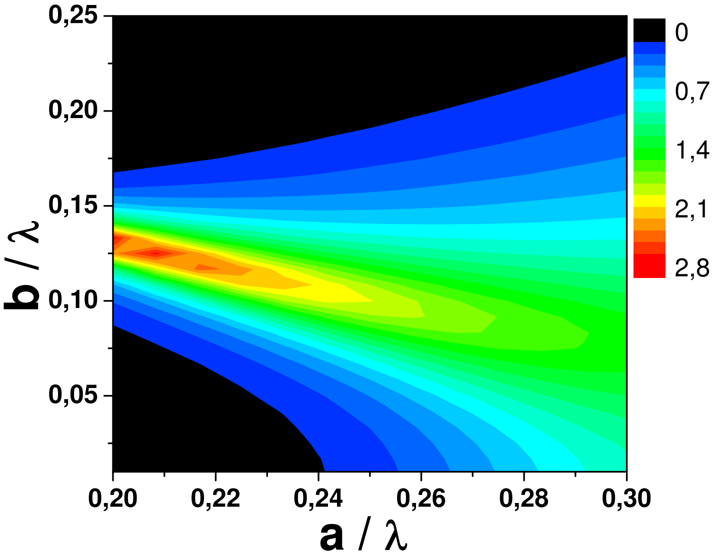

Figure 4.5: Transmission normalized to $A = \pi a^2$ of isolated annular holes pierced in a $h/\lambda = 0.35$ PEC film thickness in a free standing system. We vary both the inner (b/λ) and the outer radius (a/λ) of the annular holes.

This result also points out that optimizing a BE structure with concentric annular grooves will be a difficult task, because the EM properties of each element will be different one from each other as the average radius is varied.

4.2.2 Bull's Eye Structure

Our theoretician group was part of the European Project "PLEAS" (Plasmon Enhanced Photonics) from 2006−2010, in which, amongst other research tasks, was the design and optimization of BE structures working as photodetectors.

Several experimental groups also participated in PLEAS, and the collaboration with them was very close. In particular, concerning BE structures, our collaboration was done with the experimental groups at University of Strasbourg (ULP) (France), headed by Prof. Thomas Ebbesen, and also at Centre Suisse d'Electronique et de Microtechnique (CSEM) (Switzerland), headed by Prof. Ross Stanley.

As the project advanced due to the research and findings developed by both theoreticians and experimental groups, some of the design criteria changed, and therefore, several optimizations were performed regarding the size, the operation spectral wavelength, and other special characteristics of the photodetector. Moreover, also our theoretical studies led to different optimizations according to the degree of understanding we got by studying and tackling the problem from different points of view.

The final goal of the PLEAS project was to obtain maximum transmission with BE structures at $\lambda = 850$nm with some technological limitations for the film thickness, $h = 250$nm, and pixel size (that translates into a limitation in the number of grooves we can consider). Therefore, the parameters to optimize are the radius of the central circular hole, r_c, the number of grooves, N, and for each groove, its width w_g, depth h_g, and distance to the centre of the structure r_i.

Next, we will present 3 optimizations of Bull's Eye structures at different wavelengths:

- The First Optimization is done in the infra-red regime, guided by physical intuition.

  After optimizing a *regular* structure where all grooves have the same geometrical parameters and are periodically distributed, an optimized *irregular* system (where we let vary for each groove its depth, width and distance to the centre) is obtained through the Conjugate Gradient Method (CGM).

- The Second Optimization is done in the optical regime, for *regular* BEs, and simple optimization scaling laws are given.

- The Third Optimization is also done in the optical regime, and a Microscopic Model containing the main mechanisms controlling the enhanced transmission is presented.

4.2.3 First Optimization in the infra-red regime

Bearing in mind PLEAS constraints, let us first consider a detector that consists of a circular aperture of radius r_c surrounded at the illuminated side by annular grooves drilled in a gold film of thickness $h = 250$nm. The system is deposited on a glass substrate ($\varepsilon_3 = 2.25$).

We consider **regular** structures where both h_g and w_g are the same for all the grooves, and we let vary the distance of each groove to the centre of the structure, r_i. We denote as object 1 the central hole, object 2 the first annular groove, and so forth, so the total number of annular grooves is $N+1$. Therefore, r_2 accounts for the distance of the first annular groove, r_3 for the second one, and so on (see schematics in Fig. 4.6).

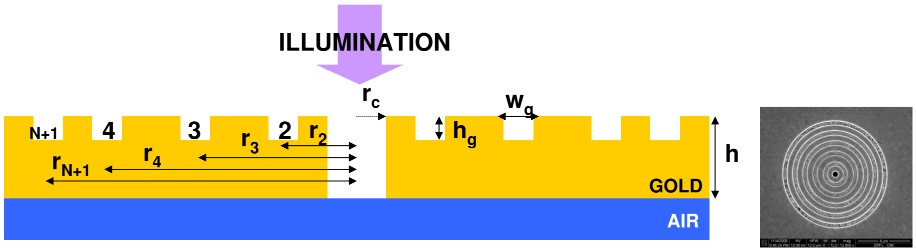

Figure 4.6: Schematic representation of the structure under study. It consists of a gold metal film of thickness h deposited on a glass substrate. The film is structured by annular grooves of width w_g, depth h_g, separated a distance r_i ($i = 2, 3, ..$) from the central hole of radius r_c.

1. Steps to find the optimized structure:

   We have to optimize an enormous space of parameters, so there will be necessary strategies to simplify this space. The most important parameter to delimit is the number of annular grooves, since as we already said, we must optimize both h_g and w_g, in addition to the distances r_i. In all cases, and as we will see next, dimensions characterizing grooves and the central hole are in the subwavelength regime.

   To start with, in this first study we have chosen 2 different cases for w_g, 3 different values for h_g, and 5 different distances of each annular groove to the centre of the structure, r_i. It means that the number of parameters to optimize n_p is:

$$n_p = N \times (2 \times 3 \times 5^N) \tag{4.4}$$

Just to gather a first idea on how these systems behave when we vary these parameters, we first choose the number of grooves equal to $N = 3$ and then, we extend this study to $N = 5$ grooves, a typical number that fulfills the compromise between small structure size and high field enhancement [63].

Systems with 3 grooves

First of all, we optimize the *radius of the central circular hole*, r_c, regarding that we must find high normalized-to-area transmittance.

After that and for simplicity, we consider periodic structures, where the distance groove-to-groove is the same for all of them. This will enable to find the suitable *groove depth* (h_g) for all grooves. In order to do it, we study the properties of the propagating wavevector k_{nz} of each annular groove, and we get conditions to achieve our aim: maximum normalized-to-area transmittance at $\lambda = 850$nm. These conditions will account for the optimum *period* and groove depth when 3 trenches are considered.

Finally, our periodic system becomes an aperiodic one by varying *the distance of each groove* to the centre of the structure, r_i.

2. Validating the Coupled Mode Method:

   We treat the problem with the Coupled Mode Method (CMM). Since the target wavelength in this optimization is $\lambda = 850$nm, and the perfect electrical conductor (PEC) approximation neglects the penetration of the fields inside the metal, considering the finite dielectric constant of metals is essential here and it can be incorporated into the formalism using the Surface Impedance Boundary Conditions (SIBCs) ([72] and Chapter 2). This impedance approach gives semiquantitative value in the optical regime and provides proper SPPs to the method.

   However, SIBC is only applied at the horizontal surfaces, but not at the vertical walls (inside the cavities), where we still consider perfect electrical conductor (PEC). To improve this approximation, inside the cavities we compute the propagating constant along the z direction of an infinite annular hole made of real metal, k_{nz}. Further details of this computation can be found in Appendix C. Additionally, having PEC inside the cavities allows the analytical computation of the waveguide eigenmodes. In our calculations we consider just the fundamental mode, TE$_{11}$, since the coupling of light at normal incidence with the TEM mode is strictly zero.

   To check the validity of our formalism when it is applied to a BE geometry, we compared FDTD and CMM simulations, for similar structures to those investigated within the PLEAS framework. In the comparison, the number of annular grooves was 3 since considering more grooves made the system too large for the FDTD simulations. Figure 4.7 shows CMM calculations (left panel) and FDTD ones (right panel) for a BE with 3 annular grooves drilled in a gold film with period p = 600nm, h = 280nm, h_g = 90nm and w_g = 220nm, and for a central circular hole with r_c = 125nm. The gold dielectric constant is taken from the experimental data appearing in Ref. [75]. Additionally, we vary the distance of the first annular groove r_2, from 300 to 500nm. Transmission is normalized to $A = \pi r_c^2$. The good agreement found between the FDTD and CMM results, both in the position (with a difference of approximately 25nm), and the relative magnitude of transmission peaks, justifies the use of the CMM model for larger systems.

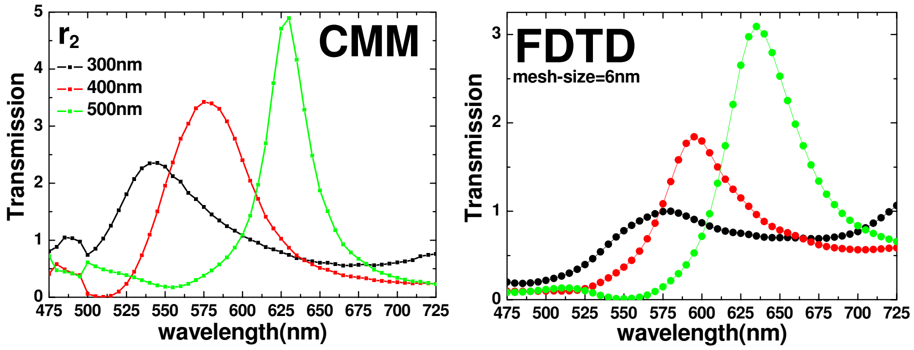

Figure 4.7: CMM calculations (left panel) and FDTD ones (right panel) of the transmission of light normalized to $A = \pi r_c^2$ of BEs with 3 annular grooves drilled in a gold film of h = 280 thickness, on a glass substrate (ε_3 = 2.25). The rest of geometrical parameters are p = 600nm, h = 280nm, h_g = 90nm and w_g = 220nm, and for a central circular hole with r_c = 125nm. The distance of the first annular groove r_2 is varied from 300 to 500nm. FDTD calculations were performed by Dr. Sergio G. Rodrigo.

3. Optimization of the radius of the central circular hole, r_c:

   Next, we further check our method comparing our calculations with the experimental results obtained at ULP. This comparison will, in turn, enable the optimization of r_c.

   In this case, the structure considered consists of 5 annular grooves periodically distributed around a central circular aperture drilled in a gold film, with p = 650nm, h = 250nm, w_g = 300nm and h_g = 100nm for all the 5 grooves. Transmission spectra for several r_c values are shown in both Fig. 4.8 and Fig. 4.9. In order to compare with the experimental results appearing in the inset of Fig. 4.8, transmission is not normalized to

A in that figure, but instead, in the theoretical calculations we normalize all the curves to the transmission maximum obtained with $r_c = 260$nm.

We observe the good agreement in both the spectral location of the maximum transmission and the trend for the transmission spectra: as r_c increases, so does the intensity. The difference between this figure and Fig. 4.9 is that, in Fig. 4.9, transmission is actually normalized to A, and this enables us to optimize r_c. In this case, for values of r_c larger than 200nm, the transmission of light starts decreasing. Therefore, from now on we will consider $r_c = 200$nm for the circular aperture.

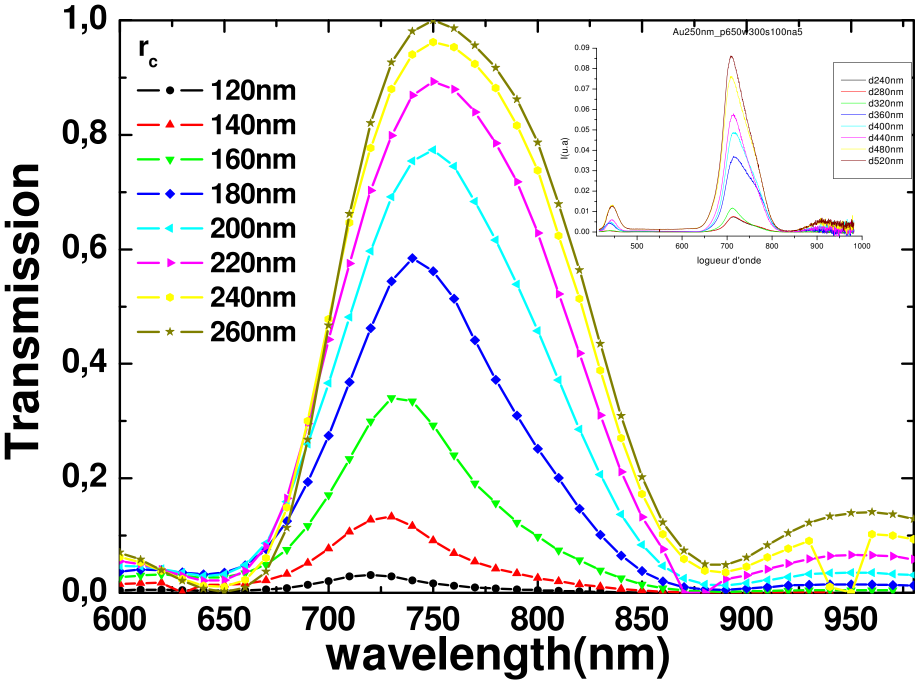

Figure 4.8: Transmission spectra in arbitrary units (and normalized to maximum transmission at $r_c = 260$nm), for a BE structure in gold on a glass substrate ($\varepsilon_3 = 2.25$) with 5 annular grooves periodically distributed ($p = 650$nm) around a central circular aperture. The geometrical parameters are $h = 250$nm, $w_g = 300$nm and $h_g = 100$nm, and several r_c values are considered. Inset corresponds to the experimental results for the same geometrical parameters.

4. Optimization of the groove depth (h_g) (Resonant Grooves):

   In general, the condition for transmission resonances in a very narrow slit in PEC is given by $2k_{nz}h_g = (2m+1)\pi$, with $m = 0, 1, 2, \ldots$ In the limit of annular structures with large average radius, these systems must behave like slits. However, as we are considering real metals through the SIBC approach, this condition can vary.

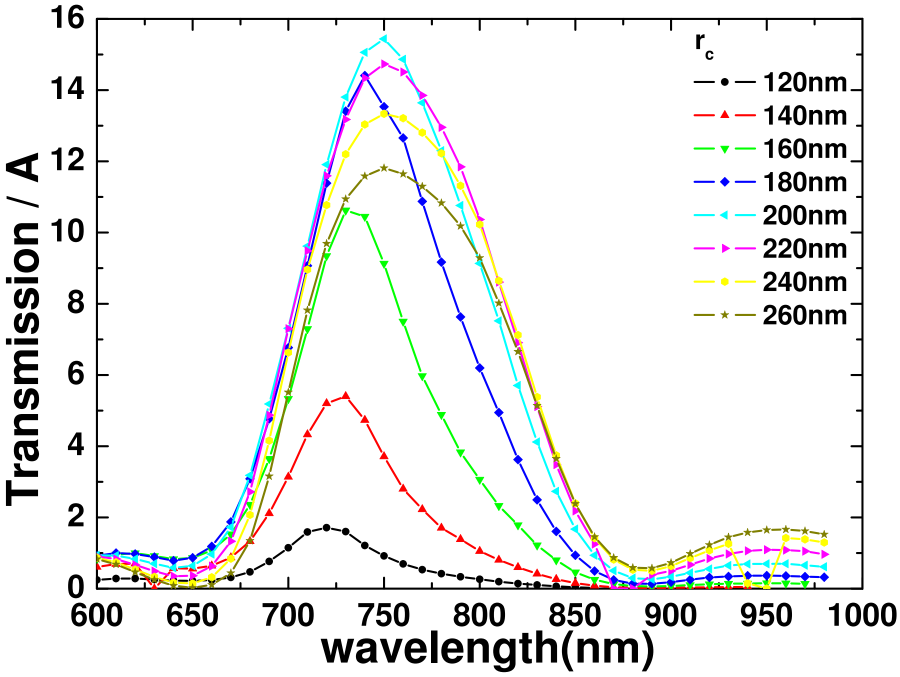

Figure 4.9: Normalized-to-area transmission of the same system appearing in Fig.4.8.

In Fig. 4.10 we show the dependence of k_{nz} of a single annular hole as a function of its distance to the centre of the structure (average annular radius) in gold at a fixed wavelength, $\lambda = 850$nm, and for two w_g values: 150 and 300nm. Surprisingly, annular grooves with the same width but extremely different average radius have practically the same propagation constant in a wide range of average annular radius.

For $w_g = 150$nm, when the distance to the centre is smaller than $\sim$ 2000nm, $k_{nz} \approx 0.0086$ nm^{-1}, and when $w_g = 300$nm, $k_{nz} \approx 0.0080$ nm^{-1} for distances smaller than $\sim$ 3000nm. Additionally, when this distance is further increased, k_{nz} tends to that of slits (see inset).

This result strongly simplifies the optimization of **regular** BE structures, where all grooves have the same w_g, as we can choose the same groove depth (h_g) for all annular grooves in order to look for the resonant condition (maximum transmission associated to the product $k_{nz} \cdot h_g$).

This is illustrated in Fig. 4.11 for a periodic BE with 3 grooves. Here we show a contour plot of the transmission of light at $\lambda = 850$nm through BEs with $w_g = 150$nm (left panel) and $w_g = 300$nm (right panel). We vary at the same time the period of the structure p and the groove depth (at a fixed k_{nz} chosen from Fig. 4.11 for each w_g value). In Fig. 4.11 it is observed that maximum transmission is obtained for $p = 750$nm, very

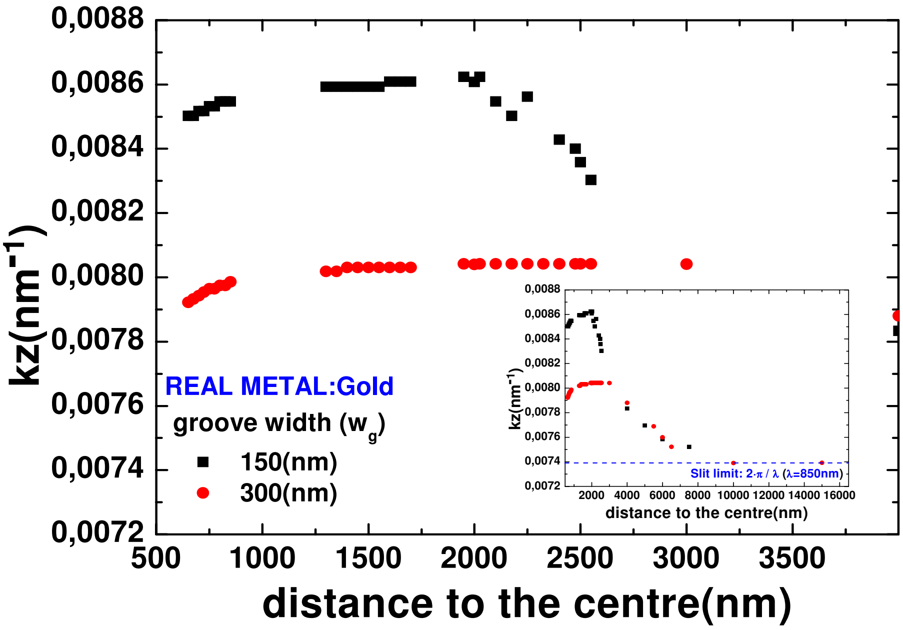

Figure 4.10: Dependence of k_{nz} with the distance to the centre of the structure for annular holes in gold. Inset depicts the same calculations for larger values of the distance to the centre.

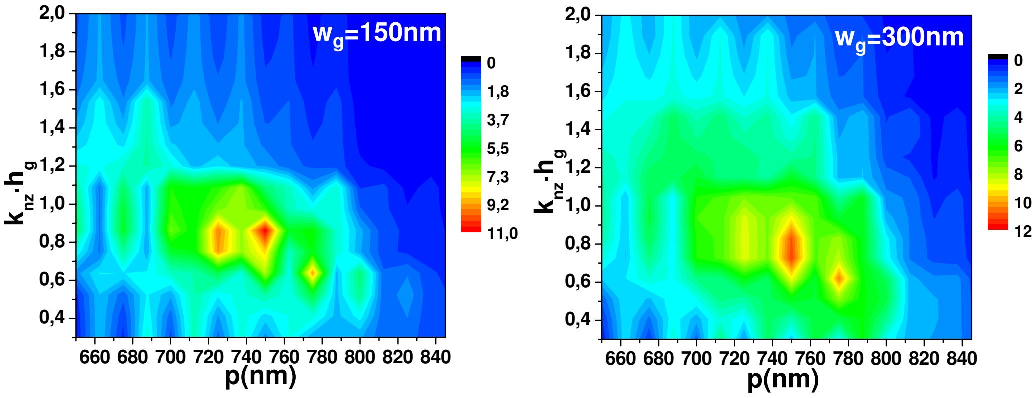

Figure 4.11: Transmission of light through annular holes with $w_g = 150$nm (left panel) and $w_g = 300$nm (right panel) as a function of the period of the structure and the groove depth. Calculations are for a fixed wavelength value, $\lambda = 850$nm.

close to the target wavelength of maximum transmission. Additionally, at that period, resonant conditions are found for:

$$\begin{aligned} k_{nz}(\bar{r}) \cdot h_g(\bar{r}) &\approx 0.9, \; (w_g = 150\text{nm}) \\ k_{nz}(\bar{r}) \cdot h_g(\bar{r}) &\approx 0.8, \; (w_g = 300\text{nm}) \end{aligned} \tag{4.5}$$

with $\bar{r}$ the average annular radius. These conditions translates into $h_g \approx$ 100nm. Therefore, we will study three cases for the groove depth: $h_g =$ 80, 90, 100nm, equal for all the grooves.

5. Distance to the centre of the structure, r_i:

   We build an *aperiodic* structure from a *periodic* one (with period $p =$ 750nm), by varying the distance of each groove to the centre of the structure, δr (nm). It is important to recall that the first groove is denoted as object 2, the second one as object 3, etc, so their distances are denoted as r_2, r_3, and so on.

   Again, we conduct calculations for $w_g = 150, 300$nm, and $h_g = 80, 90, 100$nm. As we said before, we consider 5 different cases of the distance of each annular groove to the centre of the structure, that is, we will consider $r_i \pm \delta r$, with $\delta r = (0, 25, 50)$ (nm). It means $2 \times 3 \times 5^3 = 850$ spectra, so we will show here only one example of them.

   For a fixed $r_2 = 750 \pm 0, 25, 50$nm (corresponding to the first annular groove), r_3 and r_4 are varied as: $r_3 = 2 \cdot r_2 \pm 0, 25, 50$nm and $r_4 = 3 \cdot r_2 \pm 0, 25, 50$nm. In other words, we fix $r_2 = 700$nm, and we vary at the same time, both r_3 and r_4, drawing contour plots as the one appearing in Fig. 4.12. Then, we fix $r_2 = 725$nm, and vary r_3 and r_4 again. After covering all the options for $r_2 = 750 \pm 0, 25, 50$nm; r_3 is then fixed to $r_3 = 2 \cdot 700 = 1400$nm, and r_2 and r_4 are varied following the same procedure as before.

   In the case of the illustrative map appearing in Fig. 4.12, a maximum transmission occurs at $r_3 = 1565$nm and $r_4 = 2300$nm, when r_2 is fixed at 725nm. From this kind of calculations, we will find all the optimum r_i values.

   Once all the calculations are analyzed, we finally obtain maximum transmission at $\lambda = 850$**nm** with 3 annular grooves surrounding a circular aperture with $r_c = 200$**nm**, $h = 250$**nm** and taking for all the grooves $w_g = 150$**nm** and $h_g = 90$**nm**. Concerning r_i:

   - *Periodic Structure*:
     $p = 750$nm, $T^P_{max} = 12.4$.

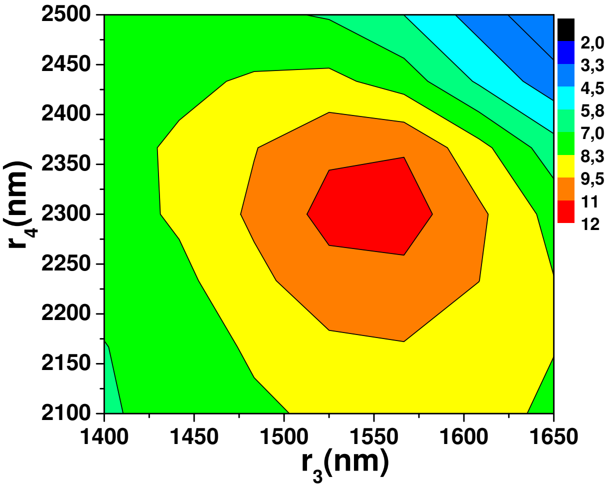

Figure 4.12: Transmission at $\lambda = 850$nm. We fix $r_2 = 725$nm and vary r_3 and r_4 some nm from a periodic structure of period $p = r_2$. The rest of parameters are $N = 3$, $h_g = 90$nm, and $w_g = 300$nm.

- *Aperiodic Structure*:

  $r_2 = 750$nm, $r_3 = 1525$nm, and $r_4 = 2300$nm, $T_{max}^{AP} = 13.0$.

  where the superscript P stands for Periodic, and AP for Aperiodic.

Systems with 5 grooves

6. First optimized parameters with 5 annular grooves at $\lambda = 850$nm:

   When we extend the previous study made for BEs with 3 grooves to a BE with $N = 5$ grooves, the “first” optimized parameters we find at $\lambda = 850$nm are $r_c = 200\mathbf{nm}$, $h = 250\mathbf{nm}$, $w_g = 300nm$, $h_g = 90\mathbf{nm}$, for an

   - *Aperiodic Structure*:

     $r_2 = 750\mathbf{nm}$, $r_3 = 1550\mathbf{nm}$, $r_4 = 2350\mathbf{nm}$, $r_5 = 3150\mathbf{nm}$, and $r_6 = 3925\mathbf{nm}$, $T_{max}^{(1)AP} = 27.9$.

   The corresponding transmission spectrum appears in Fig. 4.13. It is interesting to note that, considering the same geometrical parameters but with periodic structures ($p = 750$nm), we obtain $T_{max}^{(1)P} = 18.1$.

   Additionally, despite the study of a $3-$groove BE provides some physical insight about the behavior of these structures and about the dependance on the geometrical parameters, when 5 grooves are considered, things change considerably.

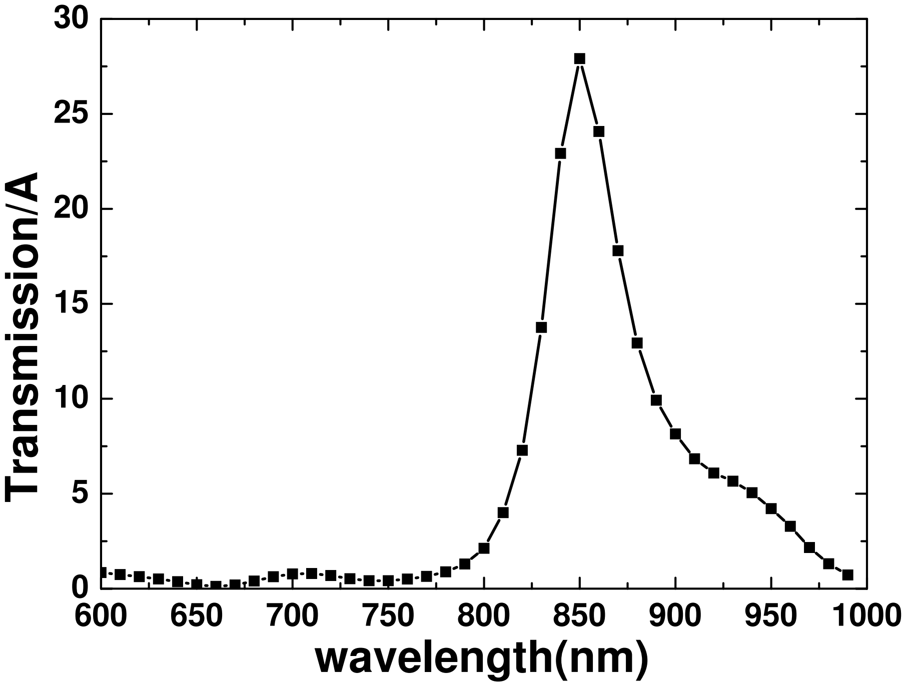

Figure 4.13: Transmission spectrum for an optimized BE in gold and a glass substrate, with maximum enhanced transmission at $\lambda = 850$nm. The geometrical parameters are $N = 5$, $r_c = 200$nm, $h = 250$nm, $w_g = 300nm$, $h_g = 90$nm, for aperiodic structures with $r_2 = 750$nm, $r_3 = 1550$nm, $r_4 = 2350$nm, $r_5 = 3150$nm, and $r_6 = 3925$nm.

This first result suggests that the study of BEs can be divided into the study of BEs with “many” ($N > 5$) or “few”($N \leqslant 5$) grooves.

7. Final optimized parameters with 5 annular grooves at $\lambda = 850$nm. Conjugate Gradient Method:

   Once we have optimized BE structures guided by intuitive physical ideas, next we can scan systematically the parameter space with help of the Conjugate Gradient Method (CGM) [130] .

   The CGM is the most prominent iterative method for solving sparse systems of linear equations, and it can be used to solve unconstrained optimization problems. Basically, this algorithm finds minima in quadratic functions from a given starting point or seed. We will use it to look for maximum transmission in *irregular* BEs, that is, BEs where w_g, h_g and r_i can be different for each groove. As starting configurations we try different seeds based on the previous periodic and aperiodic optimized BEs described in the previous subsection 6. As we will show next, the results we obtained suggest that the space of parameters looks like an “egg box”, with several local minima of similar transmission values. Therefore, according to each starting point, one of these local minima are found.

   In the calculations within the CGM, we must be careful and take into account that annular grooves cannot overlap, or that the groove depth cannot be larger than the film thickness. Indeed, we keep fixed the following parameters: layer thickness $h = 250$nm, number of grooves $N = 5$, central circular hole radius $r_c = 210$nm, and wavelength centred at 850nm; while the following parameters are led to vary: inner and outer radius of the grooves, (written in terms of the average radius r_i, and groove width w_g), and also each groove depth, h_g.

   We assume a precision of our simulation step in any length scale equal to 5nm.

   Schematics and final parameters of two different BE structures optimized through CGM appear in Fig. 4.14. In both cases, the groove depth increases for the outer radios, whereas the groove width does not seem to follow any particular rule.

   The corresponding transmission spectra to the schematics appearing in Fig. 4.14 are shown in Fig. 4.15. These transmission spectra present a transmission maximum at $\lambda = 850$nm, which, in the best theoretical case (structure 1), gets $T^{(2)}_{max} = 41.6$. If we compare the results for the previous regular BE with $T^{(1)AP}_{max} = 27.9$ we increase the efficiency of the system by at least $\sim 50\%$ (calculated as $(T^{(2)}_{max} - T^{(1)AP}_{max})/T^{(1)AP}_{max} \cdot 100$).

Structure 1:

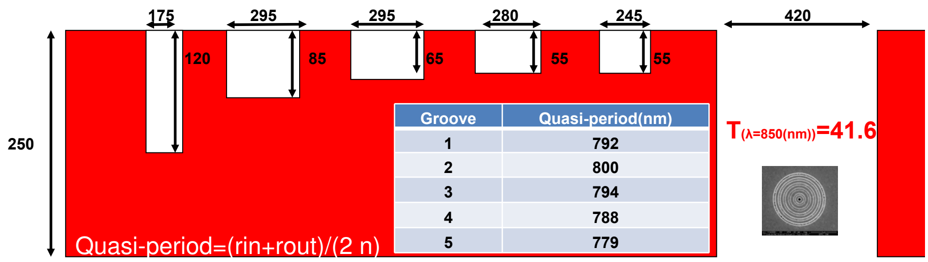

Groove	Quasi-period(nm)
1	792
2	800
3	794
4	788
5	779

Structure 2:

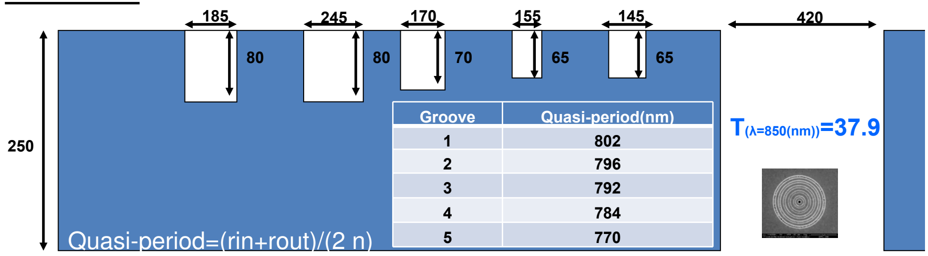

Groove	Quasi-period(nm)
1	802
2	796
3	792
4	784
5	770

Figure 4.14: Schematics and final parameters of two different BE structures optimized through CGM.

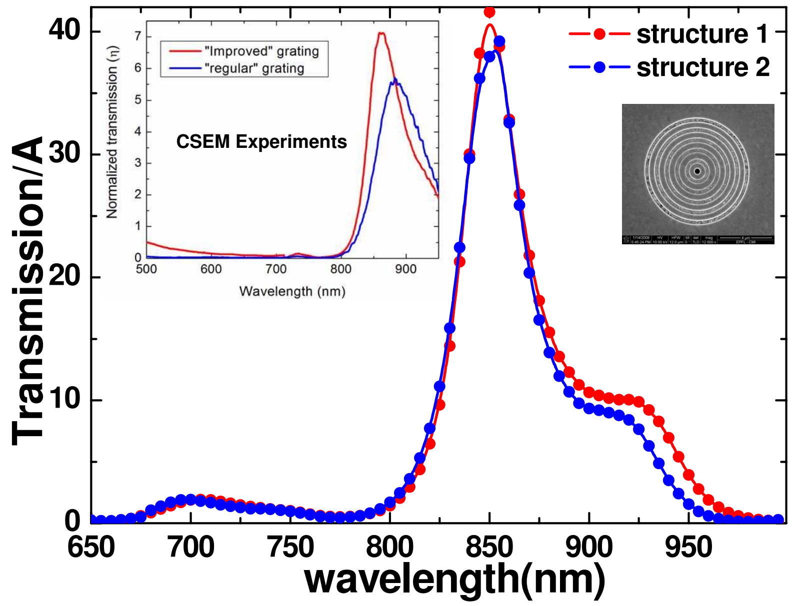

Figure 4.15: Transmission spectra for the parameters appearing in Fig. 4.14. Inset corresponds to experimental results obtained at CSEM for Structure 1 together with the results obtained for a periodic structure.

Experimental results obtained at CSEM for structure 1 together with the results obtained for a periodic structure, appear in the inset of the figure. The behavior and profiles of the experimental results are in agreement with the theoretical ones.

However, it is very important to emphasize that, if in Structure 1, for instance, h_g of the first groove is taken just 10nm less (i.e., $h_g = 45$nm) instead of the optimized 55nm, then $T^{(2)}_{max} = 35.6$. This is extremely important because, despite CGM provides large values of the transmission, in real experiments it is a challenge fitting properly to the precise theoretical optimized parameters. Moreover, to obtain converge results in the minimization within CGM is a very time consuming task.

The results provided by the CGM can be taken as theoretical limits, and CGM appears as an interesting tool for solving very specific problems such as the target transmission values and Figures Of Merit required in PLEAS, for instance.

However, since these systems are very sensitive to possible experimental imperfections, we find more convenient and efficient to consider regular systems (where all grooves have the same width and depth) and look for simple and effective scaling laws to optimize BE structures.

4.2.4 Second Optimization: Scaling Laws in the Optical regime

In order to study different wavelength ranges, also an optimization in the optical regime ($\lambda \approx 650$nm) was considered. These studies were performed in collaboration with the experimental group at ULP, and for the theoretical calculations we used the same approximation as that in Section 4.2.3.

Next, we present an exhaustive exploration of the parameter space defining the optical properties of BE structures. By studying the resonance intensity variations associated with the different geometrical features, several parameters are seen to be interlinked and scaling laws emerge. From the results it is possible to give a simple recipe to design a BE structure with more than 5 grooves (all with the same width and depth) with optimal transmission properties at a given wavelength range in the visible.

Since it is known that the efficiency of the transmission intensity is controlled mainly by the input corrugation and the hole depth (i.e. film thickness), we concentrate here on varying all the geometrical parameters on the input surface, keeping the hole depth constant. As demonstrated earlier, the transmission intensity is an exponential function of the hole depth in the subwavelength regime [27]. We compare experimental results and theoretical simulations to validate our findings. For the experimental studies, the structures were milled in a $h = 280$nm thick gold film deposited on a glass substrate using an FEI DB 235 focused ion beam (FIB).

In order to find the optimal transmission intensity the following geometrical parameters, were varied: number N of grooves, groove width w_g, groove depth h_g, periodicity p of the grating, hole diameter d, and the distance between the first groove and the hole aperture, a. The actual values that are explored are confined to those giving rise to transmission resonances in the visible and near IR regions that can be detected by the experimental setup.

Figure 4.16 (c) shows the experimental transmission spectra for BEs with three different corrugation periods. A strong transmission peak, resulting from the excitation of SPs, is evident around a wavelength slightly larger (ca. 10%) than the period of the structures. This shift is due to the slight increase in the effective index at the interface which in turn defines SP wavelength λ_{SP} roughly equal to the period.

The presence of localized modes in or at the aperture can enhance the transmission but the contribution of such modes to the overall transmission is small compared to that of the SP mode provided by the concentric grooves. The difference in the transmission intensities for the 3 different resonance wavelengths in Fig. 4.16(c) can be explained by a combination of two opposite effects. First, the dielectric constants of the gold in the wavelength range considered becomes increasingly unfavorable to SPs as the resonance wavelength decreases and approaches the gold interband transition at 550nm [131]. Secondly as the resonance wavelength increases with p for a fixed hole diameter, the aperture will cut the transmission more strongly.

In other words, we expect that the effect of the hole diameter is sensitive to the resonance wavelength since the diameter defines the cutoff wavelength of the aperture. Therefore we have studied the maximum transmission as a function of d/p for a series of BEs with different periods in which we change only the hole diameter and keep the other parameters fixed. In Fig. 4.16(a) and (b) are plotted both the calculated and experimental results and, as can be seen, the transmission intensity (corrected for hole area) versus d/p gives a maximum for $d/p \sim 0.5$ for all the curves. This can be understood as follows: at diameters smaller than half the period, and therefore half the resonance wavelength, the cutoff function of the hole becomes significant and reduces rapidly the transmission. Beyond the cutoff, the transmission is mainly defined by the area of the aperture as compared to the field distribution on the surface. The absolute transmission increases but the intensity normalized to the hole area (as plotted in Fig. 4.16(a) and (b)) decreases because the field is maximum in the center of the structure.

Note that the structures analyzed in Fig. 4.16 can give rise to transmission

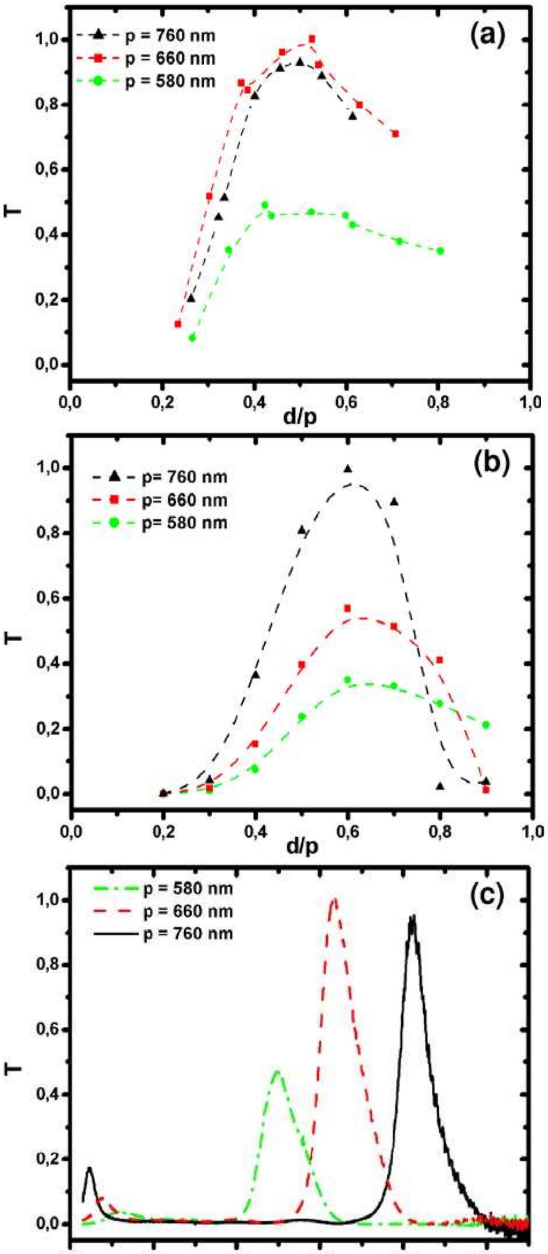

Figure 4.16: Effect of the hole diameter on the transmission of a BE ($N = 7$, $h_g = 90$nm, $w_g = 220$nm, $h = 280$nm). (a) Experimental results for the relative transmission intensities versus the ratio of hole diameter d and groove periodicity p, for the three series periods (the transmissions have been normalized to the hole area). (b) Theoretical simulations for same systems as in (a). (c) Relative transmission spectra of a BE at three different periods ($p = 580, 660, 760$nm) $d = p/2$.

intensities normalized to the hole area greater than 1, or in other words, the flux per unit area through the hole is greater than the corresponding incident beam, demonstrating unequivocally the antenna effect of the grooves. When compared to that of a single hole without corrugation, the enhancement at resonance is even greater.

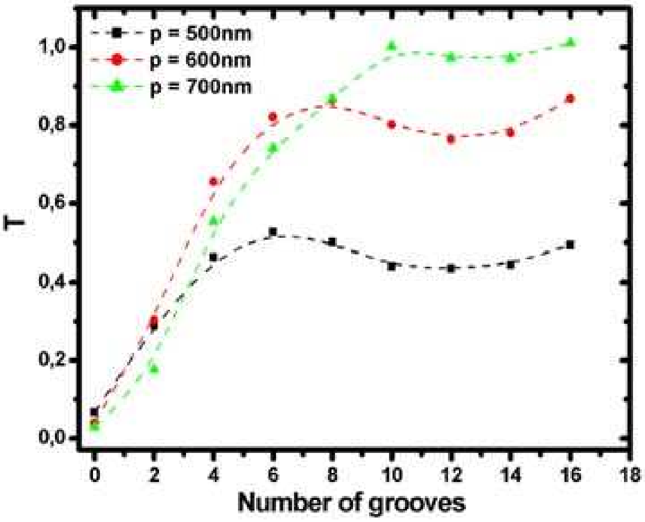

Figure 4.17: Experimental relative transmission intensities as a function of the number of grooves for three different periods ($p = 500, 600, 700$nm with $d = 250$nm, $h_g = 90$nm, $w_g = 220$nm, $h = 280$nm).

As mentioned above, the role of the periodic corrugation is to couple the incident light to SPs which concentrate the electromagnetic fields above the aperture leading to very high transmissions. The efficiency of the coupling is directly linked to the geometrical parameters of these grooves. Period p and number of grooves N are two geometrical parameters that directly define the dimension of the structure and play a key role in miniaturization of the active area. Both parameters were first varied in order to understand their interdependence and effect on the transmission enhancement. In Fig. 4.17, the experimental results obtained for spectral maxima are plotted as a function of N for three different values of p. As can be seen, the intensity saturates at a given N for all three curves. The saturation limit is defined by the SP propagation length in the corrugated surface, where it is significantly reduced due to radiation losses as compared to a flat metal surface. The saturation point and therefore the SP propagation length is seen to increase with period. This apparent period dependence is mainly due to the fact that the other parameters, such as groove depth, were kept constant as we will see further down.

When considering just the groove width w_g, the maximum transmission

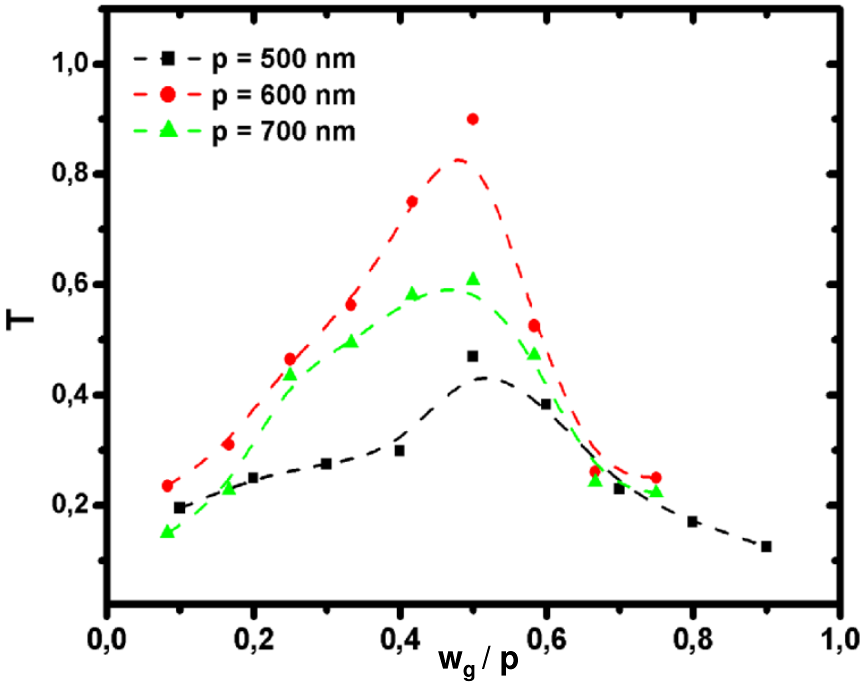

Figure 4.18: Experimental relative transmission intensities as a function of the ratio w_g/p for a series of three periods ($p = 500, 600, 700$nm) with $h_g = 90$nm, $d = 250$nm, $N = 8$.

intensity has been found experimentally for w_g close to half the period ($w_g/p \sim 0.5$) [132] which is confirmed in the present study for 3 different periods as can be seen in Fig. 4.18. This optimal ratio defines a profile in which the power spectrum is peaked at the SP resonance condition determined by the period. In addition, w_g is interlinked to the groove depth h_g of the corrugations as shown in Fig. 4.19 where h_g was varied for three different values of w_g, the other parameters being constant. All the curves show an optimum at the same h_g/w_g ratio around 0.4, in agreement with theoretical predictions [133]. It indicates a competition of light coupling to SPs and scattering by the grooves versus the damping of the SPs in the grooves [73, 134, 135]. The fact that the maximum intensity is found for the h_g/w_g curve corresponding to $w_g = 300$nm is probably due to the existence of a mode in the grooves in resonance with the SP mode which has been observed in slit and groove structures [37].

In order to complete the study of the groove parameters, we investigated separately the relationship between h_g and w_g as a function of N. The resulting experimental curves shown in Fig. 4.20 all exhibit a saturation with increasing N. As can be seen in Fig. 4.20(a), the deeper the groove the earlier the saturation intensity occurs in agreement with the h_g/w_g dependence. Note that with $h_g = 80$nm we obtained a better efficiency because this value is close to the optimal shape ratio (i.e. $h_g/w_g = 0.4$). Interestingly the saturation occurs approximately at the same value of N for different groove widths (Fig. 4.20(b)) indicating that in the parameter range studied, w_g does not influence much the SP propagation length. Again the highest intensity is obtained for the structure closest to the optimal h_g/w_g.

The last parameter that we consider is a, defined as the distance between the center of aperture to the center of the first groove. As can be seen in Fig. 4.21, the maximum intensity is obtained when a is close to the period as might be expected since the aperture is then in phase with the surrounding grating. There is a good agreement between the experimental and the calculated spectra despite a slight shift which we attribute to possible imperfections of the fabricated structures, but also to the approximations done within the CMM formalism regarding the boundary conditions at the groove and the hole walls. From a practical point of view, the more important information is that the shape and the position of the resonance changes quite significantly with a. It is therefore a parameter that can be used to tweak the resonance once the other features have been optimized.

From the above results it is clear that the geometrical parameters controlling the transmission efficiency of BEs are strongly interlinked. Nevertheless the basic optimization criteria for these systems can be formulated in a straightforward manner:

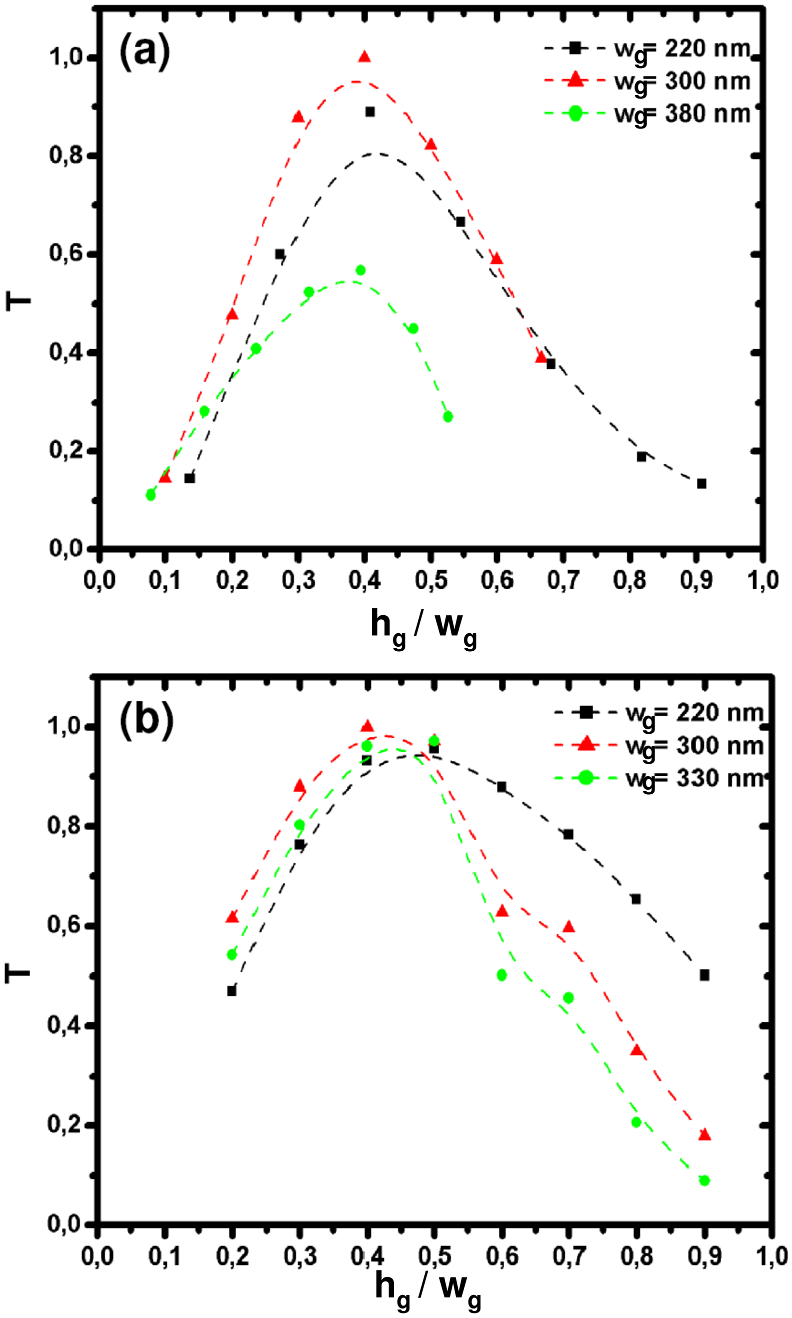

Figure 4.19: (a) Effect of shape ratio of the groove h_g/w_g on the experimental transmission (a = 600nm, d = 230nm, p = 600nm, N = 7, h = 280nm). (b) Theoretical simulations for the same system than (a).

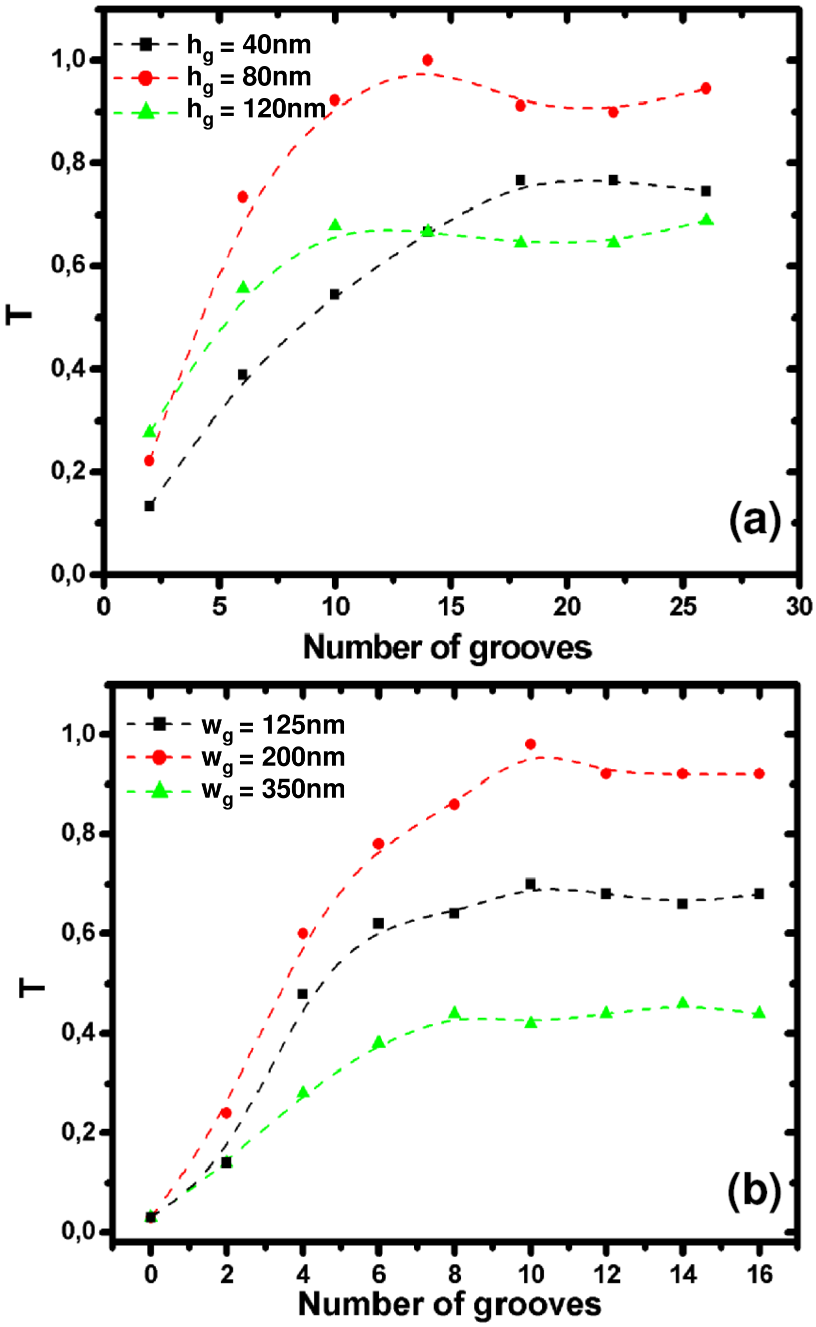

Figure 4.20: Experimental results of the effect of the number of corrugations for different values of h_g and w_g. (a) Relative transmission intensities as a function of the number of grooves for a series of three groove depths ($h_g = 40, 80, 120$nm with $p = 600$nm, $w_g = 220$nm). (b) Relative transmission intensities as a function of the number of grooves for a series of three groove widths ($w_g = 125$nm, 220nm, 350nm with $p = 600$nm, $h_g = 80$nm).

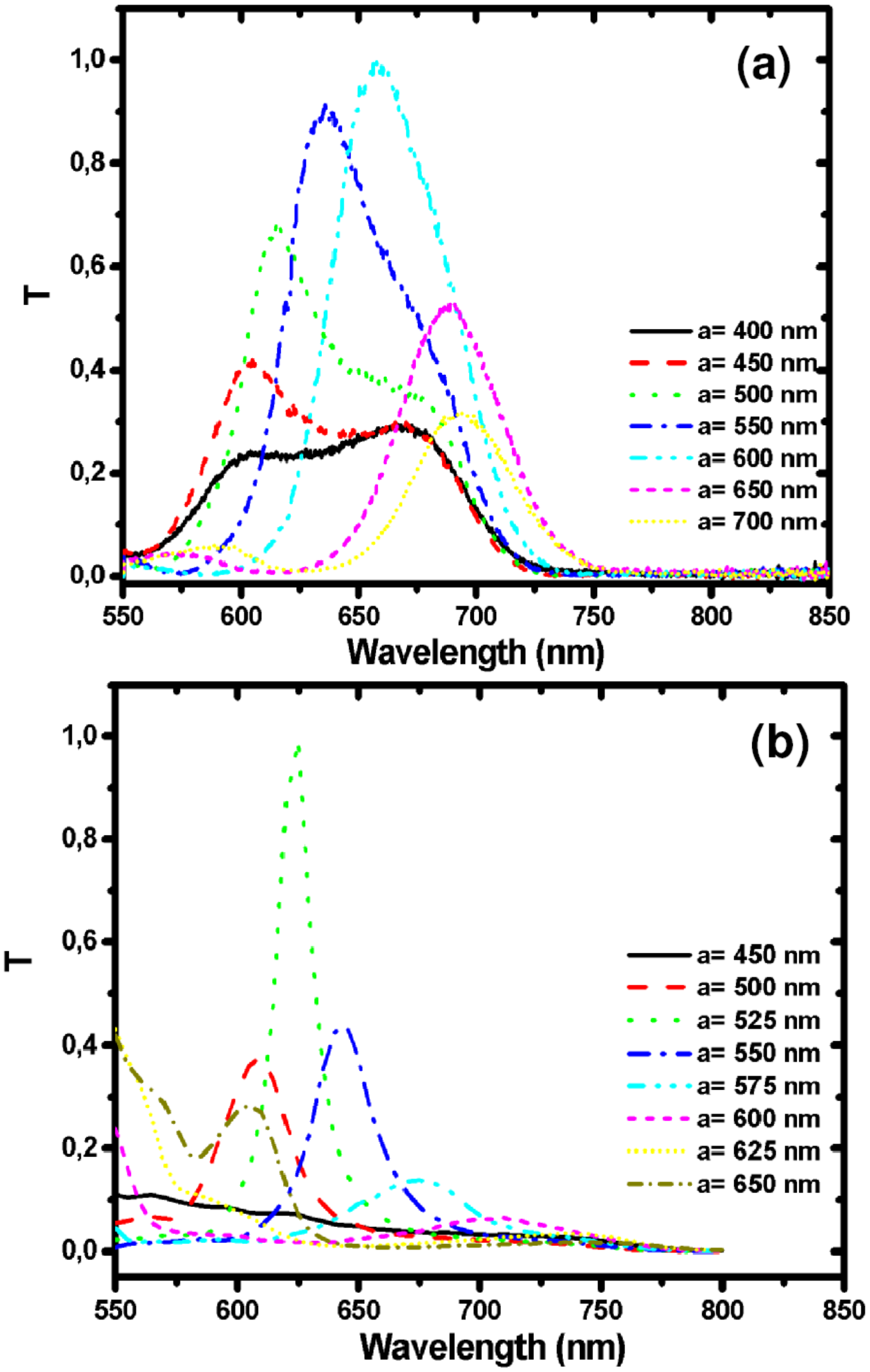

Figure 4.21: Effect of distance a on the transmission (p = 600nm, w_g = 220nm, h_g = 80nm, $N = 6$). (a) Experimental data: the distance a is varied. (b) Theoretical simulations for the same system than (a).

- The first item to define is the desired range of resonant wavelengths which in turn determines the period of the structure.
- The choice of the hole diameter will then be determined whether one would like optimal efficiency as normalized to hole area or highest absolute transmission.

  For the former, the diameter should be about half the period:

  $$d/p = 0.5 \tag{4.6}$$

  but for the latter the aperture size can be increased. It should be noted that as the hole size increases relative to the period the spectrum will eventually broaden which is a trade-off.
- The groove width should also be around half the period with an optimal depth to width ratio at 0.4:

  $$\begin{aligned} w_g/p &= 0.5 \\ h_g/w_g &= 0.4 \end{aligned} \tag{4.7}$$
- The number of grooves should be just enough to reach saturation which is typically around 6 to 10 grooves depending on the geometrical parameters and which reflects the SP propagation length in such optimized structures.

This simple optimization recipe should be useful for many applications that can be envisaged for these structures.

The main differences between this optimization and the one studied in Section 4.2.3 is that these rules work for BEs with $N > 5$ grooves. Moreover, whereas in the previous optimization λ was fixed to a value in the infrared, this new optimization is in the visible and it is based on the maximum transmission obtained in a spectral range of finite width, that is, $\lambda \pm \Delta\lambda$, with $\Delta\lambda \sim \pm 50$nm and $\lambda = 650$nm.

Nevertheless other refinements have been conceived that can be useful in certain specific applications, always bearing in mind that improvements in transmission are got only with an exquisite control in the geometrical parameters defining the system, since these are very sensitive to imperfections. For instance, geometrical features such as sharp ridge and groove profile [128], different hole shapes [26] and non-periodic grooves [136], groove depth gradients [137] or phase shifts for polarisation control [138] have been used or proposed to modify the field distribution and therefore the properties of the BE.

In order to check the validity and transference of these scaling laws to other range of wavelengths, and within the European Project "PLAISIR", similar to the "PLEAS" project where the termination "IR" stands for Infra Red, we optimized a BE structure at $\lambda = 1350$nm. Actually, the following optimization is preliminary and it is done without considering the GCM. Anyways, this is a good opportunity to test our previous findings at different wavelengths, bearing in mind the main differences previously said.

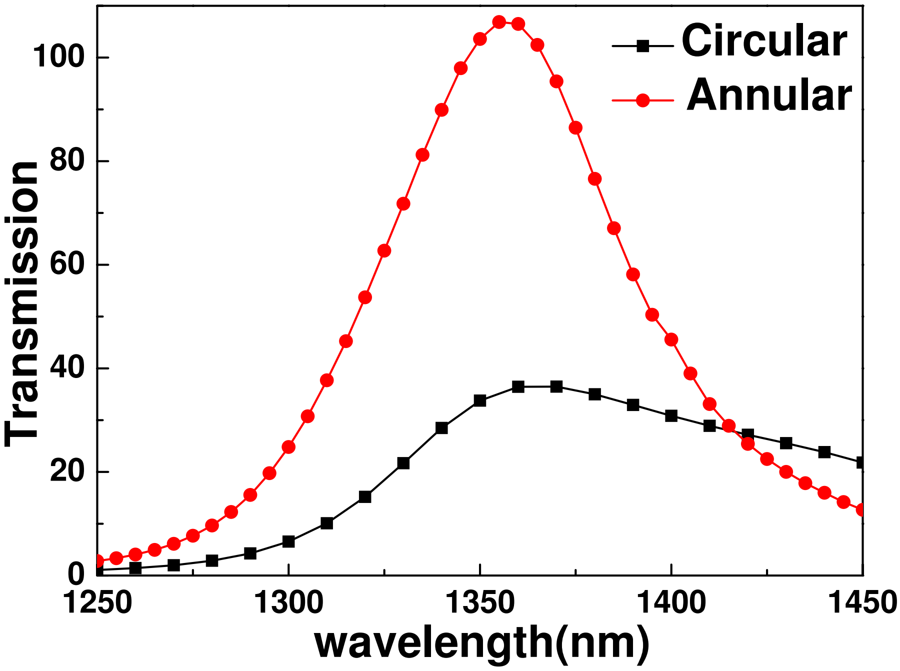

Figure 4.22: Transmission of light through a BE structure optimized at $\lambda = 1350$nm. Geometrical parameters are: 6 annular grooves drilled in a gold film of 250nm thickness ($\varepsilon_1 = \varepsilon_2 = \varepsilon_3 = 1$), with $h_g = 140$nm, $w_g = 580$, $p = 1270$, and $a = 1290$. Squares depict calculations when the central aperture is a circular hole with $r_c = 400$nm, and circles when it is an annular hole with $r_{out} = 230$nm and $r_{in} = 130$nm.

As a first approximation, we consider a free standing system ($\varepsilon_1 = \varepsilon_2 = \varepsilon_3 = 1$) with 6 annular grooves drilled in a gold film of 250nm thickness. Transmission of light is normalized to $A = \pi r_c^2$, with r_c, the radius of the central hole. Grooves are considered periodically (p) arranged, but the distance of the first groove to the centre of the structure, a, is let to vary.

The previous scaling laws predict maximum transmission at $h_g/w_g \approx 0.4$, $a \approx p$ and, $2r_c/p \approx 0.5$.

Concerning the last law, we have found a resonant circular hole at $\lambda = 1350$nm for $r_c = 400$nm. We have seen along this thesis that, in the optical regime, the cutoff of a waveguide made of real metal is larger than that of a perfect metal ($\lambda_c^{RM} > \lambda_c^{PEC}$), whereas, $\lambda_c^{RM} \approx \lambda_c^{PEC}$ in the micro- or THz-regime. This fact entails that optimum r_c values may be not directly transferable amongst different wavelength regimes, and they will have to be optimized again.

In Fig. 4.22, transmission spectra through the optimized BEs at $\lambda = 1350$nm, are presented. The geometrical parameters found are: $h_g = 140$nm, $w_g = 580$nm, $p = 1270$nm, and $a = 1290$nm, providing a maximum transmission $T_{max}^{CH} \approx 36$ (where superscript CH stands for *Circular Hole*).

Additionally, since we already know that annular holes present higher transmission than circles of the same area, and because the groove structure can be optimized irrespective of the central aperture (provided that the cross-section of the hole is much smaller than those of the grooves), we also consider a central annular hole in the centre of the structure, keeping the rest of parameters constant. In this larger spectral range, considering annular holes makes sense because experiments can be now performed since the required dimensions of the annular apertures should be attainable. In particular, we obtain an optimized annular hole with $r_{out} = 230$nm and $r_{in} = 130$nm, providing $T_{max}^{AH} \approx 100$. Note that T_{max}^{CH} is normalized to πr_c^2, and T_{max}^{AH} to πr_{out}^2.

About the validity of the previous scaling laws, it is clear that the set of optimized parameters we found fulfil both $a \approx p$, and $2r_c/p \approx 0.5$ (in the case of circles), whereas for h_g/w_g, we obtain a ratio of 0.25 instead of 0.4.

In Fig. 4.23, it is shown transmission at $\lambda = 1350$nm as a function of w_g for different h_g values and with the same geometrical parameters as those of the optimized structure in Fig. 4.22 (considering an annular hole in the centre with $r_{out} = 230$nm and $r_{in} = 140$nm). We observe that very similar transmission intensities are obtained for several w_g and h_g pairs: $w_g = [300 - 600]$nm and $h_g = [120 - 140]$nm, with almost planar curves of similar transmission.

This is also in accordance with the results obtained in Fig. 4.19, where curves around the ratio $h_g/w_g = 0.4$ are also planar. Therefore, the scaling laws obtained in the optical regime for the grooves of BE systems with more than 5 annular trenches seem to be easily transferred to the middle infrared.

4.2.5 Third Optimization: Microscopic Model

Up to now we have scanned systematically the parameter space by physical intuition, following previous ideas and studies related to slit and linear groove

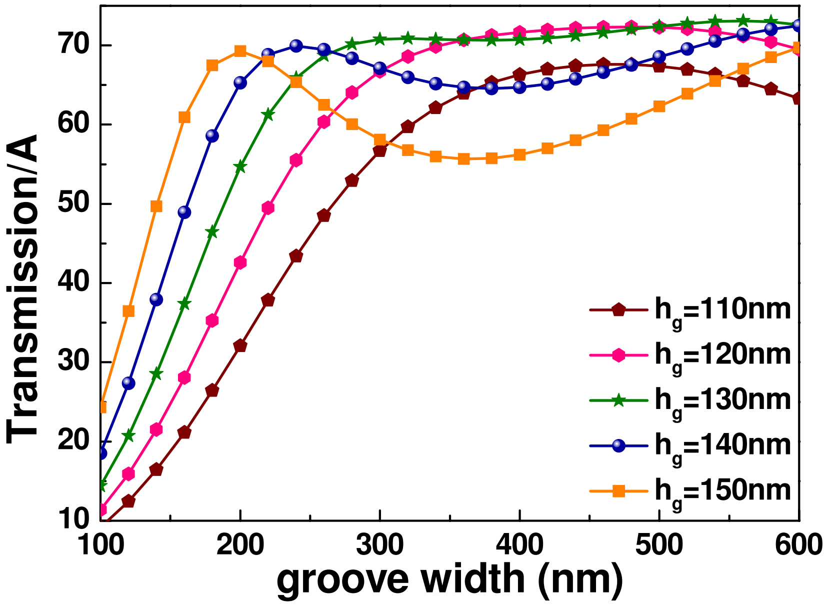

Figure 4.23: Transmission at $\lambda = 1350$nm for the same system as in Fig. 4.22 but with $r_{in} = 140$nm, as a function of w_g for several h_g values.

structures. However, we can go a step further and provide a detailed description and analysis of BE transmission properties.

As we said before, we will consider just regular BEs where all grooves have the same depth and width, since these structures are very sensitive to possible experimental imperfections.

By considering the interfering contributions of the direct transmission through the hole and the SP component in the transmission process, we will reveal both theoretically and experimentally how the two contributions determine the transmission spectra of a BE. By means of the CMM, analytical expressions for the most relevant parameters that determine the optical behavior of the BE can be given. The analytical capacity eventually leads to understanding the fundamental mechanisms involved in the physics of the BE structure: we find that the mechanism to enhance transmission is related to constructive interference at the central hole of standing SP waves emitted by the grooves. Furthermore, we find a simple phenomenological model that gathers the main mechanisms to enhance transmission.

A schematic of a BE structure is displayed in Fig. 4.24(a). The following experiments are also performed at ULP using the same technique described in Section 4.2.4. The structure is milled in a $h = 280$nm thick Au film deposited on a glass substrate ($\varepsilon_3 = 2.25$). In order to obtain EOT in the optical regime, the distance between consecutive grooves (the "period"), is chosen $p = 600$nm.

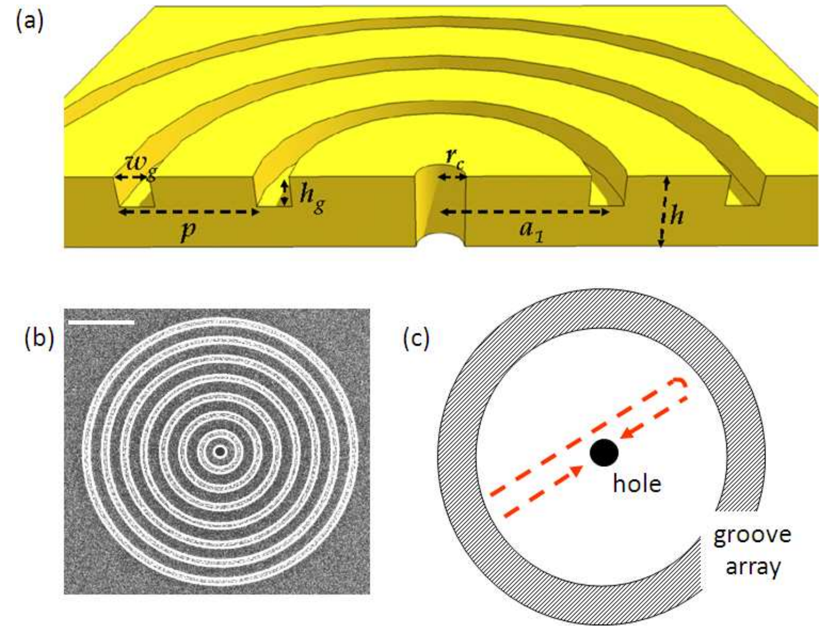

Figure 4.24: (a) Schematic representation of a BE structure, consisting of a metal film of thickness h deposited on a glass substrate, perforated by a central hole with radius r_c and N concentrical circular grooves (all with the same width w_g and depth h_g) separated by a period p. The variable distance between the hole the nearest groove is a_1. (b) SEM image of a experimental structure milled by FIB lithography. The scale bar corresponds to 2 μm. (c) Sketch of the re-illumination SP component as implemented in the phenomenological model described in the text.

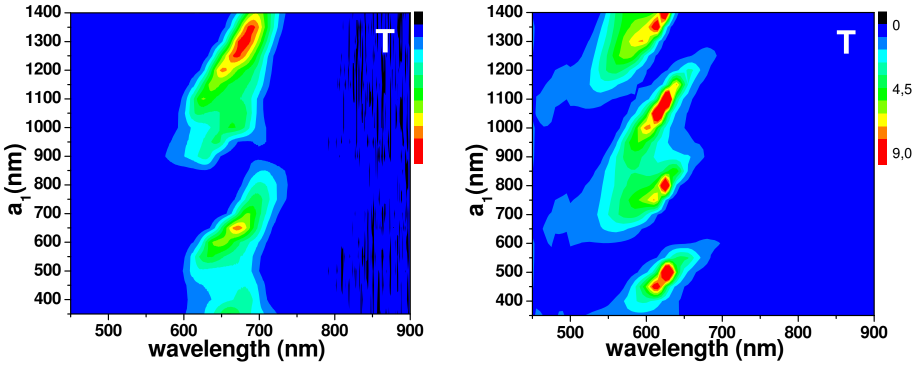

Figure 4.25: (Left panel) Experimental optical transmittance, normalized to hole area, for a bull's eye with $N = 6$ annular grooves, $h = 280$nm, $h_g = 90$nm, $w_g = 220$nm, $p = 600$nm, and $r_c = 125$nm, drilled in a gold film of 250nm thickness on a glass substrate ($\varepsilon_2 = 2.25$). The spectra are acquired as a function of both distance between the hole and the first groove, a_1, and incident wavelength λ. (Right panel) CMM calculations.

Dimensions characterizing grooves and hole are in the subwavelength regime: all grooves have $h_g = 90$nm depth and $w_g = 220$nm width, and the radius of the central hole is $r_c = 125$nm. We consider $N = 6$ annular grooves, a typical number that fulfills the compromise between small structure size and high field enhancement [63]. The sample was illuminated from the corrugated side with collimated white light.

The experimental transmission spectra of Fig. 4.25 (left panel), measured as a function of the incident wavelength λ, show the expected resonances at wavelengths λ_R slightly larger than the period (in this case $\lambda_R \approx 630$nm) [25, 30]. However, considering the possibility that additional coherent effects can modulate the optical enhancement associated with these resonances, we have explored further the transmission dynamics by changing also the distance a_1 between the central hole and its nearest groove. When the spectra are displayed in the $\lambda - a_1$ parameter space, they clearly show that the resonant profile is modified as the distance a_1 is varied. As we saw in Chapter 2, within the CMM, the EM fields are expanded in terms of eigenmodes in each different region in space (plane waves in the semi-infinite regions and waveguide modes inside the hole and grooves) and imposing the appropriate matching conditions leads to a coupled system of equations for the modal amplitudes of the electric field at the entrance, E, and at the exit, E', of the cavities. In the case of subwavelength holes or grooves, considering only one mode per cavity (the TE_{11} mode in both the hole and the grooves [84]) already provides a good approximation to the transmission properties [49, 67]. In this case, the modal amplitudes are governed by:

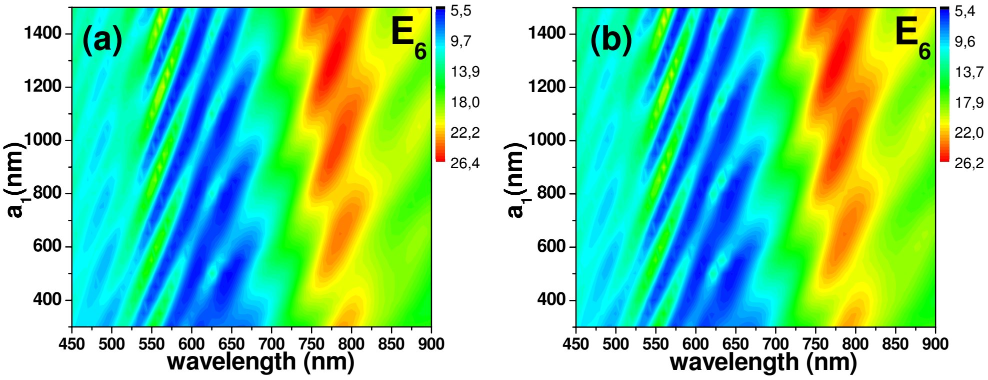

Figure 4.26: Electric Field Amplitude for the sixth groove, E_6, as a function of a_1 and the wavelength with (a) and without (b) a central hole, for the same geometrical parameters as in Fig.4.25.

$$\begin{cases} -\Sigma_n E_n + \sum_m G_{nm} E_m = & I_n + G_n^{\nu} E'_n \\ -\Sigma_n E'_n + \sum_m G_{nm} E'_n = & G_n^{\nu} E_n \end{cases} \tag{4.8}$$

where n is an index that labels cavities ($n = 0$ for the hole, and $n = 1....N$ for the grooves). Again, in the simulations we apply SIBC at the horizontal surfaces for the dielectric response of the metal, and for each cavity (groove or hole) the propagation constant along the vertical direction k_{nz} is computed exactly. The spatial profile of the fundamental waveguide mode is obtained considering PEC approach in the waveguide since, in this case, the overlap with plane waves is known analytically [84]. Based on our experience on 1D structures, we expect that the use of this approximation blue shifts the transmission spectra by $\approx$ 50nm compared to virtually exact numerical simulations.

Figure 4.25 (right panel) renders the transmittance (normalized to the hole area) computed within the CMM for the nominal parameters of the experimental setup. The dielectric constant of gold is taken from Ref. [15]. The simulations also present stripes of enhanced optical transmission in the $\lambda - a_1$ parameter space, appearing around λ_R = 630nm, i.e., within the expected accuracy of the model.

One of the main advantages of the CMM formalism is that it allows to differentiate amongst different mechanisms involved in the transmission process. For instance, we can consider BE structures with and without a central hole.

Figure 4.26 shows the computed maps for the amplitude of the electric field at the entrance of the sixth groove, $|E_6|$, which is taken as a representative illustration of the field at the surface, when the system has (left panel) or does not have (right panel) a central hole in the middle, as a function of a_1 and the wavelength. We find that E_n is not affected by the presence of the central hole, making evident that, for the range of parameters considered, the cross-section of the hole is much smaller than those of the grooves. This result reenforces the finding that, at a given wavelength, it is possible to analyze separately the optical responses of the array and the central hole.

Bearing in mind the last result, and that the central hole modulates the transmission response (as we showed in both Section 4.2.3 and Section 4.2.4), we now consider different central apertures (annular holes and circular ones filled with $\varepsilon_2 > 1$) and study how transmission can be enhanced through BE structures.

In Fig. 4.27 we show transmission panels as a function of the wavelength and a_1 values for (a) the same system as that considered in Fig. 4.25, (b) the corresponding maps when an annular aperture is taken in the centre, (c) the circular hole considered in panel (a) is now filled with a dielectric constant $\varepsilon_2 = 4.5$, and (d) the circular hole is filled with $\varepsilon_2 = 1.8$. This modification of the central aperture translates into a change of the cutoff of the aperture from (a) $\lambda_c \approx 590$nm, to (b) $\lambda_c \approx 760$nm, (c) $\lambda_c \approx 1100$nm, and (d) $\lambda_c \approx 760$nm. White lines in each case render the spectral dependence of the transmittance through the corresponding single hole (×1000). All maps have the same scale in order to highlight how transmission is boosted up by properly optimizing the central hole. In panels (b), (c), and (d) the transmittance through the single aperture in each case presents a Fabry-Perot resonance whose spectral location are designed to coincide with $\lambda_R = 630$nm. Depending on the central hole we choose, transmission can be enhanced from $T_{max} \approx 15$ to $T_{max} \approx 54$.

Moreover, in panel (c) at $\lambda \approx 850$nm and $\lambda \approx 1050$nm, it is also seen some enhancement in transmission (lighter to that observed at λ_R), since other Fabry-Perot resonances emerge in the transmission spectrum of the isolated central hole. Notably, in all cases, the response of the array appears at λ_R.

Interestingly, both panels in Fig. 4.26 present “hot spots” around λ_R for similar a_1 values as those appearing in transmission in Fig. 4.25. Therefore, in order to obtain additional insight on these findings, Fig. 4.28 shows the computed maps of the amplitude of the electric field at the entrance of all the grooves, $|E_n|$.

In the spectral band close to λ_R all panels present hot spots with locations in the $\lambda - a_1$ plane that coincide with those of the transmittance in Fig. 4.25. However, for wavelengths larger than the cutoff of the hole, $|E_n|$ present spectral features that are not observed in the total transmittance in Fig. 4.25, as the latter is strongly suppressed by the small transmittance of the central hole. In particular, *all* maps present an even stronger resonance in the *field ampli-*

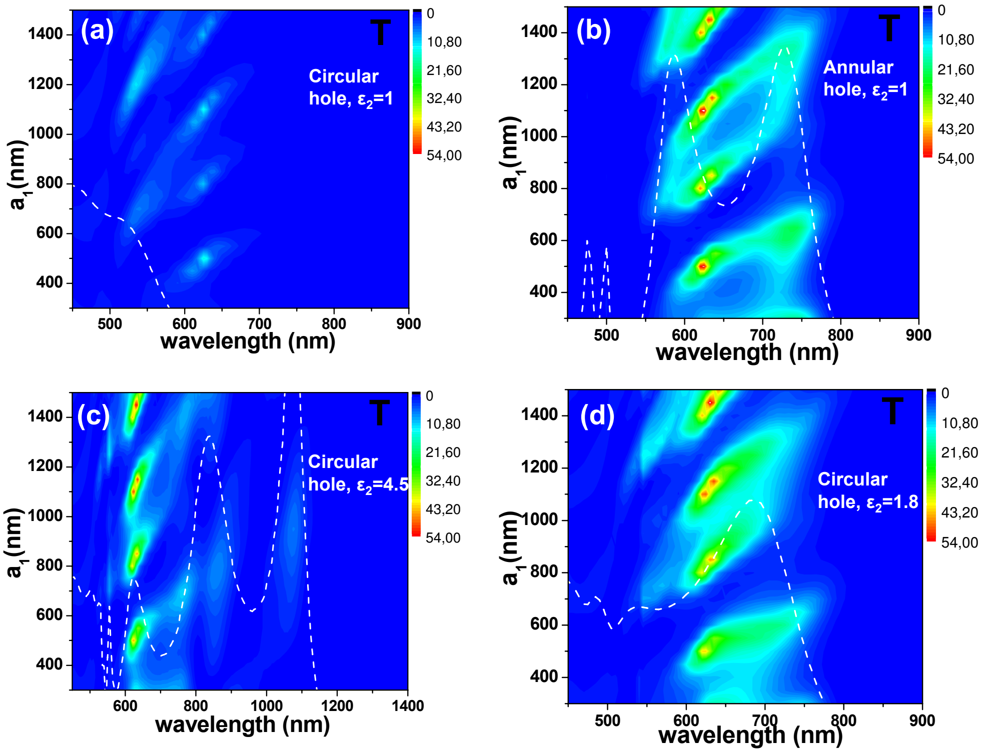

Figure 4.27: Transmission maps as a function of a_1 and the incident wavelength for (a) the same geometrical parameters as in Fig. 4.25, (b) the same as (a) but with a central annular hole with $r_{out} = 125$nm and $r_{in} = 55$nm, (c) the same as (a) but with a dielectric constant filling the circular hole $\varepsilon_2 = 4.5$, and (d) the same as (c) with $\varepsilon_2 = 1.8$. White lines in each case render the spectral dependence for the transmittance through a single hole (×1000).

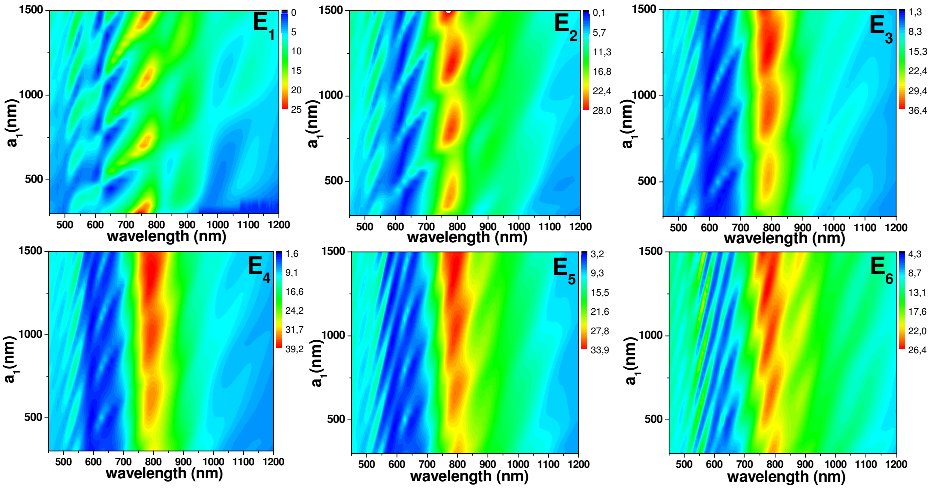

Figure 4.28: For the geometrical parameters in Fig. 4.25, amplitude of the electric field at the entrance of the grooves $|E_n|$ as a function of a_1 and λ.

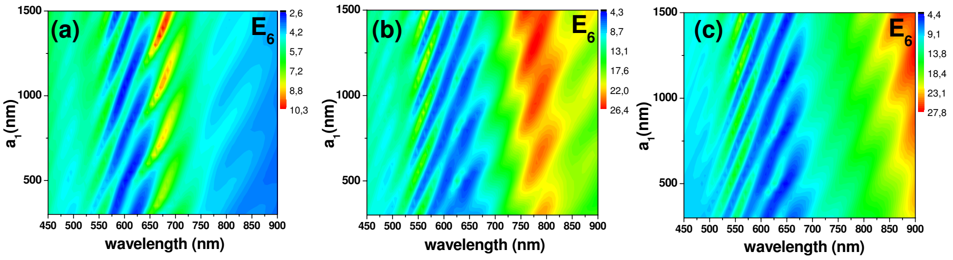

Figure 4.29: For the geometrical parameters in Fig. 4.25, amplitude of the electric field at the entrance of the sixth groove $|E_6|$ as a function of a_1 and λ, for (a) $h_g = 30$nm, (b) $h_g = 90$nm, (c) $h_g = 150$nm.

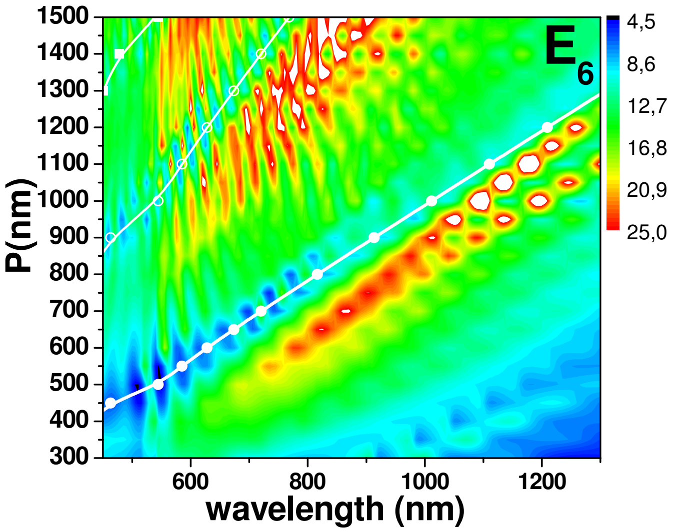

Figure 4.30: Amplitude of the electric field in the sixth groove, $|E_6|$ for the same geometrical parameters as in Fig. 4.25 at $a = 600$nm, as a function of the period and the incident wavelength. White line represents the condition $\lambda_{SP} = p$.

tude at $\lambda \approx 800$nm than at λ_R, pointing to a collective behavior. However, this resonant field does not lead to enhanced transmission.

So, can these resonant effects appearing at λ_R and at $\lambda \approx 800$nm be combined? We found that when the groove depth increases, the collective resonance enhances and red-shifts, whereas the one at λ_R also increases in intensity but its spectral position remains invariable, as it is shown in Fig. 4.29. This figure contains panels of the amplitude of the electric field at the entrance of the sixth groove, $|E_6|$ for (a) $h_g = 30$nm, (b) $h_g = 90$nm, (c) $h_g = 150$nm.

We can also study how this collective resonance varies with p. In Fig. 4.30 it is shown $|E_6|$, as a function of p and the incident wavelength for the same system as before with $a_1 = 600$nm. Note that since the collective resonance

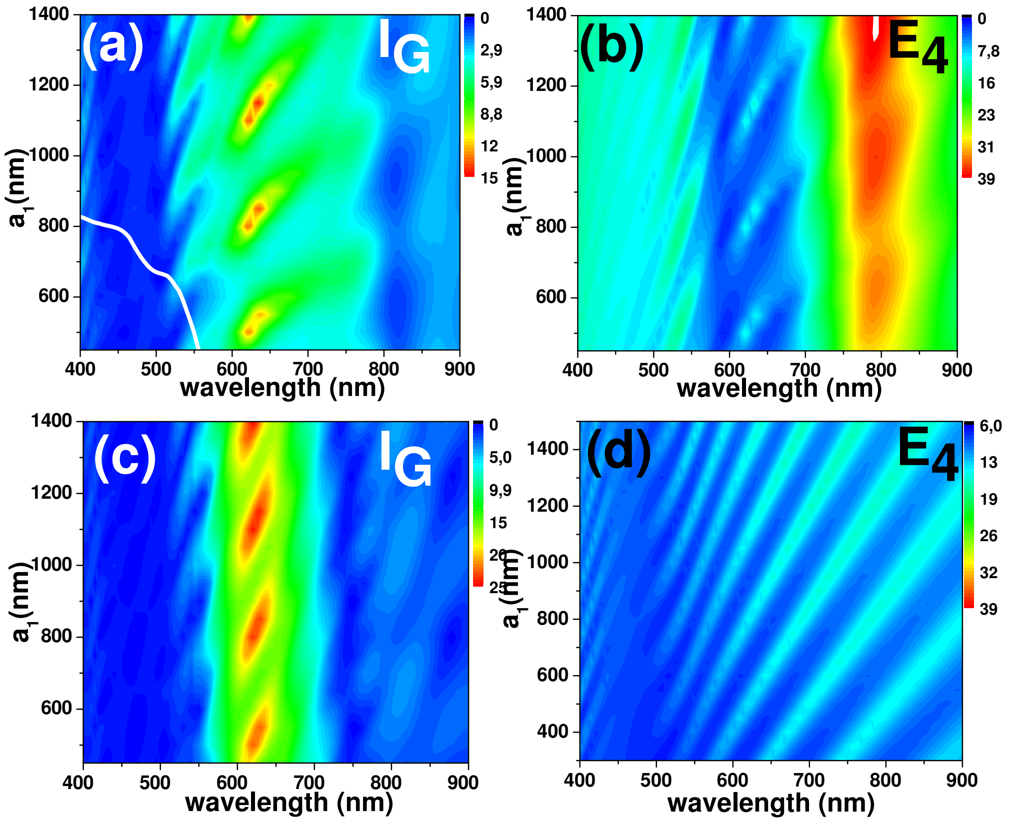

Figure 4.31: For the geometrical parameters in Fig. 4.25, computed re-illumination from the grooves in the central hole (panel (a)) and amplitude of the electric field at the entrance of the fourth annular groove $|E_4|$ (panel (b)), as a function of a_1 and λ. Panels (c) and (d) show the same as panels (a) and (b), respectively, but for a system of "disconnected" grooves, i.e. by setting $G_{nm} = 0$ for $n \neq m$. Grey lines depict the condition $2a_n = m_n \lambda_{\mathrm{SP}}$ for each annular groove. The white line in panel (a) renders the spectral dependence for the transmittance through a single hole (×1000).

for deep enough grooves does not depend on a_1, this map would be valid for any other a_1 value. In the figure, the condition $\lambda_{SP} = p$ is depicted for each period with white lines. This map shows that there is no case where these two resonances coincide, and we did not find a way to combine these two effects, neither by modifying h_g, nor by varying p.

To find out why the resonance at $\lambda = 800$nm does not appear in transmission panels, we calculate the light going from the groove array to the central hole, I_G, and compare with E_n panels. This reillumination term is defined as:

$$I_G = \sum_n G_{n0} E_n \tag{4.9}$$

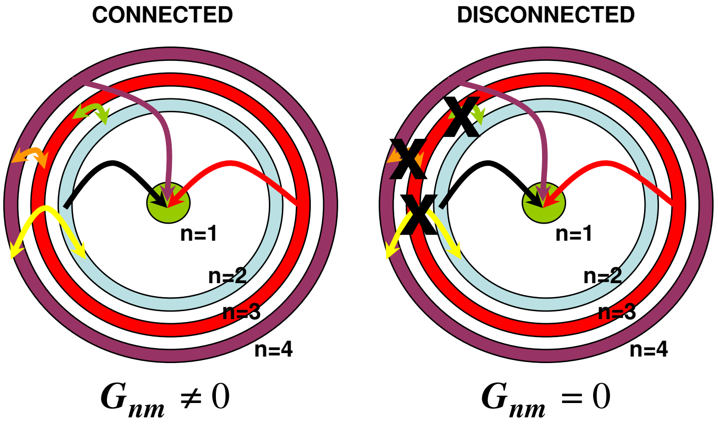

Figure 4.32: Schematics of a BE when grooves are connected (left panel) and are not (right panel).

with $n = 1, 2, .., N$.

These calculations appear in panels (a) and (b) in Fig. 4.31.

To understand the origin of the "hot stripes" in I_G and E_n that lead to EOT, we now consider the response of a set of isolated annular grooves (by simply setting $G_{nm} = 0$ for $n \neq m$, see schematics in Fig. 4.32). Panels (c) and (d) in Fig. 4.31 show the same calculations as in panels (a) and (b), respectively, but when grooves are "disconnected". The re-illumination map when grooves do not interact presents a similar pattern to that of I_G when the full interaction is considered: there are high intensity features at $\lambda_R \approx$ 630nm only for some values of a_1. This result clearly shows that maxima in I_G originate from the constructive interference at the hole of the EM fields radiated by each groove (I_g) which, at those wavelengths, can be considered as isolated. The comparison between $|E_4|$ in the connected (Fig. 4.31(b)) and isolated cases (Fig. 4.31(d)) reenforces this interpretation: in the spectral region close to λ_R, where the resonance in both I_G and T occur, $|E_4|$ is similar for both an isolated and a "connected" groove. In contrast, these two situations lead to very different $|E_4|$ in the resonance appearing at $\lambda \approx$ 800nm, adding further evidence to the association of this resonance to a collective behavior.

The previous analysis shows that, at $\lambda_R =$ 630nm, the grooves can be considered as independent of each other. So let us now consider a single groove with $h_g =$ 90nm depth, and $w_g =$ 220nm width drilled in a gold film.

Figure 4.33 shows the amplitude of the electric field of this annular hole as a function of its average radius, or equivalently, its distance to the centre, a_1, and the incident wavelength. As in panel (d) in Fig. 4.31, this contour plot presents enhanced stripes that almost follow the grey lines also shown there.

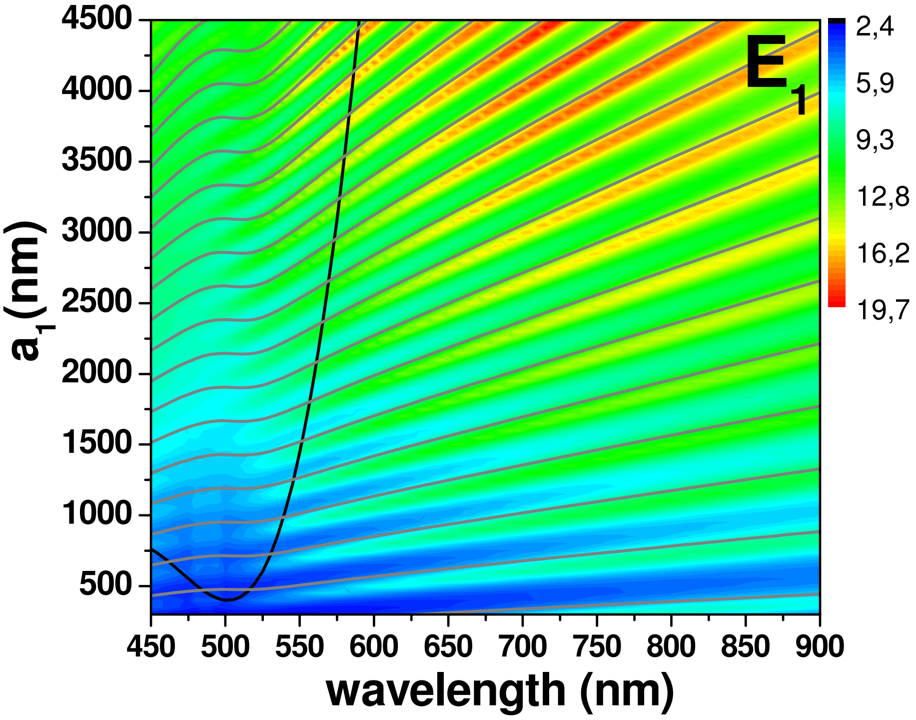

Figure 4.33: Electric field amplitude $|E_1|$ for an annular groove drilled in gold with $h_g = 90$nm and $w_g = 220$nm, as a function of the distance to the centre of the structure, a_1, and the incident wavelength. Grey lines depict the condition $2a_1 = m\lambda_{\mathrm{SP}}$.

These grey lines represent the condition to have an integer number of plasmon wavelengths inside the cavity originated by the annular groove: $2a_1 = m\lambda_{\mathrm{SP}}$.

In general, we find that an isolated shallow groove (with $h_g << \lambda$, as those considered in this work), re-illuminates the centre of the structure maximally when an integer number of SP wavelengths fits inside each ring cavity, that is, $2a_n = m_n\lambda_{\mathrm{SP}}$, where m_n is an integer and a_n is its average radius. This is consistent with the fact that, in the optical regime and at distances larger than $2-3\lambda$, SP are the main contribution to the EM field at the surface radiated by a surface defect [66, 139].

Figure 4.34 shows at the same time the previous (a) panel of Fig. 4.25 and (c) panel of Fig. 4.31. The condition $2a_n = m_n\lambda_{\mathrm{SP}}$ is represented as a collection of straight lines in Fig. 4.34(a), one for each groove ($n = 1, ..., 6$). Notice that all lines cross at several points, where the re-illumination from each groove is maximal simultaneously. For a collection of grooves with average radius $a_n = a_1 + (n-1)p$, where n does not necessary have to be consecutive (eventually providing aperiodic structures), these maximal points are given by

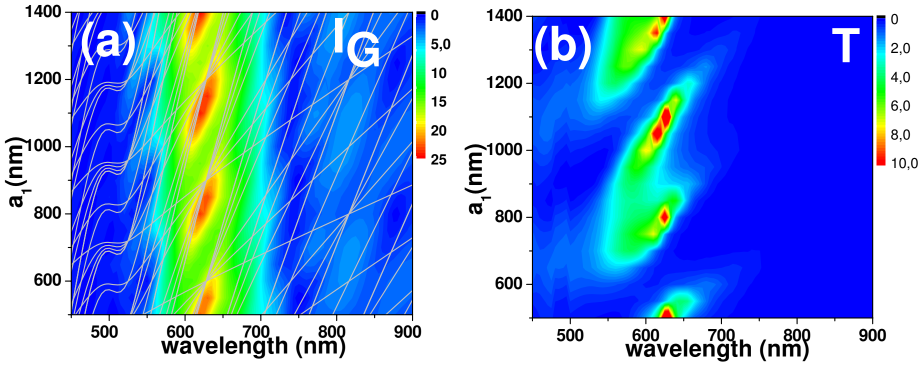

Figure 4.34: Comparison of panel (c) from Fig. 4.31 and panel (a) from Fig. 4.25 to highlight that resonances appearing in the $\lambda - a_1$ plane coincide. Grey lines depict the condition $2a_n = m_n\lambda_{\rm SP}$ for each annular groove.

the conditions

$$\lambda_{\rm SP} \approx \frac{p}{l} \tag{4.10}$$

$$a_1 \approx m\,\frac{\lambda_{\rm SP}}{2} \tag{4.11}$$

where m and l are integers. Moreover, all partial re-illuminations interfere constructively in that case. This explains the maximum in I_G that occurs in both the disconnected case (Fig. 4.31(c)) and the connected one (Fig. 4.31(a)).

The small deviation between the actual values of a_1 and λ for maximum I_G and those given by Eq. 4.10 and Eq. 4.11 are due to the influence of both groove width and, principally, groove depth which are not taken into account in the simple model outlined above. Actually, a finite h_g enlarges the optical path length that light travels, due to incursions inside the groove, which eventually translates into a larger effective $\tilde{a_1}$. Therefore, grey lines in Fig. 4.34 intersect at larger a_1 values than those where actual hot spots in the reillumination process, occur. In the limit of very shallow grooves, hot spots and the intersection of grey lines coincide.

Figure 4.35 shows I_G for the same system as before but in the limit of very shallow grooves with $h_g = 10$nm. In this case, for I_G, hot spots in the $\lambda - a_1$ plane actually coincides with the points where grey lines intersect.

Additionally, Fig. 4.36 shows the transmission of light through an aperiodic system where all grooves are located so that they fulfil the condition $2a_n = m_n\lambda_{\rm SP}$. In this particular case the position of the grooves is indicated in the schematics in that figure: $a_1 = a_1$, $a_2 = a_1 + 2p$, $a_3 = a_1 + 5p$, $a_4 = a_1 + 6p$, $a_5 = a_1 + 9p$, and $a_6 = a_1 + 11p$, with $p = 600$nm. We observe a resonance appearing in the same $a_1 - \lambda$ plane as in the case of periodic structures in

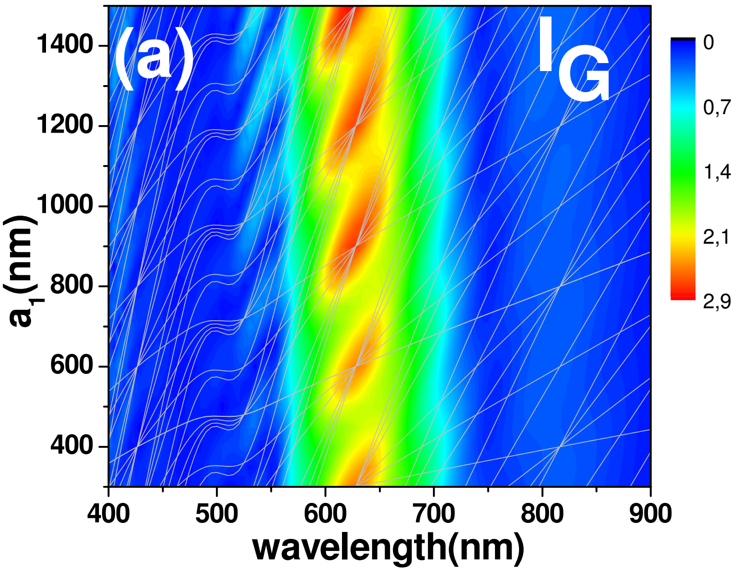

Figure 4.35: Reillumination, I_G, for the same geometrical parameters as in Fig. 4.25 with $h_g = 10$nm. Grey lines depict the condition $2a_n = m_n\lambda_{\rm SP}$ for each annular groove.

both T and I_G. At $\lambda \approx 780$nm, there is another resonance less intense in both T and I_G panels for other a_1 values, very close to the secondary points where less grey lines intersect. However, our simple scaling laws do not explain the secondary resonances and this finding would require more research.

Within the CMM and to get physical insight, we also study how transmission and reillumination are affected when grooves are not illuminated directly at the same time, just by setting $I_n = 0$ in each case. Figure 4.37 and Fig. 4.38 show transmission of light and the corresponding reillumination panels for the same system as in Fig. 4.25, but with $\varepsilon_2 = 4.5$, when grooves are illuminated successively, as it is schematically shown on top of each panel. One of the most clear results is that, as more grooves are illuminated, the resonance appearing at $\lambda = 630$nm gets stronger, and the resonance related to the Zero-order F-P of the single hole at $\lambda \approx 850$nm slightly fades away.

Besides, as more grooves are illuminated, the width of the "hot stripes" along the grey lines (corresponding to resonances in the field of the first annular groove) starts narrowing to eventually become "hot spots" at λ_R. It is also seen that the slope of these stripes, follows first the slope of the grey lines corresponding to resonances in the field of the first annular groove, and then, as the outer grooves are illuminated, these slopes increase and follow the slopes of the grey lines corresponding to the outermost grooves (i.e., with larger average radius).

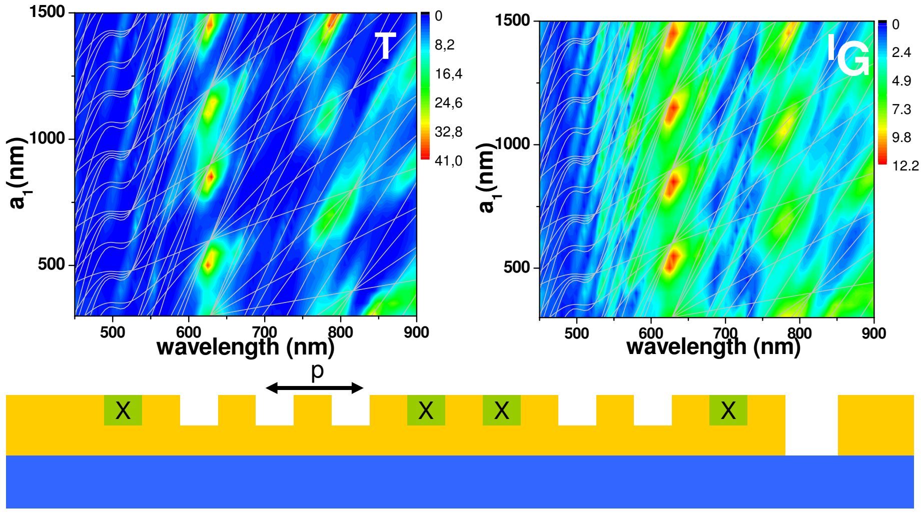

Figure 4.36: (a) Transmission of light through an aperiodic BE with the same geometrical parameters as in Fig. 4.25 and where all grooves satisfy $2a_n = m_n\lambda_{\mathrm{SP}}$.

This is a result arising from the the fact that, the nearest grooves send light to the central hole more "easily" than the outer ones (with less radiation losses), but the outer ones collect more light due to the dimension of their average radius. Therefore, there exists a trade-off between efficiency of reradiating light into the central hole, and the capacity to collect more light. Moreover, maximum transmission varies from about 8.5 to 55 as grooves are illuminated, but in order to highlight transmission features, all panels are saturated to $T_{max} = 15$. The corresponding T_{max} values for each case appear explicitly in each panel.

The scaling laws given by Eq. 4.10 and Eq. 4.11 are also in good correspondence with experimental results. Main resonances shown in Fig. 4.25 appear at $\lambda_R = 630$nm, as it is predicted by Eq. 4.10 for $l = 1$, but they also obey Eq. 4.11, with $m = 1, 2, 3, 4$, in the range of parameters here studied. In order to stress the importance of following this set of simple equations when designing BE structures, the experiments appearing in Fig. 4.39 were also conducted.

This figure shows transmission spectra and the expected resonant wavelengths λ_R for BE structures with different geometrical parameters (see caption) with $a_1 = p$ for different periods. Again the small difference between the simple prediction and the experiment is attributed mainly to the influence of groove depth. Note that these λ_R values are calculated from $Re[k_{sp}[\lambda_R]] = 2\pi/(p/l)$, being $l = 2$, and that a_1 values are properly selected with $m = 4$. This draws a straightforward analogy with periodic hole arrays where higher order SP modes can be excited at specific wavelength in agreement with a

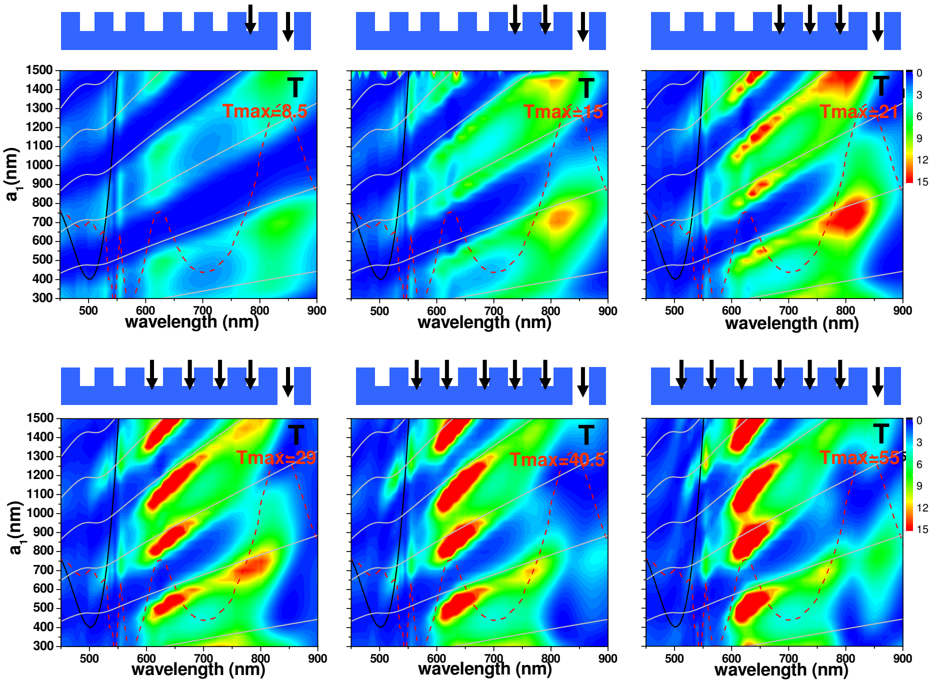

Figure 4.37: Transmission of light for the same geometrical parameters as in Fig. 4.25 with $\varepsilon_2 = 4.5$. Grey lines depict the condition $2a_2 = m_n\lambda_{\rm SP}$ for the first annular groove. The red line corresponds to the transmission of a single circular hole with $r_c = 250$nm, and $\varepsilon_2 = 4.5$, multiplied by 1000, and the black line corresponds to the propagation length of the plasmon.

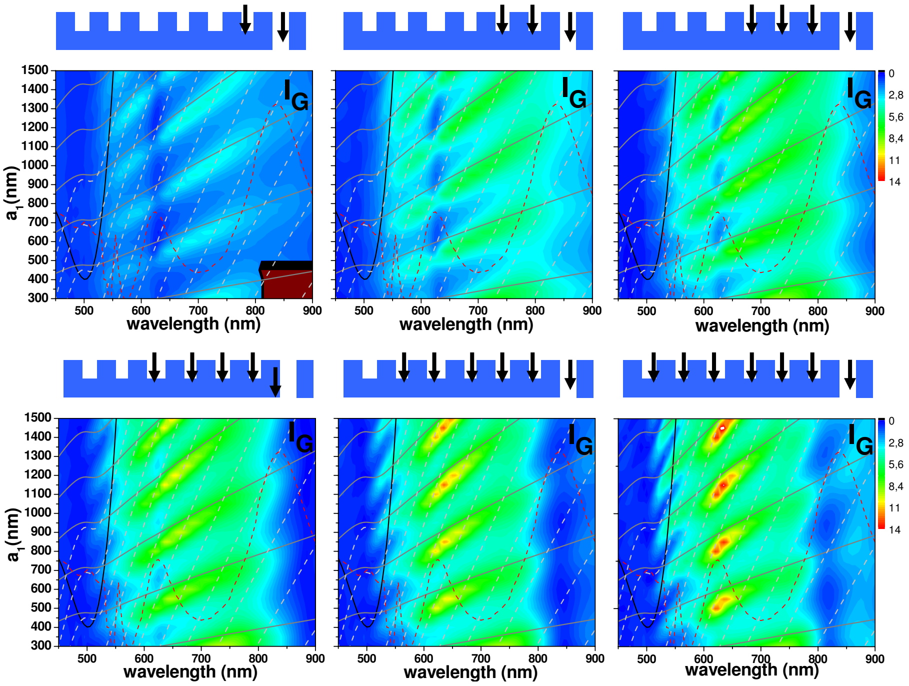

Figure 4.38: Reillumination I_G for the same geometrical parameters as in Fig. 4.25. Continuous grey lines depict the condition $2a_2 = m_n\lambda_{\mathrm{SP}}$ for the first annular groove, and the dashed ones to the outmost one. The red line corresponds to the transmission of a single circular hole with $r_c = 250$nm, and $\varepsilon_2 = 4.5$, multiplied by 1000, and the black line corresponds to the propagation length of the plasmon.

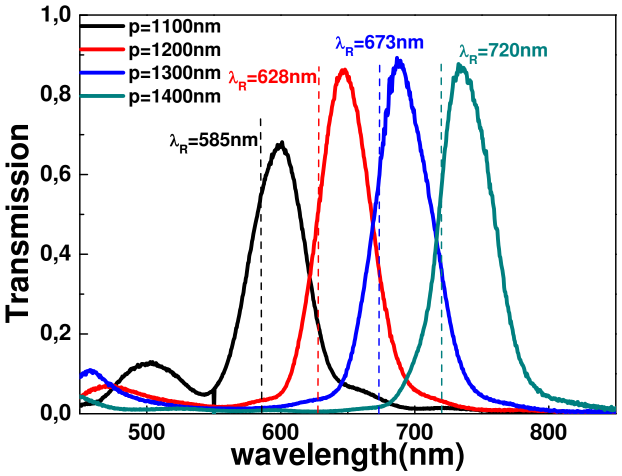

Figure 4.39: Transmission spectra measured through BE structures with $N = 5$, $h = 280$nm, $h_g = 90$nm, $w_g = 330$nm, $r_c = 170$nm, and different periods (see label) being $a_1 = p$. For each period, the predicted location of λ_R is indicated. These wavelengths follow Eq. 4.10, so that $Re[k_{sp}[\lambda_R]] = 2\pi/(p/l)$, being $l = 2$, and Eq. 4.11 with $m = 4$.

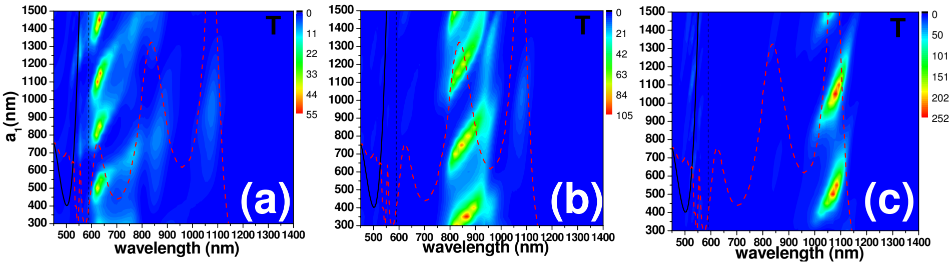

Figure 4.40: Transmission spectra as a function of a_1 measured through BE structures with $N = 6$, $h = 250$nm, $h_g = 90$nm, $w_g = 220$nm, $r_c = 125$nm, filled with $\varepsilon_2 = 4.5$, and different periods (see label) (a) $p = 600$nm, (b) $p = 800$nm, and (c) $p = 1100$nm.

grating law of the kind of Eq. 4.10.

Additionally, Fig. 4.40 shows theoretical calculations of the transmission of light through periodic BEs with (a) $p = 600$nm, (b) $p = 800$nm, and (c) $p = 1100$nm, so that Fabry-Perot resonances related to the central hole filled with $\varepsilon_2 = 4.5$ coincide with those predicted by the scaling laws. Note that transmission can be enhanced from $T_{max} = 55$ to $T_{max} = 252$, and that new a_1 resonant values arise as predicted by the scaling laws.

In order to have a first understanding of this rather complex landscape, the experimental group at ULP developed a simple phenomenological model that captures the main mechanisms playing a role at λ_R. To confront the model to actual experiments, it is considered the most simple situation of a normal incidence illumination of the BE. In its form, the model:

- treats the groove array as a resonant "black box" (see schematics in panel (c) in Fig. 4.24) with an EM response characterized by a general *complex coupling coefficient*, γ, which gives the fraction of normally incident field amplitude that the groove array *locally* couples into SP,
- considers the central hole being illuminated by the incident EM field and re-illuminated by light coming from the array via SP,
- accounts for hole re-illumination as an SP-assisted two-path scattering process: (i) one direct path from the array to the hole and (ii) and a secondary path corresponding to SP back reflected by the groove array to the central hole with *complex reflection amplitude* r (see a schematic representation in Fig. 4.24(c)),
- assumes that the hole is sufficiently small so that the illumination of the hole (by either the incident EM field or the light coming from the array) depends only on the field amplitude and not on the parallel wavevector. In this case, the transmittance through the hole can be expressed as

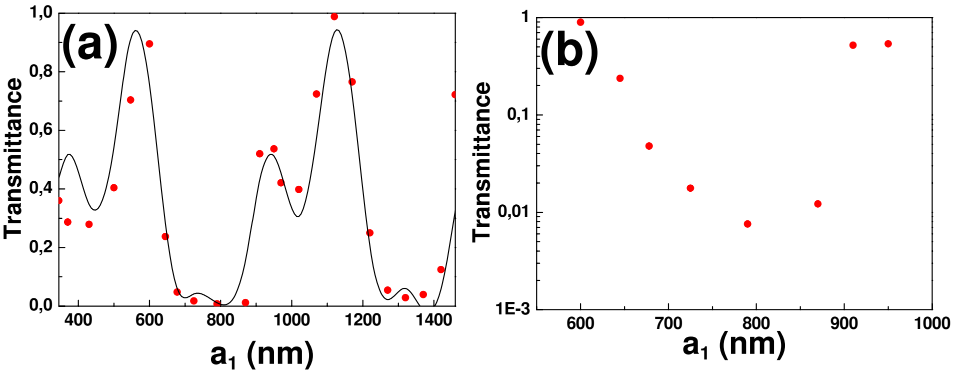

Figure 4.41: (a) Data points collected at $\lambda_\mathrm{R} \simeq 630$ nm as a function of a_1 for the same system at that appearing in Fig. 4.25. The continuous line is a fit from the phenomenological model of Eq. 4.12 with fitting parameters discussed in the text. (b) Modulation and suppression of the transmittance over a smaller region of a_1 values.

> $T = T_{SH} \left|F_{array}\right|^2$, where T_{SH} is the transmission of light through a single hole, and F_{array} is the field at the hole in the presence of the array divided by that for an isolated hole.

Under these conditions, the re-illumination term can be expressed in terms of the (complex valued) SP wavevector k_{sp} as

$$F_{array} \approx 1 + \gamma\sqrt{a_1}\ e^{(ik_{sp}a_1)} + r\gamma\sqrt{a_1}\ e^{(3ik_{sp}a_1)} \tag{4.12}$$

The first term represents the incident EM field, the second one accounts for the light mediated by SP going directly from the groove array to the central hole, whereas the third term represents the light that goes from one side of the “black box” to the other one, and then is reflected back to the central hole. In principle, the parameters γ and r are expected to depend smoothly on a_1 and λ but, as the exact dependence is unknown, they will be initially considered as constants. Only a full numerical calculation will be able to define these parameters properly and to evaluate their exact dependencies, along with the role played in enhanced transmission by the different EM couplings between BE elements. In Eq. 4.12, the cylindrical symmetry has been accounted for by considering the SP as planar cylindrical waves. For a propagation over a distance x, the field amplitude associated to a SP locally launched at the level of the cylindrical groove is proportional to $e^{(ik_{sp}x)}/\sqrt{x}$. The total field amplitude will scale as $\sqrt{x}$ after integrating over the whole cylindrical groove, explaining the $\sqrt{a_1}$ dependency in Eq. 4.12.

Figure 4.41(a) shows a fit of the transmittance obtained at 630 nm $\simeq \lambda_\mathrm{R}$ with this phenomenological model for $|\gamma| = 0.02$ and $|r| = 0.7$. This fit allows interpreting the observed spectral resonances which arise from the interference between (i) the field directly re-routed by the grooves into the hole and (ii) the field re-routed by one side of the array that, before reaching the hole, suffers a reflection at the other side of the array. The contribution (i) essentially selects a_1 values corresponding to the transmission resonances that dominate the transmission spectra in a standing-wave pattern (c.a. every $\lambda_{\mathrm{SP}}/2$) while (ii) is responsible for the secondary transmission peak at $a_1 \sim 959$nm. In other words, the optical spectra acquired in the $\lambda - a_1$ parameter space are revealing unambiguously the coherent character of the BE structure which can therefore be envisioned as a genuine sub-micron SP cavity. Controlling the optical transmission is therefore possible through the choice of a_1 values. Figure 4.41(b) demonstrates a selective modulation of the transmission of about 2 orders of magnitude. The dephasing between the SP component and the direct transmission through the hole is thus directly related to the cavity radius. At a specific value of a_1, the two components can destructively interfere, leading to a strong suppression of the transmission signal as displayed in Fig. 4.25(b). In this context, it has been realized that BEs can be carefully designed as to suppress any bright background in sensitive darkfield detection and imaging -so called SWEDA microscopy [140,141]. When the periodic surrounding grating is designed as a Bragg reflector for the illumination wavelength, the BE structure behaves as a plasmonic micro-cavity around the hole, with strong potential in nanolithography and data storage [142]. The recently shown SWEDA effect is based on the same discussion we propose with similar interference effects at play within the BE cavity [140].

It is possible to find a qualitative microscopic model with the CMM rather than the previous phenomenological model. As said before, the CMM provides analytical expressions for all objects appearing in Eq. 4.8 which, in principle, have to be evaluated numerically. However, we find that, to a very good approximation, the elements G_{nn} and G_{0n} (related to how a groove re-illuminates itself or the central hole, respectively) satisfy:

$$\begin{aligned} G_{0n}(a_n) &= \sigma(a_n)\, e^{ik_{sp}a_n} \\ G_{nn}(a_n) &= \beta(a_n) + \Gamma(a_n)\, e^{2ik_{sp}a_n} \end{aligned} \tag{4.13}$$

where $\sigma(a_n)$, $\beta(a_n)$, and $\Gamma(a_n)$ are fitting complex coefficients that depend *smoothly* on a_n. Equation 4.13 can be interpreted physically in the following way: the groove re-illuminates the hole via SP while, for the self re-illumination, the groove can be considered as composed by two parts (left and right). These parts re-illuminate themselves (leading to the $\beta(a_n)$ contribution) and one another (the $\Gamma(a_n)$ term).

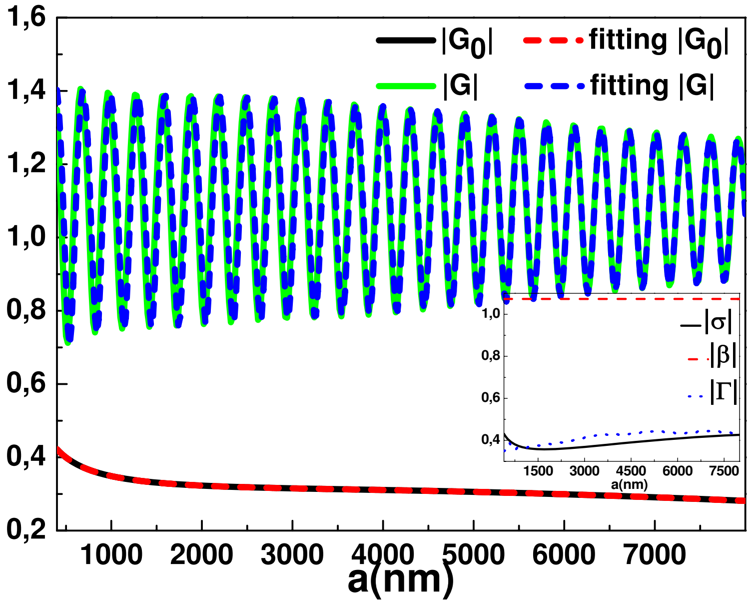

Figure 4.42: For the geometrical parameters in Fig. 4.25 and $\lambda = 630$nm, comparison between the exact values for $|G_0|$, $|G|$ and those obtained by Eq. 4.13, as a function of a. The inset shows $|\sigma(a)|$, $|\beta(a)|$, and $|\Gamma(a)|$ values as a function of a.

Since the previous analysis indicates that the array response can be understood as the response of isolated grooves, let us now consider an isolated groove with the same h_g and w_g as before and of average radius a. To simplify the notation, we write $G_{0n} = G_0(a)$ and $G_{nn} = G(a)$. As an illustration of the validity of Eq. 4.13, Fig. 4.42 shows $|G_0(a)|$ and $|G(a)|$ calculated both exactly and fitted through Eq. 4.13, together with $|\sigma(a)|$, $|\beta(a)|$, and $|\Gamma(a)|$ obtained from the fit. This illustration is for the geometrical parameters considered in Fig. 4.25, panel (a), and at $\lambda = 630$nm, but we have checked that the validity of Eq. 4.13 is not restricted to these particular case.

Equation 4.13 also allows for a simplified analysis of the re-illumination process of a single groove, $I_g(a) = G_0(a)E(a)$, which can be written in the language of the Huygens-Fresnel model [143]. Equation. 4.8 in combination with Eq. 4.13 gives

$$E(a) = \frac{I(a)}{G(a) + \Sigma(a)} \approx \frac{I(a)}{\beta(a) + \Sigma(a)} \cdot \frac{1}{1 - r(a)e^{2ik_{sp}a}} \tag{4.14}$$

where

$$r(a) \equiv \frac{-\Gamma(a)}{\beta(a) + \Sigma(a)} \tag{4.15}$$

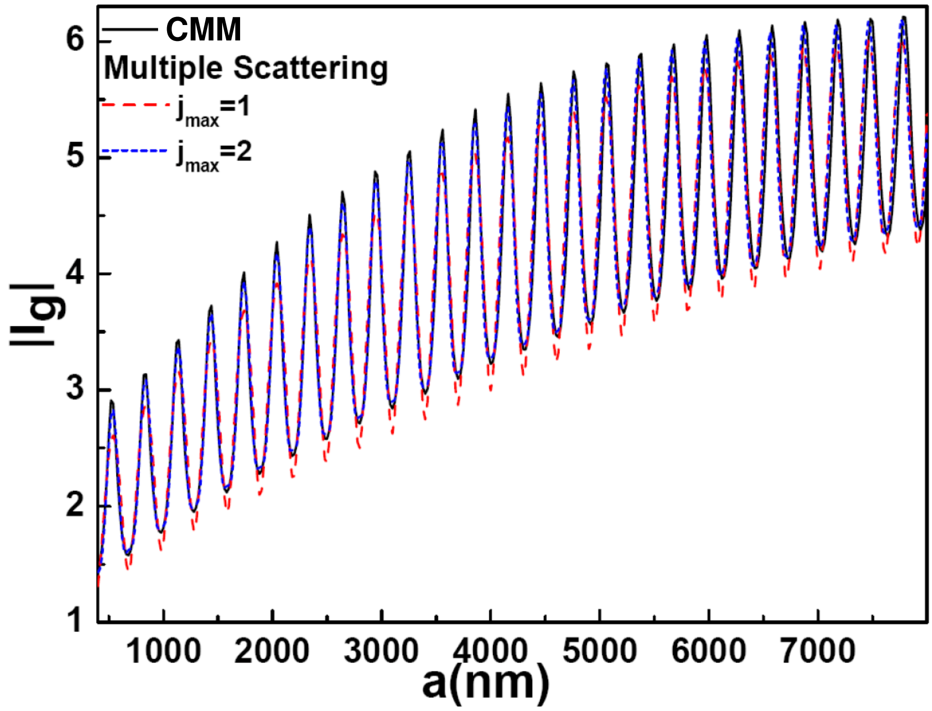

Figure 4.43: Reillumination of a single groove, $|I_g|$, as a function of a. The black curve represents the exact calculations. The blue and red curves show the result after fitting $\alpha(a)$ and $r(a)$ and truncating the sum in Eq. 4.17 to $j_{max} = 1$ and 2 terms, respectively. Geometrical parameters as those in Fig. 4.25 and $\lambda = 630$nm.

Expanding the denominator we get:

$$E(a) = \frac{I(a)}{\beta(a) + \Sigma(a)} \sum_{j=0}^{\infty} \left[r(a)\, e^{2ik_{sp}a} \right]^j \tag{4.16}$$

Notice that this expression contains the “multiple scattering” between the left and the right side of the annular groove. Finally, if we substitute the latter in $I_g(a) = G_0(a)E(a)$, we obtain:

$$I_g(a) = \alpha(a) e^{ik_{sp}a} \sum_{j=0}^{\infty} \left[r(a)\, e^{2ik_{sp}a} \right]^j \tag{4.17}$$

with

$$\alpha(a) \equiv \frac{\sigma(a)I(a)}{\beta(a) + \Sigma(a)} \tag{4.18}$$

Figure 4.43 shows the exact results for $I_g(a)$ and the fitted curve replacing $\alpha(a)$ and $r(a)$ in Eq. 4.17. The excellent agreement between the two calculations confirms the validity of the approximations involved in the derivation of the simplified model. Note also that considering just the first two terms ($j_{max} = 1$) in the sum in Eq. 4.17 already provides a good approximation.

In Fig. 4.44 we graph the coupling and reflection coefficients for the groove parameters previously considered (continuous black curves). Additionally, we present results for other representative geometries still in the subwavelength regime, which result from the ones considered throughout this section by increasing and decreasing some geometrical parameters (and, in each case, for the corresponding values of λ_R). These results show that, in all cases, the coupling amplitude α increase with groove radius, while the reflection amplitude r is practically independent of a. The dependence of α with a can be approximately fitted to $\alpha(a) \propto a^{2/3}$. This result, which is relevant to studies in BE structures based on the Huygens-Fresnel approach, can be traced back to arise from the exact $a^{1/2}$ dependence of $I(a)$ (i.e., the illumination of a groove is proportional to its area), plus an additional dependence with a of the coefficients entering Eq. 4.13 (see inset in Fig. 4.42). The computed reflection coefficient turns out to be smaller than the one given by the phenomenological model ~ 0.7 (which can only be helpful in an interpretation context). These studies also suggest that the width of the groove is not a parameter with a strong influence on the results (provided it is in the sub wavelength regime).

In the spectral region where transmission resonances occur (where grooves can be treated independently), we can obtain the total re-illumination at λ_R provided by an array of grooves placed at a_n as $I_G = \sum_n I_g(a_n)$. Thus, following Eq. 4.17

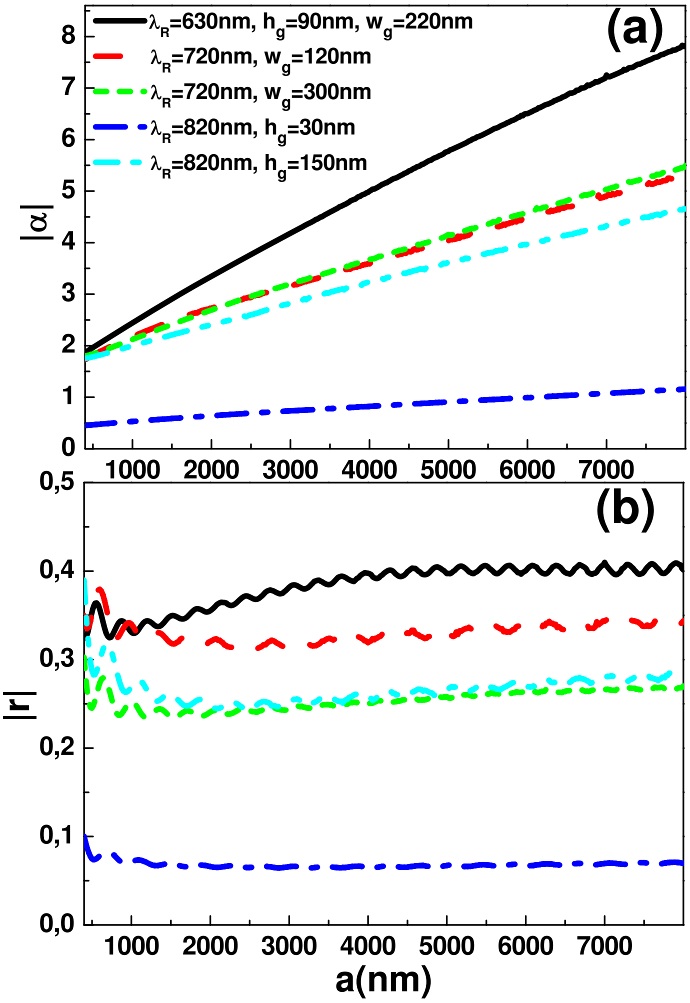

Figure 4.44: Calculation (within the CMM model) for $\alpha(a)$ (panel (a)) and $r(a)$ (panel (b)) for different set of parameters. The black curve is for the system considered in Fig. 4.25, which is taken as the reference. For the other cases, the labels give the parameters that are different from those in the reference.

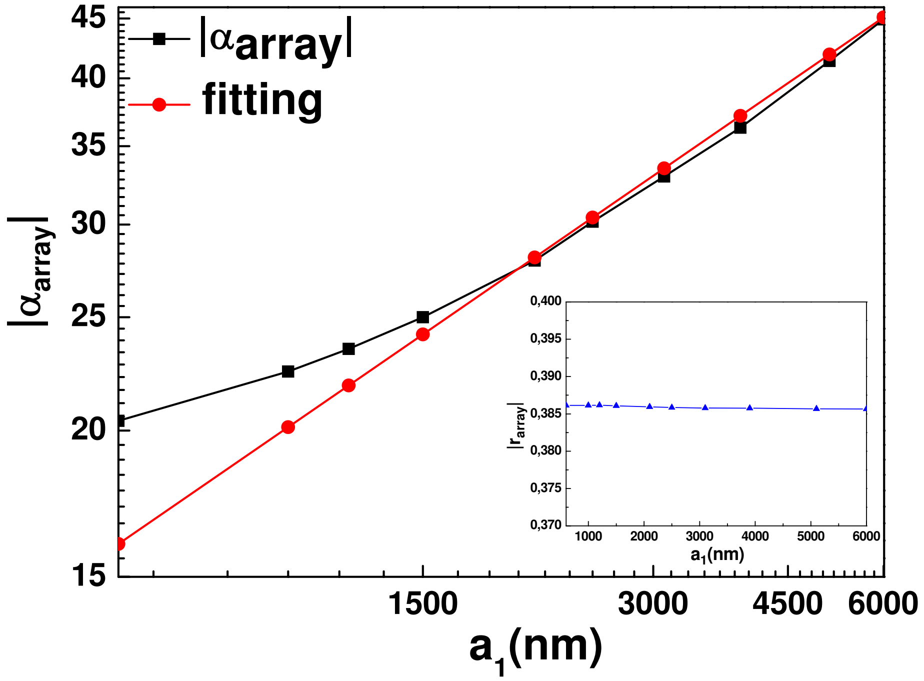

Figure 4.45: Calculation (within the CMM model) in logarithmic scale for α_{array} as a function of a_1 for the same geometrical parameters as in Fig. 4.25 at $\lambda_R = 630$nm. The black curve represents calculations from Eq. 4.20 and the red one, the fitting curve where $|\alpha_{array}| \sim {a_1}^x$ with $x = 0.45$. The inset shows the corresponding calculations for $|r_{array}|$.

$$I_G = \alpha_{array}\, e^{ik_{sp}a_1} \left(1 + r_{array}\, e^{2ik_{sp}a_1}\right) \tag{4.19}$$

with

$$\begin{aligned} \alpha_{array} &= \sum_n \alpha(a_n) e^{ik_{sp}(n-1)p} \\ r_{array} &= r \cdot \frac{\sum_n \alpha(a_n) e^{3ik_{sp}(n-1)p}}{\sum_n \alpha(a_n) e^{ik_{sp}(n-1)p}} \end{aligned} \tag{4.20}$$

where, according to Fig. 4.43 and Fig. 4.44, the reflection coefficient r is assumed to be independent of a_1, and $j_{max} = 1$. Additionally, if the condition $p \cdot Re[k_{sp}] \approx 2\pi l$ (being l an integer) is fulfilled, which is also the condition for validity of the independent-groove model, $r_{array} \approx r$ and $\alpha_{array} \approx \sum_n \alpha(a_n)$.

In the CMM formalism, $F_{array} = 1 + I_G/I_0$, so Eq. 4.19 recovers the phenomenological model given by Eq. 4.12. Moreover, in Fig. 4.45 we show $|\alpha_{array}|$ as a function of a_1 for the same geometrical parameters considered in Fig. 4.25 at $\lambda_R = 630$nm. Notably, we find for large a_1 values that $|\alpha_{array}|$ behaves as $a_1^{0.45} \sim \sqrt{a_1}$, as predicted by the simple phenomenological model. Note also that, despite the slow dependance of α_{array} with a_1, the reillumination at the centre of the hole strongly oscillates with a_1, due to the exponential terms in Eq. 4.19. Additionally, inset in Fig. 4.45 shows that $|r_{array}|$ hardly depends on a_1, as it was expected from Fig. 4.44.

4.3 Beaming

Light usually diffracts in all directions when it emerges from a subwavelength aperture, which puts a lower limit on the size of features that can be used in photonics. This limitation can be overcome by creating a periodic texture on the exit side of a single aperture in a metal film. The transmitted light emerges from the aperture as a beam with a small angular divergence (approximately $\pm 3^o$) whose directionality can be controlled. This finding was experimentally verified for the first time considering the 1D system with a slit flanked at both sides of the metal film by linear grooves [25], and it is especially surprising considering that the radiating region is mainly confined to an area with lateral dimensions comparable to the wavelength of the light.

Optical characterization of a single hole is a delicate experimental task due to the finite width of the angular distribution for the emission pattern [47, 131, 144, 145]. Therefore, great care must be taken in measuring single holes to obtain the correct spectral data due the finite collecting angle of the setup.

From the theoretical point of view, we should mention that, up to now, there are theories only on how a single hole perforated in a **perfect electrical conductor** (PEC) radiates [146, 147]. From the practical point of view, it is interesting to measure the *whole* current going through a single hole. This is a difficult task because it is necessary to integrate over 2π steradians. If there was an analytical formula, it would be enough measuring in the normal direction and use the analytical expression to integrate.

Next, we will show how this analytical expression can be obtained, and we will use it to calculate the far-field angular intensity distribution of isolated circular and annular holes made of **real metal**, and also for BE structures where both the illumination and transmission sides of the metal surface are corrugated with annular grooves. These are preliminary studies.

The specific quantity we compute is the scattering cross section, defined as the radiated power, P, by unit of solid angle, Ω,

$$\sigma(\theta,\phi)=\frac{\partial P}{\partial\Omega}=r^2 S_r \tag{4.21}$$

where S_r is the radial component of the Poynting vector, $\mathbf{S}=\mathbf{E}\times\mathbf{H}^*/2$, at an arbitrary observation point, r.

An analytical expression for $\sigma(\theta,\phi)$ within the CMM was derived by Dr. F. de Leon-Perez in our group [148]. This final expression has the following form:

$$\sigma(\theta,\phi)=\frac{k_\varepsilon k_z\sqrt{\varepsilon}}{8\pi^2}\left[\frac{k_\varepsilon}{k_z}\left|t_p(k_{||})\right|^2+\frac{k_z}{k_\varepsilon}\left|t_s(k_{||})\right|^2\right] \tag{4.22}$$

with $k_{||}^2=k_\varepsilon^2\cdot\sin^2\theta$, $k_z=k_\varepsilon\cdot\cos\theta$, and $k_\varepsilon=2\pi\sqrt{\varepsilon}/\lambda$. Besides, t_s and t_p are the transmission coefficients related to the s and p polarization, respectively, that can be written as:

$$\begin{aligned} t_s &= -\frac{sin(\phi)}{1+Z_s\,cos(\theta)}\sum_n \langle n|s\rangle\,E'_n \\ t_p &= -\frac{cos(\phi)}{1+\frac{Z_s}{cos(\theta)}}\sum_n \langle n|p\rangle\,E'_n \end{aligned} \tag{4.23}$$

In these expressions, θ measures angles with respect to the normal to the surface, and ϕ is the azimuthal angle ($\pi=0$ for observation points with in-plane projection parallel to the incident field). For further details of the definitions of these magnitudes, see Chapter 2 and Appendix A.

For convenience, we measure the normalized quantity:

$$\Sigma(\theta,\phi)=\frac{\sigma(\theta,\phi)}{\sigma(0,\phi)} \tag{4.24}$$

This will allow us to compare our results with other calculations performed for circular holes by Dr. F. de Leon-Perez using the CMM, and by Dr. J. Alegret using the Green Dyadic (GD) method. The GD method is capable of treating the optical response of an arbitrary object embedded in a layered background, which makes it very suitable for hole calculations. It has been recently used to simulate single holes and hole pairs [149], yielding very good agreement with reported experimental results. The GD method is exact, in the sense that it is derived directly from Maxwell's equations with no approximations. Its accuracy depends only on the mesh chosen to represent the objects we want to study, and also on the machine precision of the computer performing the calculations. We utilize the TEMA prescription [150] for the hole mesh, which gives a good balance between calculation speed and precision of the results.

In Fig. 4.46 there is a comparison for the spatial distribution of fields radiated by circular holes as a function for different hole radius, r_{out}. $\Sigma(\theta,\phi)$ is calculated for a single circular hole perforated in an Al film with thickness $h=100$nm, at $\lambda=630$nm. Panels (a) and (b) present calculations done with the CMM for annular holes in the limit when the inner radius $r_{in}=0$nm, and $r_{out}=190$nm, for $\phi=0^o$ and $\phi=90^o$, respectively. Panels (c) and (d) present the corresponding GD results, represented with solid lines, and CMM ones for circular holes, with dashed lines, along with a different calculation with $r_{out}=30$nm. The comparison amongst the three calculations is excellent, finding that $\Sigma(\theta,\phi)$ is more anisotropic (narrower) when the aperture size increases.

Once our calculations are checked, and before going on with the study of annular holes and BE structures, it is interesting to study the difference between PECs ($Z_s=0$) and real metals (RMs).

A fraction of the energy power radiated by an aperture in a real metal is scattered into SPPs that propagate along the metal surface. These modes, only excited by p-polarized light, are confined to the metal-air interface and do not contribute to the far-field radiation. There are not surface modes in a flat metal surface and its p-radiation is practically isotropic as function of θ.

The normalized scattering cross section, $\Sigma(\theta,\phi)$, for a gold layer and PEC are compared in Fig. 4.47 at $\lambda=630$nm, for the same system as before. In Fig. 4.47 (top panel) it is represented the p-contribution to $\Sigma(\theta,\phi)$, i.e. at

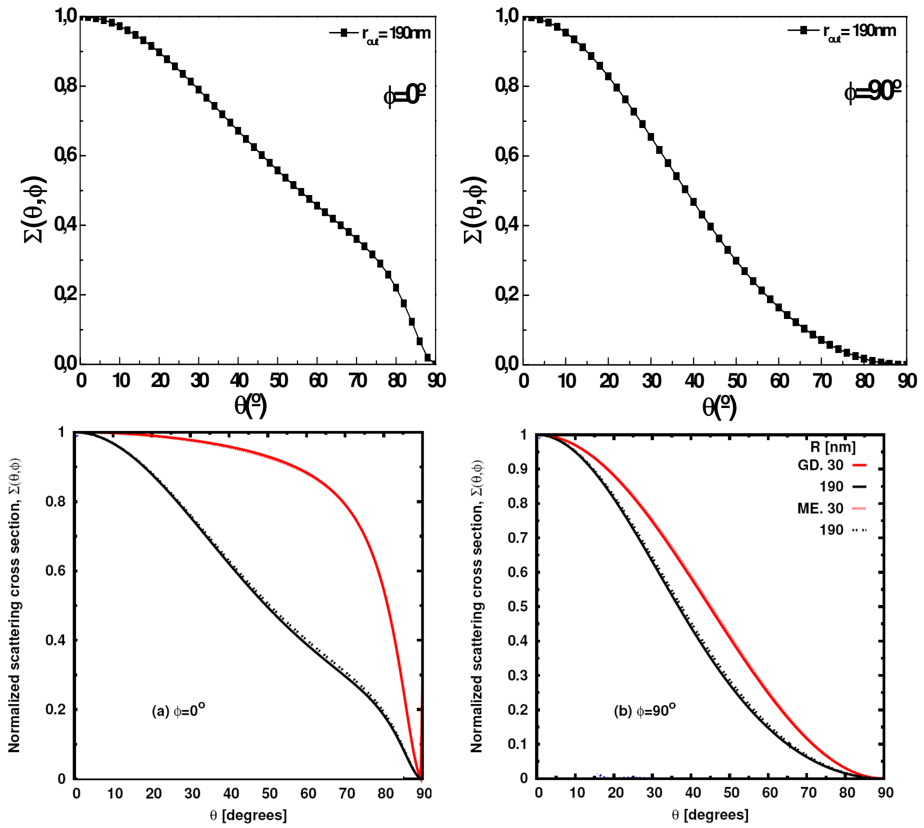

Figure 4.46: $\Sigma(\theta, \phi)$ of a single circular hole perforated in a Al film with thickness $h = 100$nm, at $\lambda = 630$nm. (a) and (b) panels correspond to CMM calculations for annular holes in the limit when the inner radius $r_{in} = 0$nm, for $\phi = 0^o$ and $\phi = 90^o$, respectively. Panels (c) and (d) present the corresponding GD results, with solid line, and CMM ones for circular holes, with dashed lines.

$\phi = 0^o$, for both a PEC (in black) and a RM (in red). These quantities are practically equal for small zenithal angles, $\theta \approx 0^o$, while its difference diverges as function of θ, being maximal at $\theta = 90^o$. However, in the s-contribution to $\Sigma(\theta, \phi)$, i.e. at $\phi = 90^o$ where SPPs are not excited, there is practically no differences between RM and PEC (see lower panel in Fig. 4.47).

Next we present similar calculations for annular holes. In Fig. 4.48 we study the evolution of the radiation pattern from a circular to an annular hole. In the subwavelength regime, the external radius is fixed to $r_{out} = 190$nm, and the internal one is varied. In this case, annular holes are drilled in a 100nm gold film, and the wavelength is fixed at $\lambda = 600$nm. The upper panel considers $\phi = 0^o$, and the lower one $\phi = 90^o$. We find that, for $\phi = 0^o$, the larger the inner radius, the more anisotropic $\Sigma(\theta, \phi)$ is; whereas calculations for $\phi = 90^o$ do not change either with θ or r_{in}.

We can also study the evolution of the radiation pattern from a circular to an annular hole, in larger systems. In Fig. 4.49, similar studies as those appearing in Fig. 4.48 are shown. Now, the external radius is fixed to $r_{out} = 1600$nm, and the inner one varies as $r_{in} = 500, 1000, 1500$nm. On the one hand, for $\phi = 0^o$, we find that $\Sigma(\theta, \phi)$ oscillates with θ, presenting maxima and minima that decrease in amplitude with θ. Moreover, the larger the inner radius, the more oscillations $\Sigma(\theta, \phi)$ presents. On the other hand, for $\phi = 90^o$, $\Sigma(\theta, \phi)$ does not change with r_{in}, and for $\theta \geq 10$, $\Sigma(\theta, \phi)$.

It is also interesting to study annular holes with very large average radius, since grooves surrounding the central aperture in BEs will behave as these ones. In Fig. 4.50 the evolution of $\Sigma(\theta, \phi)$ from a small to a large annular hole is presented. For a fixed groove width, $w_g = 150$nm, the average radius is varied as $a = 145, 350, 550, 750$nm. We find again that, at $\phi = 0^o$, the larger the ring, the more anisotropic and more oscillations $\Sigma(\theta, \phi)$ presents. In contrast, for $\phi = 90^o$, the larger the ring, the less the dependance with θ.

Finally, we can study $\Sigma(\theta, \phi)$ for BE structures where the input corrugation is replicated in the output region, as a function of both the distance of the first annular grooves to the centre of the structure, a, and the wavelength. In particular we choose the same geometrical parameters as those studied in Fig. 4.25 in Section 4.2.5: a gold system with $N = 6$ grooves, $w_g = 220$nm, $h_g = 90$, $h = 280$nm, central circular hole with radius $r_{out} = 125$nm, and $p = 600$. In this case we consider a free standing system ($\varepsilon_1 = \varepsilon_2 = \varepsilon_3 = 1.0$). The a values are chosen so that transmission is maximum ($a = 800$nm), minimum ($a = 600$nm), and of an intermediate value, ($a = 700$nm). It is clear that the oscillations related to single annular holes previously found for $\phi = 0^o$ appear as a sum when a BE structure is built up. Finally, in Fig. 4.52 it is shown the dependance with the wavelength for $a = 800$nm.

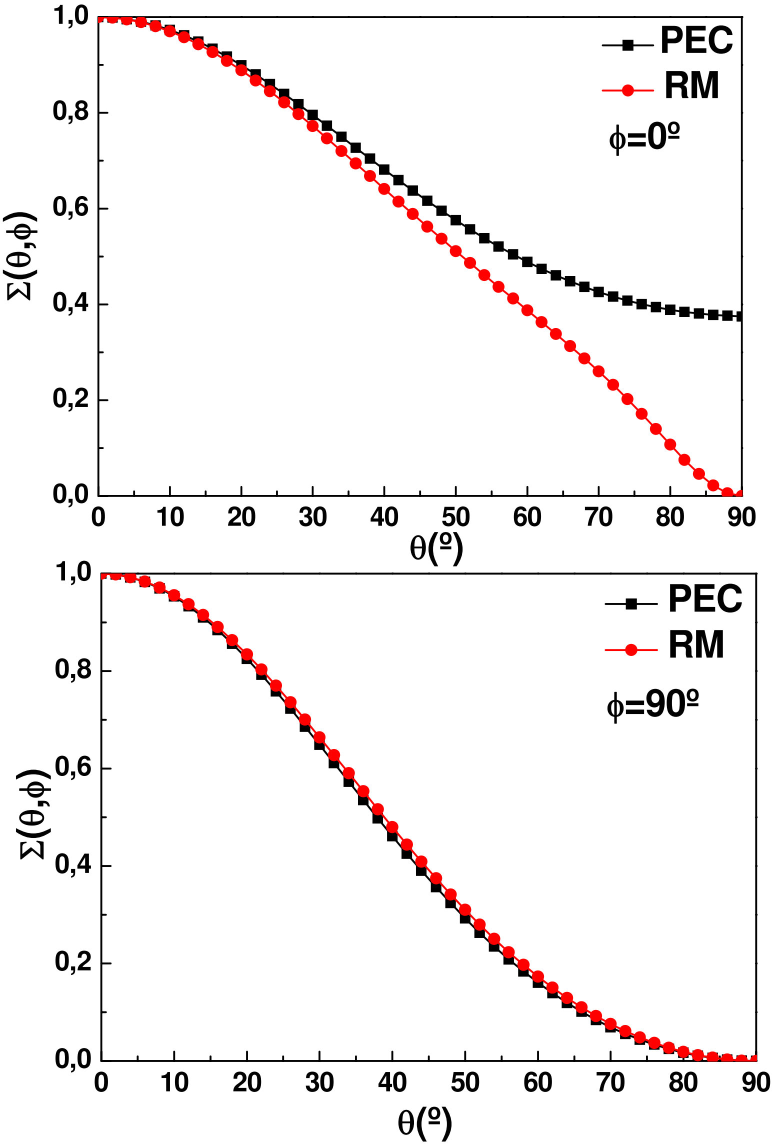

Figure 4.47: $\Sigma(\theta, \phi)$ of a single hole of radius $r_{out} = 190$nm perforated in a Au film with thickness h=100 nm as the zenithal angle at $\lambda = 630$nm. We compare the results for a PEC approximation (black line) and a real metal (RM, red line).

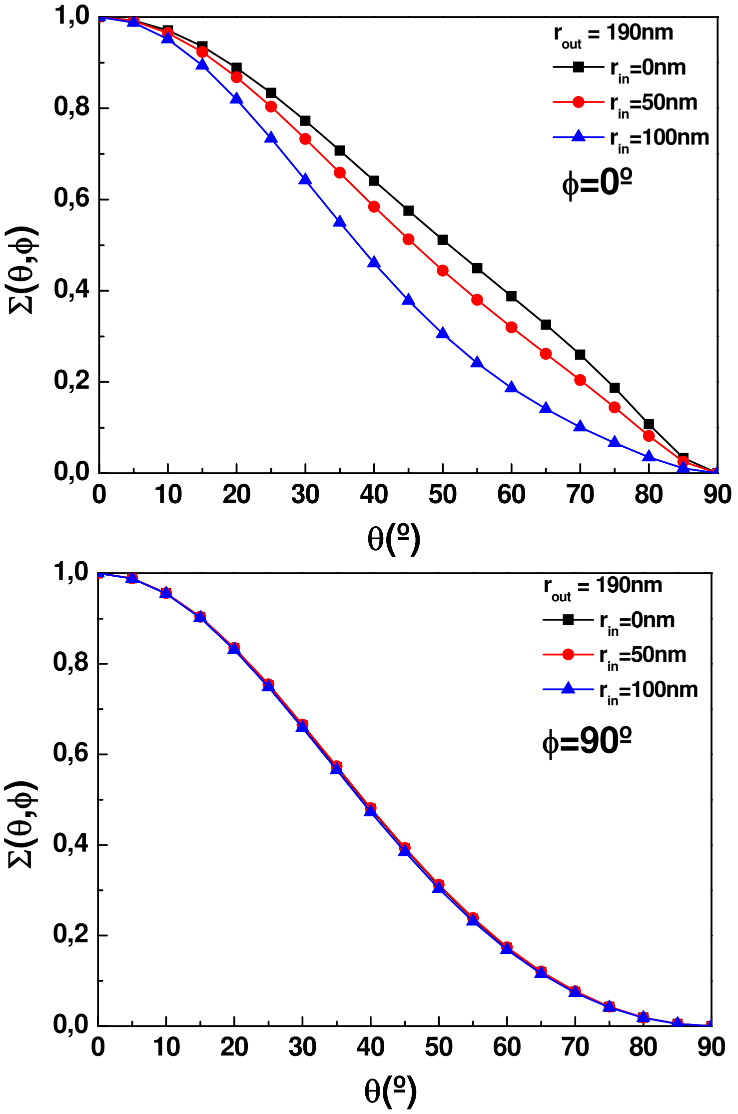

Figure 4.48: $\Sigma(\theta, \phi)$ of a single annular hole perforated in a Au film with thickness $h = 100$nm, at $\lambda = 630$nm. The external radius is fixed to $r_{out} = 190$nm, and the internal one is varied, $r_{in} = 0, 50, 100$nm. (a) $\phi = 0^o$ and (b) $\phi = 90^o$.

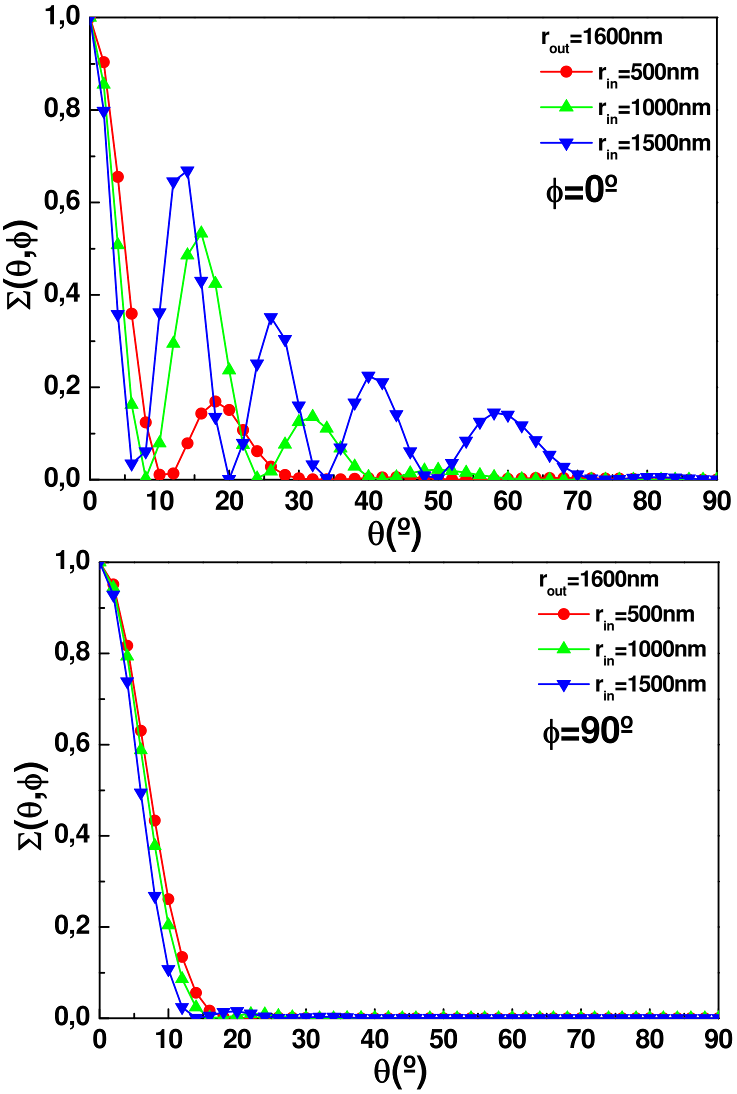

Figure 4.49: $\Sigma(\theta, \phi)$ of a single annular hole perforated in a Au film with thickness $h = 100$nm, at $\lambda = 630$nm. The external radius is fixed to $r_{out} = 1600$nm, and the internal one is varied, $r_{in} = 500, 1000, 1500$nm. (a) $\phi = 0^o$ and (b) $\phi = 90^o$.

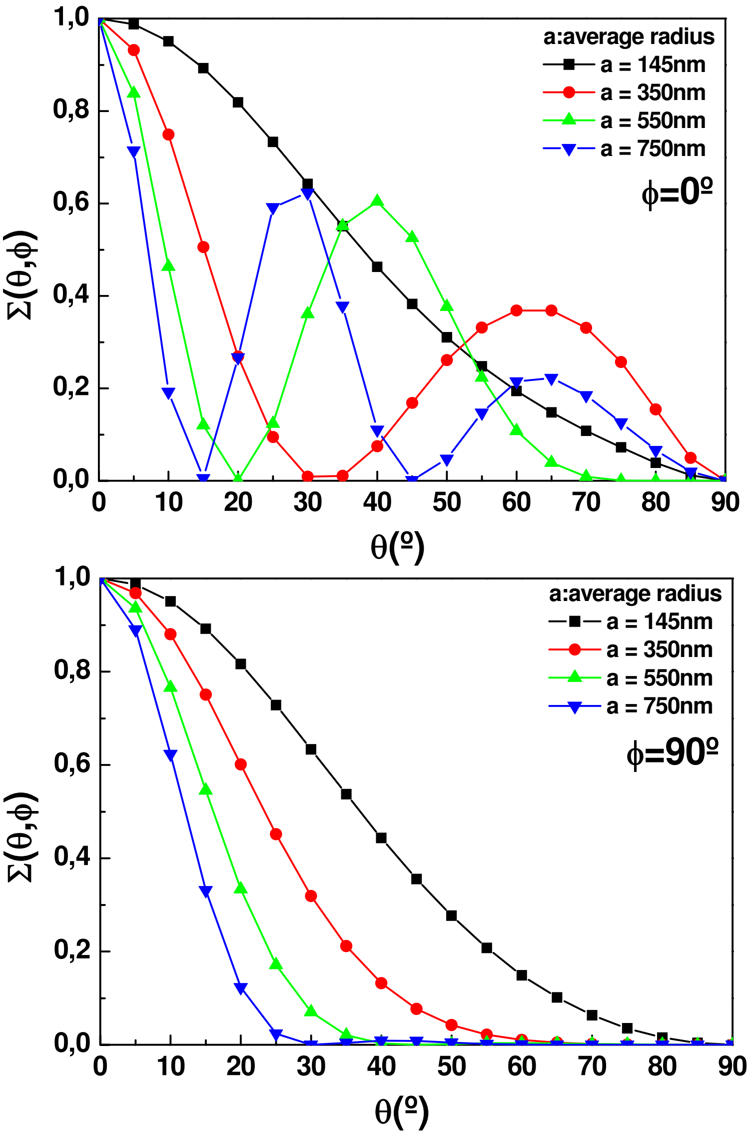

Figure 4.50: $\Sigma(\theta, \phi)$ of a single annular hole perforated in a Au film with thickness $h = 100$nm, at $\lambda = 630$nm. The hole width is fixed to $w = 150$nm, and the average radius is varied, $a = 145, 350, 550, 750$nm.

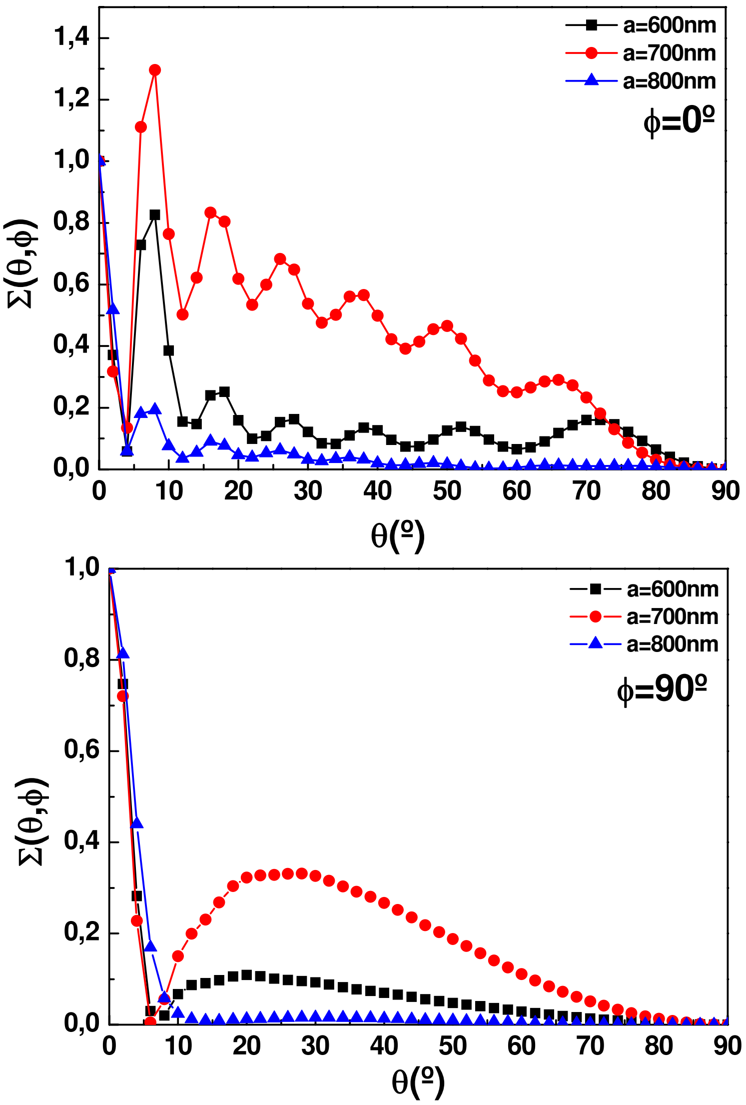

Figure 4.51: $\Sigma(\theta, \phi)$ bull's eye with $N = 6$ annular grooves, $h = 280$nm, $h_g = 90$nm, $w_g = 220$nm, $p = 600$nm, and $r_c = 125$nm, drilled at both sides of a gold film of 250nm thickness in a free standing system, at $\lambda = 630$nm. The dependance with the distance of the first annular groove to the centre of the structure, a, is presented.

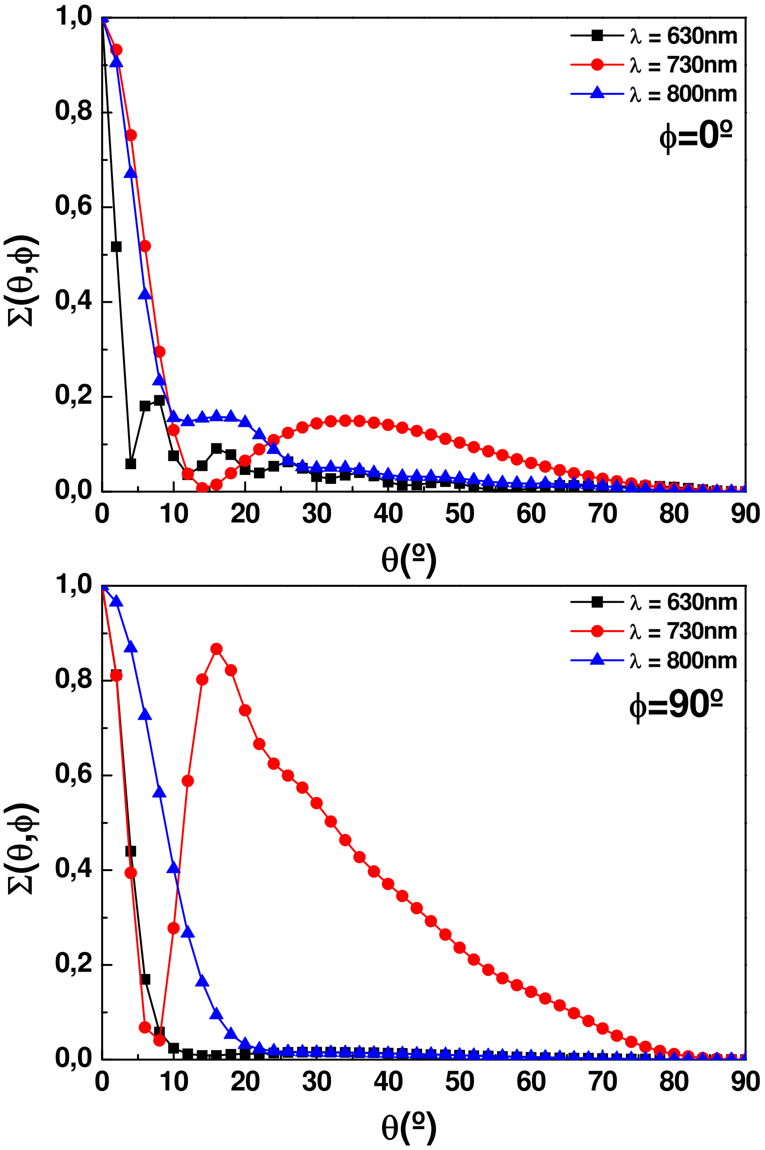

Figure 4.52: $\Sigma(\theta, \phi)$ for the same system as in Fig.4.51 at a = 800nm, as a function of the wavelength.

4.4 Conclusions

We have studied single annular and circular holes in order to get physical insight in the optical properties of these systems. We have found that annular holes present a Zero-order Fabry-Perot resonance related to the TE_{11} mode whose intensity may be 3 times the intensity of a circular hole with the same outer radius. Filling these systems with a dielectric constant $\varepsilon_2 > 1$ enhances the normalized-to-area transmittance a factor ε_2, since the cross section of the hole remains invariant but the area can be reduced by a factor ε_2.

Also BE structures have been analyzed and optimized in different spectral wavelengths, for different number of grooves, and tackling the problem from different points of view. Despite the EM properties of each annular groove depend on its average radius, we have found scaling laws to design optimized BE structures where all the geometrical parameters defining the system are contained.

In particular, we have studied the optical transmission in BE structures as a function of the distance between the central hole and its nearest groove, a_1, in the case when all groove depths and widths are subwavelength. We have shown that the transmittance presents maxima for given values of a_1 and wavelength, which are due to constructive interference of the light reemitted by grooves (which in that case behave almost independently) into the central hole. This reemitted light is in the form of surface plasmons. Furthermore, each groove acts as two connected cavities and, for fully explaining the transmittance spectra, the reflection by one cavity of the surface plasmon radiated by the other cavity must be taken into account. We have shown that the amplitude for coupling of incident radiation into a groove increases with groove radius, while the reflection coefficient of a groove for surface plasmons does not. These ingredients have been combined to give a simple Huygens-Fresnel view of the total coupling and reflection of light by the groove array. Our results show that there is not a direct correspondence between field enhancement at the surface and transmission enhancement, as there are resonances in the groove array that do not lead to strong re-illumination at the central hole.

Finally, the far-field angular intensity distribution of a single aperture and BE structures where the exit side is also corrugated have been studied as well.

Chapter 5

Localized Extraordinary Optical Transmission

5.1 Introduction

During the last decades, there has been an increasing interest in transmission resonances through holes drilled in metal films. Broadly speaking, we can sort them into two kinds of resonances, those associated to surface modes, and those identified with localized modes.

The first ones appear in hole arrays and lead to Extraordinary Optical Transmission (EOT) [23], as we have seen in Chapter 3. These resonances appear close to the periodicity of the array, $\lambda_R \approx p$, in optically thick metal films (that is, when the skin depth (δ) is smaller than both the film thickness (h) and the incident wavelength: $\delta < h < \lambda$). They were theoretically described as a resonant interplay between Surface Plasmon Polaritons (SPPs) at each side of the metal surface evanescently coupled through the holes [108]. Also EOT in optically thin metal films ($h \geq \delta$), where transmission may occur through both the holes and the metal layer, has been reported as well. In this case, the coupling of light with Short-Range Surface Plasmons red-shifts the EOT peak to wavelengths larger than the periodicity of the array [151].

The second kind of resonances can be identified with localized modes. Essentially, these are Fabry-Perot resonances, and we have also characterized them in the case of annular holes in Chapter 3 and Chapter 4. For a symmetric and uniform dielectric environment (the dielectric constant is the same in all non-metallic regions), the spectral location of λ_R occurs at approximately the cutoff wavelength of the apertures, λ_c [44–47, 59, 76, 112–115]. They have been attributed to the tunneling of light through the fundamental waveguide mode inside the holes (the least decaying one), and their appearance could be expected since the modulus of the propagating constant of such mode is almost negligible close to λ_c. Therefore, the field inside the holes does not experience a strong decay, photons spend a long time in the system, and transmission resonances could eventually take place. This localized resonance forms the basis for Frequency-Selective Surfaces (FSSs), which are designed for operating close to this resonance [152]. FSSs are 2D arrays of planar metallic scatterers or slots (usually with complex shapes) drilled in very thin metal screens, $\delta < h << \lambda$, so the thickness dependance of λ_R is not an issue. It is the shape and size of the planar scatterers/slots what control the frequency dependence of transmission and/or reflection coefficients. It has been demonstrated as well that ultranarrow plasmonic waveguide channels operating near λ_c may support an anomalous transmission resonance, almost independent of the total length or shape of this channel [153]. This result is originally inspired from systems filled with Epsilon Near Zero (ENZ) [154].

However, the *precise* spectral position of this localized resonance is not known. Recent studies and experiments of near field enhancement [155, 156] and enhanced transmission [157, 158] through isolated apertures in combination with dielectric substrates, have been developed in the terahertz (THz) regime, showing unexpected red-shifts of the near field and transmission resonances. In particular, the influence of a dielectric substrate in the electric near-field resonance of a small aperture have been numerically and experimentally studied [155, 156], and also the effect of a substrate on the transmission resonance of a rectangular aperture in a thin metal film has been theoretically reported as well [155–158].

In this chapter we go beyond the numerical study, providing a detailed description and analytical expressions for the location of this transmission resonance by localized modes, for both hole arrays and single holes. We will show that the position of the maximum is controlled by a new length-scale, λ_0, associated to all apertures of any shape provided they support large λ_c. In particular, to show the phenomenon, we will study annular and rectangular holes. Both symmetric dielectric configurations (where the dielectric constant of the cover, ε_1, and the substrate, ε_3, are the same), and asymmetric ones ($\varepsilon_1 \neq \varepsilon_3$), are considered. We also show that different combinations of the dielectrics outside and inside the apertures (ε_2) may blue- or red-shift the transmission resonance. Calculations are performed with the Coupled Mode Method (CMM) (described in Chapter 2) under the perfect electrical conductor (PEC) approach. Therefore, our results are exact in the THz and microwave regime, but we will also demonstrate that they are qualitatively valid in the optical regime as well (where Finite Difference Time Domain (FDTD) calculations have been conducted to validate our analytical results).

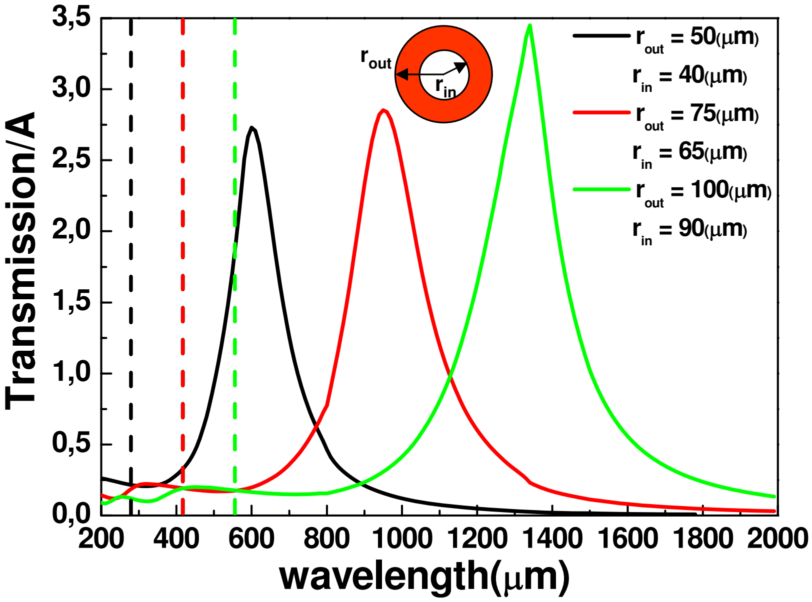

Figure 5.1: Transmission spectra through a metal film of $h = 0.2\mu$m, pierced with single annular holes of inner (r_{in}), and outer (r_{out}) radius defined in the labels, in an asymmetric configuration with $\varepsilon_1 = \varepsilon_2 = 1.0$, and $\varepsilon_3 = 11$. Vertical dashed lines represent the cutoff wavelength, $\lambda_1 = 282\mu$m, $\lambda_2 = 439\mu$m, and $\lambda_3 = 596\mu$m.

5.2 Motivation

Let us first introduce the phenomenon with several calculations. We consider different hole shapes, symmetric and asymmetric dielectric environments, isolated apertures and arrays of holes. In all cases we consider a PEC in the THz regime drilled with holes (see schematics on top of Fig. 5.2), and illuminated at normal incidence (the electric field points parallel to the x-direction).

Figure 5.1 shows transmission spectra for isolated annular holes drilled in a metal screen of $h = 0.2\mu$m thickness, in an asymmetric configuration with $\varepsilon_1 = \varepsilon_2 = 1.0$, and $\varepsilon_3 = 11$, for different inner and outer radius (see labels in the figure). For all the rings, it is found a resonance strongly red-shifted compared to the cutoff wavelength, indicated with dashed lines in each case.

Panels (a) and (b) in Fig. 5.2 depict transmission calculations through a $h = 1\mu$m thin film drilled with rectangular holes ($a_x = 10\mu$m and $a_y = 350\mu$m), as a function of the dielectric constant, in symmetric configurations (with $\varepsilon_1 = \varepsilon_3 = \varepsilon$ and $\varepsilon_2 = 1.0$), for both hole arrays (with period $p = 400\mu$m) (a), and single holes (b). In the contour plots, we observe in both panels a resonance that neither follows the Wood's anomaly condition ($\sqrt{\varepsilon}p$) in the case of the array, nor the cutoff wavelength ($\lambda_c = 2a_y = 700\mu$m), and indeed, for

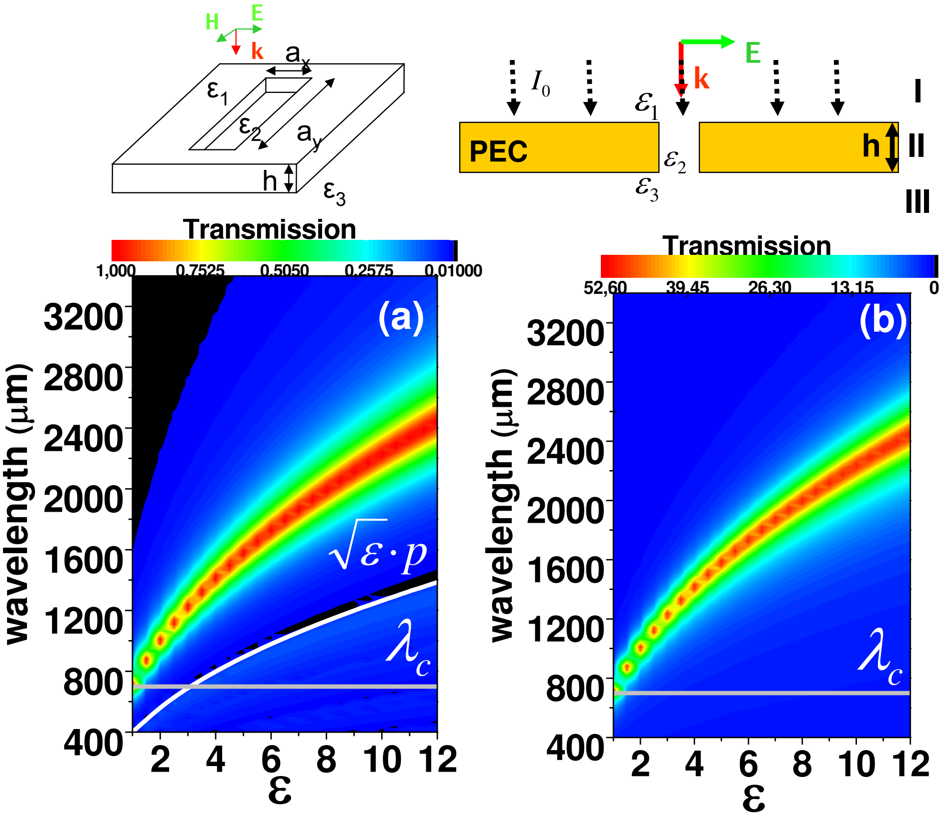

Figure 5.2: Panels (a) and (b) depict transmission of light through a metallic film of $h = 1\mu$m, pierced with rectangular holes ($a_x = 10\mu$m and $a_y = 350\mu$m) with $\varepsilon_2 = 1.0$, as a function of the incident wavelength and the dielectric constant $\varepsilon = \varepsilon_1 = \varepsilon_3$, for an array (with periodicity $p = 400\mu$m) and a single hole, respectively. Horizontal grey line represents the cutoff wavelength $\lambda_c = 2a_y = 700\mu$m, and white line in the array shows $\sqrt{\varepsilon}p$.

the set of parameters considered, these resonances appear beyond λ_c. The fact that these transmission resonances appear in both hole arrays and single holes indicates that the EM modes responsible for the resonances are localized.

5.3 Theoretical Formalism

Once the phenomenon is introduced, and in order to study the origin of this strong red-shift of λ_R, we briefly remindthe fundamentals of the CMM (extensively described in Chapter 2). We we will fit to a minimal model where accurate results for transmittance can be achieved by considering only the fundamental waveguide mode inside each aperture [56].

We remind here the set of linear equations for the modal amplitudes E_n and E'_n, which describes the behavior of the EM fields at the illumination and transmission regions:

$$\left\{ \begin{array}{rr} (G^I - \Sigma)E - G_\nu E' = & I_0 \\ (G^{III} - \Sigma)E' - G_\nu E = & 0 \end{array} \right. \tag{5.1}$$

The solution is given by:

$$\left\{ \begin{array}{rc} E = & \dfrac{(G^I - \Sigma)}{(G^+ - \Sigma)^2 - G_\nu^2 - (G^-)^2} I_0 \\ E^{'} = & \dfrac{G_\nu}{(G^+ - \Sigma)^2 - G_\nu^2 - (G^-)^2 \, I_0} \end{array} \right. \tag{5.2}$$

We also remind that, in the above expressions, I_0 accounts for the external illumination impinging directly on the holes and it measures the overlap between the incident plane wave and the fundamental mode inside the hole; Σ represents the light that comes back to the aperture after bouncing back and forth inside the cavities, and the term G_ν is linked to the coupling of EM fields at the two sides of the film through the holes. Analytical expressions for all these quantities can be found in Chapter 2.

Green's functions $G^I(\lambda, \varepsilon_1)$ and $G^{III}(\lambda, \varepsilon_3)$ represent *effective admittances* (in regions I and III, respectively) that account for the EM coupling between the aperture and the external radiation as seen by the holes. We have defined $G^+ = \left(G^I(\lambda, \varepsilon_1) + G^{III}(\lambda, \varepsilon_3)\right)/2$ and $G^- = \left(G^I(\lambda, \varepsilon_1) - G^{III}(\lambda, \varepsilon_3)\right)/2$. The general expression for hole arrays can be written as

$$G^{I,III} = i \sum_{\mathbf{k}\sigma} Y_{\mathbf{k}\sigma}^{I,III} \left| S_{\mathbf{k}\sigma} \right|^2 \tag{5.3}$$

where $Y^{I,III}_{\mathbf{k}s} = k_z/g$, $Y^{I,III}_{\mathbf{k}p} = g\,\varepsilon_{1,3}/k_z$, $k_z = \sqrt{g^2\,\varepsilon_{1,3} - k_{||}^2}$, and $g = 2\pi/\lambda$ is the modulus of free space wavevector. The overlaps are defined as an integral over the hole shape $S_{\mathbf{k}\sigma} = \int dr_{||}\vec{V}_\sigma \cdot \vec{E}_{||}(r_{||}) \cdot e^{i\vec{k}_{||}\vec{r}_{||}}$, being the bi-vectors $\vec{V}_p = (k_x, k_y)/k_{||}$, $\vec{V}_s = (-k_y, k_x)/k_{||}$ and $k_{||}^2 = k_x^2 + k_y^2$.

In the expression of G for hole arrays, $\mathbf{k}$ runs over the reciprocal lattice vectors, whereas for isolated holes the sum over $\mathbf{k}$ must be substituted by an integral $1/(2\pi)^2 \int d\mathbf{k}$. The imaginary part of the Green's function (G_i) originates from the coupling with radiative modes, whereas the real part (G_r) is related to the coupling of the aperture with evanescent modes.

An important property of the Green's function is how it transforms when the radiation region has $\varepsilon > 1$ [60]:

$$G(\lambda, \varepsilon = 1) = G(\sqrt{\varepsilon}\lambda, \varepsilon)/\sqrt{\varepsilon} \tag{5.4}$$

Finally, transmission can be written in terms of the modal amplitudes of the electric field as [56,59,60,62]:

$$T = \frac{1}{\sqrt{\varepsilon_1}} G_\nu Im\left[E^* \cdot E'\right] = \frac{1}{\sqrt{\varepsilon_1}} G_i^I \left|E'\right|^2 \tag{5.5}$$

5.4 Symmetric Configurations, $\varepsilon_1 = \varepsilon_3$

Due to the fact that the phenomenon here investigated is found in both hole arrays and single holes (i.e., the EM modes responsible for the resonance are localized), for simplicity we will concentrate on the study of isolated apertures, since then we do not have the lattice resonance.

Let us now investigate the spectral location of maximum transmission in symmetric configurations ($\varepsilon_1 = \varepsilon_3 = \varepsilon$).

In this case, $G^I = G^{III} = G$ and $G^- = 0$. We can first develop Eq. 5.5 to find an explicit expression for the transmittance. We rewrite the modal amplitudes as:

$$E = \frac{I_0}{2}(A_+ + A_-) \tag{5.6}$$

$$E' = \frac{I_0}{2}(A_- - A_+) \tag{5.7}$$

where we have defined $A_+ \equiv 1/(G - \Sigma + G_\nu)$ and $A_- \equiv 1/(G - \Sigma - G_\nu)$. With this new nomenclature,

$$\left[E^{*}E^{'}\right] = \frac{|I_0|^2}{4} \cdot \left[|A_-|^2 - |A_+|^2 - 2iIm(A_+A_-^*)\right] \tag{5.8}$$

so that:

$$T = -\frac{|I_0|^2}{2\sqrt{\varepsilon_1}}\left[Im(A_+A_-^*)\right]G_\nu \tag{5.9}$$

Finally, replacing the expressions of A_+ and A_-, we obtain:

$$T = \frac{|I_0|^2}{\sqrt{\varepsilon_1}} \frac{G_i\,|G_\nu|^2}{\left[|G-\Sigma|^2 - |G_\nu|^2\right]^2 + 4G_i^2\,|G_\nu|^2} \tag{5.10}$$

It has been already demonstrated that for resonant systems such as apertures with large λ_c [48, 59, 88, 129] (e.g., rectangles, annular holes, or circular holes filled with $\varepsilon_2 > \varepsilon_1, \varepsilon_3$, systems that fulfil the condition $\lambda_c > \sqrt{Area}$), transmission maxima associated to Fabry-Perot modes, appear when the EM energy at the entrance and exit sides of the apertures are equal [59], i.e., $|E| = \left|E^{'}\right|$, or equivalently, $|G - \Sigma| = |G_\nu|$.

For resonant holes, $G_r >> G_i$, since $G_i \propto Area/\lambda^2$ and $G_r \propto \lambda/Area$ (see Ref. [60] for further details). Therefore, when $G_r >> G_i$, Eq. 5.10 has the same form as that of a damp oscillator where the resonant frequency is hardly affected by the damping. If we now replace the last condition in Eq. 5.10, we retrieve the expression appearing in Ref. [59] for transmission at λ_R with $\varepsilon = 1$:

$$T_R = \frac{|I_0|^2}{4G_i} \tag{5.11}$$

Interestingly, G_i controls the intensity of transmission resonances, and G_r their spectral location, as it was also demonstrated in the same reference:

$$2G_r = \frac{|G|^2 - Y_{TE}^2}{Y_{TE}}\tan(q_z h) \tag{5.12}$$

Here $Y_{TE} = q_z/g$ and q_z is the propagating constant inside the apertures. Note that in this reference it was reported that transmission maxima associated to Fabry-Perot modes ($q_z = 0$) occurred *at around* the cutoff wavelength irrespective of the geometrical parameters and h.

Now we go a step further and study the spectral location of λ_R as a function of h and with a dielectric environment $\varepsilon > 1$, two elements that, as we will see next, originate the strong red-shifts observed in both Ref. [157, 158], and in the illustrative studies appearing in Fig. 5.1 and Fig. 5.2in this paper.

In order to get deeper physical insight, it is convenient to define the following change of variables:

$$\begin{cases} E_S = & \frac{1}{\sqrt{2}}\left(E - E^{'}\right) \\ E_A = & \frac{1}{\sqrt{2}}\left(E + E^{'}\right) \end{cases} \tag{5.13}$$

so that Eq. 5.1 can be written as an equivalent system of uncoupled equations in terms of two well defined transmission channels, one symmetric (E_S), when the electric field at the entrance and at the exit of the apertures point at the same direction ($E = -E^{'}$); and one antisymmetric (E_A), in different directions ($E = E^{'}$):

$$\begin{cases} (G + Y_S)E_S = & \tilde{I} \\ (G + Y_A)E_A = & \tilde{I} \end{cases} \tag{5.14}$$

Here $Y_S \equiv -(\Sigma - G_\nu)$ and $Y_A \equiv -(\Sigma + G_\nu)$ are effective admittances, and $\tilde{I} = I/\sqrt{2}$.

It is important to remark that Σ and G_ν depend on the product $(q_z h)$ as

$$\begin{aligned} \Sigma &= i\frac{q_z}{g} \cdot \frac{e^{iq_z h} + e^{-iq_z h}}{e^{iq_z h} - e^{-iq_z h}} \\ G_\nu &= 2i\frac{q_z}{g} \cdot \frac{e^{2iq_z h}}{e^{2iq_z h} - 1} \end{aligned} \tag{5.15}$$

Within the new formulation, the resonant condition [59] ($q_z \to 0$) provides $Y_A \to \infty$. This means that, except in "extraordinary" cases (close to the Rayleigh wavelength, when $G \to \infty$), E_A is not excited. In fact, it is in the limit of very thin films, when only the symmetric transmission channel E_S remains, whereas the asymmetric one $E_A \to 0$.

This is easy to understand because, taking into account that the asymmetric channel is characterized by electric fields at the entrance and at the exit of the apertures pointing at opposite directions, in thin films, there is no enough optic path for the EM field to flip direction.

Therefore, the limit for thin films ($h \to 0$) is equivalent to the limit $q_z h \to 0$, or more importantly, equivalent to $q_z \to 0$, that is, close to λ_c. Consequently,

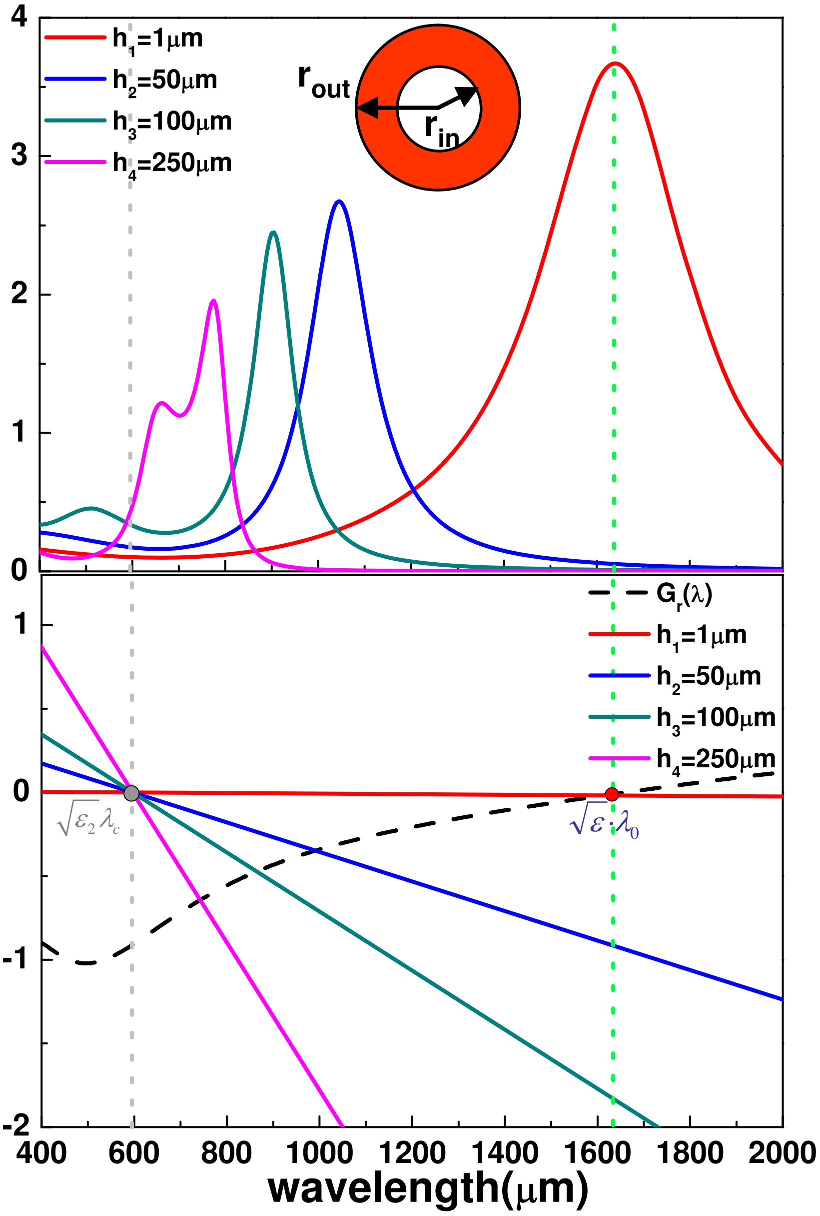

Figure 5.3: (Top) Transmission spectra of an isolated annular hole ($r_{in} = 90\mu$m, $r_{out} = 100\mu$m) drilled in a PEC of different film thickness h (see labels in the figure), in a symmetric configuration with $\varepsilon_1 = \varepsilon_3 = 9$ and $\varepsilon_2 = 1$. (Bottom) For the same system as in the upper panel, the dashed line depicts G_r as a function of the incident wavelength, and straight lines correspond to the condition $\frac{2\pi h}{\lambda_c^2}\left(\sqrt{\varepsilon_2}\lambda_c - \lambda\right)$ in Eq. 5.17, for each h value.

for thin metal films and/or close to the cutoff wavelength, provided that G does not diverge, only the equation for the symmetric channel remains $(G+Y_S)E_S = \tilde{I}$, and since $E_S/\sqrt{2} = E$, transmission can be written as:

$$T_{approx} \approx \frac{|I_0|^2}{4\sqrt{\varepsilon}} \frac{G_i}{|G+Y_S|^2} \tag{5.16}$$

with $Y_S = \frac{-hq_z^2}{2g}$.

Clearly, resonances in transmission will be given by minima in the denominator of Eq. 5.16. Because $G_i << G_r$ and $Im(Y_S) = 0$, zeroes in the denominator occur at $Re(G+Y_S) = 0$.

Close to the cutoff, the propagation constant is $q_z \approx \sqrt{\varepsilon_2(g-g_c)}$ and replacing this value in Y_S we obtain an implicit equation for the resonant wavelength ($\lambda_R = 2\pi/g_R$) that can be solved graphically:

$$-G_r(\lambda_R) \equiv \frac{2\pi h}{\lambda_c^2} \left(\sqrt{\varepsilon_2}\lambda_c - \lambda_R\right) \tag{5.17}$$

Note that in the expression above, λ_c is the cutoff wavelength of an empty hole ($\varepsilon_2 = 1.0$), we are considering $\varepsilon = 1.0$, and we have taken $g_R^2 - g_c^2 \approx 2g_R(g_R - g_c)$. Adding a dielectric constant different from unity in the cover and substrate, and using Eq. 5.4, eventually leads to an implicit equation of the same form as that given by Eq. 5.17.

Let us now solve graphically Eq. 5.17 with $\varepsilon \geq 1$:

An essential ingredient entering the condition for resonances in Eq. 5.17 appears in the left hand side of the equation, $G_r(\lambda)$. This function can take either negative or positive values. The sign and values of G_r depend on the relative contribution of p-polarized (which is negative and dominates at $\lambda \to 0$) and s-polarized (which is positive and dominates at $\lambda \to \infty$) waves. Therefore, there exist a wavelength where the two contributions cancel each other, i.e., the real part of the effective admittance, cancels. We define this wavelength as $G_r(\lambda_0) = 0$ in vacuum, or, using Eq. 5.4, $G_r(\sqrt{\varepsilon}\lambda_0) = 0$ in a dielectric environment. In uniform systems, this wavelength usually appears close to λ_c, but in general, $\lambda_0 \neq \lambda_c$. According to Babinet's principle, rectangular holes and its complementary shape resonate at $\lambda_R \approx 2a_y$, but bearing in mind that Eq. 5.17 is valid for any hole shape, we did not find a general expression for $\lambda_0 \approx \lambda_c$.

The right hand side of the equation represents straight lines whose slopes are given by the film thickness, h. According to Eq. 5.17, the intersection of these straight lines with $G_r(\lambda)$ gives the position of the resonant wavelengths,

λ_R, for each h value.

As an illustration, we consider a system with a single annular hole drilled in a PEC. In the lower panel in Fig. 5.3 we show the graphical solution of Eq. 5.17 for different h values, and in the upper one, the corresponding transmission spectra. In this case, the geometrical parameters are $r_{in} = 90\mu$m, $r_{out} = 100\mu$m ($\lambda_c = 596\mu$m), and we have taken $\varepsilon = 9$, $\varepsilon_2 = 1$.

As we can see in the graphical solution in Fig. 5.3, in the limit of very thick films two resonances emerge, one associated to the symmetric channel, and one to the asymmetric one. For the symmetric mode we observe that when the slope of the straight line tends to infinity ($h \to \infty$), the intersection with $G_r(\lambda)$ occurs at $\lambda_R^H = \sqrt{\varepsilon_2}\,\lambda_c$, where capital H in the superscript stands for *thick* films.

In contrast, in the limit of very thin films, only the symmetric channel is excited and there is just one transmission peak. In this limit, the slope of the straight line tends to zero ($h \to 0$) and $G_r(\lambda_R^h) = 0$, being $\lambda_R^h = \sqrt{\varepsilon}\,\lambda_0$. Here, h stands for *thin* films. This result where localized resonances are expected to emerge when the real part of the effective admittance cancels, is in agreement with the results reported in Ref. [159] where, from a circuit theory perspective, localized resonances are attributed to the condition of zero admittance.

Note the strong red-shift found for the set of parameters chosen: in the figure, $\lambda_c = 596\mu$m, and in the case of $h_1 = 1\mu$m, the resonance in transmission appears at $\lambda_R \approx 1700$nm $>>$ λ_c. This shift may appear surprising, but in fact, it can be easily understood as if we were considering the hole as a small perturbation where ε_2 is hardly seen by the system. Interestingly, if a system is designed for operating close to λ_c, but thin films in combination with high dielectric constants are involved, the spectral window where the resonance actually takes place may be red-shifted several microns compared to the expected location at λ_c.

To further illustrate this finding, Fig. 5.4 shows the resonant wavelength of the symmetric mode obtained through the analytical approximation (λ_R) given by Eq. 5.17, and the exact position of the maximum transmission (λ_{MaxT}) calculated with the CMM, as a function of h, for an isolated rectangular hole ($a_x = 10\mu$m and $a_y = 350\mu$m), with $\varepsilon = 12$, and $\varepsilon_2 = 1$. Clearly, the agreement between the two curves indicates that Eq. 5.17 provides the resonant wavelength for any film thickness, and the analytical expressions in the limit of thin (h) and thick (H) films are:

$$\begin{aligned} \lambda_R^h &= \sqrt{\varepsilon}\,\lambda_0 \\ \lambda_R^H &= \sqrt{\varepsilon_2}\,\lambda_c \end{aligned} \tag{5.18}$$

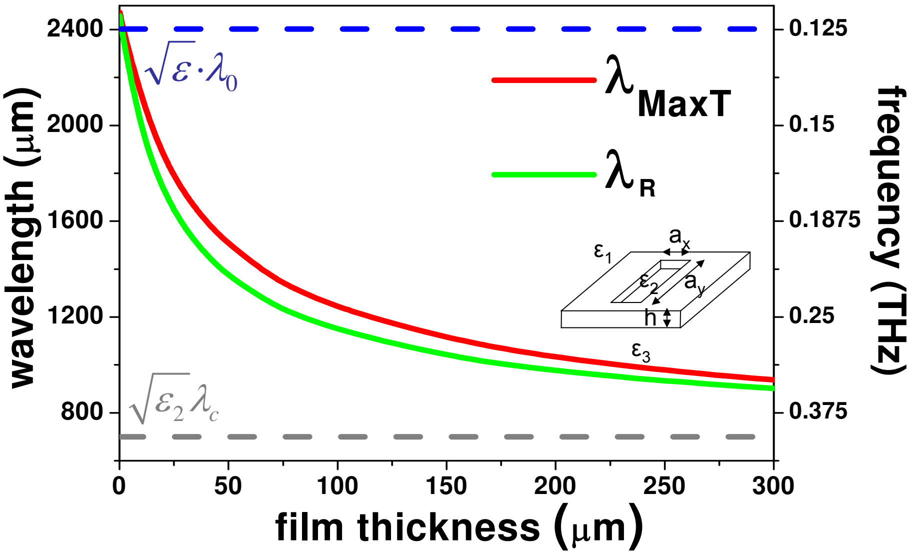

Figure 5.4: Spectral wavelength of the transmission resonance as a function of the film thickness of an isolated rectangular hole ($a_x = 10\mu$m and $a_y = 350\mu$m) with $\varepsilon = 12$, and $\varepsilon_2 = 1$. The red curve depicts exact calculations with the CMM, and the green one depicts the result obtained through the analytical approximation given by Eq.5.17.

From an intuitive picture, we can describe this phenomenon as follows: for thick films the resonance is governed by the properties of the waveguide (represented by λ_c), while for very thin films it is governed by the coupling of the hole to the radiative regions (characterized by λ_0).

Another important feature to consider when dealing with these systems composed of very thin films and dielectrics is the intensity at λ_R^h.

Equation 5.16 can be further approximated in the case of extremely thin films ($h << \lambda/2$), providing the intensity at the resonant wavelength for the symmetric mode (E_S):

$$T_{thin} \approx \frac{|I_0|^2}{4\sqrt{\varepsilon_1}} \frac{G_i}{(G_i)^2 + (G_r)^2} \tag{5.19}$$

Note that the above expression only contains information of the Green's functions. Interestingly, using Eq. 5.4, it is easy to demonstrate that

$$T_{thin}(\lambda; \varepsilon_2, \varepsilon = 1) = T_{thin}(\sqrt{\varepsilon}\lambda; \varepsilon_2, \varepsilon) \tag{5.20}$$

Therefore, the optical response of a perforated metallic thin film can be "rigidly" (blue- or red-) shifted a factor $\sqrt{\varepsilon}$ compared to the free standing system if it is embedded into an homogeneous dielectric environment of dielectric constant ε. In fact, the resonant wavelength will be given by $\lambda_R^h = \sqrt{\varepsilon/\varepsilon_2}\lambda_0$, so that, if $\varepsilon < \varepsilon_2$, the spectrum will be blue-shifted, whereas if $\varepsilon > \varepsilon_2$, then the spectrum will be red-shifted. For $\varepsilon = \varepsilon_2$, then the transmission peak will be located at λ_0.

This result will be numerically shown in Section 5.6, where hole arrays periodically arranged instead of single holes, are considered.

5.5 Asymmetric Configurations, $\varepsilon_1 \neq \varepsilon_3$

Next, we will consider asymmetric configurations, where $\varepsilon_1 \neq \varepsilon_3$. We will follow the same reasoning as in Section 5.4.

Within this new dielectric configuration, we can develop the theory again, and with the key observation that $G^- << G^+$, the exact expression for the transmission of light appearing in Eq. 5.10, can be approximated here as:

$$T \approx \frac{|I_0|^2}{\sqrt{\varepsilon_1}} \frac{G_i^I \, |G_\nu|^2}{\left[|G^+ - \Sigma|^2 - |G_\nu|^2\right]^2 + 4(G_i^I)^2 \, |G_\nu|^2} \tag{5.21}$$

Following the same procedure as in Section 5.4, in the limit $q_z h \to 0$, transmission reads:

$$T_{approx} \approx \frac{|I_0|^2}{4\sqrt{\varepsilon}} \frac{G_i^I}{|G^+ + Y_S|^2} \tag{5.22}$$

And for the location of the resonant wavelength, it is obtained:

$$-G_r^+(\lambda) \equiv \frac{2\pi h}{\lambda_c^2} \left(\sqrt{\varepsilon_2}\lambda_c - \lambda\right) \tag{5.23}$$

The last equation can also be solved graphically to get the peak location as a function of the film thickness. In Fig. 5.5 it is shown a similar calculation to that in Fig. 5.4, for the same system but with $\varepsilon_1 = \varepsilon_2 = 1$ and $\varepsilon_3 = 12$. Again, the resonant wavelength obtained through Eq. 5.23 and the exact calculations obtained with the CMM agrees very well.

Nevertheless, it is interesting to get analytical expressions for λ_R in the limits of thin and thick films, as we got for symmetric configurations. Clearly, for thick enough films, the resonant wavelength is also given by $\lambda_R^H = \sqrt{\varepsilon_2}\lambda_c$.

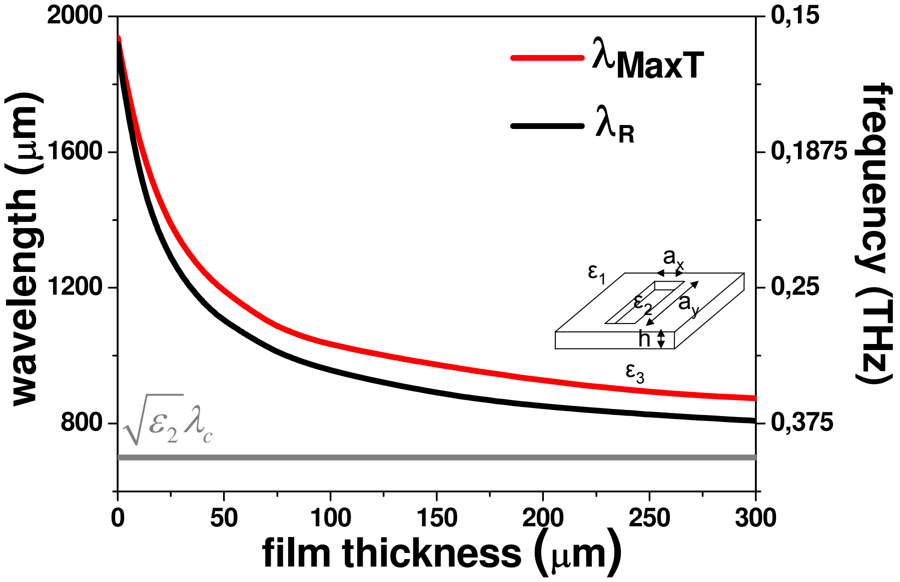

Figure 5.5: Similar calculations as those in Fig. 5.4 with $\varepsilon_1 = \varepsilon_2 = 1$ and $\varepsilon_3 = 12$, considering Eq. 5.23.

For thin films the resonant wavelength is also given by the condition $G_r^+(\lambda_R^h) = 0$, but getting an analytical expression for λ_R^h is not that easy. The main problem arises because G_r^+ does not transform with ε as G_r does in symmetric configurations:

$$G^+(\lambda;\varepsilon_1;\varepsilon_3) = \frac{G^I(\sqrt{\varepsilon_1}\,\lambda)}{\sqrt{\varepsilon_1}} + \frac{G^{III}(\sqrt{\varepsilon_3}\,\lambda)}{\sqrt{\varepsilon_3}} \tag{5.24}$$

The knowledge of λ_0 for a single interface is not sufficient to get the zeroes of G^+, so we need to know the whole dependance of G^I and G^{III}.

Fortunately, from the above property we can still obtain approximate explicit expressions for λ_R^h.

To do it, we first approximate linearly G^I and G^{III} around λ_0, what provides a simple analytical expression for the spectral location of transmission maximum as a function of ε_1, ε_3 and λ_0:

$$\lambda_R^{(1)h} = \frac{(\sqrt{\varepsilon_1} + \sqrt{\varepsilon_3})}{2}\lambda_0 \tag{5.25}$$

Interestingly, $\lambda_R^{(1)h}$ does not depend on the slope of G_r.

The result given by Eq. 5.25 is in agreement with the values reported by some authors working with FSSs [152]. In Fig. 5.6, we show in red the position

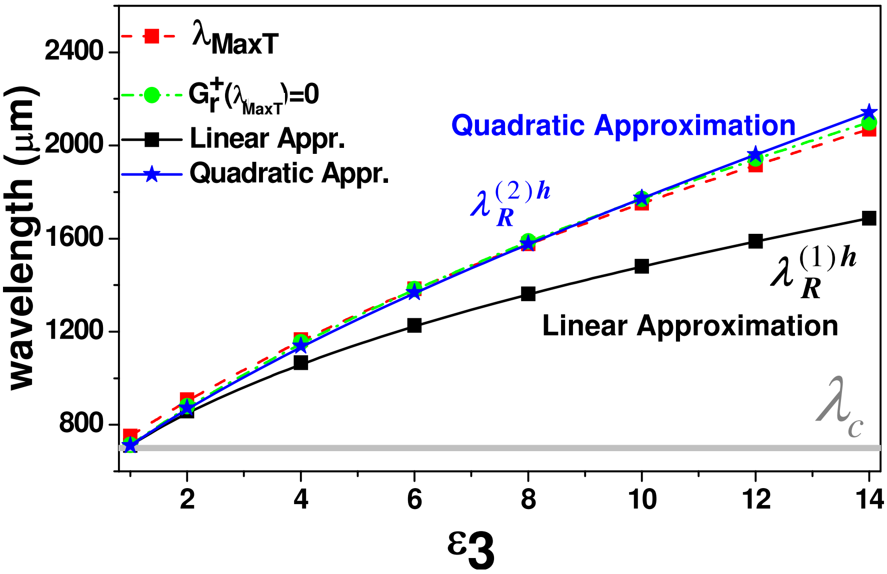

Figure 5.6: Position of transmission maximum as a function of ε_3 of an isolated rectangular hole ($a_x = 10\mu$m and $a_y = 350\mu$m) with $h = 1\mu$m and $\varepsilon_1 = \varepsilon_2 = 1$. The red curve corresponds to the exact calculations provided by the CMM, the green one shows the condition $G_r^+(\lambda_{MaxT}) = 0$, the black curve depicts calculations of λ_R obtained through Eq. 5.25, and the blue curve through Eq. 5.26.

of the maximum transmission calculated exactly with the CMM (λ_{maxT}), the condition $G_r^+(\lambda_{maxT}) = 0$ (green curve), and $\lambda_R^{(1)h}$ obtained through Eq. 5.25 (black curve) in a rectangular hole ($a_x = 10\mu$m and $a_y = 350\mu$m), with $\varepsilon_1 = \varepsilon_2 = 1$, and $h = 1\mu$m, as a function of the dielectric constant of the substrate, ε_3. Clearly, the condition $G_r^+(\lambda_R) = 0$ represents the condition of the maximum transmission, since both red and green curves in Fig. 5.6, coincide.

However, we observe that the linear approximation is rather good for small values of ε_3. This is because, as we can check in Fig. 5.3, Green's functions behaves almost linearly at $\lambda \approx \lambda_0$. But, the large shifts when high dielectric constants are considered, may bring λ_R very far from $G_r^+(\lambda_0)$, i.e., in principle, we should need all $G_r^+(\lambda)$ dependence and consider the curvature of this function at larger wavelengths.

We can improve this approximation and get some information from fitting $G_r^+(\lambda)$ to a quadratic function close to λ_0, with the form $G_r^+(\lambda, 1) \approx A(\lambda - \lambda_0) + B(\lambda - \lambda_0)^2$. After some algebra, we obtain a better analytical expression for the peak location that now depends on two constants, C and λ_0, as follows:

$$\lambda_R^{(2)h} = \frac{(\sqrt{\varepsilon_1}+\sqrt{\varepsilon_3})}{2}\lambda_0\left[1-\frac{(\sqrt{\varepsilon_1}-\sqrt{\varepsilon_3})^2}{\sqrt{\varepsilon_1\varepsilon_3}}(C\lambda_0)\right] \tag{5.26}$$

being $C = \frac{G_r{}''(\lambda_0;\varepsilon=1)}{2G_r{}'(\lambda_0;\varepsilon=1)}$ and with $G_r(\lambda_0;\varepsilon=1)=0$.

Note that, since $C \equiv A/B < 0$, Eq. 5.26 predicts larger shifts of λ_0 than Eq. 5.25. Additionally, C does not depend on either ε_1 or ε_3, but only on the geometry of the hole.

The blue curve in Fig. 5.6 depicts the calculations obtained for $\lambda_R^{(2)h}$ using Eq. 5.26. On the one hand, from the theoretical point of view, Eq. 5.26 is an analytical expression that predicts the position of the maximum transmission that depends on two constants, λ_0 and C, that can be calculated numerically. On the other hand, from the experimental point of view, the performance of two different experiments allows to fit these two constants that in turn, let predict the position of λ_R^h for any pair of ε_1 and ε_3 values, for a given hole shape. Remember that λ_0 is defined as the spectral location of transmission maximum in a thin film in a free standing system.

Therefore, the whole dependance with h, ε_1, ε_2, and ε_3 for transmission resonances can be obtained through Eq. 5.23 once λ_0 and C are known.

Finally, the same approximation done in Section 5.4 for extremely thin films can be taken for asymmetric systems, finding:

$$T_{thin} \approx \frac{|I_0|^2}{4\sqrt{\varepsilon_1}}\frac{G_i^I}{(G_i^+)^2+(G_r^+)^2} \tag{5.27}$$

5.6 Hole arrays

In this section we will show how the previous results found for isolated holes can also be applied to hole arrays. This theory will be valid provided that the localized resonance does not interfere with the excitation of surface modes, i.e., $\lambda_R >> \sqrt{\varepsilon}p$. In particular, in Fig. 5.7 we consider an array ($p = 400\mu$m) of rectangular holes ($a_x = 10\mu$m, $a_y = 350\mu$m) in a symmetric configuration ($\varepsilon_1 = \varepsilon_3 = \varepsilon$), drilled in a thin perfect metal of $h = 25\mu$m thickness. In this case we take $\varepsilon_2 = 4.0$, so $\lambda_c = 2a_y\sqrt{\varepsilon_2} = 1400\mu$n.

Upper panel shows three different transmission spectra for $\varepsilon = 2, 4, 6$ calculated using the expressions of T, T_{approx}, and T_{thin} given by Eq. 5.5, Eq. 5.16, and Eq. 5.27, respectively. The agreement of the three transmission curves confirm the validity of the approximations done.

Moreover, here it can be seen that the resonant wavelength can be blue-

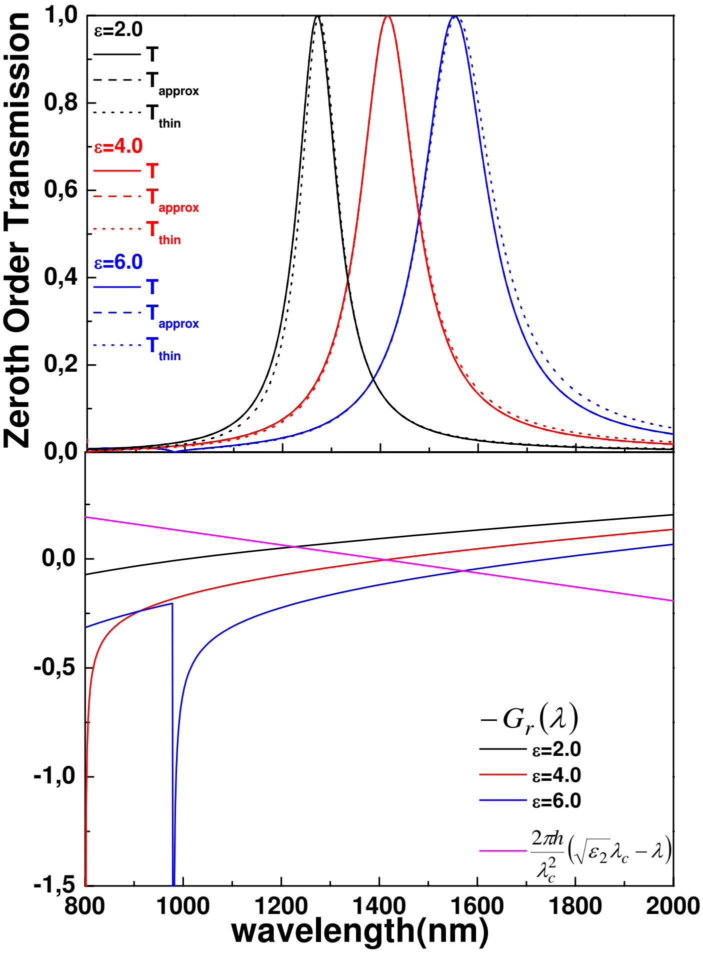

Figure 5.7: (Top) Transmission of light using Eq. 5.5, Eq. 5.16, and Eq. 5.19 (see labels) through a hole array ($p = 400\mu$n) with rectangles ($a_x = 10\mu$m, $a_y = 350\mu$m) drilled in a perfect metal of thickness $h = 25\mu$m and filled with $\varepsilon_2 = 4.0$. Symmetric configurations are considered: black curves corresponds to $\varepsilon = 2.0$, red curves to $\varepsilon = 4.0$, and green curves to $\varepsilon = 6.0$. (Bottom) For the same system as in the upper panel, $G_r(\lambda)$ for $\varepsilon_2 = 2.0, 4.0, 6.0$, and the condition $\frac{2\pi h}{\lambda_c^2}\left(\sqrt{\varepsilon_2}\lambda_c - \lambda\right)$ in Eq.5.17.

or red- shifted compared to λ_0 as a result of the combination of ε_2 and ε since $\lambda_R^h = \sqrt{\varepsilon/\varepsilon_2}\lambda_0$.

Finally, in the lower panel it is also shown the graphical solution of Eq.5.17 for these hole arrays where the divergencies in G_r that account for the excitation of surface modes appear at $\lambda << \lambda_R$.

5.7 Optical Regime

Finally, we show that the previous description in the THz regime, is *qualitatively* valid in the optical regime. Taking into account the finite dielectric constant of metals in the optical regime makes the analytical study with the CMM too complex to find compact expressions for λ_R.

Therefore, as an example and using the FDTD method, Fig. 5.8 shows the position of the maximum transmission of a single rectangular hole ($a_x = 50$nm, $a_y = 400$nm) drilled in a gold film, as a function of the film thickness. We observe that, as in the case of PECs, for thick enough films, transmission resonances appear close to the cutoff wavelength, whereas for thin enough films the peak position appears red-shifted compared to λ_c. Interestingly, once $h \approx 2$ skin-depths (~ 60nm), the resonant wavelength eventually blue-shifts as a result of the typical decaying behavior due to the direct transmission through the metal film. Note also that Short-Range Surface Plasmons are not here involved, since we are considering an isolated aperture.

5.8 Conclusions

We have developed a theory for transmission resonances aided by localized modes in the THz, for both hole arrays and single holes, and for any hole shape of large cutoff. We have shown that the maximum transmission presents large shifts as a function of both the metal thickness and the dielectric constants of the cover and the substrate. We provide analytical expressions for the peak position, which is controlled by the effective admittance of the cover and the substrate as seen by the holes, G^I and G^{III}. Finally, we have demonstrated that there are two different length scales related to thick or thin films that control the spectral wavelength, λ_c and λ_0, respectively. The first one represents the properties of the waveguides and it governs transmission resonances in thick films, while the second one characterizes the coupling of the hole to the radiative regions and it governs in thin films.

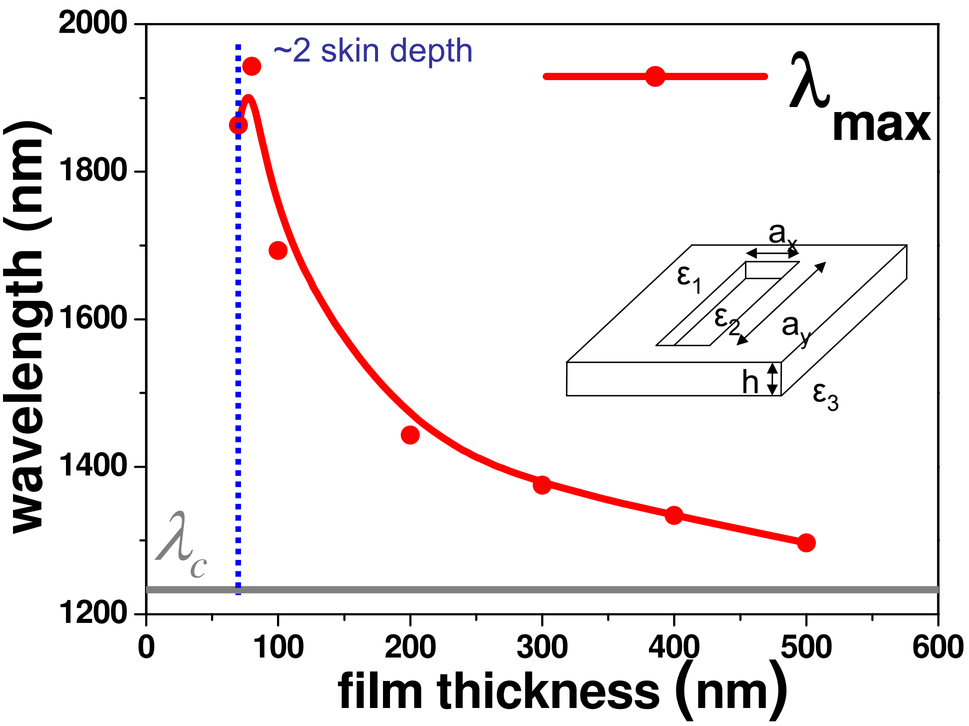

Figure 5.8: Calculations performed with the FDTD method for the position of transmission maximum as a function of the film thickness in an isolated rectangular hole ($a_x = 50$nm and $a_y = 400$nm) drilled in a gold film with $\varepsilon_1 = \varepsilon_3 = 2.25$ and $\varepsilon_2 = 1$. The vertical blue line depicts $h = 2$ skin depths ~ 60nm, and the horizontal grey line corresponds to λ_c.

Chapter 6

Non Linear Phenomena

6.1 Introduction

Nonlinear optics is the study of phenomena that occurs as a consequence of the modification of the optical properties of a material system by the presence of light. Typically, only laser light is sufficiently intense to modify the optical properties of a material system. Nonlinear optical phenomena are “nonlinear” in the sense that they occur when the response of a material system to an applied optical field depends in a nonlinear manner upon the strength of the optical field. In order to describe more precisely what we mean by an optical nonlinearity, let us consider how the dipole moment per unit volume, or polarization $P(t)$, of a material system depends upon the strength $E(t)$ of the applied optical field. In the case of conventional or linear optics, the induced polarization depends linearly upon the electric field strength in a manner that can be often be described by the relationship [39]:

$$P(t) = \chi^{(1)} E(t) \tag{6.1}$$

where the constant of proportionality $\chi^{(1)}$ is known as the linear susceptibility.

In nonlinear optics, the optical response can often be described by generalizing Eq. 6.1 by expressing the polarization $P(t)$ as a power series in the field strength $E(t)$ as:

$$P(t) = \chi^{(1)} E(t) + \chi^{(2)} E^2(t) + \chi^{(3)} E^3(t) + ... \tag{6.2}$$

The quantities $\chi^{(2)}$ and $\chi^{(3)}$ are known as the second- and third-order nonlinear optical susceptibilities, respectively. For simplicity, here in this introductory section we have taken the fields $P(t)$ and $E(t)$ to be scalar quantities in writing Eq.6.1 and Eq.6.2.

Let us now present a brief qualitative description of a number of nonlinear optical interactions.

- Second Harmonic Generation (SHG)

  The process of second-harmonic generation is illustrated schematically in Fig. 6.1 (a). Here, a laser beam is incident upon a crystal for which the second-order susceptibility $\chi^{(2)}$ is nonzero. The nonlinear polarization that is created in such a crystal is given according to Eq. 6.2 as $P^{(2)}(t) = \chi^{(2)}E^2(t)$. We see that the second-order polarization consists of a contribution at zero frequency and a contribution at frequency 2ω, that leads to the generation of radiation at the second-harmonic frequency.

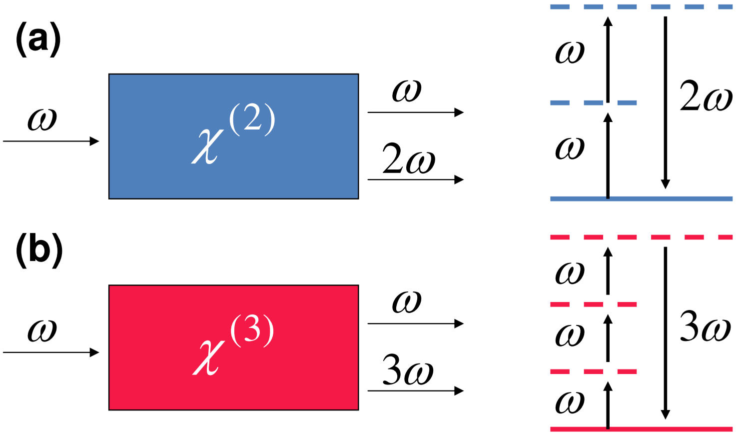

Figure 6.1: (a) Geometry of second-harmonic generation and energy-level diagram describing it. (b) Third-harmonic generation: geometry of interaction and energy-level description.

- Third Harmonic Generation (THG)

  The process of third-harmonic generation describes a response at frequency 3ω that is due to an applied field at frequency ω (see schematics in Fig. 6.1 (b)).

- Optical Kerr Effect (OKE)

  A different term in Eq. 6.2 may describe a nonlinear contribution to the polarization at the frequency of the incident field; this term leads to a nonlinear contribution to the refractive index experienced by a wave at frequency ω. The refractive index in the presence of this type of nonlinearity can be represented as

$$n = n_0 + n_2 \cdot I \tag{6.3}$$

where n_0 is the usual refractive index, n_2 is an optical constant that characterizes the strength of the optical nonlinearity, usually known as the Kerr coefficient, and where I is the intensity of the incident wave.

One of the phenomena occurring when OKE is present is Self-Focusing phenomenon: this process can occur as a result of the intensity-dependent refractive index. It may appear when a beam of light having a nonuniform transverse intensity distribution propagates though a material in which n_2 is positive. Under these conditions, the material effectively acts as a positive lens, which causes the rays to curve toward each other.

- Two-Photon Absorption

  In the process of two-photon absorption, an atom makes a transition from its ground state to an excited state by the simultaneous absorption of two laser photons.

- Stimulated Raman Scattering

  In stimulated Raman scattering, a photon of frequency ω is annihilated and a photon at the Stokes shifted frequency $\omega_s = \omega - \omega_v$ is created, leaving a molecule or atom in an excited state with energy $\hbar\omega_v$. The excitation energy is referred to as ω_v because stimulated Raman scattering was first studied in molecular systems, where $\hbar\omega_v$ corresponds to a vibrational energy.

Along this chapter we will study the optical properties of systems composed by nonlinear dielectrics in combination with slit arrays in metal films.

In particular, we first propose a scheme for an optical limiter and switch of the transmitted light intensity in an array of subwavelength metallic slits placed on a nonlinear Kerr-type dielectric substrate of finite thickness, where the geometrical parameters are designed for operation at telecom wavelengths. This work is done in collaboration with the group headed by Yuri S. Kivshar, at the Australian National University, in Canberra (Australia).

Next, a theoretical study on the nonlinear optical properties of both gold and nickel slit arrays inlaid with a third order nonlinear dielectric medium is presented. We investigate again the Optical Kerr Effect (OKE) but also Third Harmonic (TH) Generation. The geometrical parameters, along with the optical properties of each metal, determine the electromagnetic environment near the slits and, in turn, the nonlinear optical response. The Optical Kerr Effect is only seen for slit arrays in gold, where the transmitted and reflected currents are modified with the incident intensity, while nickel slit arrays behave linearly within the same range of input intensities. However, Third Harmonic emission occurs for both systems, unveiling third order nonlinearities taking place also in nickel structures.

6.2 Nonlinear Phenomena: PEC, CMM and FDTD

In order to start with this new nonlinear physics, we decided to consider first one of the simplest landscapes: 1D structures (slits) made of perfect electrical conductor (PEC) in combination with nonlinear Kerr-type dielectrics. This would enable us to, first, work with the Coupled Mode Method (CMM) (described in Chapter2) what provides analytical expressions and physical insight in the mechanisms here involved; second, check energy conservation; and third, compare CMM results and those calculated with the Finite Difference Time Domain method (FDTD) (also described in Chapter2).

Following a previous work developed by Porto et al. [68], we used the same algorithm to study the optical response of metallic gratings with nonlinear media embedded within their subwavelength slits made of PEC. An optical Kerr effect (OKE) is considered. Within the algorithm, just the fundamental mode is considered inside the slits, and in order to account for the nonlinear response of the dielectric, an iterative self-consistent method is used. The slit region is divided into N thin slices perpendicular to the z direction (it is schematically shown in Fig. 6.5). For a given iteration, the magnetic field in the nth slice is expressed as:

$$H_y = \frac{1}{\sqrt{a}}(A_n e^{i\sqrt{\varepsilon_n}k_0 z} + B_n e^{-i\sqrt{\varepsilon_n}k_0 z}) \tag{6.4}$$

where k_0 is the wavevector of the incident light in vacuum, ε_n is the dielectric constant in the nth slide, A_n and B_n are the modal expansion coefficients, and a is the slit width. Within each slide, we can compute the electric field E_x by means of Maxwell's equations, and after matching E_x and H_y, the coefficients of the modal expansion in two consecutive slices can be related by a 2×2 matrix (see Ref [68] for more details).

In order to check our first calculations, we considered a slit array with periodicity $p = 1350$nm, film thickness $h = 200$nm, and $a = 300$nm, having vacuum at both the illuminated and transmission regions. The slits are supposed to be filled with a Kerr nonlinear media, whose dielectric constant at point r depends on the intensity of the electric field at this point $|E(\vec{r})|^2$,

$$\varepsilon(\vec{r}) = \varepsilon_l + \frac{3}{4}\chi^{(3)}\,|E(\vec{r})|^2 \tag{6.5}$$

where $\varepsilon_l = 7.84$ is the value of the dielectric constant at low intensities, and $\chi^{(3)} = 3.04385e^{-19}$(V/m), following Miller's rule [39] (see Fig. 6.2). Figure 6.2

shows several calculations of $\chi^{(3)}$ and n_2 as a function of n_0 given by Miller's rule, together with similar experimental results obtained in Ref. [160].

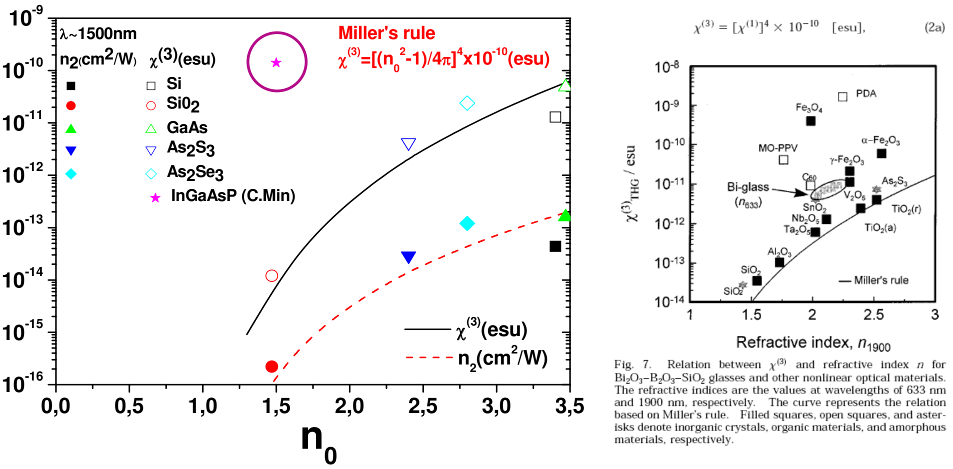

$$\chi^{(3)} = [\chi^{(1)}]^4 \times 10^{-10} \quad [\text{esu}], \tag{2a}$$

Fig. 7. Relation between $\chi^{(3)}$ and refractive index n for Bi_2O_3–B_2O_3–SiO_2 glasses and other nonlinear optical materials. The refractive indices are the values at wavelengths of 633 nm and 1900 nm, respectively. The curve represents the relation based on Miller's rule. Filled squares, open squares, and asterisks denote inorganic crystals, organic materials, and amorphous materials, respectively.

Figure 6.2: Miller's Rule: relation between $\chi^{(3)}$ (or n_2) and n_0 for several materials.

Note that some theoretician authors use pairs of n_0 and n_2 that are not realistic and do not follow this rule (one example is highlighted with a pink circle in the figure). In all our calculations we will consider values following Miller's rule in order to design devices attainable in real experiments.

Since the change of the dielectric constant is not very large, it is common to approximate the refractive index as $n(I) = n_0 + n_2 I$, retrieving the same expression as that described in the previous "Optical Kerr Effect" section.

In Fig. 6.3, it is shown the linear spectrum associated to the previous set of parameters. We compare CMM calculations for transmission of light, and zero*th* order transmission FDTD results. As expected, a transmission minimum at $\lambda = p = 1350$nm followed by a resonant transmission peak, is obtained. Inset in the same figure shows a zoom around the maximum, finding that $\lambda_{max} \approx 1460$nm.

In Fig. 6.4, we plot nonlinear calculations performed with both the CMM and the FDTD method, at a fixed wavelength (which is chosen to be the spectral location of the maximum in the linear spectrum in each case), as a function of the incident power. We can see that, at low incident intensities, the nonlinear transmission follows $T = 1$, as in the linear case, and when the intensity is increased, transmission deviates from the linear behavior giving $T < 1$. As the incident intensity is increased, the dielectric constant filling the slits increases as well. This effect could be understood as an induced "rigid" shift of the linear spectrum to larger wavelengths, what would translate into a decrease in transmission, as it is schematically shown in Fig. 6.5. As

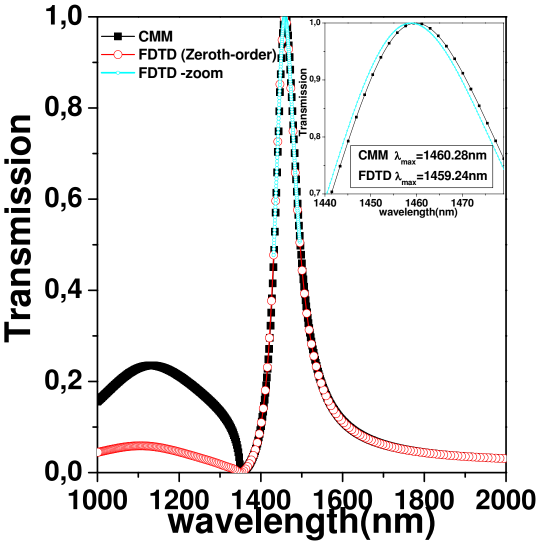

Figure 6.3: Linear transmittance through a PEC drilled with an array of slits with $P = 1350\,\text{nm}$, $a = 300\,\text{nm}$, $h = 200\,\text{nm}$) inlaid with a dielectric constant with $\varepsilon_l = 7.84$. The black curve corresponds to CMM calculations, the red one to zero*th* order transmission calculated with the FDTD method, and the blue one are also FDTD calculations with a small step in wavelengths around the maximum. Inset shows a zoom of the blue curve.

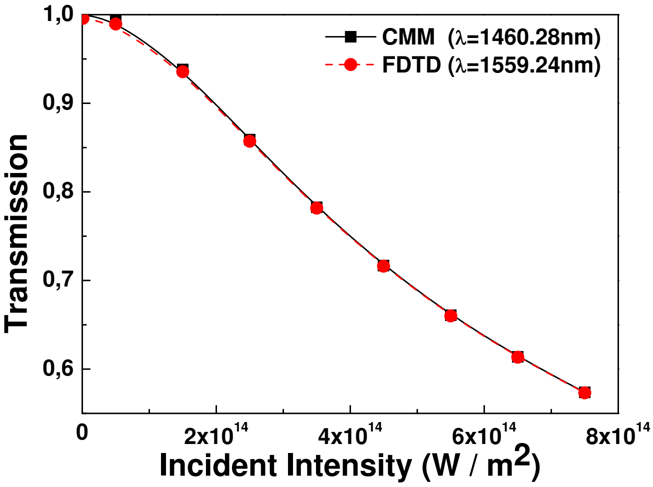

Figure 6.4: Nonlinear CMM and FDTD calculations of the transmission of light as a function of the incident intensity, for the same system at that considered in Fig. 6.3. The wavelength is fixed at maximum in each case (see labels).

said before, nonlinear calculations are performed considering slightly different wavelengths that correspond to maximum in linear transmission curves done with the CMM and FDTD method. Otherwise, although this difference is $\sim$ 1nm, nonlinear curves would be a bit difference.

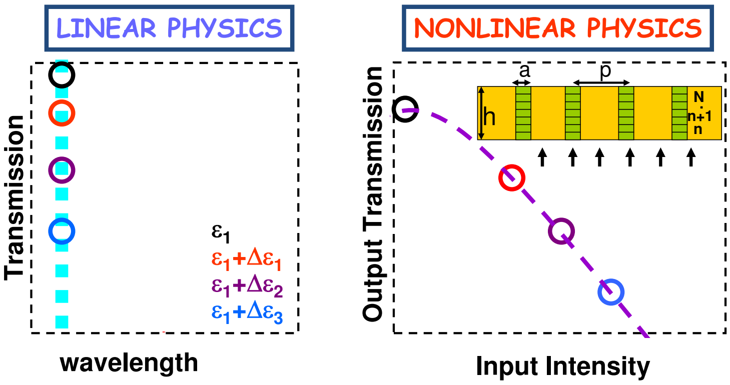

Figure 6.5: Schematics of linear and nonlinear transmission in a slit array filled with a Kerr-type dielectric. Left panel represents how a linear spectrum is redshifted when the dielectric constant filling the slits is increased. Right panels shows nonlinear schematics at $\lambda = \lambda_{max}$ (blue vertical dashed line in the linear scheme), as a function of the incident intensity.

These calculations were very useful to us since we checked that our two home-made CMM and FDTD codes produced the same results, and because they helped us to understand some of the physics underneath.

For instance, some remarks about illumination sources and their effect in OKE and THG must be done before going on.

For an isotropic, homogeneous and dispersionless material the optical response due to a third-order nonlinear susceptibility is described by the relations of both displacement ($\vec{D}$) and polarization ($\vec{P}$) vectors with the electric field, ($\vec{E}$) [39]:

$$\begin{aligned} \vec{D} &= \varepsilon_0 \vec{E} + \vec{P} \\ \vec{P} &\simeq \varepsilon_0 \left[\chi^{(1)} \vec{E} + \chi^{(3)} (\vec{E} \cdot \vec{E}) \vec{E} \right] \end{aligned} \tag{6.6}$$

Considering a plane wave of the form $E = E_o \frac{(e^{-i\omega t} + e^{i\omega t})}{2} = E_o \cos(\omega t)$, and after some algebra, we can find the nonlinear contribution for different harmonics:

- 0: Optical Rectification $\rightarrow P^0 = \frac{\varepsilon_o \chi^{(2)} E_o^2}{2}$

- ω: OKE $\rightarrow P^{\omega} = \varepsilon_o[\chi^{(1)}E_o + \frac{3\chi^{(3)}E_o^3}{4}]\cos(\omega t)$
- 2ω: SHG$\rightarrow P^{2\omega} = \frac{\varepsilon_o\chi^{(2)}E_o^2}{2}\cos(2\omega t)$
- 3ω: THG$\rightarrow P^{3\omega} = \frac{\varepsilon_o\chi^{(3)}E_o^3}{4}\cos(3\omega t)$

Within the CMM, we have explicitly considered just the OKE term (P^{ω}), without taking into account THG. Then, polarization reads $P = P_L + P_{NL} = \varepsilon_o\chi^{(1)}E + \frac{3}{4}\chi^{(3)}E^3$ and it is implemented in the code as we described previously.

However, within the FDTD method, things can be a bit different. As we showed before, the relation between the displacement vector $\vec{D}$ and the electric field $\vec{E}$ is given by:

$$\vec{D} = \varepsilon_o[\varepsilon + \chi^3(\vec{E}\cdot\vec{E})]\vec{E} \tag{6.7}$$

In Chapter 2 we described how to implement these fields within the FDTD method: the displacement vector at instant $n+1$ is obtained from itself at the previous instant and the curl of the magnetic field at $n - 1/2$. Once $\vec{D}^{n+1}$ is known, the electric field at $n + 1$ is nothing else than the solution of Eq. 6.7 in terms of $|E|^2$. Thus it is finally found:

$$\vec{E}^{n+1} = \frac{\vec{D}^{n+1}}{\varepsilon_o(\varepsilon + \chi^{(3)}|\vec{E}^{n+1}|^2)} \tag{6.8}$$

Depending on the illumination source we use (plane waves, gaussian pulses, or complex plane waves, for instance), we can just consider the OKE or also THG.

A plane wave pulse can also be defined as a complex function $\propto e^{i\omega t}$. Despite this source has no physical meaning because realistic sources must be real numbers, within the FDTD method a source like that is useful to discriminate between effects due to OKE and THG ones. In the right side of denominator of the Eq. 6.8 the electric field at $n + 1$ step is expressed in terms of its modulus, so if the electric field is proportional to a complex exponential, then the term associated to THG appearing in Eq. 6.6, is equal to zero. Additionally, in order to get the same nonlinear response when real-valued plane waves are considered, we must take $\chi^{(3)} \rightarrow (3/4)\chi^{(3)}$.

These kind of tricks were very useful to discriminate amongst different processes, and to validate CMM and FDTD calculations.

Once the codes were checked, we decided to go a bit further and consider the optical properties of real metals (instead of PECs, as we did up to now) and study THG as well. As a result, next calculations will be performed by using the FDTD method.

But, before going on with these studies, we must answer the following question arising when nonlinear effects in these systems are studied: why do not we consider Second Harmonic Generation (SHG)?

Well, one of the symmetry properties that some, but not all, crystals possess is inversion symmetry. For a material system that is centrosymmetric (i.e., possesses a center of inversion) the $\chi^{(2)}$ nonlinear susceptibility must vanish identically. Although the result that $\chi^{(2)}$ vanishes for a centrosymmetric medium is general in nature, we shall demonstrate this fact for the special case of second harmonic generation in a medium that responds instantaneously to the applied optical field, as those considered in our studies.

We assume that the nonlinear polarization is given by

$$P(t) = \chi^{(2)} E^2(t) \tag{6.9}$$

where the applied field is given by

$$E(t) = E_o \cos(\omega t) \tag{6.10}$$

If we now change the sign of the applied electric field $E(t)$, the sign of the induced polarization $P(t)$ must also change, because we have assumed that the medium possesses inversion symmetry. Hence the relation given by Eq. 6.9 must be replaced by

$$-P(t) = \chi^{(2)} [-E(t)]^2 \tag{6.11}$$

which shows that

$$-P(t) = \chi^{(2)} E^2(t) \tag{6.12}$$

By comparison of this result with Eq. 6.9, we see that $P(t)$ must be equal $-P(t)$, which can occur only if $P(t)$ vanishes identically. This result shows that

$$\chi^{(2)} = 0 \tag{6.13}$$

However, in the surfaces of both dielectrics and metals, the system is not centrosymmetric, and SHG may occur. Nevertheless, due to the symmetry of the problems we treat (normal incidence, slits,...), this generation is very weak. If, for instance, we would like to study nonlinear effects with angular incidence, neglecting the contribution in the second harmonic could be a bad approximation since symmetry reflection around the plane that divides the unit cell is broken and emission of second harmonic may become very efficient. Additionally, since this is a second order process, this emission should be higher than the third harmonic generation.

However, this is not our case, and bearing in mind that processes occurring at 2ω or 3ω will not affect each other, the fact of not considering SHG when studying TH emission is justified.

6.3 Optical switching in metal-slit arrays on nonlinear dielectric substrates

Nanostructuring of metal surfaces appears exceptionally attractive for novel nonlinear photonic applications due to a strong enhancement of the electromagnetic (EM) field near corrugated surfaces. As we said before, prominent examples include the surface enhanced Raman scattering [38] and plasmon-enhanced high-harmonic generation [161].

However, the drawback of using metallic elements is the introduction of strong loss. Therefore, when metals are involved, only schemes utilizing short device lengths can be tolerated in practice to observe noticeable nonlinear phenomena, while any schemes relying on phase accumulation are intrinsically excluded.

A proposed platform for enhanced nonlinear optical manipulation is the array of sub-wavelength apertures in metal films [162,163]. Nonlinear properties of sub-wavelength metallic apertures in combination with nonlinear dielectrics, have been studied for their potential uses in enhanced nonlinear beam manipulation [164,165], optical bistability [68,166], and switching [167,168]. Such geometries rely on the phenomenon of enhanced optical transmission [23,49,169] associated with distinct resonances in the linear transmission spectrum.

Here we present a proposal for **i)** an optical limiter (OL) of the transmitted intensity, in which the output intensity decreases when the incident one increases, and **ii)** an optical switch (OS), where the output intensity increases abruptly under a small change of the incident power. These two operating modes are found in an array of metallic slits placed on a nonlinear Kerr-type dielectric layer, at the telecom regime. The inset of Fig. 6.6 shows schematically the structure analyzed as well as the direction of illumination considered. We assume air at the illuminated and transmission regions, and also inside the slits.

We study the nonlinear optical response at a fixed wavelength close to the transmission minimum (see Fig. 6.6(top)), where sharp variations in the spectrum take place within a short wavelength range.

We assume nonlinear response only in the dielectric layer, while the nonlinear susceptibility in the metal [170] is neglected. In the MKS system of units, the optical response of the dielectric material due to a third-order nonlinear susceptibility is described by the relations of both displacement ($\vec{D}$) and polarization ($\vec{P}$) vectors with the electric field, ($\vec{E}$) [39]: $\vec{D} = \varepsilon_0 \vec{E} + \vec{P}$, where $\vec{P} \simeq \varepsilon_0 \left[\chi^{(1)} \vec{E} + \chi^{(3)} (\vec{E} \cdot \vec{E}) \vec{E} \right]$, and ε_0 is the dielectric constant of vacuum. The scalar quantities $\chi^{(1)}$ and $\chi^{(3)}$ represent the linear and third-order nonlinear susceptibilities, respectively. Since the change of the dielectric constant yielded by the local EM field is percentually small, it is common to approximate the refractive index as $n = n_0 + n_2 I$, where $I = n_0 c \varepsilon_0 \left| E(\vec{r}) \right|^2 / 2$, n_0 is the linear refractive index, and $n_2 = \frac{3\chi^{(3)}}{4n_0^2 c}$ [39] is the Kerr coefficient.

We have employed the Finite Difference Time Domain method to simulate both the linear [78] and nonlinear optical response of the structure [80] (see Chapter2 for further details of this implementation). The system is illuminated with a normal incident p-polarized plane wave. Unless otherwise stated, the duration of the pulse is $\tau \sim 2.4\,\text{ps}$. This pulse is slowly switched on and off, so it has a smooth Fourier transform (in this case with spectral bandwidth of $\sim 3\,\text{nm}$). We have checked that under such excitation the process of third harmonic generation forms less than 1% of the total output energy, and therefore only the optical properties at the fundamental frequency are considered. A more detailed explanation of illumination and data processing for retrieving the optical properties of this kind of problems within the FDTD method, can be found next in Chapter 2.

The dielectric constant of gold (ε_m) is obtained from the experimental values tabulated in Ref. [15] and fitted to a Drude-Lorentz model [82]. The nonlinear dielectric is assumed to be isotropic, homogeneous and dispersionless. Furthermore, absorption in the dielectric is neglected in our simulations. The linear refractive index is chosen to be $n_0 = 2.8$, a typical value for materials with large Kerr coefficients, following Miller's rule [39] (see Fig. 6.2).

To illustrate our proposal, we have chosen the following set of parameters: a 1650nm thickness dielectric slab, array period $p = 520\,\text{nm}$, metal film thickness $h = 350\,\text{nm}$, and slit width $a = 300\,\text{nm}$. The precise values of these parameters are arbitrary but are chosen in order to **i)** be within the range accessible to experiments and **ii)** provide a sharp transmission minimum at near infrared, in this case, $\lambda_{\min} = 1451\,\text{nm}$ [Fig. 6.6 (top)]. The spectral position of this minimum depends on the geometrical parameters in a complex way. We tried to find an analytical expression for $\lambda_{\min}$, but we were not able to do it.

It is well known that for arrays of very "narrow" slits ($a << p$) the mini-

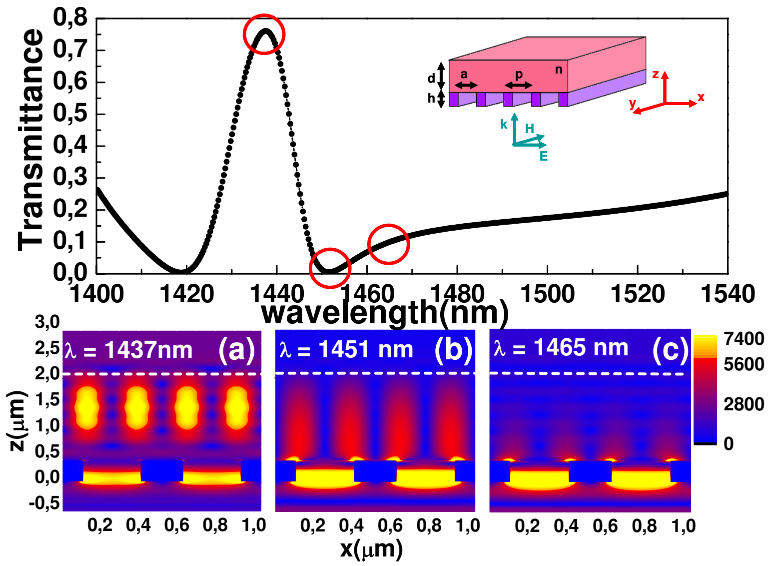

Figure 6.6: Linear transmittance through a gold slit array ($P = 520\,\text{nm}$, $a = 300\,\text{nm}$, $h = 350\,\text{nm}$) on a dielectric substrate of finite thickness ($n_0 = 2.8$ and $d = 1650\,\text{nm}$). (a-c) Modulus of the electric field, $|\vec{E}|$, evaluated at the xz plane for two unit cells at $\lambda_{\text{max}} = 1437\,\text{nm}$, $\lambda_{\text{min}} = 1451\,\text{nm}$ and $\lambda_1 = 1465\,\text{nm}$, respectively. The dashed white lines mark the end of the dielectric layer.

mum in transmission is given by the surface plasmon polariton ($\lambda_{\text{min}} = \lambda_{\text{spp}}$) that can be excited by the grating. However, the system we are studying here is more complex, as the slits cover a large percentage of the unit cell and, moreover, they are placed on a dielectric substrate of finite thickness. We tried to relate transmission features (maxima and minima) to the EM modes supported by the structure. Figure 6.7 shows the transmittance (in logarithmic scale) together with the wavelengths for the bound modes in both the corrugated (vertical blue line) and uniform structure, with (red line) and without (green line) the metal film (these modes are obtained from additional calculations of the band structure (BE) for each structure). Note that for these “wide” slits there is a good correspondence between the spectral position of transmission *maxima* and that of the modes in the noncorrugated systems (at $k = 2\pi/d$). However, the spectral position of the transmission minimum is not given by any of these modes.

Thus, the consideration of other ranges of working wavelengths would require a fine tuning of geometrical parameters (i.e. other λ_{min}) through computation of the linear transmittance. In Fig. 6.6(a-c) we plot the modulus of the electric field, $|\vec{E}|$ (evaluated at the xz plane for two unit cells) for three different wavelengths: $\lambda_{\text{max}} = 1437\,\text{nm}$, λ_{min}, and $\lambda_1 = 1465\,\text{nm}$, respectively. For λ_1 and λ_{min} we observe field enhancement inside the slits and around their

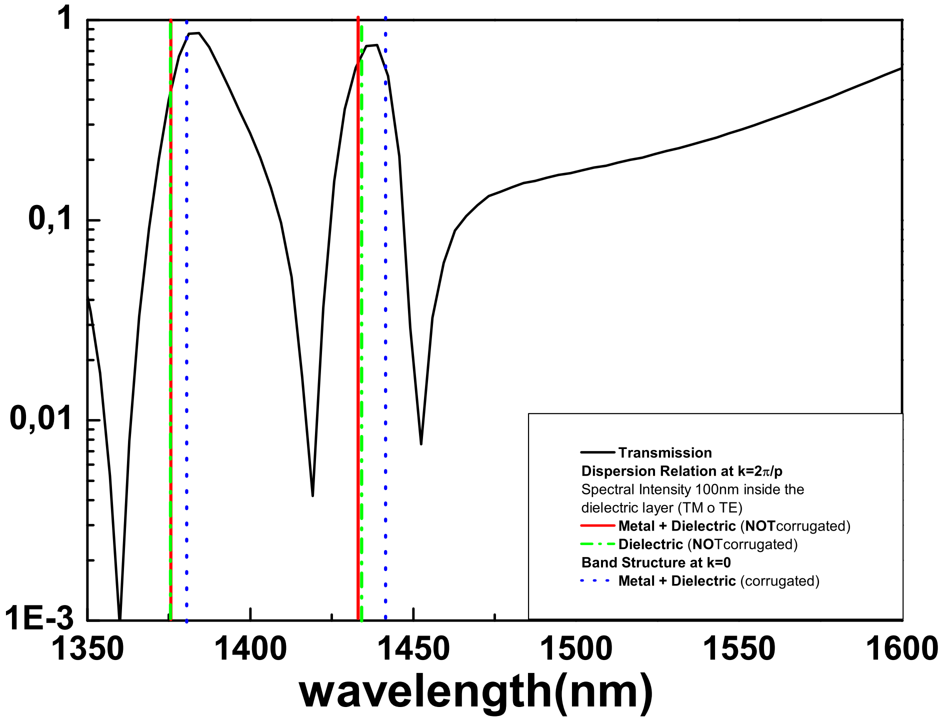

Figure 6.7: In black, linear transmittance in logarithmic scale through a gold slit array ($P = 520\,\text{nm}$, $a = 300\,\text{nm}$, $h = 350\,\text{nm}$) on a dielectric substrate of finite thickness ($n_0 = 2.8$ and $d = 1650\,\text{nm}$). Blue lines depict the spectral position of the EM modes supported by the corrugated structure. Red and green lines accounts for the EM modes supported by a metal-dielectric and dielectric structures without corrugation, respectively.

corners, while at $\lambda_{\max}$ a guided mode appears inside the dielectric layer. Interestingly, the linear transmission spectrum at shorter wavelengths present several maxima and minima, that in some cases, maxima are related to the formation of guided modes of higher order (with high electric fields inside the slab), and in other cases, they seem to be associated to Fabry-Perot modes inside the metallic slits (high electric fields inside the slits).

Next, we study the changes in the transmission through the metal slits with increase of the light intensity for four different wavelengths red-shifted compared to $\lambda_{\min}$. We scale both the incident (I^{in}) and transmitted (I^{out}) intensities by n_2, so our results are valid for different (current or future) nonlinear materials. Also, $n_2 I^{\mathrm{out}}$ reflects the average change of the refractive index, Δn, in the dielectric film (we will discuss spatial distribution of Δn later on).

Figure 6.8 presents with solid symbols the results for $n_2 I^{\mathrm{out}}$ as a function of $n_2 I^{\mathrm{in}}$, together with the corresponding linear results ($n_2 I^{\mathrm{out}}_{\mathrm{Lin}}$). As expected, at low input intensities the transmission follows the linear dependence. However, as the intensity is increased the transmission saturates and then drops. This behavior corresponds to *nonlinear intensity limiter*. For higher I^{in}, the transmission exhibits a steep rise, *switching to a high-transparency state*. This can be heuristically understood by noting that, nonlinear effects correspond to an increase of n and that, in the linear regime, the increase of n shifts the transmission spectrum to longer wavelengths. In the OL regime, as the incident intensity increases, the linear transmittance decreases. Eventually, after the minimum transmittance is reached, the output intensity would be boosted by both the increase of the incident intensity and the corresponding increase in linear transmittance, leading to a large increment of I^{out} within a narrow range of incident intensities.

Clearly, the incident intensity to achieve OL or OS strongly depend on the incident wavelength. The vertical scale in Fig. 6.8 breaks in the region $n_2 I^{\mathrm{out}} = (8-12)\cdot 10^{-4}$ in order to mark up the features visibility at low output intensities. In Fig. 6.8 the switching is seen for two wavelengths $\lambda_1 = 1465\,\mathrm{nm}$ and $\lambda_2 = 1475\,\mathrm{nm}$, in the range of intensities chosen, being the final I^{out} much larger than $I^{\mathrm{out}}_{\mathrm{Lin}}$. Precisely, OL occurs for all considered wavelengths (and also OS, although this is not shown in the figure for the two largest wavelengths), but the input intensities for minimum output increase as the working wavelength separates from $\lambda_{\min}$. Figure 6.8 also shows that the considered nonlinear effects are still present for shorter pulses ($\tau \sim 500$ fs, although the OL is less pronounced and the OS occurs within a wider range of I^{in}) which in real experiments would reduce the influence of the free carrier absorption or thermal effects.

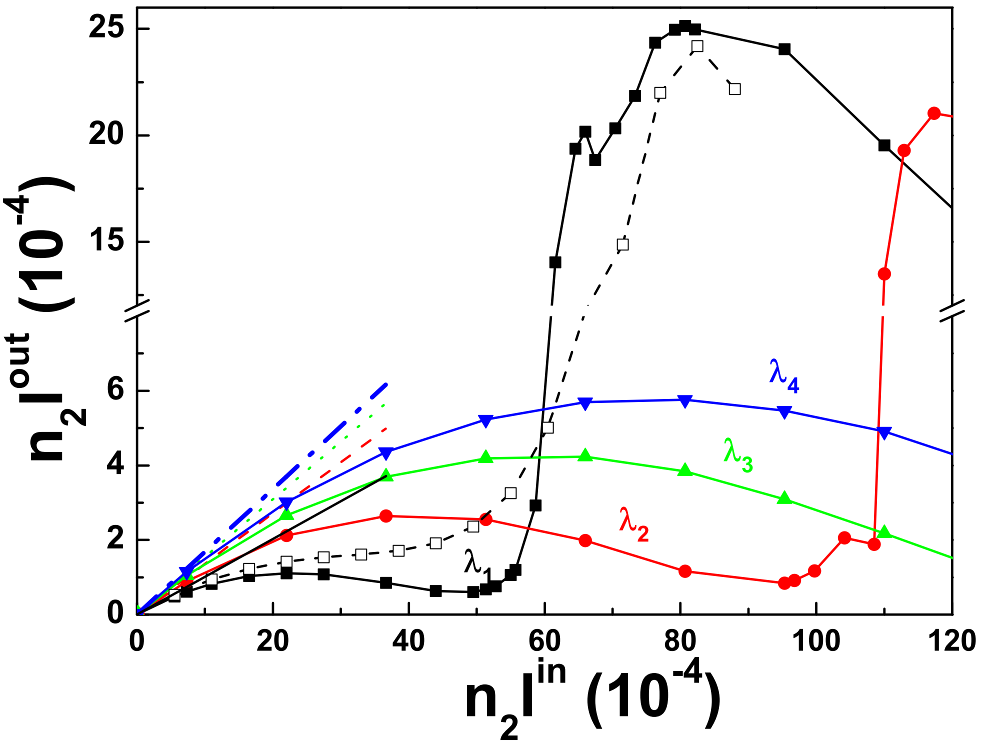

Figure 6.8: Transmitted intensity vs. incident intensity for: (Solid symbols) $\lambda_1 = 1465\,\text{nm}$, $\lambda_2 = 1475\,\text{nm}$, $\lambda_3 = 1485\,\text{nm}$ and $\lambda_4 = 1495\,\text{nm}$. Linear output in each case is given by straight dashed, dot, and dash-dot lines, respectively. (Open symbols) $\lambda_1 = 1465\,\text{nm}$, for a short pulse of ~ 500 fs duration (spectral bandwidth of ~ 12nm).

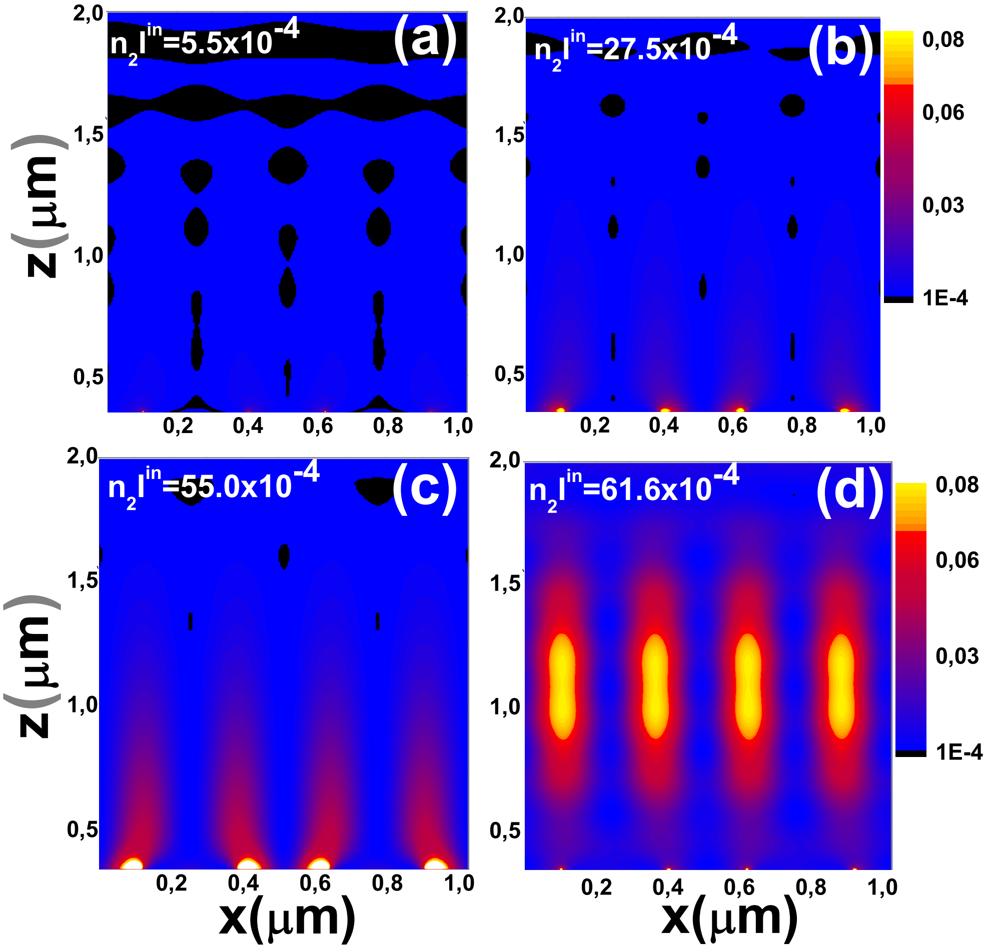

Figure 6.9: Local change in the refractive index, Δn, within the dielectric slab for the same structure considered in Fig. 6.6 at $\lambda_1 = 1465\,\text{nm}$. For different input intensities (a) $n_2 I^{in} = 5.5 \cdot 10^{-4}$, (b) $n_2 I^{in} = 27.5 \cdot 10^{-4}$, (c) $n_2 I^{in} = 55 \cdot 10^{-4}$ and (d) $n_2 I^{in} = 61.6 \cdot 10^{-4}$.

In Fig. 6.9, panels $(a-d)$ show the local change in the refractive index within the nonlinear dielectric slab (evaluated at the xz plane for two unit cells) for the structure in Fig. 6.6 and for four different input intensities at $\lambda_1 = 1465\,\mathrm{nm}$ at a moment just before the plane wave is switched off ($\sim$ 2.4ps). The intensity values cover both the linear regime as well as the intensity range when the OL and the OS occur. Importantly, the variation of the refractive index is not uniform and resembles the profiles of the modulus of the electric field in the linear regime (Fig. 6.6(a-c)) at the related wavelengths.

Let us finally discuss possible materials to operate the OL and OS. Chalcogenide glasses like $\mathrm{As_2Se_3}$ posses $n_0 \approx 2.8$ and high $n_2 \approx 1.1 \times 10^{-4}$ cm^2/GW [171], featuring low linear and two photon absorption at infrared wavelengths. However, in real experiments dielectric slabs made of these materials support a maximum change in the refractive index, $\Delta n^{\max} \approx 0.0001$ before being damaged, a threshold much smaller than the change of the refractive index here obtained when metals are involved ($\Delta n^{\max} \approx 0.1$ in some regions of Fig. 6.9). Nevertheless, semiconductors could appear as better candidates since they have similar linear and nonlinear refractive indexes to that of chalcogenides, but support a much higher $\Delta n^{\max} \approx 0.1$ as it is reported in Ref. [172, 173]. In any case, appropriate candidates for real experiments must have both high Δn and n_2, and also must behave as Kerr-type materials with low absorption in a wide range of local intensities.

6.4 Metallic slit arrays filled with third order nonlinear media: Optical Kerr Effect and Third Harmonic Generation

As we said in the introductory section in this chapter, interaction of light with matter gives rise to a great number of nonlinear optical phenomena, like Raman scattering, Photo-Luminesce in metals, Second Harmonic (SH) Generation, Four Wave Mixing (FWM), Third Harmonic (TH) Generation or Optical Kerr Effect (OKE) [39]. The nonlinear response of dielectrics has been long exploited in technological applications. In general, dielectrics in bulk present weak nonlinear response at moderately low laser powers. On the contrary, if metallic inclusions are present, the electric field can be efficiently enhanced and nonlinear effects in metallo-dielectric structures may occur at lower laser powers [166, 174]. Different configurations of metal slit arrays combined with nonlinear dielectrics have been widely investigated for their potential uses in optical bistability [68, 175, 176], nonlinear beam manipulation [177, 178] and switching [168, 179]. As we showed before, among the possible arrangements, an interesting example is a slit array deposited over a nonlinear dielectric slab of finite thickness, but also a slit array filled with it, investigated in Ref. [68,176,178], where the non- linear phenomena described originates from OKE, and in Ref. [180], where several aspects of harmonic generation has been analyzed. However, the physical mechanisms behind these two effects have not been correlated and to our knowledge, OKE and TH Generation have not been investigated within the same theoretical framework (and for the same system) so far. Furthermore, the influence of absorption of metals in combination with nonlinear dielectrics and the relation to field enhancement have not been described either.

Next, we will investigate theoretically the optical response of metallic slit arrays inlaid with a Kerr-type nonlinear medium (see Fig. 6.10), where both TH Generation and OKE phenomena are present. The former describes processes in which light at frequency 3ω is generated from an applied field at frequency ω, whereas OKE processes, as we saw before, have an influence on the fundamental harmonic through a variation of the local dielectric constant. We will also describe how the absorption of metals and slit widths affect the EM field near subwavelength slits which, in turn, determines the overall nonlinear response.

These studies are organized as follows: In Section 6.4.1 we provide the geometrical and material parameters used for both the linear and nonlinear numerical simulations in Section 6.4.2 and Section 6.4.3, respectively. The later contains results for OKE (Section 6.4.4) as well as TH Generation (Section 6.4.5).

6.4.1 Geometrical and material properties

The geometrical parameters of the slit arrays (See top panel of Fig. 6.10) are selected so that a transmission resonance appears at telecom wavelengths ($\sim$ 1500nm). The location of this resonance is mostly dictated by the period (which is chosen to be $P = 1200$nm), and the film thickness [20] (in this case $h = 185$nm). We consider free standing systems ($\varepsilon_1 = \varepsilon_3 = 1$). As we did in the previous study of the OL and OS, we use the FDTD method [78] to treat both the linear optical properties of metals and the nonlinear third order response of dielectrics [80].

Since the nonlinear material filling the slits is chosen to be isotropic, homogeneous and dispersionless in frequency, the EM field responds instantaneously. Materials with high ε values usually possess also large values of $\chi^{(3)}$, following Miller's rule [39]. Chalcogenide glasses such as As_2Se_3 fit well the later requirements [171,181–184] at telecom, and additionally, these glasses feature low linear and two photon absorption (TPA) at infrared wavelengths, where they are transparent. However, as we remarked in Section 6.3, in real experiments these materials support a maximum change in the refractive index $\Delta n \approx \Delta\varepsilon/2\sqrt{\varepsilon} \sim 0.0001$ before being damaged. This value is too small for nonlinear applications based on a strong change of the local dielectric constant, as the OKE considered here. As an alternative to chalcogenides, semiconductors such as GaAs appear as good candidates, with an index change threshold four orders of magnitude higher than the one for chalcogenides [172,173], while still featuring high $\chi^{(3)}$. In any case, appropriate candidates for real experiments must have both high ε and $\chi^{(3)}$, and also must behave as Kerr-type materials with low absorption in a wide range of local intensities and wavelengths. For the sake of illustration in what follows we take $\varepsilon = 10.0$ and $\chi^{(3)} \approx 3.682 \cdot 10^{-19}(m^2/V^2)$ (from Miller's rule) which are typical semiconductor values.

Concerning metals, both gold and nickel are considered, because they are representative cases of low- and high- absorbing metals, respectively. The dielectric constant, ε_m, is taken from the experimental values tabulated in Ref. [15,116], and conveniently fitted into Drude-Lorentz formulas [82,185]. In this work, we neglect the non-linear response of metals. Note that the change in the metal dielectric constant due to OKE would be orders of magnitude lower than the dielectric constant of metals at telecom, making a noticeable OKE related effect unlikely. In contrast, if the considered dielectric presents a strong nonlinear coefficient, TH generation and emission from the metal itself is expected to be hidden by the high-index medium response, according to recent FWM experiments by Renger et al. [186].

6.4.2 Linear response

Let us start with the linear optical response ($\chi^{(3)} = 0$). Fig. 6.10 depicts the zeroth order transmittance (T_L), reflectance (R_L) and absorbance (A_L), through gold slit arrays [upper panels] and nickel ones [lower panels]. Two different slit widths have been considered: $w = 300$nm and $w = 100$nm (left and right panels, respectively).

For gold systems, panels (a) and (b) in Fig. 6.10, show resonances emerging at $\lambda \approx 1550$nm, while the simulations for nickel present an almost flat spectra (panels (c) and (d)). Resonances in gold originate from the hybridization of Surface Plasmon Polaritons, and a localized Fabry-Perot resonance [20,49]. As we will see next, the nonlinear response is determined by both the intensity and width in frequency of the different spectral features in the linear regime. For slit arrays, transmission features strongly depend on both the width of the aperture and the optical properties of the metal (like in two-dimensional arrays of holes [82, 109]). In particular, absorption reduces the time photons stay inside the apertures, and this is evidenced in the full-width at half-maximum of the transmission peaks, $\Delta\lambda$. The fact that peaks in nickel are much wider than those in gold for the same geometrical parameters, suggests that absorption losses are dominant in the former case. In the same way, radiation losses are expected to depend mainly on the width of the opening. Hence, when studying $\Delta\lambda$ for slit arrays in gold where actual transmission resonances take place, we find wider transmittance peaks for wider openings because coupling with radiation is easier in them. Additionally, as photons stay less time inside wide apertures, absorbance is also lower in systems with wider openings, as can be seen in panels (a) and (b) in Fig. 6.10.

6.4.3 Nonlinear response

Next, we will characterize the nonlinear response of the slit arrays investigated in Fig. 6.10. We describe the nonlinear behavior for wavelengths fixed at transmittance maxima for gold, where intense EM fields are expected to occur. As slit arrays in nickel do not show resonant behavior, for a given slit width the same wavelengths are chosen for nickel and gold (see inset in each panel of Fig. 6.11) .

6.4.4 Optical Kerr Effect

Unless otherwise stated, we employ in our calculations a gaussian wave packet (GW), centered at a carrier frequency ω_o. All details concerning illumination sources can be found in Chapter 2. We are interested in nonlinear optical responses at a fixed wavelength, hence long standing pulses (narrow in frequency) must be launched. For these nonlinear calculations we illuminate the structure with a 820fs GW ($\sigma \approx 84\mu m$), so that the spectral width is $\Delta\lambda \approx$ 10nm. Left panels in Fig. 6.11 and Fig. 6.12 show the results of the First Harmonic (FH) transmitted and reflected intensities as a function of the maximum instantaneous input intensity (I_{in}), for gold and nickel systems, respectively. Two slit widths are considered: (a) w = 300nm and (c) w = 100nm. In the same figures thin lines represent transmitted, reflected and absorbed intensities obtained from extrapolation of the linear case. In arrays in gold (Fig. 6.11), when I_{in} increases the transmitted output intensity decreases to values lower than those expected from the linear transmittance. This reduction is more clear for w = 100nm. Interestingly, this transmitted output “limitation” occurs mostly at expense of the reflected current, so the absorption levels are restrained to values $<$ 10 GW/cm^2 within the input intensity range here studied. This reduction in transmitted output can be understood as follows:

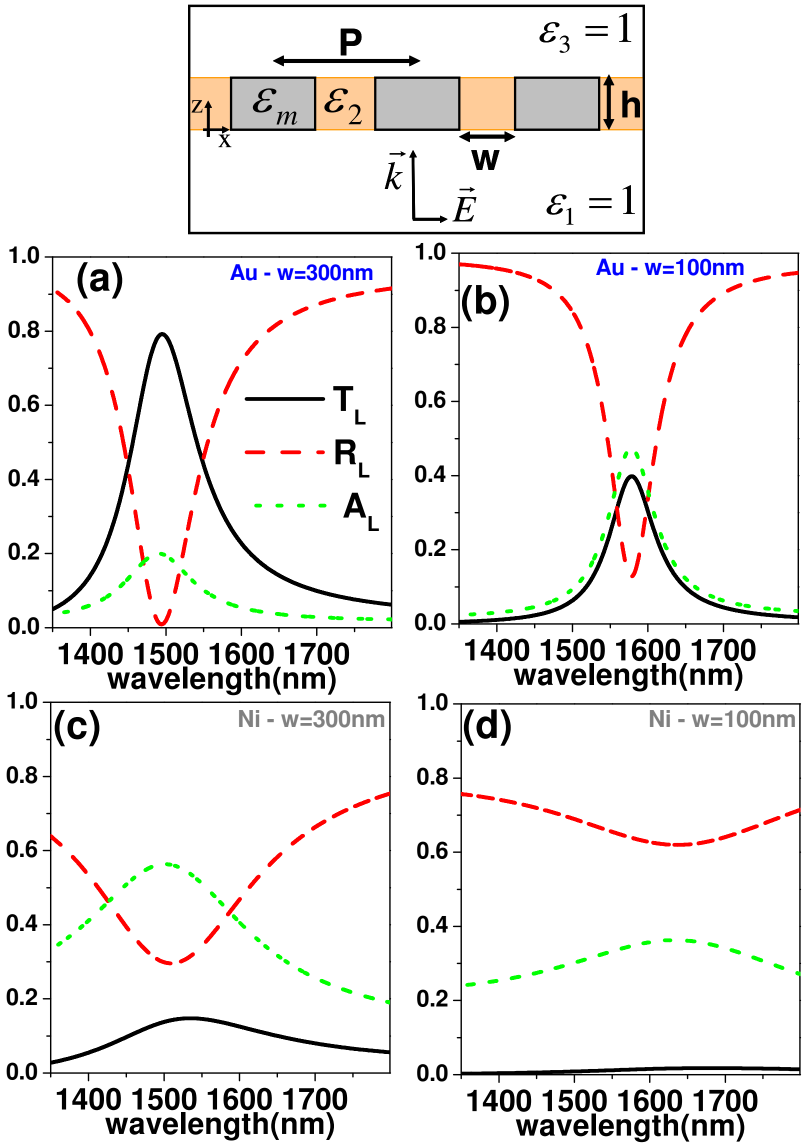

Figure 6.10: Panels (a) and (b) render transmission, reflection and absorption through gold metal films pierced by slits periodically arranged, as a function of wavelength. Two different slit widths $w = 300$nm and $w = 100$nm are chosen in panels (a) and (b), respectively. The slits are filled with a dielectric constant $\varepsilon_2 = 10.0$. The rest of geometrical parameters are $P = 1200$nm and $h = 185$nm. Panels (c) and (d) correspond to nickel. Figure top: schematic of the system.

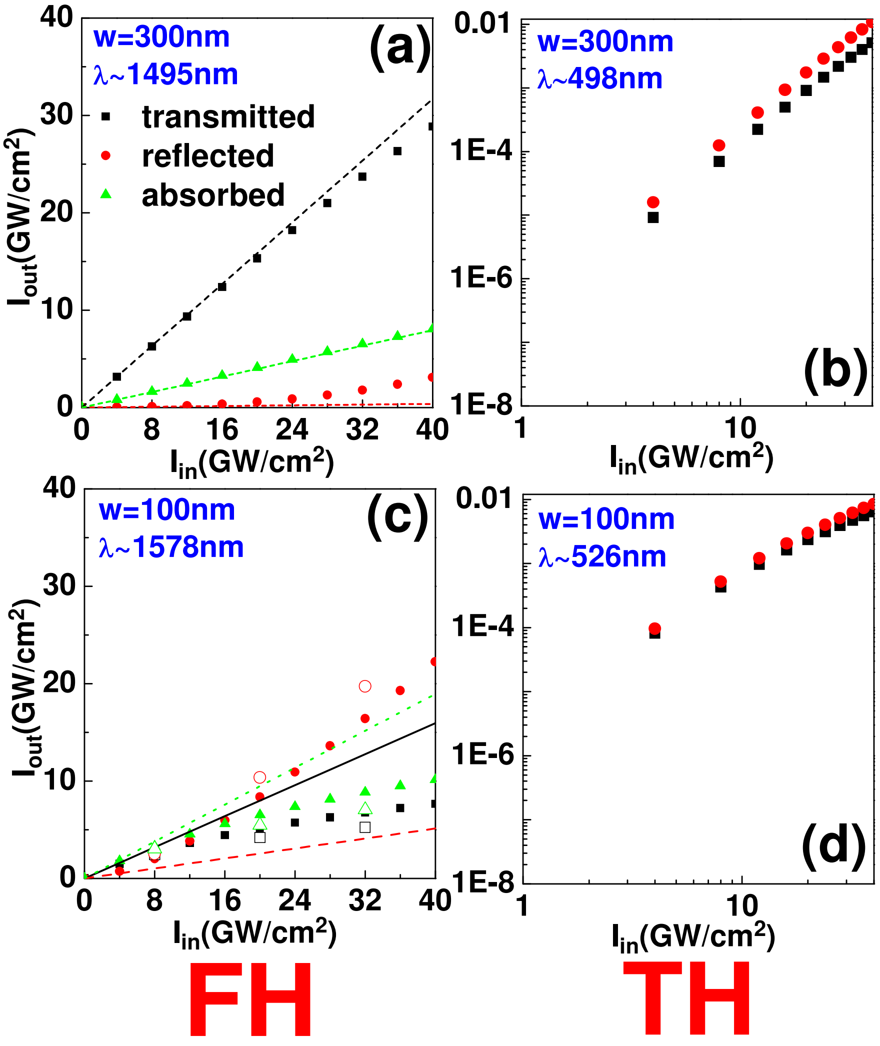

Figure 6.11: Slit arrays in gold (P = 1200nm, h = 185nm). Panels (a), (c) depict the calculated FH non-linear transmitted and reflected intensities, along with the absorption (symbols), as a function of the maximum instantaneous input intensity, at $\lambda \sim 1495$nm and $\lambda \sim 1578$nm, respectively. Additionally, the corresponding linear curves are depicted with thin lines. Panels (b) and (d) show TH emission (double logarithm scale), at $\lambda \sim 498$nm and $\lambda \sim 526$nm, respectively. The empty symbols in (c) renders the results for a plane wave.

OKE increases the dielectric constant of the Kerr-type dielectric filling the slits [Eq. (2.35)]. Therefore, the effect of increasing the input intensity can, in a first approximation, be understood by a rigid redshift of the linear spectrum. As we consider wavelengths for maximum transmittance in the linear case, the intensity-induced shift reduces the differential transmittance.

Figures 6.12(a) and (c) depict FH emission for nickel systems with $w =$ 300nm and $w = 100$nm, respectively. Notice that, for nickel, T and R hardly deviate from their values in the linear regime. As we will show later, for the considered intensities the induced change of the dielectric constant inside the slits is much smaller than for gold. Moreover, as the linear transmission and reflection spectra present very smooth variations, the small non-linear induced change in the dielectric constant translates into an even smaller change in the scattering coefficients.

Phenomena related to OKE occur due to local variations of the refractive index modulated by the average of the electric field intensity [Eq. (2.35)]. Since this change in the refractive index is not very large, for nonlinear dielectrics in bulk it is common to approximate it as $\Delta n = n_2 I_{in}$, where $n_2 = \frac{3\chi^{(3)}}{4n^2 c\varepsilon_0}$ is the Kerr coefficient, with $n = \sqrt{\varepsilon}$, and c the speed of light. However, this approximation assumes that no field enhancement takes place in the structure. If a nonlinear dielectric filling a slit array behaved as a dielectric in bulk, then: **i)** the electric field intensity should be homogeneous inside the slits, and **ii)** the field enhancement should be constant and close to unity for all wavelengths.

Let us investigate if the above postulations are fulfilled in the chosen structures. First, we consider another case where the illumination source is a plane wave (PW). To simulate this PW source ($e^{\imath\omega_o s/c}$), an exponentially increasing function is employed to switch on the source from zero to the stationary state at the Total Field Scattered Field boundaries (described in Chapter 2). This smooth “switching on” is necessary because otherwise there would be EM fields different from zero at $t = 0$ along these boundaries, provoking instabilities in the FDTD time evolution. Once the stationary state is reached, this source carries an instantaneous intensity identical to that of a GW at maximum. For comparison, Fig. 6.11(c) renders with empty symbols the FH intensity obtained with this source. We get slightly different results, which highlights an important consequence when dealing with nonlinear materials: the nonlinear optical response not only depends on the geometrical parameters, materials and intensity of the impinging light considered, but also on the spatial profile of the beam and its temporal dependence. These differences may be attributed to “memory effects”, precisely related to the particular EM field time evolution.

Next, Fig. 6.13 and Fig. 6.14 show a field enhancement coefficient defined as $\alpha = |\vec{E}(x,z)|/|\vec{E}_0|$ (left panels) and the corresponding local change in the

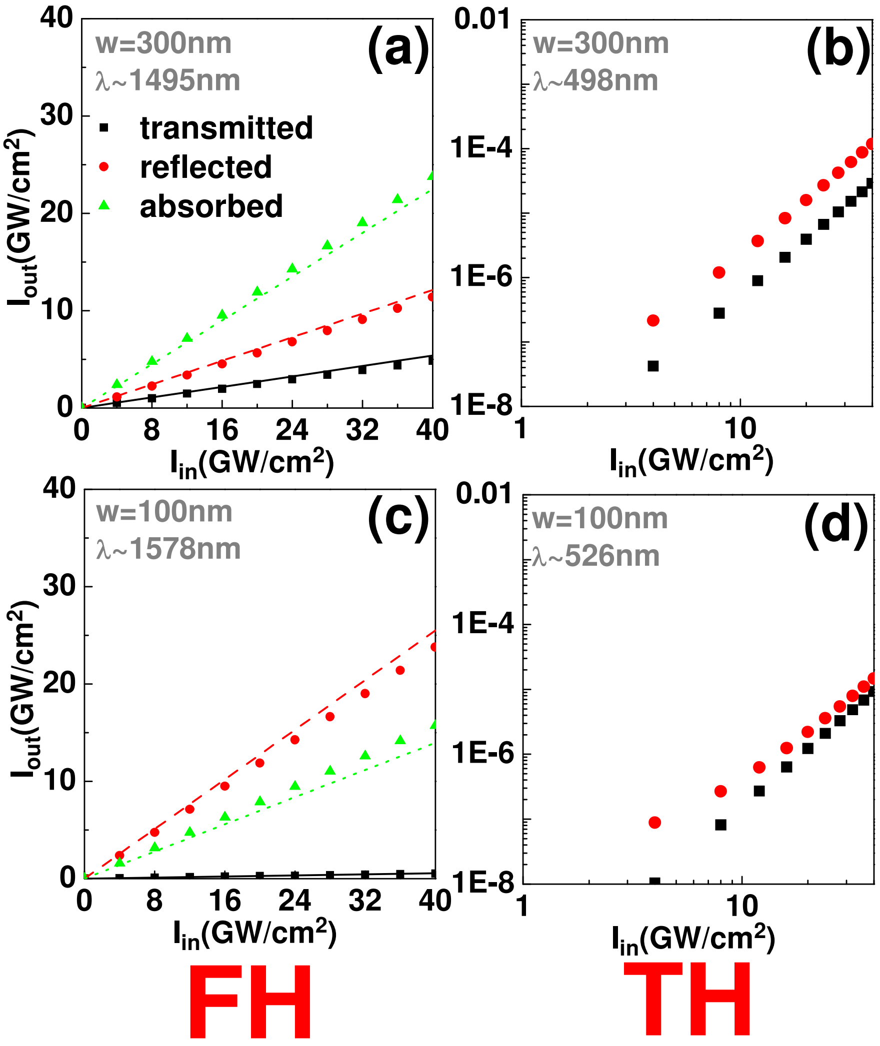

Figure 6.12: Slit arrays in nickel ($P = 1200$nm, $h = 185$nm). Panels (a), (c) depict the calculated FH non-linear transmitted and reflected intensities, along with the absorption (symbols), as a function of the the maximum instantaneous input intensity, at $\lambda = 1495$nm and $\lambda = 1578$nm, respectively. Additionally, the corresponding linear curves are depicted with thin lines. Panels (b) and (d) show the corresponding TH calculations, at $\lambda \sim 498$nm and $\lambda \sim 526$nm, respectively.

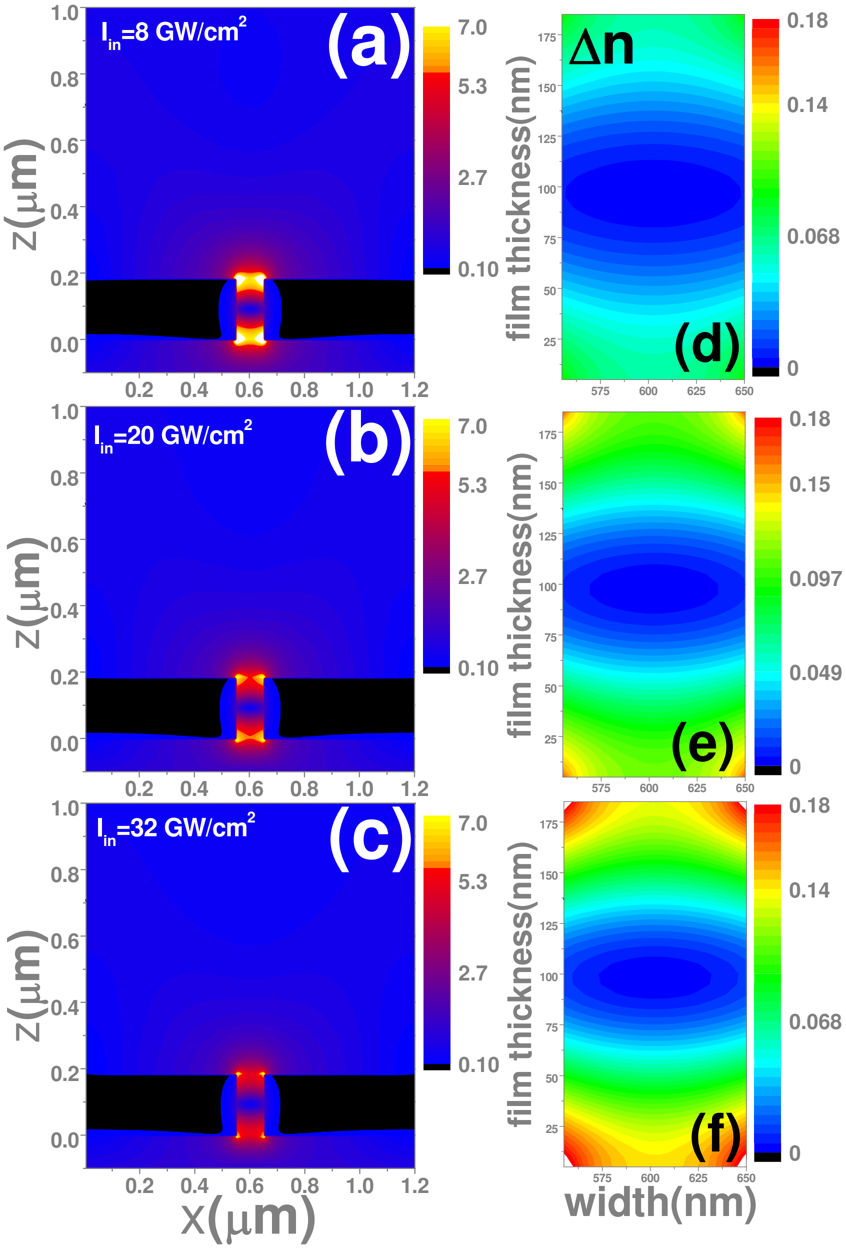

Figure 6.13: For a slit array in gold (P = 1200nm, h = 185nm, w = 100nm) illuminated with a PW ($\lambda \sim$ 1578nm), panels (a), (b), (c) display $|\vec{E}(x,z)|/|\vec{E}_0|$ for an unit cell, for three different values of I_{in}: 8GW/cm^2, 20GW/cm^2 and 32GW/cm^2, respectively. The corresponding local change in the refractive index inside the slits, $\Delta n(x,z)$, is depicted in panels (d), (e) and (f).

refractive index only inside the slits, $\Delta n(x,z)$ (right panels), for slit arrays in gold and in nickel, respectively. Three different instantaneous input intensities are considered, and the slit width is chosen to be $w = 100$nm. The local change of the refractive index inside the slits is computed from the values of the electric field amplitude at the stationary state. These figures show that for gold systems both the field enhancement coefficient and $\Delta n(x,z)$ strongly depend on the incident intensity (where different patterns are obtained for each incident intensity), whereas the panels for nickel systems present negligible changes in the pattern for any I_{in}. Additionally, both metals present inhomogeneous $\alpha(x,z)$ field enhancements with high intensity lobes at the entrance and at the exit of the slits, and a field decrease through the middle.

For a slit array in gold ($P = 1200$nm, $h = 185$nm, $w = 100$nm) illuminated with a PW ($\lambda \sim 1578$nm), panels (a), (b), (c) display $|\vec{E}(x,z)|/|\vec{E}_0|$ for an unit cell, for three different values of I_{in}: 8GW/cm^2, 20GW/cm^2 and 32GW/cm^2, respectively. The corresponding local change in the refractive index inside the slits, $\Delta n(x,z)$, is depicted in panels (d), (e) and (f).

These results indicate that OKE in gold systems arises from two effects: **i)** linear transmission spectra depend on the incident wavelength and **ii)** $\alpha(x,z)$ are inhomogeneous spatial coefficients that depend on the incident intensity. Therefore, when the incident intensity increases, so does the field enhancement coefficient, and this translates into an increase of $\Delta n(x,z)$. As an increase of the dielectric constant in the linear regime produces a rigid redshift of the linear spectrum, only for gold systems where sharp transmission features take place, the nonlinear response deviates rapidly from the linear regime. On the contrary, in nickel systems, neither the linear spectra depend on the wavelength, nor the field enhancement coefficient depend on the incident intensity, and as a result, the nonlinear optical response associated to the OKE hardly deviates from the linear regime.

6.4.5 Third Harmonic Generation

In this section we investigate Third Harmonic (TH) emission arising from the nonlinear dielectric filling the slits. As in Section 6.4.4, Fig. 6.11 corresponds to calculations for slit arrays in gold, and Fig. 6.12 to nickel systems. Panels (b) and (d) correspond to TH calculations. For gold systems we observe that TH currents are several orders of magnitude smaller than either the input intensity or the corresponding FH values (depicted with full symbols in panels (a) and (c)). For nickel systems, despite FH transmission does not deviate from what would be expected if the system responded linearly [panels (a) and (c)], the appearance of TH radiation unveils third order nonlinear processes

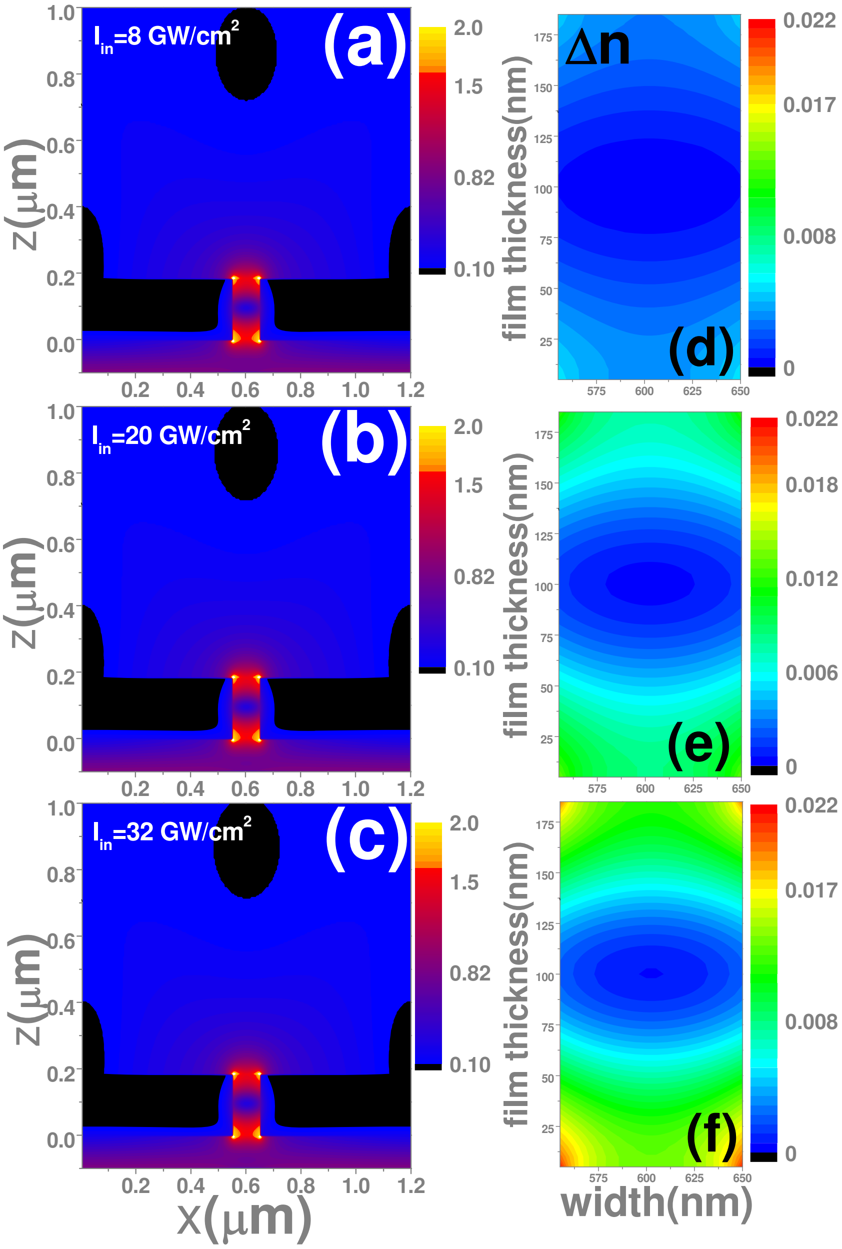

Figure 6.14: Similar study to the one shown in Fig. 6.13 but for a slit array in nickel ($P = 1200$nm, $h = 185$nm, $w = 100$nm) illuminated with a PW ($\lambda = 1578$nm).

taking place inside the slits.

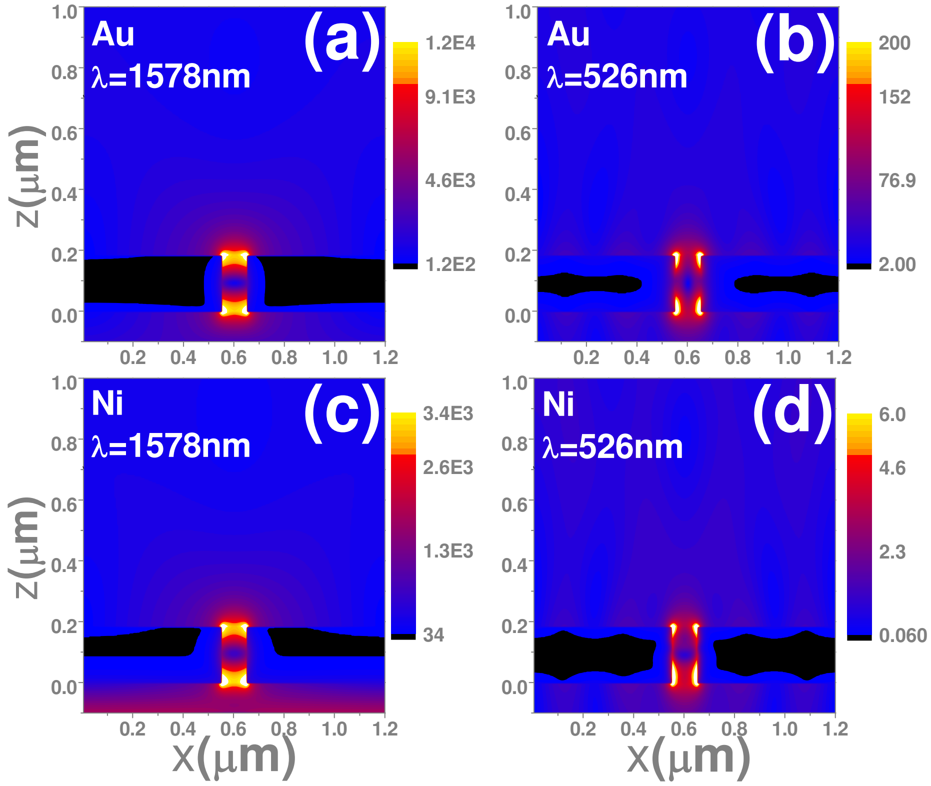

Figure 6.15: Electric field amplitude in a slit array at $\lambda = 1578$nm (FH) and $\lambda = 526$nm (TH). Panels (a) and (b) are for gold and (c) and (d) for nickel. The incident intensity is $I_{in} = 32\text{GW/cm}^2$, $w = 100$nm and the rest of geometrical parameters as in Fig. 6.10.

Interestingly, despite R_L in the linear regime at the corresponding wavelength where TH emission takes place, $\lambda = 526$nm, is orders of magnitude larger than T_L, nonlinear calculations in Fig. 6.11 and Fig. 6.12 show almost identical TH radiated currents. For instance, in the linear regime for slits in gold and $w = 100$nm, $R_L = 0.67$ and $T \approx 2.4 \cdot 10^{-4}$ at $\lambda = 526$nm, while in the nonlinear regime emission into the reflection region is only 1.3 times larger than the one emitted into the transmission half-space. Because TH emission goes as the cubed local intensity, it is expected to be a function of both time and space. Figure 6.15 shows the electric field amplitudes for the $w = 100$nm slits at $I_{in} = 32\text{GW/cm}^2$. Panels (a) and (b) depict near field in the case of gold at $\lambda = 1578$nm (FH) and $\lambda = 526$nm (TH), respectively. The bottom panels, (c) and (d), show the same but for nickel. This figure suggests that if the structure is designed so that FH is efficiently transmitted, the field at the exit of slits must be comparable to the fields at the entrances. In that case, transmission coefficients at the wavelength where TH generates do not play an important role because light is generated directly close to the slit exits. Besides, although gold and nickel show similar distributions of the electric field amplitudes, local intensity is much higher in gold slits than in nickel ones (compare panels (a) and (c)).

6.5 Conclusions

In Section 6.3 we have theoretically studied the nonlinear response of a metallic-slit structure deposited on a dielectric substrate with Kerr nonlinearity. We have described both a nonlinear intensity limiter and an optical switch, at the telecom range. The physical mechanism of both operation modes is based on sharp variations in the linear transmission close to the transmission minima present in arrays of sub-wavelength apertures in metal films.

In Section 6.4, we have theoretically analyzed the nonlinear optical response of arrays of slits, drilled on either gold or nickel films, filled with a third order nonlinear material. A priori all of them should display optical effects related to OKE and TH Generation. However, these effects strongly depend on the material properties of both the dielectric filling the slits and the metal chosen. We attribute to OKE the behavior found in the transmitted and reflected currents calculated for the slit arrays in gold. However, in nickel OKE is not strong enough for boosting noticeable modifications in the optical spectra. This shows that the efficiency of the nonlinear response strongly depends on the intrinsic losses, and that losses due to absorption play the most important role in these systems. Furthermore, TH Generation is observed for both metals.

Appendix A

Annular hole waveguide modes

In this Appendix, we provide analytical expressions appearing in our Coupled Mode Method for the waveguide modes sustained by annular holes with outer radius a and inner radius b under PEC approximation.

The transverse electromagnetic mode (TEM) using cylindrical polar coordinates is given by

$$\langle r|T(r,\theta)\rangle = \frac{1}{\sqrt{2\pi Ln(c)}}\frac{1}{r}\,\hat{u_r} \tag{6.14}$$

The transverse-electric modes (TE) are distinguished by a subscript $s = 1$ and are expressed in terms of the Bessel-Neumann combination

$$I_n(\chi'_{nm}\frac{r}{b}) = \frac{\sqrt{\pi\epsilon_n}}{2}\frac{J_n(\chi'_{nm}\frac{r}{b})Y'_n(\chi'_{nm}) - Y_n(\chi'_{nm}\frac{r}{b})J'_n(\chi'_{nm})}{\left\{\left[\frac{J'_n(\chi'_{nm})}{J'_n(c\chi'_{nm})}\right]^2\left[1-\left(\frac{n}{c\chi'_{nm}}\right)^2\right] - \left[1-\left(\frac{n}{\chi'_{nm}}\right)^2\right]\right\}^{1/2}} \tag{6.15}$$

where the quantity χ'_{nm} is the mth non-vanishing root of the function $I'_n(cx)$, $'$ stands for derivative and $c = a/b$.

In describing TM ($s = 2$) modes, it is convenient to introduce the combination

$$Z_n(\chi_{nm}\frac{r}{b}) = \frac{\sqrt{\pi\epsilon_n}}{2}\frac{J_n(\chi_{nm}\frac{r}{b})Y_n(\chi_{nm}) - Y_n(\chi_{nm}\frac{r}{b})J_n(\chi_{nm})}{\left[\frac{J_n^2(\chi_{nm})}{J_n^2(c\chi_{nm})} - 1\right]^{1/2}} \tag{6.16}$$

where χ_{nm} is the mth root of the function $Z_n(cx)$

The roots χ_{nm} and χ'_{nm} are determined numerically using the Bisection method. A fourth index, l, is required to distinguish those modes having zero azimuthal component of $\mathbf{E_t}$ along the aperture diameter defined by $\theta = 0, \pi$ from those having zero radial component of $\mathbf{E_t}$ along the same diameter (vertical modes). Then, the TE and TM modes are given by

$$\langle r|\Psi_{1nm1}(r,\theta)\rangle = \frac{n}{r} I_n(\chi'_{nm}\frac{r}{b}) \sin(n\theta)\hat{u}_r + \frac{\chi'_{nm}}{b} I'_n(\chi'_{nm}\frac{r}{b}) \cos(n\theta)\hat{u}_\theta \quad (6.17)$$

$$\langle r|\Psi_{1nm2}(r,\theta)\rangle = -\frac{n}{r} I_n(\chi'_{nm}\frac{r}{b}) \cos(n\theta)\hat{u}_r + \frac{\chi'_{nm}}{b} I'_n(\chi'_{nm}\frac{r}{b}) \sin(n\theta)\hat{u}_\theta \quad (6.18)$$

$$\langle r|\Psi_{2nm1}(r,\theta)\rangle = -\frac{\chi_{nm}}{b} Z'_n(\chi'_{nm}\frac{r}{b}) \sin(n\theta)\hat{u}_r - \frac{n}{b} Z_n(\chi'_{nm}\frac{r}{b}) \cos(n\theta)\hat{u}_\theta \quad (6.19)$$

$$\langle r|\Psi_{2nm2}(r,\theta)\rangle = -\frac{\chi_{nm}}{b} Z'_n(\chi'_{nm}\frac{r}{b}) \cos(n\theta)\hat{u}_r + \frac{n}{b} Z_n(\chi'_{nm}\frac{r}{b}) \sin(n\theta)\hat{u}_\theta \quad (6.20)$$

The above set of modes, $\langle r|\Psi_{snml}(r,\theta)\rangle$, together with the TEM mode, forms a complete orthonormal set on the aperture region, $b \leq r \leq a$ and $0 \leq \theta \leq 2\pi$. The dependance along the z direction is taken $e^{ik_z z}$, where $k_z = \sqrt{g^2 - \frac{\chi^2_{nm}}{b^2}}$ for TM modes, and with the corresponding χ'_{nm} for TE ones. Note that $g = 2\pi/\lambda$.

In particular, as we said along Chapter 2, for subwavelength holes good convergency is attained only considering the less decaying TE mode (the fundamental waveguide mode). We will label this mode as TE_{11}-mode. In this case,

$$\langle r|TE_{11}\rangle = \langle r|\Psi_{1111}(r,\theta)\rangle = \frac{1}{r} I(\chi'\frac{r}{b}) sin(\theta)\hat{u}_r + \frac{\chi'}{b} I'(\chi'\frac{r}{b}) cos(\theta)\hat{u}_\theta \quad (6.21)$$

Appendix B

Overlapping integrals between Bloch waves and annular hole waveguide modes

As we stated in Chapter 2, overlapping integrals between Bloch waves and annular hole waveguide modes $\langle \mathbf{k}_{||}\sigma|n\rangle$ are known analytically [85]. And as we also said in that Chapter, every compact "object" n denotes any waveguide EM mode considered in the expansion, characterized by the indices $n = (r, s, n, m, l)$ where r denotes the position of the aperture, and the other four ones are defined in Appendix A.

Let us then define $\langle \mathbf{k}_{||}\sigma|n\rangle = S^{\sigma}$ for the TEM mode, and also $\langle \mathbf{k}_{||}\sigma|n\rangle = S^{\sigma}_{snml}$ where $\sigma = 1$ denotes s-polarization, and $\sigma = 2$ p-polarized light. With pq indexes we will define $\tan(\theta_{pq}) = \frac{k_y/|k_{||}|}{k_x/|k_{||}|}$, and $k_{||} = \sqrt{k_x^2 + k_y^2}$ in the xy plane.

By using

$$\begin{aligned} \hat{u}_x &= \cos(\theta)\hat{u}_r - \sin(\theta)\hat{u}_\theta \\ \hat{u}_y &= \sin(\theta)\hat{u}_r + \cos(\theta)\hat{u}_\theta \end{aligned} \tag{6.22}$$

and

$$\begin{aligned} x &= r\cos(\theta) \\ y &= r\sin(\theta) \end{aligned} \tag{6.23}$$

we can write for the TEM mode:

$$\begin{aligned} S^{(1)} &= 0 \\ S^{(2)} &= \frac{2\pi i}{\sqrt{2\pi \mathrm{Lnc}}} \frac{J_0(k_{||}a) - J_0(k_{||}b)}{k_{||}} \end{aligned} \tag{6.24}$$

and for TE and TM modes:

$$
\begin{aligned}
S^1_{1nm1} &= 2\pi\chi'^2_{nm}b(-i)^{n-1}\cos(n\theta_{pq})\cdot\frac{\left[I_n(\chi'_{nm})J'_n(bk_{||})-cI_n(c\chi'_{nm})J'_n(ak_{||})\right]}{(b^2k^2_{||}-\chi'_{nm})}\\
S^1_{1nm2} &= -\tan(n\theta_{pq})\cdot S^1_{1nm1}\\
S^1_{2nm1} &= 0\\
S^1_{2nm2} &= 0\\
S^2_{1nm1} &= 2\pi(-i)^{n-1}\sin(n\theta_{pq})\cdot\frac{\left[I_n(c\chi'_{nm})J_n(ak_{||})-I_n(\chi'_{nm})J_n(bk_{||})\right]}{k_{||}}\\
S^2_{1nm2} &= -\cot(n\theta_{pq})\cdot S^2_{1nm1}\\
S^2_{2nm1} &= -2\pi\chi^2_{nm}b(-i)^{n-1}\sin(n\theta_{pq})\cdot\frac{\left[cZ_n(c\chi_{nm})J_n(ak_{||})-Z'_n(\chi_{nm})J_n(bk_{||})\right]}{(b^2k^2_{||}-\chi'_{nm})}\\
S^2_{2nm2} &= \cot(n\theta_{pq})\cdot S^2_{2nm1}
\end{aligned}
\tag{6.25}
$$

For the sake of clarity, let us remark that only S^1_{1111}, S^2_{1111} and $S^{(2)}$ will be used along the thesis within the minimal model approach (accounting for the overlaps with the TE_{11}, and the TEM, respectively).

Green Function for Finite Systems

In this section we provide full details for the computation of G_{nm} when dealing with finite systems. As it was said in Chapter 2, $G^{\sigma=p}_{nm}$, within SIBC, diverges whenever $1 + Z_s Y_{\mathbf{k}_{||}\sigma} = 0$.

If we rewrite this object in terms of the normalized wavevector $\mathbf{q}$, where $\mathbf{k} = \sqrt{\varepsilon}g\mathbf{q}$, it is easy to find out that $G^{\sigma=p}_{nm}$ presents a branch point at $q = 1$, and a pole at $q_p = \sqrt{1 - Z_s^2}$ very close to the real axes which contains the contribution of the plasmon. These two singularities must be treated specially when computing $G^{\sigma=p}_{nm}$.

These integrals can be calculated both in real axes and in complex plane, and therefore, Cauchy integral theorem in complex plane must be fulfilled. This theorem in complex analysis establishes that if two different paths connect the same two points, and a function is holomorphic everywhere 'in between' the two paths, then the two path integrals of the function will be the same. For the sake of clarity, Fig. 6.16 schematically presents different paths along real axes and complex plane to show that if Cauchy theorem is fulfilled, the results integrating along any of these paths will be the same. Moreover, at long distances, only the plasmon contribution must remain, hence some strategic paths in the complex plane may separate this contribution.

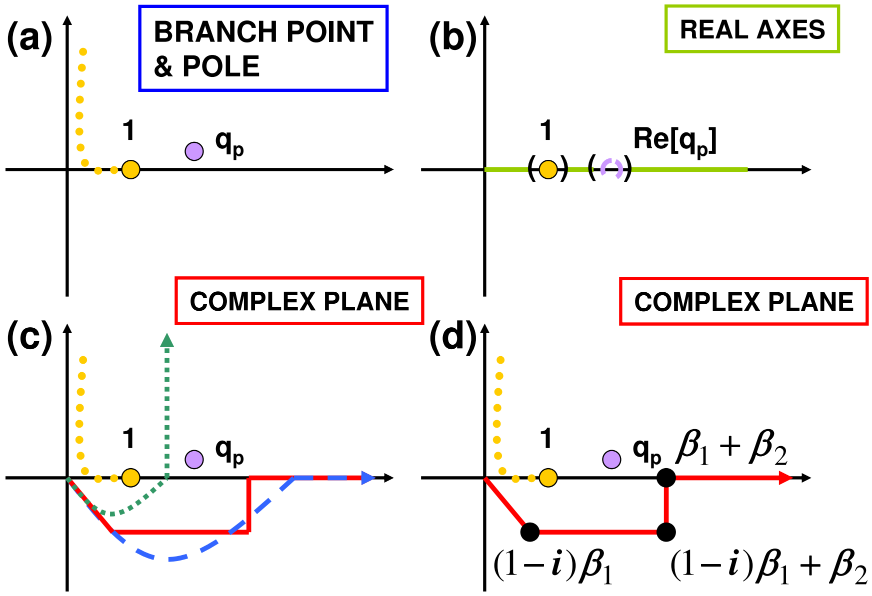

Figure 6.16: Illustration of (a) the branch point with a dashed curve close to $q = 1$, and the plasmon pole at $q = q_p$, (b) the possible integration path along the real axes, (c) the possible integration paths in the complex plane where Cauchy theorem must be fulfilled, and (d) the integration path considered in our calculations.

We conducted three different calculations to check the results. First, I decided to start with the integral in the real k-axes simply because I understood this case better. Next, I checked its validity by implementing the integral in the complex plane without splitting off the plasmon contribution in order to compare that both integrals provided the same results. Moreover, I used Cauchy integral theorem by choosing different paths in the complex plane. Finally, I also obtained the proper plasmon contribution at large distances.

1. Real Axes

   Let us start by treating the branch point and the pole with the integral along real axes (schematics in panel (b) of Fig.6.16). Apart from a function $F(q)$ which contains the overlaps that depend upon some linear combinations of $J_1(x)$ and $Y_1(x)$, we must pretty much calculate the following integral for $G_{11}^{\sigma=p}$:

$$\int_0^\infty dq \frac{1}{\sqrt{1-q^2}+Z_s} \tag{6.26}$$

   The linearity of integration allows us to break this complicated integral into simpler ones around the branch point and the pole:

$$\int_0^\infty = \int_0^{1-\delta_1} + \int_{1-\delta_1}^{1+\delta_1} + \int_{1+\delta_1}^{q_p-\delta_2} + \int_{q_p-\delta_2}^{q_p+\delta_2} + \int_{q_p+\delta_2}^{10q_p} + \int_{10q_p}^{q_{max}} \tag{6.27}$$

where $2\delta_1$ and $2\delta_2$ in the 2^{nd} and 4^{th} terms are small intervals around $q = 1$ and $q = q_p$ where the integrals must be treated specially, whereas the other ones as well as $G_{11}^{\sigma=s}$ can be computed numerically. Additionally, since the integrand oscillates for large q_p values, we divide the last part of the integral into two to obtain numerical convergency. Here q_{max} is the value which provides converged results.

Panels in Fig. 6.17 show a representative case of the real and imaginary parts of the TE and TM components of an integrand. In particular, this is the integrand of G_{12} as a function of $q_{||}$ at $\lambda = 630$nm in a system with a circular hole of radius $r_c = 125$nm, and a concentric annular groove at a distance $a = 5000$nm whose width and depth are $w_g = 220$nm and $h_g = 90$nm, respectively, drilled in a 280nm gold film thickness on a glass substrate. In this system, at $\lambda_0 = 630$nm we excite a plasmon with $k_p/k_0 = 1.04 + 0.0052\,i$. It can be seen in panel (a) and inset in panel (b) that the TE-integrand presents an abrupt behavior at $q = 1$. Moreover, panel (b) also shows that this integrand still oscillates for large q values. Panels (c) and (d) show the TM-integrand with different colors corresponding to the six simpler integrals appearing in Eq. 6.27. Again, both panels show abrupt changes at $q = 1$, but also at $q = q_p = 1.04$.

To calculate the 2^{nd} term:

$$\int_{1-\delta_1}^{1+\delta_1} = \int_{1-\delta_1}^{1} + \int_{1}^{1+\delta_1} \tag{6.28}$$

If we make the substitution $q = 1 + x$, where $x << 1$, we obtain $dq = dx$ and the proper integration limits:

$$\begin{aligned} \int_{1-\delta_1}^{1} dq \frac{1}{\sqrt{1-q^2+Z_s}} &= \int_{-\delta_1}^{0} dx \frac{1}{\sqrt{-2x+Z_s}} \\ &= \sqrt{2\delta_1} + Z_s Ln\left(\frac{Z_s}{\sqrt{2\delta_1}+Z_s}\right) \end{aligned} \tag{6.29}$$

In the same way:

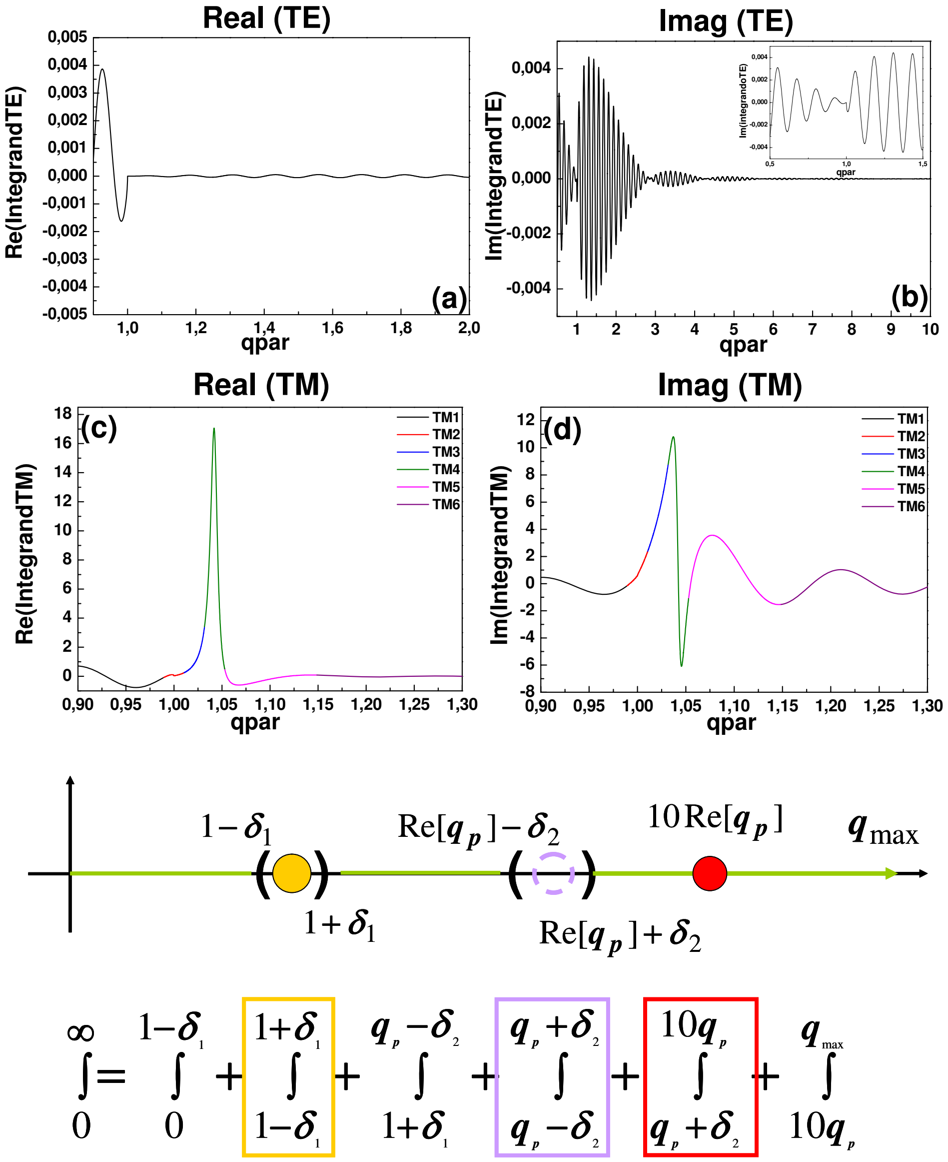

$$\int_0^\infty = \int_0^{1-\delta_1} + \boxed{\int_{1-\delta_1}^{1+\delta_1}} + \int_{1+\delta_1}^{q_p-\delta_2} + \boxed{\int_{q_p-\delta_2}^{q_p+\delta_2}} + \boxed{\int_{q_p+\delta_2}^{10q_p}} + \int_{10q_p}^{q_{max}}$$

Figure 6.17: Real and Imaginary parts of the TE- and TM-integrand of G_{12} as a function of $q_{||}$ at $\lambda = 630$nm in a system with a circular hole of radius $r_c = 125$nm, and a concentric annular groove at a distance $a = 5000$nm whose width and depth are $w_g = 220$nm and $h_g = 90$nm, respectively, drilled in a 280nm gold film thickness on a glass substrate.

$$\begin{aligned}\int_1^{1+\delta_1} dq\frac{1}{\sqrt{1-q^2+Z_s}} &= -i\int_0^{\delta_1} dx\frac{1}{\sqrt{2x-iZ_s}} \\ &= -i\sqrt{2\delta_1} - Z_s Ln\left(\frac{Z_s}{i\sqrt{2\delta_1}+Z_s}\right) \qquad (6.30)\end{aligned}$$

Finally:

$$\int_{1-\delta_1}^{1+\delta_1} dq\frac{1}{\sqrt{1-q^2+Z_s}} = \sqrt{2\delta_1}(1-i) + Z_s Ln\left(\frac{Z_s+\sqrt{2\delta_1}}{Z_s+i\sqrt{2\delta_1}}\right) \qquad (6.31)$$

where $F(q)$ must be evaluated at $q=1$.

Next, to calculate the 4^{nd} term where a pole is involved, we first define q_p from $\sqrt{1-q^2}+Z_s=0 \longrightarrow q_p=\sqrt{1+|Z_i|^2}$, where $Z_s=Z_r+iZ_i$, and then we operate on integrand:

$$\begin{aligned}\int_{q_p-\delta_2}^{q_p+\delta_2} dq\frac{1}{\sqrt{1-q^2+Z_s}} &= \int_{q_p-\delta_2}^{q_p+\delta_2} dq\frac{1}{i\sqrt{q^2-1}+Z_s} \\ &= \int_{q_p-\delta_2}^{q_p+\delta_2} dq\frac{-i\sqrt{q^2-1}+Z_s^*}{(\sqrt{q^2-1}+Z_i)^2+Z_r^2} \qquad (6.32)\end{aligned}$$

If we make the substitution $q=q_p+x$, where $x << q_p$ and $x << Z_i^2/2$, the root becomes

$$\sqrt{q^2-1} \approx (q_p^2-1+2q_p x)^{1/2} \approx Z_i\left(1+\frac{2q_p x}{2Z_i^2}\right) \approx |Z_i| + \frac{q_p x}{Z_i} \qquad (6.33)$$

By replacing the latter in Eq. 6.32, then:

$$\begin{aligned}\int_{q_p-\delta_2}^{q_p+\delta_2} dq\frac{-i\sqrt{q^2-1}+Z_s^*}{(\sqrt{q^2-1}+Z_i)^2+Z_r^2} &\approx \int_{-\delta_2}^{\delta_2} dx\frac{-i|Z_i| - i\frac{q_p x}{|Z_i|} + Z_r - iZ_i}{\frac{q_p^2 x^2}{|Z_i|^2}+Z_r} \\ &= -i\frac{|Z_i|}{q_p} Ln\left(\frac{\delta_2 - i\alpha}{\delta_2+i\alpha}\right) \qquad (6.34)\end{aligned}$$

where we have defined $\alpha=\frac{Z_r|Z_i|}{q_p}$ and $F(q)$ must be evaluated at $q=q_p$.

Once we compute the whole integral we must ensure its convergency with q_{max}. As an example, in Fig. 6.18 we calculate G_{11}, G_{12} and G_{22} at $\lambda = 630$nm for the same system as in Fig. 6.17. We observe that convergency is attained at very low values of q_{max}.

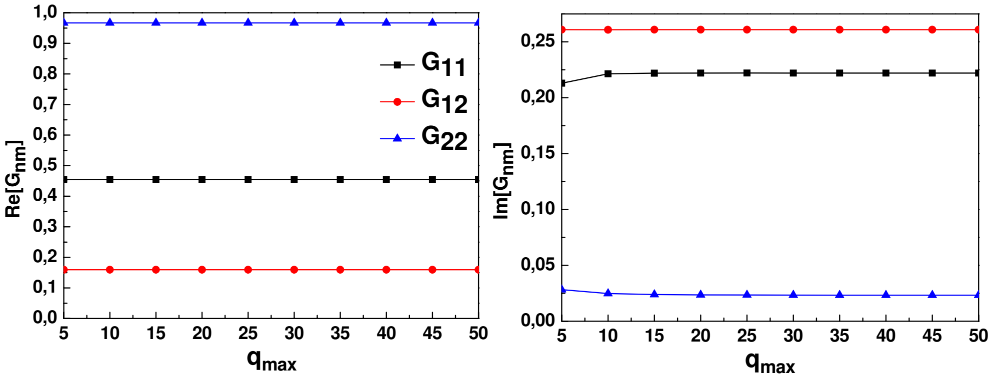

Figure 6.18: Real and Imaginary parts of G_{11}, G_{12}, and G_{22} as a function of q_{max} at $\lambda = 630$nm for a system with a circular hole of radius $r_c = 125$nm, and a concentric annular groove at a distance $a = 5000$nm whose width and depth are $w_g = 220$nm and $h_g = 90$nm, respectively drilled in a 280nm gold film thickness on a glass substrate.

2. Complex Plane

   To calculate the same integral but in the complex plane we first choose the path appearing in panel (d) in Fig. 6.16, avoiding both the branch point and the pole at the same time, so the plasmon contribution is not extracted analytically. With the same q_{max} that provides convergency in the real axes ($q_{max} \approx 20$), in the upper panel in Fig. 6.19 we depict the results obtained for the same system as in Fig. 6.18 but just for G_{12}, as a function of the distance of the annular groove to the central hole, a. As expected, both results are equivalent. Additionally, varying the values of β_1 (see schematics in Fig. 6.16(a)) we also checked that Cauchy integral theorem is fulfilled. Finally, we know that at large distances only the plasmon contributes. As we said before, in this system at $\lambda_0 = 630$nm we excite a plasmon with $k_p/k_0 = 1.04 + 0.0052\,i$. Taking Fourier transform of G_{12}, in the lower panel in Fig. 6.19 we find an isolated resonance which verifies the fact that at large distances only the plasmon contributes.

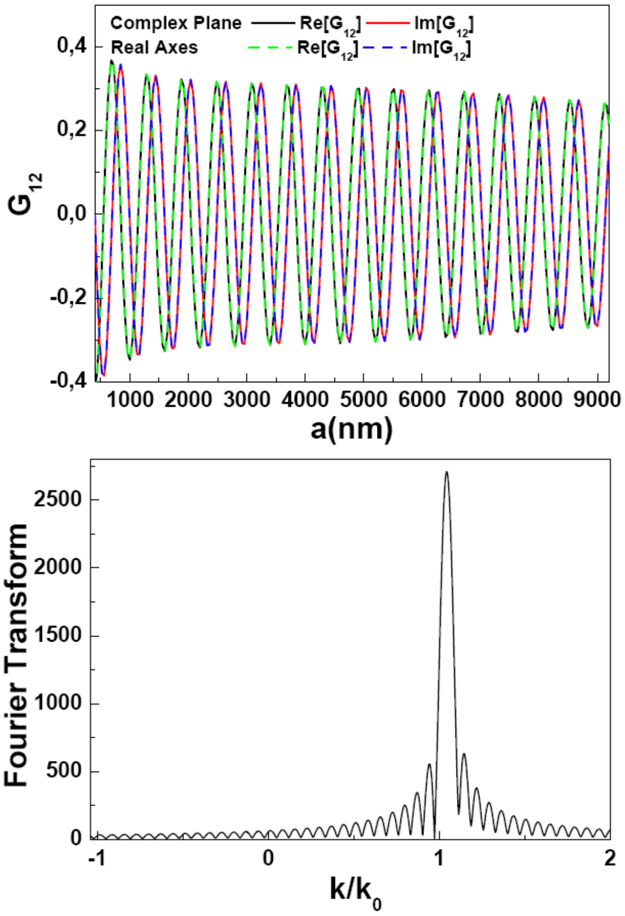

Figure 6.19: (Top) Real and Imaginary parts of G_{12} at $\lambda = 630$nm for a system with a circular hole of radius $r_c = 125$nm, and a concentric annular groove whose width and depth are $w_g = 220$nm and $h_g = 90$nm, respectively, drilled in a 280nm gold film thickness on a glass substrate, as function of the distance of the annular groove to the central hole, a. (Bottom) Fourier transform showing the plasmon contribution of the same system as in left panel.

Appendix C

Wavevector of a real metal waveguide, k_{nz}

To improve the approximation where PEC is taken at vertical walls inside the apertures, we can consider inside them the propagating constant along the z direction of an infinite annular hole made of real metal, k_{nz}. The corresponding calculation for circular cylinders applicable to circular holes can be found in some electromagnetic books [187]. In that case, the continuity of the tangential components of the EM fields leads to a homogeneous system that admits a nontrivial solution only in case its 4×4 determinant is zero. The expansion of this determinant gives rise to a transcendental equation whose roots are the allowed values of the propagation factor. In contrast, the result for the corresponding calculation in annular holes does not appear explicitly in literature (to our knowledge) and, although the study is straight forward, the roots of an 8×8 determinant need to be compute. In Fig.6.20 it is schematically presented a transverse section of the system under study. Regions i and e correspond to the interior and exterior metallic regions, and the region in the middle m, corresponds to the aperture. Finally, a and b are the outer and inner radius, respectively.

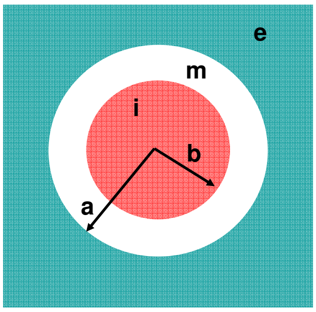

Figure 6.20: Schematics of an annular aperture. Regions i and e correspond to the interior and exterior metallic regions, respectively, and the region in the middle m, to the aperture. a and b are the outer and inner radius, respectively.

We are dealing with solutions of the Helmholtz equation in cylindrical coordinates, so amongst the ingredients in our study there will be Bessel functions of integer order n, $J_n(x)$; of the second kind, $Y_n(x)$; and also linear combinations of the last two, Hankel functions, $H_n^{(1)} = J_n(x) + iY_n(x)$. Within regions i and e every EM field component can be represented by linear combinations of the elementary wave functions:

$$\langle \mathbf{r}|\Psi_i\rangle = e^{in\theta} J_n\left(\sqrt{k_{iz}^2 - k_{nz}^2}\cdot r\right) e^{ik_{nz}z} \tag{6.35}$$

$$\langle \mathbf{r}|\Psi_e\rangle = e^{in\theta} H_n^{(1)}\left(\sqrt{k_{ez}^2 - k_{nz}^2}\cdot r\right) e^{ik_{nz}z} \tag{6.36}$$

where Ψ are auxiliary functions from which the electric and magnetic fields can be computed. $J_n(x)$ are finite at the origin ($x = 0$), and $H_n^{(1)}(x)$ must be employed at great distances because it reduces asymptotically to a wave traveling radially outward. As a technical note let us point out that Bessel functions admitting complex arguments have to be computed. Additionally, in some cases, large values of the argument are obtained, and asymptotic expansion in Hankel functions must be taken:

$$H_n^{(1)}(z) = \sqrt{\frac{2}{\pi z}} e^{i\left(z-(n+\frac{1}{2})\frac{\pi}{2}\right)}(P_\mu(z) + iQ_\mu(z)), \quad -\pi < arg(z) < 2\pi \tag{6.37}$$

with

$$\begin{aligned} P_\mu(z) &\approx 1 - \frac{(\mu-1)(\mu-9)}{2!(8z)^2} + \frac{(\mu-1)(\mu-9)(\mu-25)(\mu-49)}{4!(8z)^4} - ... \\ Q_\mu(z) &\approx \frac{(\mu-1)}{1!(8z)} - \frac{(\mu-1)(\mu-9)(\mu-25)}{3!(8z)^3} + ... \end{aligned} \tag{6.38}$$

and $\mu = 4n^2$.

Due to the fact that the propagation constant in metallic regions (i.e., i and e regions) is the same, then $k_{iz} = k_{ez} = g\epsilon_m$ (remember that $g = 2\pi/\lambda$ and ε_m is the dielectric constant of metals).

In the same way, modes in region m can be expressed as:

$$\langle \mathbf{r}|\Psi_m\rangle = e^{in\theta}\left(J_n\left(\sqrt{k_{mz}^2 - k_{nz}^2}\cdot r\right) + Y_n\left(\sqrt{k_{mz}^2 - k_{nz}^2}\cdot r\right)\right) e^{ik_{nz}z} \tag{6.39}$$

with $k_{mz} = g\varepsilon_2$ (with ε_2 the dielectric constant inside the aperture).

We shall suppose that the time variable enters only in the harmonic factor $e^{-i\omega t}$. Then, the field components of a transverse-magnetic (TM) field are:

$$\begin{array}{lll} E_r = \pm ik_{nz}\frac{\partial\Psi}{\partial r} & E_\theta = \pm\frac{ik_{nz}}{r}\frac{\partial\Psi}{\partial\theta} & E_z = (k^2 - k_{nz}^2)\Psi \\ H_r = \pm\frac{-ik}{\omega r}\frac{\partial\Psi}{\partial\theta} & H_\theta = \pm\frac{ik}{\omega}\frac{\partial\Psi}{\partial r} & H_z = 0 \end{array} \tag{6.40}$$

and for a transverse-electric (TE) field:

$$\begin{array}{lll} E_r = \pm\frac{i\omega}{r}\frac{\partial\Psi}{\partial\theta} & E_\theta = \pm - i\omega\frac{\partial\Psi}{\partial r} & E_z = 0 \\ H_r = \pm ik_{nz}\frac{\partial\Psi}{\partial r} & H_\theta = \pm\frac{ik_{nz}}{r}\frac{\partial\Psi}{\partial r} & H_z = (k^2 - k_{nz}^2)\Psi \end{array} \tag{6.41}$$

While for perfect metals the EM fields can be separated into TE and TM independent wave functions, when initial conditions are prescribed for real metals, the solution for the EM field in cylindrical coordinates can be built by superposition of the previous elementary TM and TE wave functions as follows [187]:

$$\begin{aligned} E_r &= ik_{nz}\sum_{n=-\infty}^{\infty} a_n\frac{\partial\Psi_n}{\partial r} - \frac{\omega}{r}\sum_{n=-\infty}^{\infty} nb_n\Psi_n \\ E_\theta &= -\frac{k_{nz}}{r}\sum_{n=-\infty}^{\infty} na_n\Psi_n - i\omega\sum_{n=-\infty}^{\infty} b_n\frac{\partial\Psi_n}{\partial r} \\ E_z &= \left(k^2 - k_{nz}^2\right)\sum_{n=-\infty}^{\infty} a_n\Psi_n \end{aligned} \tag{6.42}$$

$$\begin{aligned} H_r &= \frac{k^2}{\omega r}\sum_{n=-\infty}^{\infty} na_n\frac{\partial\Psi_n}{\partial r} + ik_{nz}\sum_{n=-\infty}^{\infty} b_n\frac{\partial\Psi_n}{\partial r} \\ H_\theta &= \frac{ik^2}{\omega}\sum_{n=-\infty}^{\infty} a_n\frac{\partial\Psi_n}{\partial r} - \frac{k_{nz}}{r}\sum_{n=-\infty}^{\infty} nb_n\Psi_n \\ H_z &= \left(k^2 - k_{nz}^2\right)\sum_{n=-\infty}^{\infty} b_n\Psi_n \end{aligned} \tag{6.43}$$

Here a_n and b_n are coefficients to be determined from initial conditions.

With the above description we can write now the EM field components in each region. For the interior region, i, $(r < b)$:

$$\begin{aligned}
E_r^i &= \sum_{n=-\infty}^{\infty} \left(\frac{ik_{nz}}{\lambda_1} J_n'(\lambda_1 r) a_n^i - \frac{\omega n}{\lambda_1^2 r} J_n(\lambda_1 r) b_n^i \right) F_n \\
E_\theta^i &= \sum_{n=-\infty}^{\infty} \left(\frac{nk_{nz}}{\lambda_1^2 r} J_n(\lambda_1 r) a_n^i + \frac{i\omega}{\lambda_1} J_n'(\lambda_1 r) b_n^i \right) F_n \\
E_z^i &= \sum_{n=-\infty}^{\infty} \left(J_n(\lambda_1 r) a_n^i \right) F_n \qquad (6.44)
\end{aligned}$$

$$\begin{aligned}
H_r^i &= \sum_{n=-\infty}^{\infty} \left(\frac{nk_{iz}^2}{\omega \lambda_1^2 r} J_n(\lambda_1 r) a_n^i + \frac{ik_{nz}}{\lambda_1} J_n'(\lambda_1 r) b_n^i \right) F_n \\
H_\theta^i &= \sum_{n=-\infty}^{\infty} \left(\frac{ik_{iz}^2}{\omega \lambda_1} J_n'(\lambda_1 r) a_n^i - \frac{nk_{nz}}{\lambda_1^2 r} J_n(\lambda_1 r) b_n^i \right) F_n \\
H_z^i &= \sum_{n=-\infty}^{\infty} \left(J_n(\lambda_1 r) b_n^i \right) F_n \qquad (6.45)
\end{aligned}$$

In the same way, for the middle region, m, $(b < r < a)$:

$$\begin{aligned}
E_r^m &= \sum_{n=-\infty}^{\infty} \left(\frac{ik_{nz}}{\lambda_2} \left(J_n'(\lambda_2 r) a_n^m + Y_n'(\lambda_2 r) b_n^m \right) - \frac{\omega n}{\lambda_2^2 r} \left(J_n(\lambda_2 r) c_n^m + Y_n(\lambda_2 r) d_n^m \right) \right) F_n \\
E_\theta^m &= -\sum_{n=-\infty}^{\infty} \left(\frac{nk_{nz}}{\lambda_2^2 r} \left(J_n(\lambda_2 r) a_n^m + Y_n(\lambda_2 r) b_n^m \right) + \frac{i\omega}{\lambda_2} \left(J_n'(\lambda_2 r) c_n^m + Y_n'(\lambda_2 r) d_n^m \right) \right) F_n \\
E_z^i &= \sum_{n=-\infty}^{\infty} \left(J_n(\lambda_2 r) a_n^m + Y_n(\lambda_2 r) b_n^m \right) F_n \qquad (6.46)
\end{aligned}$$

$$\begin{aligned}
H_r^m &= \sum_{n=-\infty}^{\infty} \left(\frac{nk_{mz}^2}{\omega \lambda_2^2 r} \left(J_n(\lambda_2 r) a_n^m + Y_n(\lambda_2 r) b_n^m \right) + \frac{ik_{nz}}{\lambda_2} \left(J_n'(\lambda_2 r) c_n^m + Y_n'(\lambda_2 r) d_n^m \right) \right) F_n \\
H_\theta^m &= \sum_{n=-\infty}^{\infty} \left(\frac{ik_{mz}^2}{\omega \lambda_2} \left(J_n'(\lambda_2 r) a_n^m + Y_n'(\lambda_2 r) b_n^m \right) - \frac{nk_{nz}}{\lambda_2^2 r} \left(J_n(\lambda_2 r) c_n^m + Y_n(\lambda_2 r) d_n^m \right) \right) F_n \\
H_z^m &= \sum_{n=-\infty}^{\infty} \left(J_n(\lambda_2 r) c_n^m + Y_n(\lambda_2 r) d_n^m \right) F_n \qquad (6.47)
\end{aligned}$$

And finally, for the exterior region, e, $(r > a)$:

$$\begin{aligned}
E_r^e &= \sum_{n=-\infty}^{\infty} \left(\frac{ik_{nz}}{\lambda_1} H_n'^{(1)}(\lambda_1 r) a_n^e - \frac{\omega n}{\lambda_1^2 r} H_n^{(1)}(\lambda_1 r) b_n^e \right) F_n \\
E_\theta^e &= \sum_{n=-\infty}^{\infty} \left(\frac{nk_{nz}}{\lambda_1^2 r} H_n^{(1)}(\lambda_1 r) a_n^e + \frac{i\omega}{\lambda_1} H_n'^{(1)}(\lambda_1 r) b_n^e \right) F_n \\
E_z^e &= \sum_{n=-\infty}^{\infty} \left(H_n^{(1)}(\lambda_1 r) a_n^e \right) F_n \qquad (6.48)
\end{aligned}$$

$$\begin{aligned}
H_r^e &= \sum_{n=-\infty}^{\infty} \left(\frac{nk_{iz}^2}{\omega \lambda_1^2 r} H_n^{(1)}(\lambda_1 r) a_n^e + \frac{ik_{nz}}{\lambda_1} H_n'^{(1)}(\lambda_1 r) b_n^e \right) F_n \\
H_\theta^e &= \sum_{n=-\infty}^{\infty} \left(\frac{ik_{iz}^2}{\omega \lambda_1} H_n'^{(1)}(\lambda_1 r) a_n^e - \frac{nk_{nz}}{\lambda_1^2 r} H_n^{(1)}(\lambda_1 r) b_n^e \right) F_n \\
H_z^e &= \sum_{n=-\infty}^{\infty} \left(H_n^{(1)}(\lambda_1 r) b_n^e \right) F_n \qquad (6.49)
\end{aligned}$$

In these relations, $\lambda_1^2 = k_{iz}^2 - k_{nz}^2$, $\lambda_2^2 = k_{mz}^2 - k_{nz}^2$, $F_n = e^{in\theta} e^{ik_{nz}z - \omega t}$, and the prime above a cylinder function denotes differentiation with respect to the argument $\lambda_j r$ $(j = 1, 2)$. The 8 coefficients of the expansions and the propagation constant k_{nz} are yet undetermined. However, at the boundaries $r = b$ and $r = a$, the tangential components of the EM fields $(E_\theta, E_z, H_\theta, H_z)$ must be continuous and these conditions imposes a relation between the coefficients. After imposing continuity conditions, we get a homogeneous system of linear relations which depend on both k_{nz} and the wavelength, and that are satisfied by the eight coefficients a_n^i, b_n^i, a_n^m, b_n^m, c_n^m, d_n^m, a_n^e and b_n^e given by the following determinant:

$$\begin{vmatrix}
AJ_n(u) & A^{'} J_n'(u) & -CJ_n(s) & -CY_n(s) & -C^{'} J_n'(s) & -C^{'} Y_n'(s) & 0 & 0 \\
J_n(u) & 0 & -J_n(s) & -Y_n(s) & 0 & 0 & 0 & 0 \\
0 & 0 & BJ_n(v) & BY_n(v) & B^{'} J_n'(v) & B^{'} Y_n'(v) & -DH_n^{(1)}(t) & -D^{'} H_n^{'(1)}(t) \\
0 & 0 & J_n(v) & Y_n(v) & 0 & 0 & -H_n^{(1)}(t) & 0 \\
A^{''} J_n'(u) & -AJ_n(u) & -C^{''} J_n'(s) & -C^{''} Y_n' & BJ_n(s) & BY_n(s) & 0 & 0 \\
0 & J_n(u) & 0 & 0 & -J_n(s) & -Y_n(s) & 0 & 0 \\
0 & 0 & B^{''} J_n'(v) & B^{''} Y_n'(v) & -BJ_n(v) & -BY_n(v) & -D^{''} H_n^{'(1)}(t) & -DH_n^{(1)}(t) \\
0 & 0 & 0 & 0 & J_n(v) & Y_n(v) & 0 & -H_n^{(1)}(t)
\end{vmatrix} \qquad (6.50)$$

being

$$\begin{array}{cccc} A = \frac{nk_{nz}}{u^2}, & B = \frac{nk_{nz}}{v^2}, & C = \frac{nk_{nz}}{s^2}, & D = \frac{nk_{nz}}{t^2} \\ A^{'} = \frac{i\omega}{u}, & B^{'} = \frac{i\omega}{v}, & C^{'} = \frac{i\omega}{s}, & D^{'} = \frac{i\omega}{t} \\ A^{''} = \frac{ik_1^2}{u\omega}, & B^{''} = \frac{ik_2^2}{v\omega}, & C^{''} = \frac{ik_2^2}{s\omega}, & D^{''} = \frac{ik_1^2}{t\omega} \end{array} \tag{6.51}$$

with $u = \lambda_1 b$, $v = \lambda_2 a$, $s = \lambda_2 b$, $t = \lambda_1 a$ and $\omega = ck$.

The system admits a nontrivial solution only in case its determinant is zero. Therefore, the unknown propagation constant, k_{nz}, is determined for each wavelength when the above determinant shall vanish. Besides, for each n value there are infinite solutions. However, we restrict our study to a unique solution for k_{nz} with $n = 1$, since we will apply the minimal-model for subwavelength apertures where a single mode (the less decaying one) is considered inside the apertures. The roots are determined numerically using the Bisection method.

The resolution of this system is easier by neglecting absorption in the metal, and we have checked that this provides good agreement with FDTD results.

Bibliography

[1] A. Rey, Les sciences orientales avant les grecs, 1942.

[2] R. Rashed, A pioneer in anaclastics: Ibn Sahl on burning mirrors and lenses, Isis, 81, 1990.

[3] R. Descartes, Ouvres completes de Descartes, TT. IV, Paris, Paris, 1965.

[4] P. de Fermat, Varie opera math., 1679.

[5] F. Catrou, Memoires pour L'Histoire des Sciences et des Beaux Arts, Trevour, Impr. de S. A. S; Paris, Chez E. Ganeau, Paris, 1734.

[6] I. Newton, Opticks: or a treatise of the reflexions, refractions, inflexions and colours of light, London, 1704.

[7] T. Young, The bakerian lectures. On the theory of light and colours., Phil. Trans., 1802.

[8] A Dynamical Theory of the Electromagnetic Field, Philosophical Transactions of the Royal Society of London, London, 1865.

[9] A. Sommerfeld, Optics, Lectures on theoretical Physics., Vol. IV, Academic Press Inc., New York, 1954.

[10] F. E. Wagner, S. Haslbeck, L. Stievano, S. Calogero, Q. A. Pankhurst, K. P. Martinek, Before striking gold in gold-ruby glass, Nature 407 (2000) 691–692.

[11] A. Sommerfeld, Ann. Phys. und Chemie (1899) 303–233.

[12] J. Zenneck, Ann. Phys. 23 (1907) 846.

[13] R. W. Wood, Proc. Phys. Soc. London 18 (1902) 269.

[14] R. H. Ritchie, Plasma losses by fast electrons in thin films, Phys. Rev. 106 (1957) 874–881.

[15] E. D. Palik, Handbook of optical constants of solids II, Boston: Academic Press, 1991, edited by Palik, Edward D., 1991.

[16] A. Otto, Excitation of nonradiative surface plasma waves in silver by the method of frustrated total reflection, Z. Phys. 216 (4) (1968) 398–410.

[17] B. Lamprecht, J. R. Krenn, G. Schider, H. Ditlbacher, M. Salerno, N. Felidj, A. Leitner, F. R. Aussenegg, J. C. Weeber, Surface plasmon propagation in microscale metal stripes, Applied Physics Letters 79 (1) (2001) 51–53.

[18] R. H. Ritchie, E. T. Arakawa, J. J. Cowan, R. N. Hamm, Surface-plasmon resonance effect in grating diffraction, Phys. Rev. Lett. 21 (22) (1968) 1530–1533.

[19] H. Ditlbacher, J. R. Krenn, N. Felidj, B. Lamprecht, G. Schider, M. Salerno, A. Leitner, F. R. Aussenegg, Fluorescence imaging of surface plasmon fields, Applied Physics Letters 80 (3) (2002) 404–406.

[20] F. J. García-Vidal, L. Martín-Moreno, Transmission and focusing of light in one-dimensional periodically nanostructured metals, Phys. Rev. B 66 (15) (2002) 155412.

[21] H. A. Bethe, Theory of difraction by small holes, Phys. Rev. 66 (1944) 163–182.

[22] C. Genet, T. W. Ebbesen, Light in tiny holes, Nature 445 (2007) 39–46.

[23] T. W. Ebbesen, H. L. Lezec, H. F. Ghaemi, T. Thio, P. A. Wolff, Extraordinary optical transmission through subwavelength hole arrays, Nature 391 (1998) 667–669.

[24] T. Thio, H. L. Lezec, T. W. Ebbesen, K. M. Pellerin, G. D. Lewen, A. Nahata, R. A. Linke, Giant optical transmission of subwavelength apertures: physics and applications, Nanotechnology 13 (2002) 429–432.

[25] H. J. Lezec, A. Degiron, E. Devaux, R. A. Linke, L. Martin-Moreno, F. J. Garcia-Vidal, T. W. Ebbesen, Beaming light from a subwavelength aperture, Science 297 (5582) (2002) 820–822.

[26] F. I. Baida, D. V. Labeke, B. Guizal, Enhanced confined light transmission by single subwavelength apertures in metallic films, Appl. Opt. 42 (34) (2003) 6811–6815.

[27] A. Degiron, T. Ebbesen, Analysis of the transmission process through single apertures surrounded by periodic corrugations, Opt. Express 12 (16) (2004) 3694–3700.

[28] A. Agrawal, H. Cao, A. Nahata, Time-domain analysis of enhanced transmission through a single subwavelength aperture, Opt. Express 13 (9) (2005) 3535–3542.

[29] Z.-B. Li, J.-G. Tian, Z.-B. Liu, W.-Y. Zhou, C.-P. Zhang, Enhanced light transmission through a single subwavelength aperture in layered films consisting of metal and dielectric, Opt. Express 13 (22) (2005) 9071–9077.

[30] L. Martín-Moreno, F. J. García-Vidal, H. J. Lezec, A. Degiron, T. W. Ebbesen, Theory of highly directional emission from a single subwavelength aperture surrounded by surface corrugations, Phys. Rev. Lett. 90 (16) (2003) 167401.

[31] F. J. García-Vidal, L. Martín-Moreno, H. J. Lezec, T. W. Ebbesen, Focusing light with a single subwavelength aperture flanked by surface corrugations, Applied Physics Letters 83 (22) (2003) 4500–4502.

[32] C. K. Chang, D. Z. Lin, C. S. Yeh, C. K. Lee, Y. C. Chang, M. W. Lin, J. T. Yeh, J. M. Liu, Similarities and differences for light-induced surface plasmons in one- and two-dimensional symmetrical metallic nanostructures, Opt. Lett. 31 (15) (2006) 2341–2343.

[33] P. D. Flammer, I. C. Schick, R. T. Collins, R. E. Hollingsworth, Interference and resonant cavity effects explain enhanced transmission through-subwavelength apertures in thin metal films, Opt. Express 15 (13) (2007) 7984–7993.

[34] O. T. A. Janssen, H. P. Urbach, G. W. t' Hooft, Giant optical transmission of a subwavelength slit optimized using the magnetic field phase, Phys. Rev. Lett 99 (2007) 043902.

[35] Y. Cui, S. He, A theoretical re-examination of giant transmission of light through a metallic nano-slit surrounded with periodic grooves, Opt. Express 17 (16) (2009) 13995–14000.

[36] L. Cai, G. Li, Z. Wang, A. Xu, Interference and horizontal fabry-perot resonance on extraordinary transmission through a metallic nanoslit surrounded by grooves, Opt. Lett. 35 (2) (2010) 127–129.

[37] F. J. García-Vidal, H. J. Lezec, T. W. Ebbesen, L. Martín-Moreno, Multiple paths to enhance optical transmission through a single subwavelength slit, Phys. Rev. Lett. 90 (2003) 213901.

[38] S. Nie, S. R. Emory, Probing single molecules and single nanoparticles by surface-enhanced raman scattering, Science 275 (5303) (1997) 1102–1106.

[39] R. W. Boyd, Nonlinear Optics, Academic Press, San Diego, 2003.

[40] M. Nagel, P. H. Bolivar, M. Brucherseifer, H. Kurz, A. Bosserhoff, R. Buttner, Integrated thz technology for label-free genetic diagnostics, Applied Physics Letters 8 (154) (2001) 1428619–1428621.

[41] K. Yamamoto, M. Yamaguchi, F. Miyamaru, M. Tani, M. Hangyo, T. Ikeda, A. Matsushita, K. Koide, M. Tatsuno, Y. Minami, Noninvasive inspection of c-4 explosive in mails by terahertz time-domain spectroscopy, Japanese Journal of Applied Physics 43 (3B) (2004) L414–L417.

[42] R. Piesiewicz, T. Kleine-Ostmann, N. Krumbholz, D. Mittleman, M. Koch, J. Schoebel, T. Kurner, Short-range ultra-broadband terahertz communications: Concepts and perspectives, Antennas and Propagation Magazine, IEEE 49 (6) (2007) 24 –39.

[43] S. G. Rodrigo, O. Mahboub, A. Degiron, C. Genet, F. J. García-Vidal, L. Martín-Moreno, T. W. Ebbesen, Holes with very acute angles: a new paradigm of extraordinary optical transmission through strongly localized modes, Opt. Express 18 (2010) 23691–23697.

[44] R. Gordon, A. G. Brolo, A. McKinnon, A. Rajora, B. Leathem, K. L. Kavanagh, Strong polarization in the optical transmission through elliptical nanohole arrays, Phys. Rev. Lett. 92 (2004) 037401.

[45] K. J. K. Koerkamp, S. Enoch, F. B. Segerink, N. F. van Hulst, L. Kuipers, Strong influence of hole shape on extraordinary optical transmission through periodic arrays of subwavelength holes, Phys. Rev. Lett. 92 (2004) 183901.

[46] H. Cao, A. Nahata, Influence of aperture shape on the transmission properties of a periodic array of subwavelength apertures, Opt. Express 12 (16) (2004) 3664–3672.

[47] A. Degiron, H. J. Lezec, N. Yamamoto, T. W. Ebbesen, Optical transmission properties of a single subwavelength aperture in a real metal, Optics Communications 239 (2004) 61–66.

[48] F. Baida, D. Van Labeke, G. Granet, A. Moreau, A. Belkhir, Origin of the super-enhanced light transmission through a 2-d metallic annular aperture array: a study of photonic bands, Applied Physics B: Lasers and Optics 79 (2004) 1–8.

[49] F. J. Garcia-Vidal, L. Martin-Moreno, T. W. Ebbesen, L. Kuipers, Light passing through subwavelength apertures, Rev. Mod. Phys. 82 (2010) 729–787.

[50] J. A. Porto, F. J. García-Vidal, J. B. Pendry, Transmission resonances on metallic gratings with very narrow slits, Phys. Rev. Lett. 83 (14) (1999) 2845–2848.

[51] J. Bravo-Abad, L. Martín-Moreno, F. J. García-Vidal, Transmission properties of a single metallic slit: From the subwavelength regime to the geometrical-optics limit, Phys. Rev. E 69 (2) (2004) 026601.

[52] A. I. Fernández-Domínguez, F. J. García-Vidal, L. Martín-Moreno, Resonant transmission of light through finite arrays of slits, Phys. Rev. B 76 (23) (2007) 235430.

[53] L. Martín-Moreno, F. J. García-Vidal, Optical transmission through circular hole arrays in optically thick metal films, Opt. Express 12 (2004) 3619–3628.

[54] F. J. García-Vidal, L. Martín-Moreno, J. B. Pendry, Surfaces with holes in them: new plasmonic metamaterials, J. Opt. A: Pure Appl. Opt. 7 (2005) S97–S101.

[55] J. Bravo-Abad, A. Degiron, F. Przybilla, C. Genet, F. J. Garcia-Vidal, L. Martin-Moreno, T. W. Ebbesen, How light emerges from an illuminated array of subwavelength holes, Nature Phys. 2 (2006) 120–123.

[56] L. Martín-Moreno, F. J. García-Vidal, Minimal model for optical transmission through holey metal films, J. Phys.: Condens. Matter 20 (2008) 304214.

[57] J. Bravo-Abad, A. I. Fernández-Domínguez, F. J. García-Vidal, L. Martín-Moreno, Theory of extraordinary transmission of light through quasiperiodic arrays of subwavelength holes, Phys. Rev. Lett. 99 (20) (2007) 203905.

[58] A. I. Fernández-Domínguez, I. Hernández-Carrasco, L. Martín-Moreno, F. J. García-Vidal, Transmission resonances through a fibonacci array of subwavelength slits, Electromagnetics 28 (2008) 186–197.

[59] F. J. García-Vidal, E. Moreno, J. A. Porto, L. Martín-Moreno, Transmission of light through a single rectangular hole, Phys. Rev. Lett. 95 (2005) 103901.

[60] A. Y. Nikitin, D. Zueco, F. J. García-Vidal, L. Martín-Moreno, Electromagnetic wave transmission through a small hole in a perfect electric conductor of finite thickness, Phys. Rev. B 78 (16) (2008) 165429.

[61] A.-L. Baudrion, F. de Leon-Perez, O. Mahboub, A. Hohenau, H. Ditlbacher, F. J. Garcia-Vidal, J. Dintinger, T. W. Ebbesen, L. Martin-Moreno, J. R. Krenn, Coupling efficiency of light to surface plasmon polariton for single subwavelength holes in a gold film, Opt. Express 16 (5) (2008) 3420–3429.

[62] J. Bravo-Abad, F. J. García-Vidal, L. Martín-Moreno, Resonant transmission of light through finite chains of subwavelength holes in a metallic film, Phys. Rev. Lett. 93 (2004) 227401.

[63] O. Mahboub, S. C. Palacios, C. Genet, F. J. Garcia-Vidal, S. G. Rodrigo, L. Martin-Moreno, T. W. Ebbesen, Optimization of bull's eye structures for transmission enhancement, Opt. Express 18 (11) (2010) 11292–11299.

[64] L. A. Dunbar, M. Guillaumee, F. de Leon-Perez, C. Santschi, E. Grenet, R. Eckert, F. Lopez-Tejeira, F. J. Garcia-Vidal, L. Martin-Moreno, R. P. Stanley.

[65] A. I. Fernandez-Dominguez, C. R. Williams, F. J. Garcia-Vidal, L. Martin-Moreno, S. R. Andrews, S. A. Maier, Terahertz surface plasmon polaritons on a helically grooved wire, Applied Physics Letters 93 (14).

[66] F. López-Tejeira, F. J. García-Vidal, L. Martín-Moreno, Scattering of surface plasmons by one-dimensional periodic nanoindented surfaces, Phys. Rev. B (R) 72 (2005) 161405.

[67] F. de León-Pérez, G. Brucoli, F. J. García-Vidal, L. Martín-Moreno, Theory on the scattering of light and surface plasmon polaritons by arrays of holes and dimples in a metal film, New J. Phys. 10 (2008) 105017.

[68] J. A. Porto, L. Martín-Moreno, F. J. García-Vidal, Optical bistability in subwavelength slit apertures containing nonlinear media, Phys. Rev. B 70 (8) (2004) 081402.

[69] E. Moreno, A. I. Fernández-Domínguez, J. I. Cirac, F. J. García-Vidal, L. Martín-Moreno, Resonant transmission of cold atoms through subwavelength apertures, Phys. Rev. Lett. 95 (2005) 170406.

[70] J. Christensen, A. I. Fernández-Domínguez, F. de León-Pérez, L. Martín-Moreno, F. J. García-Vidal, Collimation of sound assisted by acoustic surface waves, Nature Phys. 3 (2007) 851–852.

[71] J. B. Pendry, L. Martín-Moreno, F. J. García-Vidal, Mimicking surface plasmons with structured surfaces, Science 305 (2004) (5685): 847–848.

[72] L. D. Landau, E. M. Lifshitz, L. P. Pitaevskii, Electrodynamics of Continous Media, Pergamon Press, New York, 1960.

[73] F. López-Tejeira, F. J. García-Vidal, L. Martín-Moreno, Scattering of surface plasmons by one-dimensional periodic nanoindented surfaces, Phys. Rev. B 72 (16) 161405.

[74] F. de Leon-Perez, G. Brucoli, F. J. Garcia-Vidal, L. Martin-Moreno, Theory on the scattering of light and surface plasmon polaritons by arrays of holes and dimples in a metal film, New J. Phys. 10 (2008) 105017.

[75] P. B. Johnson, R. W. Christy, Optical constants of the noble metals, Phys. Rev. B 6 (12) (1972) 4370–4379.

[76] F. J. García-Vidal, L. Martín-Moreno, E. Moreno, L. K. S. Kumar, R. Gordon, Transmission of light through a single rectangular hole in a real metal, Phys. Rev. B 74 (2006) 153411.

[77] K. Yee, Numerical solution of initial boundary value problems involving maxwell's equations in isotropic media, IEEE Transactions on Antennas and Propagation 14 (1966) 302–307.

[78] A. Taflove, S. Hagness, Computational Electrodynamics: The Finite-Difference Time-Domain Method, Artech House, Boston, 2000.

[79] A. Taflove, S. C. Hagness, Computational Electrodynamics: The Finite-Difference Time-Domain Method (Third edition), Artech House, Boston, 2005.

[80] P. Tran, Photonic-band-structure calculation of material possessing kerr nonlinearity, Phys. Rev. B 52 (15) (1995) 10673–10676.

[81] S. G. Rodrigo, Study of the optical properties of nano-structured metallic systems with the Finite-Difference Time-Domain method, Vol. 80, Prensas Universitarias de Zaragoza, New York, 2010.

[82] S. G. Rodrigo, F. J. García-Vidal, L. Martín-Moreno, Influence of material properties on extraordinary optical transmission through hole arrays, Phys. Rev. B 77 (7) (2008) 075401.

[83] F. I. Baida, D. Van Labeke, Three-dimensional structures for enhanced transmission through a metallic film: Annular aperture arrays, Phys. Rev. B 67 (15) (2003) 155314.

[84] A. Roberts, S. M. Orbons, Bandpass grids with annular apertures, Antennas and Propagation, IEEE Transactions on Antennas and Propagation 36 (3232459) (1988) 607–611.

[85] N. Marcuvitz, Waveguide Handbook, McGraw-Hill, New York, 1955.

[86] C. R. Williams, M. Misra, S. R. Andrews, S. A. Maier, S. Carretero-Palacios, S. G. Rodrigo, F. J. García-Vidal, L. Martín-Moreno, Dual band terahertz waveguiding on a planar metal surface patterned with annular holes, Applied Physics Letters 96.

[87] F. I. Baida, A. Belkhir, D. V. Labeke, O. Lamrous, Subwavelength metallic coaxial waveguides in the optical range: Role of the plasmonic modes, Physical Review B 74 (20) (2006) 205419.

[88] S. M. Orbons, A. Roberts, Resonance and extraordinary transmission in annular aperture arrays, Opt. Express 14 (26) (2006) 12623–12628.

[89] M. I. Haftel, C. Schlockermann, G. Blumberg, Enhanced transmission with coaxial nanoapertures: Role of cylindrical surface plasmons, Phys. Rev. B 74 (23) (2006) 235405.

[90] J. Salvi, M. Roussey, F. I. Baida, M.-P. Bernal, A. Mussot, T. Sylvestre, H. Maillotte, D. V. Labeke, A. Perentes, I. Utke, C. Sandu, P. Hoffmann, B. Dwir, Annular aperture arrays: study in the visible region of the electromagnetic spectrum, Opt. Lett. 30 (13) (2005) 1611–1613.

[91] Y. Poujet, J. Salvi, F. I. Baida, 90 extraordinary optical transmission in the visible range through annular aperture metallic arrays, Opt. Lett. 32 (20) (2007) 2942–2944.

[92] S. Orbons, D. Freeman, B. Luther-Davies, B. Gibson, S. Huntington, D. Jamieson, A. Roberts, Optical properties of silver composite metamaterials, Physica B: Condensed Matter 394 (2) (2007) 176 – 179, proceedings of the Seventh International Conference on Electrical Transport and Optical Properties of Inhomogeneous Media.

[93] S. Nowy, B. C. Krummacher, J. Frischeisen, N. A. Reinke, W. Brutting, Light extraction and optical loss mechanisms in organic light-emitting diodes: Influence of the emitter quantum efficiency, J. Appl. Phys 104 (2008) 123109.

[94] A. Drezet, F. Przybilla, E. Laux, O. Mahboub, C. Genet, T. W. Ebbesen, J. S. Bouillard, A. Zayats, I. S. Spevak, A. V. Zayats, A. Y. Nikitin, L. Martin-Moreno, Opening the light extraction cone of high index substrates with plasmonic gratings: Light emitting diode applications, Appl. Phys. Lett 95 (2009) 021101.

[95] T. Onishi, T. Tanigawa, T. Ueda, D. Ueda, Polarization control of vertical-cavity surface-emitting lasers by utilizing surface plasmon resonance, Quantum Electronics, IEEE Journal of 43 (2007) 1123 –1128.

[96] J.-S. Bouillard, J. Einsle, W. Dickson, S. G. Rodrigo, S. Carretero-Palacios, L. Martín-Moreno, F. J. García-Vidal, A. V. Zayats, Optical transmission of periodic annular apertures in metal film on high-refractive index substrate: The role of the nanopillar shape (2010).

[97] J.-S. Bouillard, W. Dickson, J. Einsle, S. Gutierrez Rodrigo, S. Carretero, L. Martin-Moreno, F. Garcia-Vidal, A. Zayats, Annular holes and their arrays for light extraction from high refractive index substrates., in: IEEE/LEOS Winter Topicals Meeting Series, 2009, 2009, pp. 71 –72.

[98] M. Tonouchi, Cutting-edge terahertz technology, Nat. Photonics 97 (1).

[99] D. Grischkowsky, S. Keiding, M. van Exter, C. Fattinger, Far-infrared time-domain spectroscopy with terahertz beams of dielectrics and semiconductors, J. Opt. Soc. Am. B 7.

[100] R. M. Woodward, B. E. Cole, V. P. Wallace, R. J. Pye, D. D. Arnone, E. H. Linfield, M. Pepper, Terahertz pulse imaging in reflection geometry of human skin cancer and skin tissue, Physics in Medicine and Biology 47 (21) (2002) 3853.

[101] C. J. Strachan, P. F. Taday, D. A. Newnham, K. C. Gordon, J. A. Zeitler, M. Pepper, T. Rades, Using terahertz pulsed spectroscopy to quantify pharmaceutical polymorphism and crystallinity, Journal of Pharmaceutical Sciences 94.

[102] M. Nagel, F. Richter, P. Haring-Bolívar, H. Kurz, A functionalized thz sensor for marker-free dna analysis, Physics in Medicine and Biology 48 (22) (2003) 3625.

[103] J. Zhang, D. Grischkowsky, Waveguide terahertz time-domain spectroscopy of nanometer water layers, Opt. Lett. 29 (14) (2004) 1617–1619.

[104] H. Hirori, K. Yamashita, M. Nagai, K. Tanaka, Attenuated total reflection spectroscopy in time domain using terahertz coherent pulses, Japanese Journal of Applied Physics 43 (10A) (2004) L1287–L1289.

[105] C. R. Williams, S. R. Andrews, S. A. Maier, A. I. Fernández-Domínguez, L. Martín-Moreno, F. J. García-Vidal, Highly confined guiding of terahertz surface plasmon polaritons on structured metal surfaces, Nat. Photonics 2 (2008) 175–179.

[106] L. Yang, H. Sun, S. Weng, K. Zhao, L. Zhang, G. Zhao, Y. Wang, Y. Xu, X. Lu, C. Zhang, J. Wu, C. Jia'er, Terahertz absorption spectra of some saccharides and their metal complexes, Spectrochimica Acta Part A: Molecular and Biomolecular Spectroscopy 69 (1) (2008) 160 – 166.

[107] T.-I. Jeon, D. Grischkowsky, Thz zenneck surface wave (thz surface plasmon) propagation on a metal sheet., Appl. Phys. Lett. 88 (2006) 061113–061115.

[108] L. Martín-Moreno, F. J. García-Vidal, H. J. Lezec, K. M. Pellerin, T. Thio, J. B. Pendry, T. W. Ebbesen, Theory of extraordinary optical transmission through subwavelength hole arrays, Phys. Rev. Lett. 86 (6) (2001) 1114–1117.

[109] F. Przybilla, A. Degiron, J.-Y. Laluet, C. Genet, T. W. Ebbesen, Optical transmission in perforated noble and transition metal films, J. Opt. A: Pure Appl. Opt. 8 (2006) 458–463.

[110] A. Krishnan, T. Thio, T. J. Kim, H. L. Lezec, T. W. Ebbesen, P. A. Wolff, J. B. Pendry, L. Martín-Moreno, F. J. García-Vidal, Evanescently coupled resonance in surface plasmon enhanced transmission, Optics Communications 200 (2001) 1–7.

[111] A. P. Hibbins, B. R. Evans, J. R. Sambles, Experimental verification of designer surface plasmons, Science 308 (5722) (2005) 670–672.

[112] A. Degiron, T. W. Ebbesen, The role of localized surface plasmon modes in the enhanced transmission of periodic subwavelength apertures, J. Opt. A: Pure Appl. Opt. 7 (2005) S90–S96.

[113] K. L. van der Molen, K. J. K. Koerkamp, S. Enoch, F. B. Segerink, N. F. van Hulst, L. Kuipers, Role of shape and localized resonances in extraordinary transmission through periodic arrays of subwavelength holes: Experiment and theory, Phys. Rev. B 72 (2005) 045421.

[114] A. Mary, S. G. Rodrigo, L. Martín-Moreno, F. J. García-Vidal, Theory of light transmission through an array of rectangular holes, Phys. Rev. B 76 (2007) 195414.

[115] Z. Ruan, M. Qiu, Enhanced transmission through periodic arrays of subwavelength holes: The role of localized waveguide resonances, Phys. Rev. Lett. 96 (23) (2006) 233901.

[116] E. D. Palik, Handbook of optical constants of solids, Academic Press Handbook Series, New York: Academic Press, 1985, edited by Palik, Edward D., 1985.

[117] A. V. Zayats, I. I. Smolyaninov, A. A. Maradudin, Nano-optics of surface plasmon polaritons, Physics Reports 408 (2005) 131 – 314.

[118] A. Lewis, M. Isaacson, A. Harootunian, A. Murray, Development of a 500 a spatial resolution light microscope i. light is efficiently transmitted through $\lambda/16$ diameter apertures, Ultramicroscopy 13.

[119] D. W. Pohl, W. Denk, M. Lanz, Optical stethoscopic: Image recording with resolution $\lambda/20$, Appl. Phys. Lett. 44.

[120] J. Prikulis, P. Hanarp, L. Olofsson, D. Sutherland, M. Käll, Optical spectroscopy of nanometric holes in thin gold films, Nano Letters 4 (6) (2004) 1003–1007.

[121] S.-H. Chang, S. Gray, G. Schatz, Surface plasmon generation and light transmission by isolated nanoholes and arrays of nanoholes in thin metal films, Opt. Express 13 (8) (2005) 3150–3165.

[122] E. Popov, N. Bonod, M. Nevière, H. Rigneault, P.-F. Lenne, P. Chaumet, Surface plasmon excitation on a single subwavelength hole in a metallic sheet, Appl. Opt. 44 (12) (2005) 2332–2337.

[123] P. B. Catrysse, H. Shin, S. Fan, Propagating modes in subwavelength cylindrical holes, J. Vac. Sci. Techno. B 23.

[124] K. J. Webb, J. Li, Waveguide cavity surface-enhanced raman scattering, Phys. Rev. B 73.

[125] L. Wang, J.-X. Cao, Y. Lv, L. Liu, T.-Y. Niu, Y.-C. Du, Experimental study of surface-wave-assisted microwave transmission through a single subwavelength slit, J. Appl. Phys 105 (2009) 093115.

[126] H. Ko, H. C. Kim, M. Cheng, Light focusing at metallic annular slit structure coated with dielectric layers, Appl. Opt. 49 (6) (2010) 950–954.

[127] L.-L. Wang, X.-F. Ren, R. Yang, G.-C. Guo, G.-P. Guo, Transmission of doughnut light through a bull's eye structure, Appl. Phys. Lett 95 (2009) 111111.

[128] T. Ishi, J. Fujikata, K. Ohashi, Large optical transmission through a single subwavelength hole associated with a sharp-apex grating, Japanese Journal of Applied Physics 44 (4) (2005) L170–L172.

[129] F. G. de Abajo, Light transmission through a single cylindrical hole in a metallic film, Opt. Express 10 (25) (2002) 1475–1484.

[130] J. R. Shewchuk, An Introduction to the Conjugate Gradient Method Without the Agonizing Pain, School of Computer Science, Carnegie Mellon University, Pittsburgh, PA 15213, 1994.

[131] F. Przybilla, A. Degiron, C. Genet, T. Ebbesen, F. de Léon-Pérez, J. Bravo-Abad, F. J. García-Vidal, L. Martín-Moreno, Efficiency and finite size effects in enhanced transmission through subwavelength apertures, Opt. Express 16 (13) (2008) 9571–9579.

[132] T. Thio, K. M. Pellerin, R. A. Linke, H. J. Lezec, T. W. Ebbesen, Enhanced light transmission through a single subwavelength aperture, Opt. Lett. 26 (24) (2001) 1972–1974.

[133] K. Shuford, M. Ratner, S. Gray, G. Schatz, Finite-difference time-domain studies of light transmission through nanohole structures, Applied Physics B: Lasers and Optics 84 (2006) 11–18.

[134] J. A. Sanchez-Gil, Surface defect scattering of surface plasmon polaritons: Mirrors and light emitters, Appl. Phys. Lett. 73 (1998) 3509–3511.

[135] M. Kuttge, F. J. G. de Abajo, A. Polman, How grooves reflect and confine surface plasmon polaritons, Opt. Express 17 (12) (2009) 10385–10392.

[136] E. Popov, M. Nevière, A.-L. Fehrembach, N. Bonod, Optimization of plasmon excitation at structured apertures, Appl. Opt. 44 (29) (2005) 6141–6154.

[137] E. Laux, C. Genet, T. Sakuli, T. W. Ebbesen, Plasmonic photon sorters for spectral and polarimetricimaging, Nat. Photonics 2 (2008) 161–164.

[138] A. Drezet, C. Genet, T. W. Ebbesen, Miniature plasmonic wave plates, Phys. Rev. Lett. 101 (4) (2008) 043902.

[139] P. Lalanne, J. P. Hugonin, Interaction between optical nano-objects at metallo-dielectric interfaces, Nature Phys. 2 (2006) 551–556.

[140] G. Zheng, X. Cui, C. Yang, Surface-wave-enabled darkfield aperture for background suppression during weak signal detection, PNAS 107 (20) (2010) 9043–9048.

[141] G. Zheng, C. Yang, Improving weak-signal identification via predetection background suppression by a pixel-level, surface-wave-enabled dark-field aperture, Opt. Lett. 35 (15) (2010) 2636–26348.

[142] M. Consonni, J. Hazart, G. Lérondel, Fabry-perot type enhancement in plasmonic visible nanosource, Appl. Phys. Lett. 94 (20) (2009) 051105–1–051105–3.

[143] J.-Y. Laluet, E. Devaux, C. Genet, T. W. Ebbesen, J.-C. Weeber, A. Dereux, Optimization of surface plasmons launching from subwavelength hole arrays: modelling and experiments, Opt. Express 15 (2007) 3488.

[144] C. Obermuller, K. Karrai, Far field characterization of diffracting circular apertures, Appl. Phys. Lett. 67 (1995) 3408–3410.

[145] C. Obermuller, K. Karrai, G. Kolb, G. Abstreiter, Transmitted radiation through a subwavelength-sized tapered optical fiber tip, Ultramicroscopy 61 (1-4) (1995) 171 – 177.

[146] J. D. Jackson, Classical Electrodynamics 2nd edition, Wiley, New York, 1975.

[147] E. Popov, M. Neviere, A. Sentenac, N. Bonod, A.-L. Fehrembach, J. Wenger, P.-F. Lenne, H. Rigneault, Single scattering theory of light diffraction by a circular subwavelength aperture in a finitely conducting screen, J. Opt. Soc. Am A 24 (2007) 339–358.

[148] F. de León-Pérez, J. Alegret, F. J. García-Vidal, L. Martín-Moreno, Scattering cross section, (in preparation).

[149] J. Alegret, P. Johansson, M. Käll, Green's tensor calculations of plasmon resonances of single holes and hole pairs in thin gold films, New Journal of Physics 10 (10) (2008) 105004.

[150] J. Alegret, M. Käll, P. Johansson, Top-down extended meshing algorithm and its applications to green's tensor nano-optics calculations, Phys. Rev. E 75 (4) (2007) 046702.

[151] S. G. Rodrigo, L. Martín-Moreno, A. Y. Nikitin, A. V. Kats, I. S. Spevak, F. J. García-Vidal, Extraordinary optical transmission through hole arrays in optically thin metal films, Opt. Lett. 34 (1) (2009) 4–6.

[152] B. A. Munk, Frequency Selective Surfaces: Theory and design, John Wiley & Sons, New York, 2000.

[153] A. Alù, N. Engheta, Light squeezing through arbitrarily shaped plasmonic channels and sharp bends, Phys. Rev. B 78 (3) (2008) 035440.

[154] M. Silveirinha, N. Engheta, Tunneling of electromagnetic energy through subwavelength channels and bends using ϵ-near-zero materials, Phys. Rev. Lett. 97 (15) (2006) 157403.

[155] A. J. L. Adam, J. M. Brok, M. A. Seo, K. J. Ahn, D. S. Kim, J. H. Kang, Q. H. Park, M. Nagel, P. C. Planken, Advanced terahertz electric near-fieldmeasurements at subwavelengthdiameter metallic apertures, Opt. Express 16 (10) (2008) 7407–7417.

[156] L. Guestin, A. J. L. Adam, J. R. Knab, M. Nagel, P. C. M. Planken, Influence of the dielectric substrate on the terahertz electric near-field of a hole in a metal, Opt. Express 17 (20) (2009) 17412.

[157] J. H. Kang, J.-H. Choe, D. S. Kim, Q.-H. Park, Substrate effect on aperture resonances in a thin metal film, Opt. Express 17 (18) (2009) 15652.

[158] M. A. Seo, A. J. L. Adam, J. H. Kang, J. W. Lee, K. J. Ahn, Q. H. Park, P. C. M. Planken, D. S. Kim, Near field imaging of terahertz focusing ontorectangular apertures, Opt. Express 16 (25) (2008) 20484–20489.

[159] F. Medina, F. Mesa, R. Marques, Equivalent circuit model to explain extraordinary transmission, in: Microwave Symposium Digest, 2008 IEEE MTT-S International, 2008, pp. 213 –216.

[160] N. Sugimoto, H. Kanbara, S. Fujiwara, K. Tanaka, Y. Shimizugawa, K. Hirao, Third-order optical nonlinearities and their ultrafast response in bi2o3–b2o3–sio2 glasses, J. Opt. Soc. Am. B 16 (11) (1999) 1904–1908.

[161] S. Kim, J. H. Jin, Y. J. Kim, I. Y. Park, Y. Kim, S. W. Kim, High-harmonic generation by resonant plasmon field enhancement, Nature 453 (7196) (2008) 757–760.

[162] G. A. Wurtz, A. V. Zayats, Nonlinear surface plasmon polaritonic crystals, Laser & Photonics Reviews 2 (3) (2008) 125–135.

[163] S. Xie, H. Li, H. Xu, X. Zhou, S. Fu, J. Wu, The optical transmission characteristics through gold nanoslit arrays embedded in nonlinear medium, Opt. Commun. 283 (6) (2010) 998–1003.

[164] C. Min, P. Wang, X. Jiao, Y. Deng, H. Ming, Beam manipulating by metallic nano-optic lens containing nonlinear media, Opt. Express 15 (15) (2007) 9541–9546.

[165] M. A. Vincenti, A. D'Orazio, M. Buncick, N. Akozbek, M. J. Bloemer, M. Scalora, Beam steering from resonant subwavelength slits filled with a

nonlinear material, Journal of the Optical Society of America B-Optical Physics 26 (2) (2009) 301–307.

[166] G. A. Wurtz, R. Pollard, A. V. Zayats, Optical bistability in nonlinear surface-plasmon polaritonic crystals, Phys. Rev. Lett. 97 (5) (2006) 057402.

[167] C. Min, P. Wang, X. Jiao, Y. Deng, H. Ming, Optical bistability in subwavelength metallic grating coated by nonlinear material, Opt. Express 15 (19) (2007) 12368–12373.

[168] C. Min, P. Wang, C. Chen, Y. Deng, Y. Lu, H. Ming, T. Ning, Y. Zhou, G. Yang, All-optical switching in subwavelength metallic grating structure containing nonlinear optical materials, Opt. Lett. 33 (8) (2008) 869–871.

[169] A. Christ, S. G. Tikhodeev, N. A. Gippius, J. Kuhl, H. Giessen, Waveguide-plasmon polaritons: Strong coupling of photonic and electronic resonances in a metallic photonic crystal slab, Phys. Rev. Lett. 91 (18) (2003) 183901.

[170] P. Ginzburg, A. Hayat, N. Berkovitch, M. Orenstein, Nonlocal ponderomotive nonlinearity in plasmonics, Opt. Lett. 35 (10) (2010) 1551–1553.

[171] V. Ta'eed, N. J. Baker, L. Fu, K. Finsterbusch, M. R. E. Lamont, D. J. Moss, H. C. Nguyen, B. J. Eggleton, D.-Y. Choi, S. Madden, B. Luther-Davies, Ultrafast all-optical chalcogenide glass photonic circuits, Opt. Express 15 (15) (2007) 9205–9221.

[172] W. C. Hurlbut, Y.-S. Lee, K. L. Vodopyanov, P. S. Kuo, M. M. Fejer, Multiphoton absorption and nonlinear refraction of gaas in the mid-infrared, Opt. Lett. 32 (2007) 668–670.

[173] L. Brzozowski, E. H. Sargent, A. S. Thorpe, M. Extavour, Measurement of large near-bandedge nonlinearities in ingaas/inalgaas multi-quantum-wells in 1.48-1.55 μm spectral range, Appl. Phys. Lett. 82 (2003) 4429–4431.

[174] G. A. Wurtz, A. V. Zayats, Nonlinear surface plasmon polaritonic crystals, Laser and Photonics Review 2 (3) (2008) 125–135.

[175] S. Xie, H. Li, H. Xu, X. Zhou, S. Fu, J. Wu, The optical transmission characteristics through gold nanoslit arrays embedded in nonlinear medium, Optics Communications 283 (6) (2010) 998 – 1003.

[176] S. Xie, H. Li, H. Xu, X. Zhou, S. Fu, J. Wu, The effect of the kerr nonlinearity on the transmission through the nanoslit gold film, SCIENCE CHINA Physics, Mechanics and Astronomy 53 (3) (2010) 474–480.

[177] C. Min, P. Wang, X. Jiao, Y. Deng, H. Ming, Beam manipulating by metallic nano-optic lens containing nonlinear media, Opt. Express 15 (15) (2007) 9541–9546.

[178] M. A. Vincenti, A. D'Orazio, M. Buncick, N. Akozbek, M. J. Bloemer, M. Scalora, Beam steering from resonant subwavelength slits filled with a nonlinear material, J. Opt. Soc. Am. B 26 (2) (2009) 301–307.

[179] C. Min, P. Wang, X. Jiao, Y. Deng, H. Ming, Optical bistability in subwavelength metallic grating coated by nonlinear material, Opt. Express 15 (19) (2007) 12368–12373.

[180] M. A. Vincenti, D. de Ceglia, V. Roppo, M. Scalora, Harmonic generation in metallic, gaas-filled nanocavities in the enhanced transmission regime at visible and uv wavelengths, Opt. Express 19 (3) (2011) 2064–2078.

[181] N. Bloembergen, W. Burns, M. Matsuoka, Reflected third harmonic generated by picosecond laser pulses, Optics Communications 1 (4) (1969) 195 – 198.

[182] G. P. Agrawal, Non-linear fiber optics, Academic Press, San Diego, 2001.

[183] J. Troles, F. Smektala, M. Guignard, P. Houizot, V. Nazabal, H. Zeghlache, G. Boudebs, V. Couderc, Third and second order non linear optical properties of chalcogenide glasses on bulk and fibers, in: Transparent Optical Networks, 2005, Proceedings of 2005 7th International Conference, Vol. 2, 2005, pp. 242–244 Vol. 2.

[184] J. Troles, F. Smektala, G. Boudebs, A. Monteil, B. Bureau, J. Lucas, Chalcogenide glasses as solid state optical limiters at 1.064 [mu]m, Optical Materials 25 (2) (2004) 231 – 237.

[185] F. Hao, P. Nordlander, Efficient dielectric function for fdtd simulation of the optical properties of silver and gold nanoparticles, Chemical Physics Letters 446 (1-3) (2007) 115 – 118.

[186] J. Renger, R. Quidant, L. Novotny, Enhanced nonlinear response from metal surfaces, Opt. Express 19 (2011) 138720.

[187] J. A. Stratton, Electromagnetic Theory, Mc-Grau Hill, New York and London, 1941.

List of Publications

- C. R. Williams,M. Misra, S. R. Andrews, S. A. Maier, **S. Carretero-Palacios**, S. G. Rodrigo, F. J. Garcia-Vidal, and L. Martin-Moreno, “Dual band terahertz waveguiding on a planar metal surface patterned with annular holes”, **Appl. Phys. Lett.** 96, 011101 (2010)

- J.-S. Bouillard, J. Einsle, W. Dickson, S. G. Rodrigo, **S. Carretero-Palacios**, L. Martin-Moreno, F. J. Garcia-Vidal, and A. V. Zayats, “Optical transmission of periodic annular apertures in metal film on high-refractive index substrate: The role of the nanopillar shape”, **Appl. Phys. Lett.** 96, 201101 (2010)

- O. Mahboub, **S. Carretero Palacios**, C. Genet, F. J. Garcia-Vidal, Sergio G. Rodrigo, L. Martin-Moreno, and T. W. Ebbesen1, “Optimization of bull’s eye structures for transmission enhancement”, **Opt. Express** 18(11), 11292-11299 (2010)

- **S. Carretero-Palacios**, Alexander Minovich, Dragomir N. Neshev, Yuri S. Kivshar, F. J. Garcia-Vidal, L. Martin-Moreno, and Sergio G. Rodrigo, “Optical switching in metal-slit arrays on nonlinear dielectric substrates”, **Opt. Lett** 35(24), 4211-4213 (2010)

- **S. Carretero-Palacios**, O. Mahboub, F. J. Garcia-Vidal, L. Martin-Moreno, Sergio G. Rodrigo, C. Genet, and T. W. Ebbesen, “Mechanisms for extraordinary optical transmission through bull’s eye structures”, **Opt. Express** 19(11), 10429-10442 (2011)

- Sergio G. Rodrigo, **S. Carretero-Palacios**, F. J. García-Vidal, and L. Martín-Moreno, “Metallic slit arrays filled with third-order nonlinear media: Optical Kerr effect and third-harmonic generation”, accepted in **Phys. Rev. B** 83, 235425 (2011)

- **S. Carretero-Palacios**, F. J. García-Vidal, L. Martín-Moreno, and Sergio G. Rodrigo, “ Effect of film thickness and dielectric environment on the optical transmission through sub-wavelength holes", submitted to **Phys. Rev. B**

Acknowledgements

Para mí, esta tesis ha sido una carrera de resistencia que solo he podido terminar gracias a un buen entrenador, un gran equipo, y un público incondicional que no ha parado de animarme. Estos son los protagonistas de mi particular carrera:

Primero quiero agradecer esta tesis a Luis. Por su confianza, tiempo infinito, paciencia, su manera de explicar las cosas, por sus ánimos constantes, y su espíritu luchador. A mi grupo de Zaragoza, Alexey, los 3 Fernandos, Sergio y Gianni, por todo lo que me han enseñado y por compartir tantos buenos momentos.

Por supuesto al grupo de FJ, en la UAM (Madrid), empezando por él mismo y continuando por Diego, Antonio, Paloma, Juan Antonio, Esteban, Max y Jorge. Por los increíbles viajes y conversaciones que hemos tenido juntos. Me llevo grandes amigos de allí.

También quiero agradecer las colaboraciones con Thomas Ebbesen, Oussama y Cyriac, en la ULP; a Anatoly Zayats y Jean Sebastian en la QUB; a Stefan Maier en el Imperial College, y a S. R. Andrews, C. R. Williams y M. Misra en la Universidad de Bath. También a Ross Stanley, Andrea y Mickael en CSEM, así como a Yuri Kivshar, Dragomir y Alex en la ANU (Australia).

Gracias a Arturo y Guillermo en el BIFI, por solucionar todos mis problemas de acceso al cluster...habéis sido fundamentales, sin duda.

Todos los cursos, estancias y congresos a los que he asistido también han contribuido a terminar esta carrera de resistencia. Se lo quiero agradecer a Olalla, Aitzol, Santiago, Viktor, Jacqui y Eike, y a mi pequeña familia australiana, Kim, Clea y Tom. Por apoyarme y animarme, enseñarme tantas cosas y hacerme reír horas y horas.

Los 4 años en este departamento han sido sin duda mucho mejores gracias a las sonrisas de unos cuantos becarios y profesores en los pasillos. Gracias a ellos, por hacernos ver que no somos invisibles, en especial a Zueco, Jesús, Boada, Cris, Ana, Carlos, Adriana, Marta, Albertito y Poncela...A todos mis compis de todos los despachos en los que he estado, Pablo, Fran, Campana, Diego y Saeid. Y en especial quiero darle las gracias a mi grupo de “autistas” favo: Clara, Vera, María, Enrique, Raquel, Pepa y Sara. Por hacerme sentir como en casa, por las pelucas, risas, mudanzas y Desafinados. Por enseñarme 7 puntos de vista distintos cada día, con los que he aprendido a salir del “blanco o negro”. Nada habría sido igual sin vosotros. Pero además quiero agradecérselo especialmente a Pepa y Clara. A Pepa, mi pequeña alma gemela a pesar de que nos parezcamos tanto como un huevo y una castaña. Por acogerme aquel mes en tu casa, cuidar de mí, estar siempre que te he necesitado, que han sido muchas veces. Por enseñarme que la vida son 2 días, y que sin emociones y aventuras todo es infinitamente más aburrido. Por tu sonrisa constante. Y a Clara, por nuestras 24h juntas, llenas de miles de risas y locuras. Gracias también a Jesús y Mr. Pons.

Fuera de Zaragoza, quiero agradecérselo a mis amigos de Jaca. A todos los “tinis” sin excepción, pero principalmente a Patata, Otis, Hirnon, Osito, Cuarter, Txabu, Txupi, los Empans, Nacho, Segu, Guelo y Pololo, y con más ilusión aún a Berges, Pollo, Bako y Simón. Os debo una vida a cada uno, por todo lo que me habéis demostrado, por escuchar mis chapadas de física y cuidarme siempre. También a Txuan, porque sin ti nunca hubiera empezado esta tesis, y porque fuiste mi mejor apoyo en la primera etapa. No me olvido de un pequeño sector loco: Maite, Anakin, Loreto e Isabel.

Con especial cariño me acuerdo de todos mis colegas de Madrid. Nunca he sentido que me hubiera ido de allí. Gracias por hacerme sentir que mi rareza es normal. Todos vuestros mails, mensajes, llamadas, y visitas han sido fundamentales para que cada día hiciera un cálculo nuevo con más ilusión que el anterior. Gracias Chofo, Xavi, Arandela, Julita, Willy, Zinnia, Mery, Gon, Rizo, Claus, Cris, Lauser, Valans, Nere, Nacho y Blau. Qué haría yo sin vosotros?! Pero fundamentalmente a ti, Nere, por contagiarme tu serenidad y demostrarme que nunca te fuiste de mi lado. Gracias a Mario. A Jaime, Tucho, Luis-Luis y Birras...por todas las risas que nos hemos echado durante años y por no olvidaros nunca de mí.

Y para terminar, mi pequeña burbuja de tranquilidad: mis padres, mi hermano y mis perritas. Nunca lo hubiera conseguido sin vosotros. Gracias con todo mi corazón. Papá, esta tesis, es también la tuya. Espero que la hayáis disfrutado tanto como yo. Os quiero mil. Gracias también a Marta y Javo, a Sebas y Marimar, Andrés, Juan, y la Marga. A Gé. Por vuestros constantes ánimos y por escuchar también grandes chapadas. A la abuela Laly, a mis tíos y mis primas de Torremayor. A Martita, y a Laia.

Gracias a todos. Lo conseguimos*

ISBN 978-84-15274-57-5

9 788415 274575

1542

Prensas Universitarias
Universidad Zaragoza